THE EXPERIMENTAL CAMPAIGN AND NUMERICAL SIMULATIONS OF THE CONSTRAIN PROJECT

TECHNICAL REPORT – PART 1

INTERPRETATION OF EXPERIMENTAL RESULTS

N. Gattesco[a], I. Boem[a], E. Rizzi[a], A. Bez[a], M. Gams[b], M. Farič[b], V. Pučnik[b], A. Dudine[c]

[a]*University of Trieste, Department of Engineering and Architecture, Via Alfonso Valerio 6/1, 34127 Trieste, Italy*
[b]*University of Ljubljana, Faculty of Civil and Geodetic Engineering, Jamova cesta 2, 1000 Ljubljana, Slovenia*
[c]*Fibre Net S.p.a., Via Jacopo Stellini, 3 – Z.I.U., 33050 Pavia di Udine (UD), Italy*

CONTENTS

1 Introduction

Assessing the structural behaviour of existing masonry structures under seismic excitation is a complex engineering problem, and planning and estimating the effect of an intervention to improve the seismic response is even more complicated. The problem includes engineering issues, such as how to improve the response of structures built of weak and flexible old masonry with new materials, which are much stronger and stiffer. But the problems encountered when planning an intervention are not only engineering ones. Owners may wonder, does the intervention require that the residents move out temporarily? For how long do they have to move out? If there is an extensive intervention inside the building, how will it affect existing installations? Finally, the direct and indirect costs of interventions to improve the seismic response of masonry structures are not cheap. All these factors make it difficult for owners to decide for such interventions. Therefore, they often keep the buildings in their existing state, which is vulnerable to earthquakes. The impact of this risk on society is significant because of a large share of such buildings in building stock. Alternatively, they may choose a demolition and brand new construction, which requires a lot of resources and, by extension, produces many emissions.

The CONSTRAIN project aims to develop new methods of strengthening that are less invasive and more comfortable for the residents. This is achieved mainly by limiting the interventions to one side of the structure. The proposed strengthening technology is based on coating the walls with composite (GFRP mesh) reinforced mortars (CRM system) and advanced anchors on only one side.

One of the problems with proposing a strengthening intervention only on one side of the wall is that the confidence of the professional community in such interventions is low. In the case of seismic loads with many load reversals and potentially large compressive stresses in the wall, the coating can lose the bond to the wall and detach. If this happens, the composite action of the wall and the coating is lost, and the coating becomes ineffective. In the case of coating on both sides of the wall, the situation is much better. Coatings on both sides can be connected by anchors, which confine the wall in the middle, connect all leaves of the wall and increase the compatibility with the (weak) masonry wall. The structural engineer will prefer two-sided coating and consider one-sided coating only if there are enough proofs that it works.

Due to scepticism of the professional community about one-sided coatings, the experimental campaign in the project was extensive (Table 1). It consists of eight full-scale in-plane cyclic shear compression tests on piers, three full-scale out-of-plane cyclic tests on piers, eight full-scale cyclic tests on spandrels, strengthened with the CRM system; moreover, two tests on the strengthened tie-beams, with GFRP mesh in bed mortar joints, and two tests on mid storey tie-beams made by using strips of a carbon fibre reinforced polymer (CFRP).

Three types of masonry were considered in the tests: two-leaf rubble stone masonry and single and double-leaf brick masonry. The strengthening intervention was specially designed for each of the masonry types.

A test setup had to be designed, manufactured, and assembled for each type of test. Furthermore, a sample had to be constructed for each individual test, equipped with instruments, tested, and the results processed. After each test, the sample had to be demolished and the rubble disposed of.

Finally, a full-scale pilot building was tested in reference and strengthened state to demonstrate the efficiency of the proposed strengthening technique (CRM system) in real-life conditions and in a systematic way. The results of the tests conclusively show that the proposed strengthening works well, improves structural response, is cost-effective and quick and easy to apply.

This report presents the results of all the tests performed within the project. The report, in its second part also includes the results of many numerical simulations. Some numerical simulations were performed to derive crucial material parameters required for design, and these parameters are calculated and presented in the report next to each test. Other numerical simulations were done to evaluate the performance of existing mathematical models by comparing them to the experimental results. These comparisons were successful, which shows that the developed strengthening intervention can be designed using existing design software and mathematical models. Furthermore, the abovementioned material parameters obtained from the tests can be used in the design.

The last numerical analysis is a case study on an actual five-storey building to compare the costs of a standard intervention using coating on both sides and the newly developed method with coating on only one side. The results overwhelmingly show that the newly developed method is more cost-efficient. Crucially, when the new method is used, the residents can stay in the building, and the business is not interrupted.

2 Experimental program

Table 1: Experimental program of CONSTRAIN project

Type of test	Masonry type	Wall wythes	Label	Strengthening
Shear compression tests on masonry piers	Stone	2	P-R2U	/
	Stone	2	P-R2R-1	CRM on one-side
	Stone	2	P-R2R-2	CRM on two-sides
	Solid brick	2	P-B2U	/
	Solid brick	2	P-B2R-1	CRM on one-side
	Solid brick	2	P-B2R-2	CRM on two-sides
	Solid brick	1	P-B1U	/
	Solid brick	1	P-B1R	CRM on one-side
Out-of-plane bending tests on piers	Solid brick	1	B-B1	CRM on one-side
	Solid brick	2	B-B2	CRM on one-side
	Stone	2	B-R2	CRM on one-side
Shear-bending tests on masonry spandrels	Stone	2	S-R2-1	/
	Stone	2	S-R2R-1	CRM on one-side
	Stone	2	S-R2-2	/
	Stone	2	S-R2R -2	CRM on two-sides
	Solid brick	2	S-B2	/
	Solid brick	2	S-B2R	CRM on one-side
	Solid brick	1	S-B1	/
	Solid brick	1	S-B1R	CRM on one-side
Out-of-plane bending on top tie beams	Stone	2	T-R2	GFRP mesh embedded in bed joints
	Solid brick	1	T-B1	GFRP mesh embedded in bed joints
Out-of-plane bending tests on masonry C walls	Stone	2	C-R2	CFRP strips
	Solid brick	1	C-B1	CFRP strips
Pilot building	Stone	2	PB-U	/
	Stone	2	PB-R	CRM on one-side

Each specimen is identified with an alphanumeric string split into three parts, as shown in Table 2.

The specimen drawings are reported in the Appendix.

Table 2: Naming convention

Type of specimen or test	Masonry typology	State	Number of strengthened sides or sample number
P: pier in shear compression	R2: two leaf rubble stone	U: unreinforced	1 / 2
S: spandrel	B1: one leaf brick	R: reinforced	
B: pier in three-point out-of-plane bending	B2: two leaf brick		
C: out-of-plane bending on C walls			
T: out-of-plane bending of top tie beams			
PB: pilot building			

3 Materials

3.1 Materials for construction

3.1.1 Stones

The stone masonry specimens were built using two varieties of Credaro stone: Berrettino and Medolo. The mechanical properties of the stones were taken from the available technical data sheet[1] and reported in Table 3.

Berrettino is a sandstone with calcareous composition and a compressive strength of about 165 MPa. It's made up entirely of calcite and contains traces of quartz. Medolo is a microcrystalline limestone with a compressive strength of about 144 MPa. Carbonates make up more than 50% of this stone.

Stones with different lengths and widths were supplied from the quarry in bulk and sorted by Kolektor CPG d.o.o. (partner in the project). Because of their varying size, the stones were shaped by hammers on-site before being used for construction. This process is shown in Fig. 1.

Table 3: Mechanical properties of stones.

Stone type	Density [kg/m³]	Compressive strength – perpendicular to bedding [MPa]	Compressive strength – parallel to bedding [MPa]	Flexural strength [MPa]
Medolo	2658	172	165	23
Berrettino	2579	149	144	19

Fig. 1: Sorted stones ready for construction (left) and shaping of stones by hammer (right).

---

[1] http://www.naturalstoneinfo.com/download/bgcamcom.pietra_credaro.pdf

3.1.2 Bricks

The commercial name of the solid bricks is *San Marco rosso vivo – Terreal.* A complete description can be found on the producer's website[2]. The photo of the units is shown in Fig. 2, left.

Fig. 2: Sorted bricks (left)and hammering in halves (right).

The nominal dimensions of the bricks were length/height/thickness=25/5.5/12 cm. The peculiarity of the bricks is that they have a rough surface, similarly to bricks in old buildings. Table 4 presents the mechanical properties of the bricks.

Table 4: Mechanical properties of bricks.

Property	
Dimensional stability	≤ 0.6 mm/m
Compressive strength	18 N/mm2

3.1.3 Mortar for construction

The mortar used in the tests simulated an old, weak mortar. It was a specially designed mixture of natural hydraulic lime and sand in a mass ratio of about 1:8. The ready-to-use mix was provided in sacks, and only a required amount of water had to be added before construction.

The grain size distribution of the aggregate ranged between 0.05 and 3 mm, and about 45% of sand had a size smaller than 0.5 mm.

The mortar's bending (f_{tmo}) and compressive (f_{cmo}) strength were determined on prisms with dimensions of 160/40/40 mm. The prisms were sampled at regular intervals during the construction of each specimen. Compression tests on the halves resulting from the three-point bending tests were performed according to EN 1051-11, as shown in Fig. 3.

The test results are summarized in Table 5.

---

[2] https://www.sanmarco.it/it/gamma-facciate/vivo
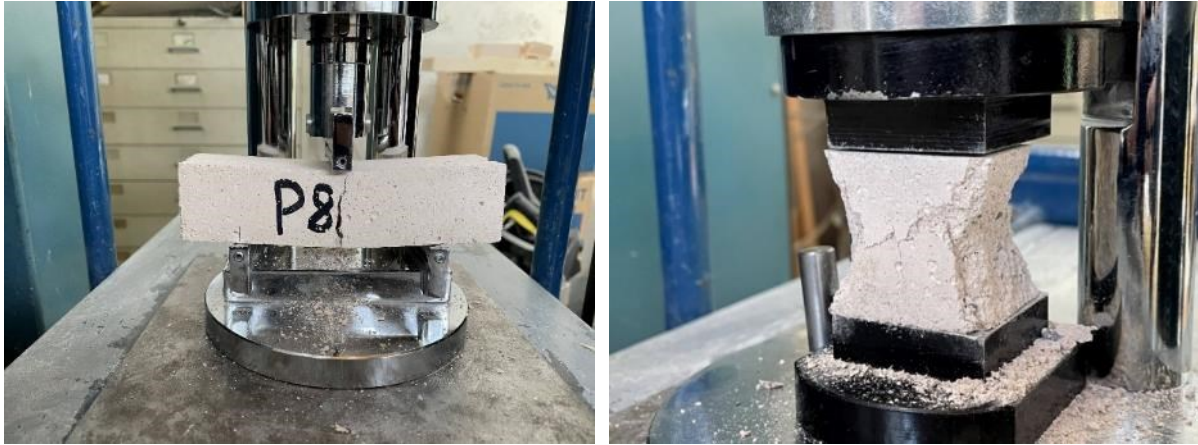
Fig. 3: Testing flexural (left) and compressive strength (right).

Table 5: Mechanical properties from tests on masonry prisms.

Specimen name	Number of samples	Age at testing [days]	Mechanical properties	
			f_{tmo}[MPa] (CoV [%])	f_{cmo}[MPa] (CoV [%])
S-R2-1, A3_1, A3_1	-	-	0,23 (18 %)	1,11 (17 %)
S-R2-2	21	36	0,36 (23%)	1,95 (12 %)
S-B1	/	/	/	/
S-B2	21	38	0,30 (15 %)	1,86 (6 %)
A2_1, A2_2	6	34	0,30(10 %)	1,50 (9 %)
A1_1, A1_1	6	97	0,29 (12 %)	1,63 (7 %)
T1	12	43	0,76 (10 %)	1,99 (11 %)
T2	6	43	0,59 (5 %)	1,62 (7 %)
P-R2U, P-R2R-1, P-R2R-2,B-R2	12	66	0.17 (16%)	0,93 (5 %)

*CoV = Coefficient of Variation
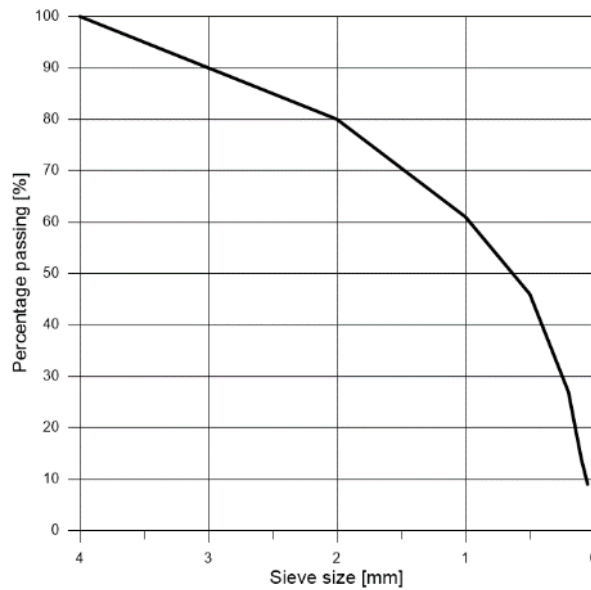
Fig. 4: Sieve mortar curve

3.2   Materials for strengthening

3.2.1   Mortar for strengthening

The mortar used for the reinforced coating was *Epoca Calce – NHL 115*, a commercially available product, produced by Fibre Net S.p.A. The thickness of the coating on the walls was about 30 mm from the most external parts of the masonry face. The mortar's bending and compressive strength were determined on prisms with dimensions of 160/40/40 mm. The results for each specimen are summarized in Table 6.

Table 6: Mechanical properties of mortar for strengthening.

Specimen name	Number of samples	Age at testing [days]	Mechanical properties	
			f_{tmo}[MPa] (CoV [%])	f_{cmo}[MPa] (CoV [%])
S-R2-1	3	40	4,2 (5 %)	22,9 (10 %)
S-R2-2	12	38	5,6 (4%)	24,6 (5 %)
S-B1	12	84	4,4 (7 %)	20,1 (8 %)
S-B2	15	39	3,87 (15 %)	14,99 (20 %)
P-R2R-1, P-R2R-2,B-R2	6	35	3,0 (10 %)	30,1 (4%)

*CoV = Coefficient of Variation

3.2.2   GFRP mesh

The GFRP mesh was provided in rolls and cut to size at the construction site (as shown in Fig. 5)

Mesh had grid spacing of 66 × 66 mm and an average thickness of 3 mm. Fibre yarns sections had an 8.8 mm² and 8.0 mm² cross-sectional area in the warped and weft direction, respectively, determined on the average of three samples. The mechanical properties presented in Table 7 were obtained from the available datasheet [3] and tests on three samples per direction.

Smaller meshes with the same yarns but with 33 mm spacing were used with the GFRP L connectors shown later. These meshes were cut to 150 x 150 mm (Fig. 6).

Table 7: Mechanical properties of the GFRP mesh.

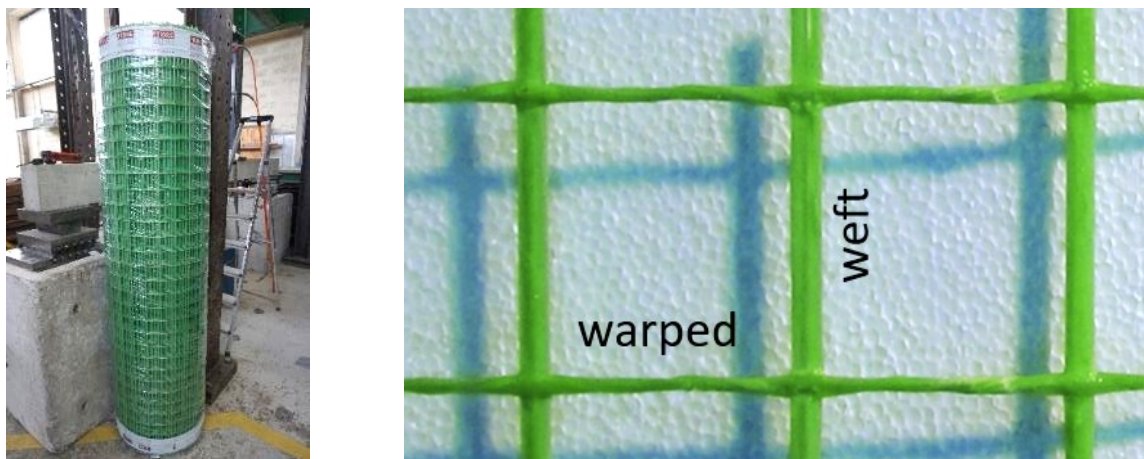|	Elasticity modulus [GPa]	Average tractional strength [MPa]	Characteristic tractional strength [MPa]	Average deformation at rupture [%]
Technical datasheet	25000	490	375	1.8
Test on warped yarns	$3.32 \cdot 10^4$	611	-	1.85*
Test on weft yarns	$3.64 \cdot 10^4$	883	-	2.50

* determined on only one sample

Fig. 5: GFRP mesh for reinforcing was provided in rolls (left). Close-up of the mesh(right).

Fig. 6: Mesh sheets with smaller spacing to use with L connectors.

---

[3]Fibre Net mesh: https://www.fibrenet.it/product/fbmesh66x66t96ar/?lang=en
 Fibre Net mesh sheet: https://www.fibrenet.it/product/fbfaz33x33t96ar/?lang=en

3.2.3 Connectors

The strengthening technique performed in this study required two types of connectors. The first type is the GFRP "L-shaped" connector (Fig. 7). This connector has a $s_1 \times s_2 = 10 \times 7$ mm cross-section. The shorter side (L_2) of the connector was 10 cm long, while the longer one (L_1) was 20 or 30 cm long. As per the technical datasheet[4], connectors had a characteristic tensile strength of 380 MPa and 1.9% ultimate strain. Material characteristics are shown in Table 8.

GFRP connectors were inserted into previously drilled holes and injected with FCVIN 400 CE[5], a two-component vinylester chemical anchor.
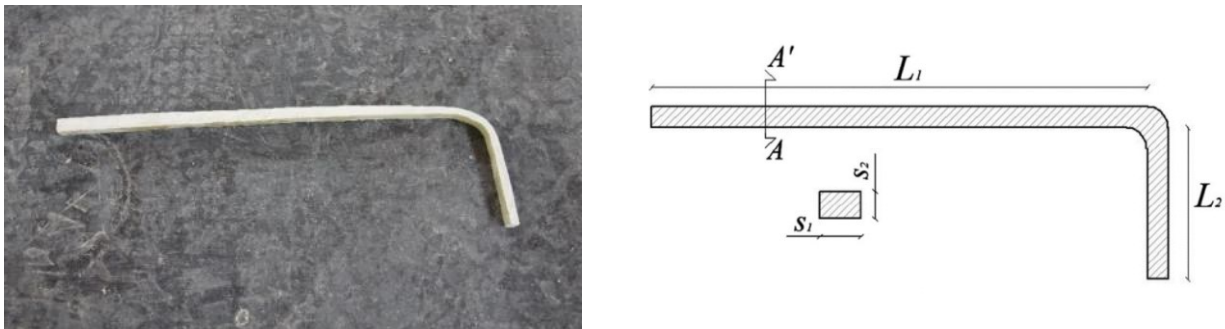
Fig. 7: GFRP "L-shaped" connector.

The second type of connector (called "diaton") consists of a threaded stainless-steel M16 bar and a perforated circular steel plate (Fig. 8). The steel plate had a diameter of 150 mm and a thickness of 4 mm. These connectors served two purposes. Firstly, they improve the connection between wall wythes as such connections are often poor in old masonry walls. Secondly, they anchor the mesh to the wall.

The "diaton" anchors were inserted into 50 mm diameter holes. The hole was then injected with Struttura Tixo – TX 100, a two-component, shrinkage-compensated, fibre-reinforced cementitious mortar with synthetic fibers. Datasheet reports that after 28 days, the mortar reaches a compressive strength of 55 MPa[6].

Fig. 8: Steel connector or "artificial diaton".

---

[4] https://www.fibrenet.it/wp-content/uploads/2018/05/FBCONL.pdf
[5] https://www.fibrenet.it/wp-content/uploads/2018/03/FB-TEC-0502-FCVIN-400CE-rev.-1.1.pdf
[6] https://www.fibrenet.it/product/struttura-tixo-tx-351/?lang=en

Table 8: Characteristics of the L-shaped connectors[7].

Ultimate strain [%]	Traction resistance – average/median value [MPa]	Traction resistance – characteristic value [MPa]
1.9	450	380

3.3   Stone masonry

Stone masonry was built as a two-leaf wall without connector stones. A view of a typical row is shown in Fig. 9, left. There was an overlapping of stones between different rows, as shown in Fig. 9, right.

Fig. 9: Stones in two-leaf masonry wall (left). Overlapping of stones between rows (right).

The compressive strength and elastic modulus of stone masonry were determined on two samples. Results are shown in Table 9. The ultimate strain was 1.2 % and 2.8 % for samples A3_1 and A3_2, respectively.

Table 9: Mechanical properties of stone masonry.

Specimen number	Age [days]	Fracture force [kN]	Compressive strength [MPa]	Modulus of elasticity [MPa]	Ultimate strain [%]
A3_1	77	451.64	2.58	1162.0	1.2 %
A3_2	77	416.96	2.38	986.4	2.8 %
Average/total	77	434.30	2.48	1074.2	2 %

3.4   Double leaf brick masonry

Double leaf brick masonry was built with all bricks oriented in one direction, and the mortar was the only connection between the wythes. The view of the masonry is shown in Fig. 10. Note that the vertical joint is running the entire wall height.

---

[7] https://www.fibrenet.it/product/fbcon/?lang=en

Fig. 10: Double-leaf brick masonry.

The compressive strength and the elastic modulus of stone masonry were determined on two samples. Results are shown in Table 10.

Table 10: Mechanical properties of double-leaf brick masonry.

Specimen number	Fracture force [kN]	Compressive strength [MPa]	Modulus of elasticity [MPa]	Ultimate strain [%]
A2_1	875.60	6.86	2073.5	1.1
A2_2	750.68	6.00	2293.1	*
Average	**813.14**	**6.43**	**2183.3**	**1.1**

* Instruments were damaged after reaching a strain of 0.37%

3.5 Single leaf brick masonry

Single-leaf brick masonry was built in classical English bond. The bricks in one row were oriented perpendicularly to the other row. The view of the masonry is shown in Fig. 11.

Fig. 11: Single leaf brick masonry.

Table 11: Mechanical properties of single-leaf brick masonry.

Specimen number	Fracture force [kN]	Compressive strength [MPa]	Modulus of elasticity [MPa]	Ultimate strain [%]
A1_1*	490.3	3.8	1589.1	0.35
A1_2	852.4	6.7	2341.1	**
Average/total	**852.4**	**6.7**	**2341.1**	-

* Failure of the sample was not centric. Values are not considered.
** Instruments were damaged after reaching a strain of 0.3%

3.6 Materials for repairing

Some specimens were first tested in their original state up to significant damage and repaired.

Cracks were injected with *Kemagrout CI50*[8], a mixture of cement and plasticizing additives with shrinkage compensation and high initial and final strength. The injection mass has low viscosity.

After 24 h, the grout has a compressive strength of 33.7 MPa. After 28 days, it reaches 65.4 MPa.

It should be noted that repair was used only for walls damaged from earlier testing, and these walls had to be repaired (cracks sealed and filled) before strengthening could be applied.

---

[8] https://formatiq.pl/produkt/kemagrout-ci-50-mieszanka-cementow-i-dodatkow-uplastyczniajacych/

4 Construction

4.1 Stone masonry

The concrete foundation block for stone masonry was wetted before the first layer of mortar was spread, and the stones were soaked in water and shaped by a hammer before laying.

Mortar was prepared by mixing the dry mortar mix with a prescribed amount of water, and it was used to fill the head and bed joints. In all of the samples, to avoid the sliding of the wall at the masonry – concrete interface, in the first and last mortar bed joints, a mass of 2.5 kg of R 32.5 pozzolanic cement was added to the mix for every 25 kg of dry mortar. The thickness of the joints was about 1 cm but varied significantly due to the irregular shape of the stones.

Different steps of the construction are shown in Fig. 12 and Fig. 13.
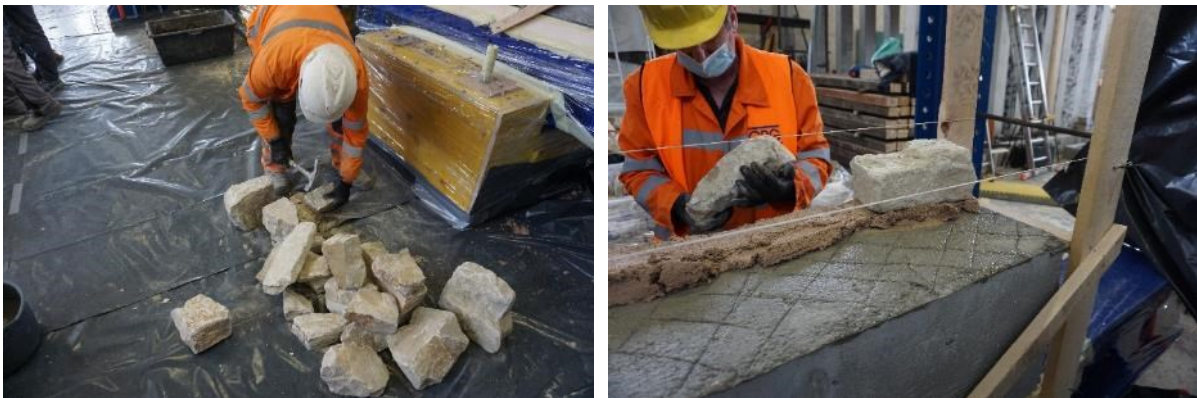

Fig. 12: Hammering of stones before installation (left) and construction of the first row (right).

Fig. 13: Construction of stone masonry wall.

4.2 Brick masonry

The concrete foundation block for brick masonry was wetted before the first layer of mortar was spread, and the bricks were soaked in water and cut to size if needed by a circular saw before laying.

The mortar was prepared by mixing the dry mortar mix with a prescribed amount of water, and it was used to fill the head and bed joints. The thickness of the joints was 1 cm.

Different steps of the construction are shown in Fig. 14 and Fig. 15.

Fig. 14: Soaking the bricks before laying (left) and cutting by a circular saw (right).

Fig. 15: Filling joints (left) and specimen during construction (right).

4.3 Installation of L connectors

The holes for the L connectors were drilled using a 16 mm or 24 mm diameter bit. The holes were filled using FCVIN 400 CE vinylester chemical anchor (Fig. 16, left), and the anchors were inserted. The anchors were inserted once the mesh was already in position. Finally, the smaller spacing mesh is placed under the anchor to provide better stress distribution (Fig. 16, right).
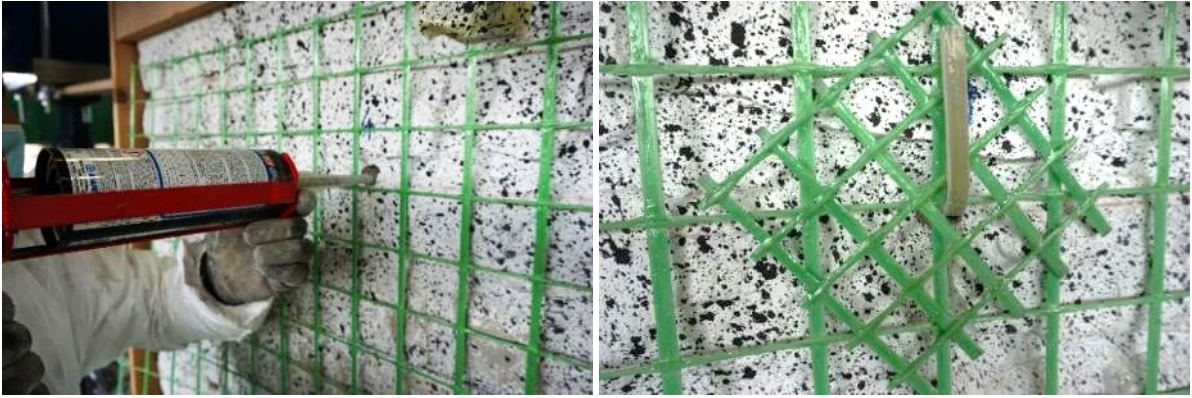
Fig. 16: Injection with resin (left); L-shaped connector with additional mesh (right).

4.4 Installation of diaton connectors

In the first step, the 50 mm holes for diatons were drilled to the prescribed depth or through the wall (Fig. 20, left). Next, the steel bar was placed into the hole and temporarily fixed in position (Fig. 20, right). The TX100 grout was injected using a manual grout syringe (Fig. 16, left). After the coating was applied, the anchor plate was screwed on the threaded bar (Fig. 16, right), and the protruding part was cut off.

Fig. 17: Drilling of 50 mm holes (left); temporary fixing of diaton (right)

Fig. 18: Injecting TX100 grout (left); installed anchor plate (right).

4.5 Repair of damaged walls

Repair of damaged walls was performed in the same way for stone and brick masonry. In the first step, the surface of the walls was cleaned with a wire brush (Fig. 19, left). Next, the cracks were sealed using the fast-

setting mortar (Fig. 19, right). Finally, two holes were drilled into the crack at the top of the wall (Fig. 20, left). The injection was poured through one of them (Fig. 20, right). The injection filled the cracks by gravity.

Fig. 19: Cleaning the surface (left) and sealing the cracks (right).

Fig. 20: Drilling the holes for the injection (left) and gravitational injection of the wall (right).

4.6 The procedure for strengthening on one side

The steps of the strengthening procedure are:

1. Remove existing plaster to expose the load-bearing masonry and remove mortar in joints to a depth of about 10-15 mm, only on the outside.

2. Drill 25 cm deep $\phi16$ mm holes (approx. 4 / m^2) for the L-shaped connectors and almost or entirely through the wall (2 / m^2) for diatons (ϕ 50 mm). The holes must be made close to the mortar and cleaned before injection.

3. Insert the threaded rods and inject the holes with thixotropic mortar to create artificial diatons (Fig. 21). In the case of voids inside the wall, use a sock or a metal mesh sleeve to contain the grout.

4. Apply GFRP mesh over the entire surface of the wall.

5. Insert L-shaped connectors (4 / m^2) in the previously made holes (Fig. 22).

6. Inject epoxy resin in the holes for L connectors until completely filled.

7. Apply GFRP smaller spacing mesh locally under the L connectors to improve anchoring (Fig. 16, right).

8. Anchor the coating into the foundation with ϕ 8mm AISI 316 steel bars. The bars should be anchored with epoxy resin 300 mm deep into the foundation. The position of the anchors is 15 mm from masonry, and the anchors should protrude at least 400 mm from the foundation.

9. Wet the surface and apply a 30 mm thick mortar coating for strengthening.
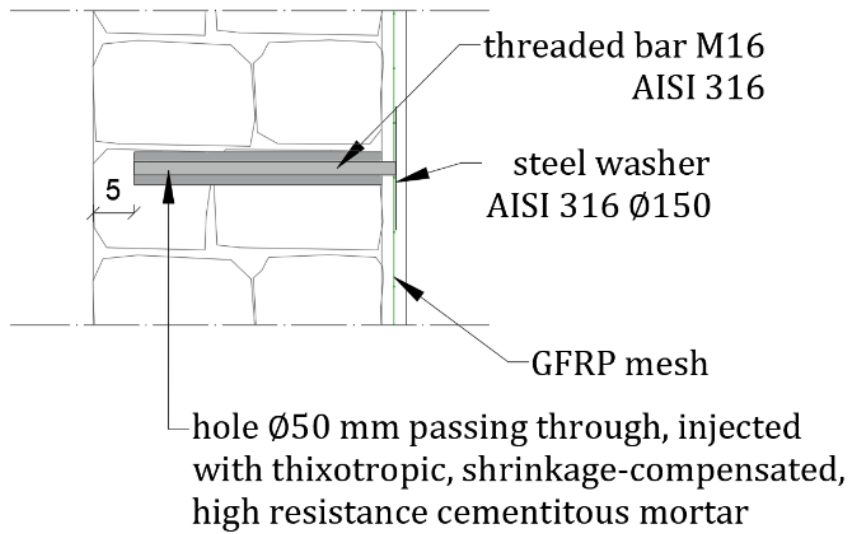
Vertical section view

threaded bar M16
AISI 316

steel washer
AISI 316 Ø150

5

GFRP mesh

hole Ø50 mm passing through, injected
with thixotropic, shrinkage-compensated,
high resistance cementitous mortar

Fig. 21: Detail of the diaton for single-sided strengthening

Vertical section view

GFRP "L" connector

GFRP mesh sheet

GFRP mesh

hole Ø16 mm - L=22 cm
injected with epoxy resin
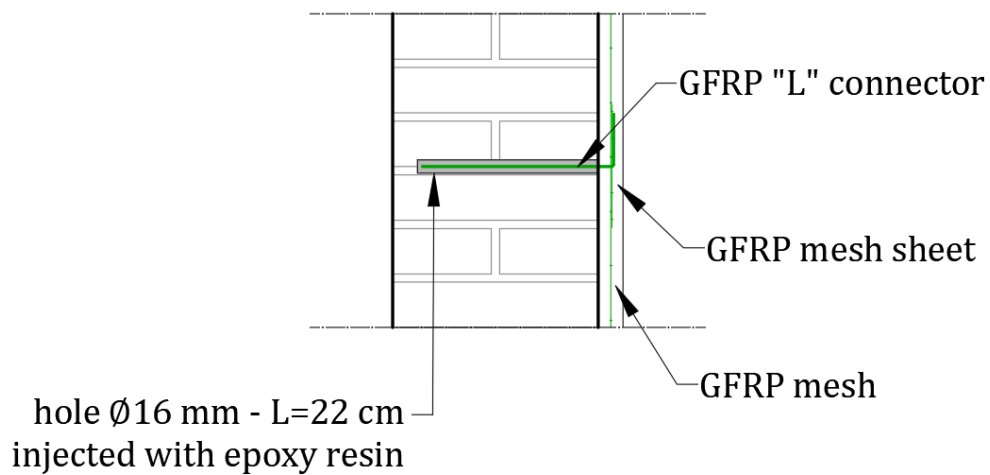
Fig. 22: Detail of the L connector for single-sided strengthening

Vertical section view

GFRP "L" connectors, overlap ≥ 16 cm

GFRP mesh sheet

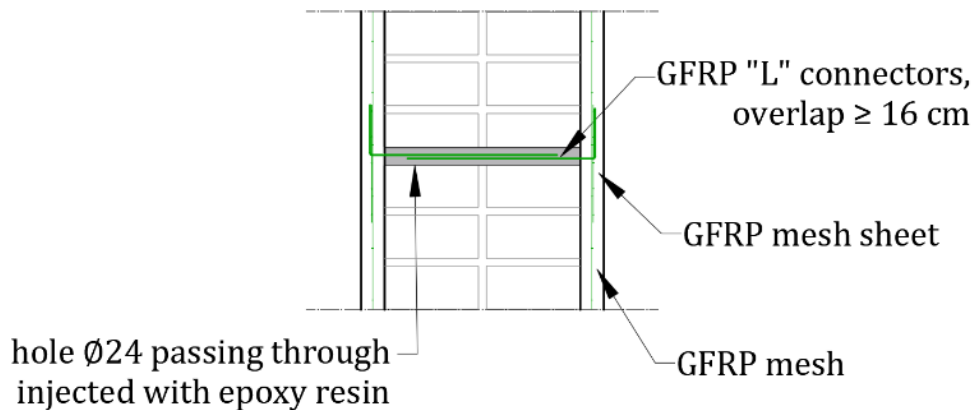hole Ø24 passing through injected with epoxy resin

GFRP mesh

Fig. 23: Detail of the L connector for double-sided strengthening

4.7 The procedure for strengthening on both sides

The steps of the strengthening procedure are:

1. Remove existing plaster to expose the load-bearing masonry and remove mortar in joints to a depth of about 10-15 mm; on both sides of the wall.

2. Drill ϕ24 mm holes through the wall (approx. 6 / m2) for the L-shaped connectors. The L connectors should overlap at least 16 cm inside the wall.

3. Apply GFRP mesh over the entire surface of the wall.

4. Insert L-shaped connectors (6 / m2) into the previously made holes (Fig. 23).

5. Inject epoxy resin in the holes for L connectors until completely filled.

6. Apply smaller spacing GFRP mesh locally under the L connectors to improve anchoring (Fig. 16, right).

7. Anchor the coating into the foundation with ϕ 8mm AISI 316 steel bars. The bars should be anchored with epoxy resin 300 mm deep into the foundation. The position of the anchors is 15 mm from masonry, and the anchors should protrude at least 400 mm from the foundation.

8. Wet the surface and apply a 30 mm thick mortar coating for strengthening.

5 Instrumentation

5.1 Displacement transducers

Linear (Fig. 24a) and multi turn wire wound (Fig. 24b) potentiometric transducers were used during the tests to measure the displacements of the samples. These work by transforming the relative displacement of the shaft (linear) or its winding (wire wound) in an electric signal that is read by the control unit, that converts it in an equivalent displacement, based on the instrument calibration constant.
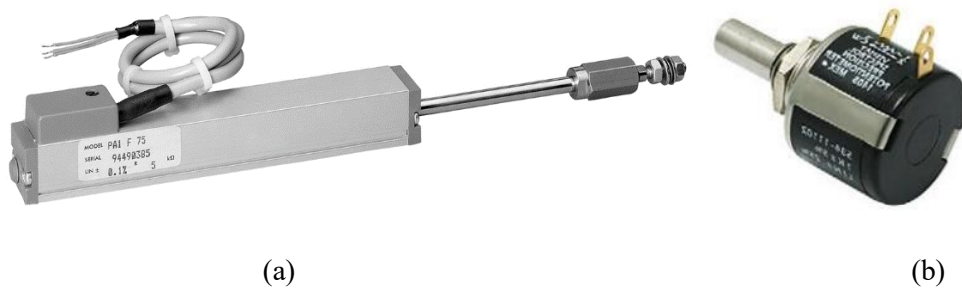

(a)   (b)

Fig. 24: (a) linear potentiometer transducer; (b) multi-turn wire wound potentiometer transducer

5.2 Digital image correlation system

The digital image correlation system (DIC) works by comparing photographs taken at different times. A pair of cameras are used to obtain a 3D position using the same principle as the stereo vision of humans (see Fig. 25). The system is calibrated to give accurate measurements.

The computation difficulty lies in identifying the same point in images from both cameras and at different times. For this process to work, a random speckle pattern is required.

The system works best with flat surfaces. The advantage of the system is that it gives the displacement field over the entire visible surface. Strains and other quantities can be calculated based on measured displacement fields.

Fig. 25: The concept of locating a point in 3D using two cameras, left. The cameras used in the project, right.

An example of a displacement and strain field is shown in Fig. 26. The horizontal displacement field in Fig. 26 clearly shows that the left part of the wall moved to the left (blue colour is negative displacement). The

right part moved to the right (red colour is positive displacements). The amount of displacement is indicated by the colour according to the legend on the right-hand side.

The strain field in Fig. 26, right, shows the strain concentrations. Warm (red) colour indicates cracks, which are mostly diagonal due to shear loads. The system makes it possible to see which cracks open the most.
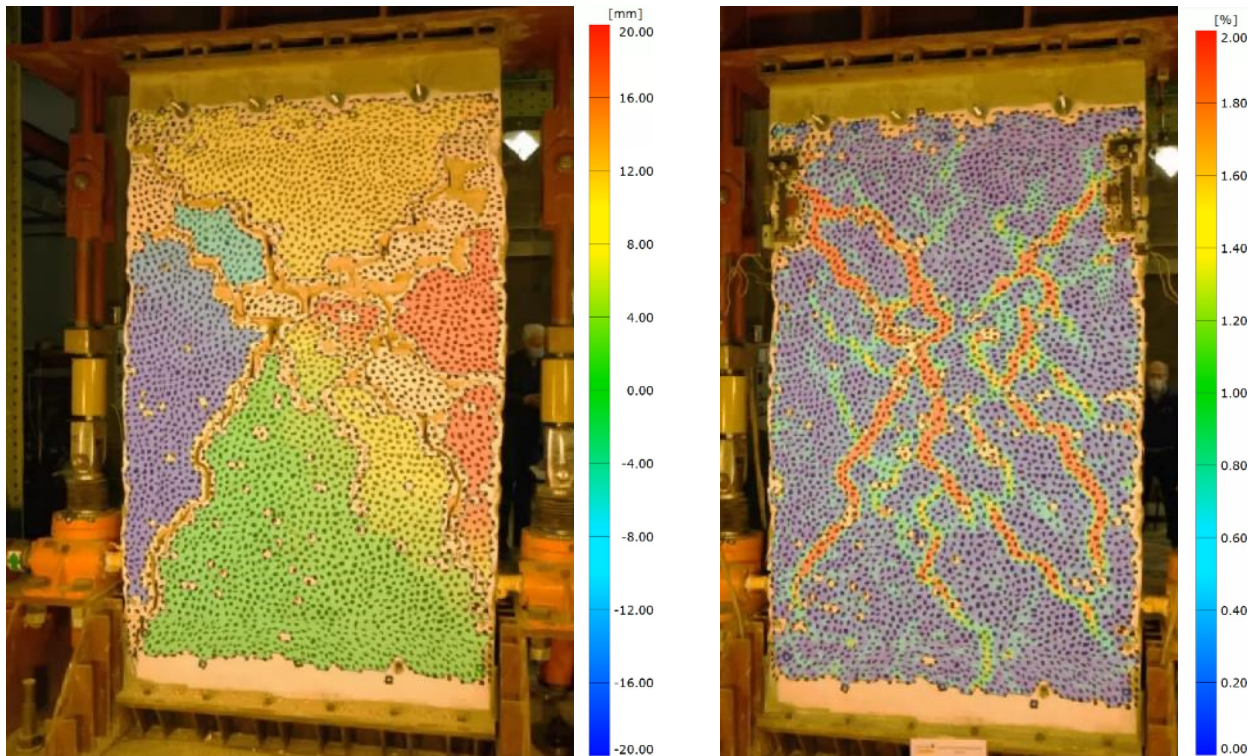

Fig. 26: Horizontal displacement field by DIC system, left. Strain field by DIC system, right.

5.3   Seismic accelerometers

Seismic accelerometers are instruments that measure accelerations at specific locations, and they were used to measure the dynamic properties of the pilot building. The accelerometers (model 3741B122G, Fig. 27) were chosen as they are the most suitable for measuring the vibrations of structures due to ambient excitations. Their measurement range is ± 0.5 g.

Fig. 27: Accelerometer

6 Shear compression tests on piers

In a shear-compression test, a single masonry pier is tested under the conditions which simulate the earthquake horizontal action. The tests are essential for determining material characteristics of masonry, assessment of seismic response/behaviour and failure mechanism of structures.

The compressive stress state due to the weight of the building above the tested wall is simulated by vertical forces. The earthquake (seismic) load is imposed on the wall in the form of prescribed displacements, which act cyclically in positive and negative directions and with increasing amplitude until collapse. Finally, the boundary conditions during the test must be similar to those in a structure. The so-called fixed-fixed (no rotation at the bottom and at the top and with constant vertical force) boundary conditions are most commonly used.
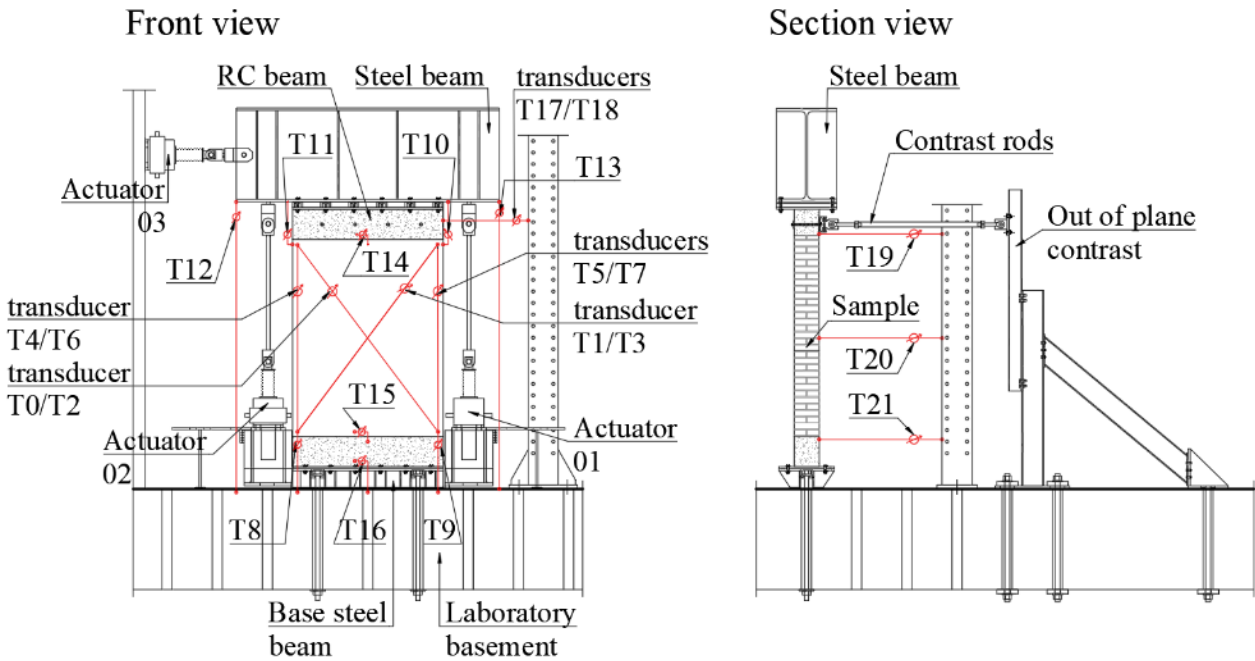
6.1 Test setup

Fig. 28: Test apparatus and instrumentation

The test apparatus in Fig. 28 consists of a strong laboratory floor, to which the foundation block (bottom RC beam) of the wall is fixed using pre-stressed bolts, and a strong steel lattice structure which supports the electro-mechanical actuator (Actuator 03) for imposing horizontal (seismic) loads. A stiff steel beam on the top of the tested pier transfers horizontal and vertical loads to the pier. The vertical load is applied using two electro-mechanical actuators (Actuator 01 and Actuator 02) at the sides of the beam, which are anchored to the laboratory floor. Each electro-mechanical actuator is equipped with a class 1 strain gauge load cell.

The samples dimensions are attached in the Appendix.

6.2 Instrumentation

Each specimen was equipped with 19 displacement transducers, as shown in Fig. 28. A digital image correlation system (DIC) was used to measure the displacement and strain fields on one surface of the wall. The side facing the cameras of the DIC system was painted with a contrasting random speckle pattern, and the other was painted white to facilitate visual examination of cracks.

The transducers are explained in Table 12.

Table 12: Description of instruments in shear-compression tests

Transducer	Measurement
T0/T3	Displacements along the diagonal
T1/T2	Displacements along the diagonal
T4/T7	Vertical displacement of the specimen along the right edge
T5/T6	Vertical displacement of the specimen along the left edge
T8, T9	Uplift of the specimen (foundation relative to the strong floor)
T10, T11	Uplift between masonry and top RC beam
T12, T13	Vertical displacements at the sides (rotation) of the top steel beam
T14, T15	Slip between masonry and RC beam (top and bottom)
T16	Slip of bottom RC beam relative to the strong floor
T17, T18	Horizontal displacement at the top RC beam

6.3 Test protocols

The test starts with applying the vertical load by the two jacks at the sides of the wall. The vertical load is gradually increased until the desired stress state of 0.5 MPa is attained. After that, the horizontal load is applied according to a pre-planned program. The horizontal load is imposed in the form of imposed displacement, which is applied in the positive and negative directions. After a cycle of horizontal loading is complete, the displacement amplitude is increased, and the procedure is repeated. The loading program is schematically shown in Fig. 29. For practical reasons, the displacement amplitudes in different phases varied from wall to wall. The exact data for each wall is shown in Table 13 and 14.

Throughout the test, the vertical forces are controlled so that the top steel beam remains horizontal, and the total vertical force is constant.
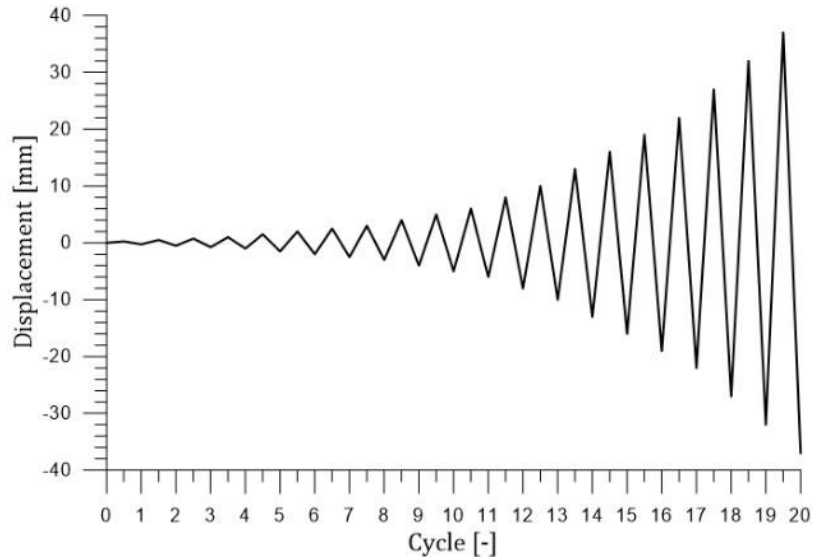
Fig. 29: Horizontal loading

Table 13: Actual program of loading

Wall	P-R2U		P-R2R-1		P-R2R-2		P-B2U	
Cycle	Amplitude [mm]	Rotation [%]	Amplitude [mm]	Rotation [%]	Amplitude [mm]	Rotation [%]	Amplitude [mm]	Rotation [%]
1.	0.25	0.01	0.25	0.00	0.25	0.01	0.25	0.01
2.	0.50	0.03	0.50	0.01	0.50	0.03	0.50	0.03
3.	0.75	0.04	0.75	0.03	0.75	0.04	0.75	0.04
4.	1.0	0.05	1.0	0.04	1.00	0.05	1.0	0.05
5.	1.5	0.08	1.5	0.05	1.50	0.08	1.25	0.06
6.	2.0	0.10	2.0	0.08	2.00	0.10	1.50	0.08
7.	2.5	0.13	2.5	0.10	2.50	0.13	2.0	0.10
8.	3.0	0.15	3.0	0.13	3.00	0.15	2.5	0.13
9.	4.0	0.20	4.0	0.15	4.00	0.20	3.0	0.15
10.	5.0	0.26	5.0	0.20	5.00	0.26	3.5	0.18
11.	6.0	0.31	6.0	0.26	6.00	0.31	4.0	0.20
12.	8.0	0.41	8.0	0.31	8.00	0.41	5.0	0.26
13.	10.0	0.51	10.0	0.41	10.00	0.51	6.0	0.31
14.	13.0	0.66	13.0	0.51	13.00	0.66	8.0	0.41
15.	15.0	0.77	16.0	0.82	16.00	0.82	10.0	0.51
16.			19.0	0.97	20.00	1.02	12.0	0.61
17.			22.0	1.12	26.50	1.35	15.0	0.77
18.			27.0	1.38	30.00	1.53		
19.			32.0	1.63	40.00	2.04		
20.			37.0	1.89	50.00	2.55		
21.					70.00	3.57		

Table 14: Actual program of loading

Wall	P-B2R-1		P-B2R-2		P-B1U		P-B1R	
Cycle	Amplitude [mm]	Rotation [%]	Amplitude [mm]	Rotation [%]	Amplitude [mm]	Rotation [%]	Amplitude [mm]	Rotation [%]
1.	0.25	0.01	0.25	0.01	0.25	0.01	0.25	0.01
2.	0.50	0.03	0.50	0.03	0.50	0.03	0.50	0.03
3.	0.75	0.04	0.75	0.04	0.75	0.04	0.75	0.04
4.	1.0	0.05	1.0	0.05	1.00	0.05	1.0	0.05
5.	1.5	0.08	1.5	0.08	1.25	0.06	1.5	0.08
6.	2.0	0.10	2.0	0.10	1.5	0.08	2.0	0.10
7.	2.5	0.13	2.5	0.13	2.0	0.10	2.5	0.13
8.	3.0	0.15	3.0	0.15	2.5	0.13	3.8	0.19
9.	5.0	0.26	4.0	0.20	3.0	0.15	5.0	0.26
10.	6.0	0.31	5.0	0.26	3.5	0.18	6.0	0.31
11.	8.0	0.41	6.0	0.31	4.0	0.20	8.0	0.41
12.	10.0	0.51	8.0	0.41	5.0	0.26	10.0	0.51
13.	13.0	0.66	10.0	0.51	6.0	0.31	13.0	0.66
14.	16.0	0.82	13.0	0.66	8.0	0.41	16.0	0.82
15.	20.0	1.02	16.0	0.82	10.0	0.51	20.0	1.02
16.	24.0	1.22	20.0	1.02	12.0	0.61	23.0	1.17
17.	28.0	1.43	25.0	1.35	15.0	0.77	28.0	1.43
18.	33.0	1.68	30.0	1.53	18.0	0.92	32.0	1.63
19.	38.0	1.94	40.0	2.04				
20.	44.0	2.24	50.0	2.55				
21.			60.0	3.06				
22.			70.0	3.57				

6.4   Parameters of seismic resistance of walls

Hysteretic response (curve)

The main quantities observed in the response analysis are horizontal (seismic) force H and horizontal displacement u, or drift ratio Φ. The drift ratio (from here on drift) is calculated by dividing the horizontal displacement at the top of the wall by the height of the wall ($\Phi = u/h$). The graph of force H as a function of displacement u (or rotation Φ) is called a hysteretic curve and is one of the main results of the test.

Limit states

Based on the hysteretic curve, its envelope and observations during the test, we can determine three limit states for each of the walls:

- *Damage limit state*; is when the first substantial reduction of stiffness of the wall can be observed on the hysteretic curve, and there is visual damage (cracks) on the wall. The limit state is defined as the average of limit states in the positive and negative directions;

- *Maximum resistance limit state;* is when the wall reaches maximum resistance to horizontal force. The peak forces and displacements at which they were attained are averaged for both directions to obtain the limit state;
- *Near collapse limit state*; is when the maximum horizontal displacement (incipient collapse) is reached in the test.

Envelope of the hysteretic curve and bilinear idealisation

The envelope of the hysteretic curve is determined separately for positive and negative directions (denoted on graphs by $H+$ and $H-$, respectively). Each of the envelopes is idealised into a bilinear curve according to the following rules:

- Stiffness of the bilinear response (K_e) corresponds to secant stiffness at 60 % peak force
- Ultimate displacement (u_u) of the bilinear response is limited to the displacement at the drop to 80 % residual resistance
- The area under the bilinear curve and the envelope (A_{env}) are the same (principle of equality of energy). From this condition, the force (H_u) on the plateau of the bilinear curve is calculated.
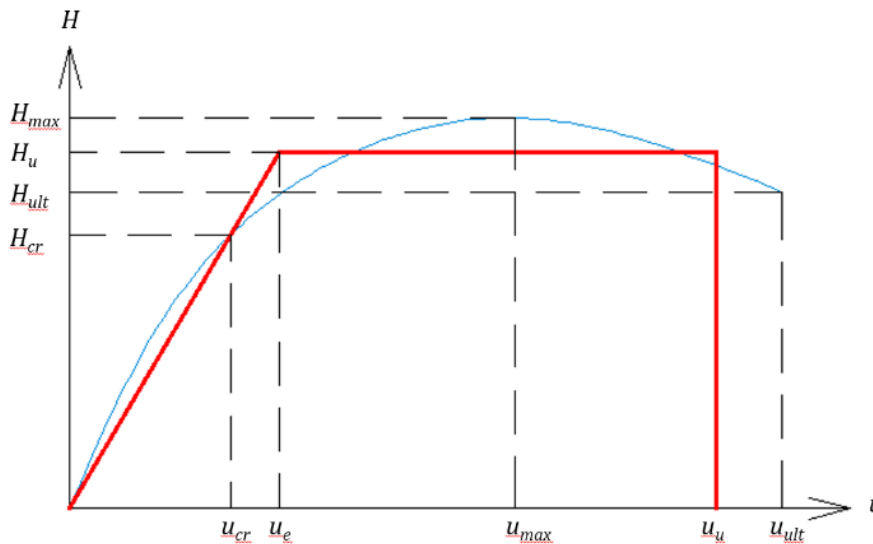
Fig. 30: Bilinear idealisation

The force H_u can be calculated using the following equation:

$$H_u = K_e\, u_u - \sqrt{K_e} \cdot \sqrt{-2A_{env} + K_e\, u_u^2}$$

The final bilinear response curve of the wall is obtained by averaging bilinear curves for both directions.

Tensile strength of masonry

Tensile strength of masonry (f_t), according to the model of Turnšek and Čačovič, is calculated by the following formula:

$$f_t = \sqrt{\left(\frac{\sigma_0}{2}\right)^2 + (b \cdot \tau_{max})^2} - \frac{\sigma_0}{2}$$

Where σ_0 is the compressive stress, τ_{max} is peak shear average stress in the cross-section ($\tau_{max} = H_{max}/A$), and b is the shear distribution factor, which depends on the height to length ratio:

$$b = \begin{cases} 1.1; & \frac{h}{l} \leq 1.1 \\ \frac{h}{l}; & 1.1 < \frac{h}{l} < 1.5 \\ 1.5; & \frac{h}{l} > 1.5 \end{cases}$$

Shear strength of masonry (NTC2018)

According to NTC2018, shear strength, τ_0, can be calculated from the tensile strength f_t using:

$$\tau_0 = f_t/1.5$$

Note that in the calculation of f_t NTC2018 assumes factor b can have values from 1.0 to 1.5.

Shear modulus

Shear modulus is calculated from the assumption that a wall can be modelled as a beam with shear and bending deformability (Timoshenko beam). The stiffness of Timoshenko beam is calculated as:

$$K_e = \frac{G \cdot A}{1.2 \, h \left(1 + \alpha' \cdot \frac{G}{E} \cdot \left(\frac{h}{l}\right)^2\right)}$$

Where E and G are the elastic and shear modulus, respectively. A is the cross-section of the wall, and α' is the boundary conditions parameter. For fixed walls, it is 0.83, whereas for cantilever walls, it is 3.33. Shear modulus can be expressed from the above equation as:

$$G = \frac{6 \, E \, h \, K_e \, l^2}{5 \, A \, E \, l^2 - 6 \, h^3 \, K_e \, \alpha'}$$

Energy dissipation (hysteretic energy) and total (input) energy

Energy dissipation of a wall can be estimated from the hysteretic curve. It is the total area enclosed by the loops of the hysteretic curve:

$$E_{hys} = \int H \, du$$

The total (input) energy is calculated as:

$$E_{tot} = \int dE_{tot}$$

Where:

$$dE_{tot} = \begin{cases} H \cdot du; & \text{if } H \cdot du > 0 \\ 0; & \text{if } H \cdot du \leq 0 \end{cases}$$

The total and hysteretic energy are schematically shown in Fig. 31.
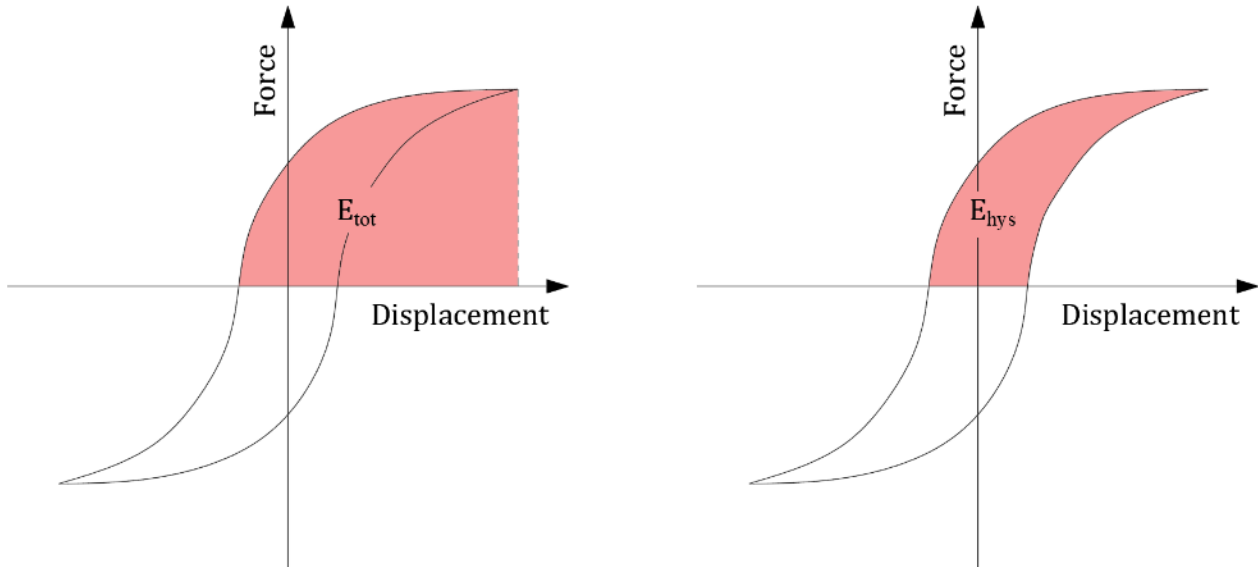
Fig. 31: Input (total) and dissipated (hysteretic) energies.

Equivalent tensile strength of strengthened walls

The equivalent tensile strength of strengthened walls was calculated according to the previously presented model of Turnšek and Čačovič, where τ_{max} is calculated using H_{max} from the tests.

6.5 Tests

6.5.1 P-R2U (stone; unstrengthened)

P-R2U	Two leaf stone masonry;
	unstrengthened
Date of test (age):	2021/4/30 (age: 57 days)
Dimensions ($l/h/t$):	1500/1960/350 mm
Vertical stress (σ_0):	0.5 MPa
Material characteristics	
f_c	2.48 MPa
E	1074 MPa
G	333 MPa
Tensile strength	
f_t (for design)	0.105 MPa
f_t (at H_{max})	0.121 MPa
Bilinear idealisation	
u_e	2.0 mm (0.1 %)
u_u	11.2 mm (0.56 %)
H_u	99.3 kN
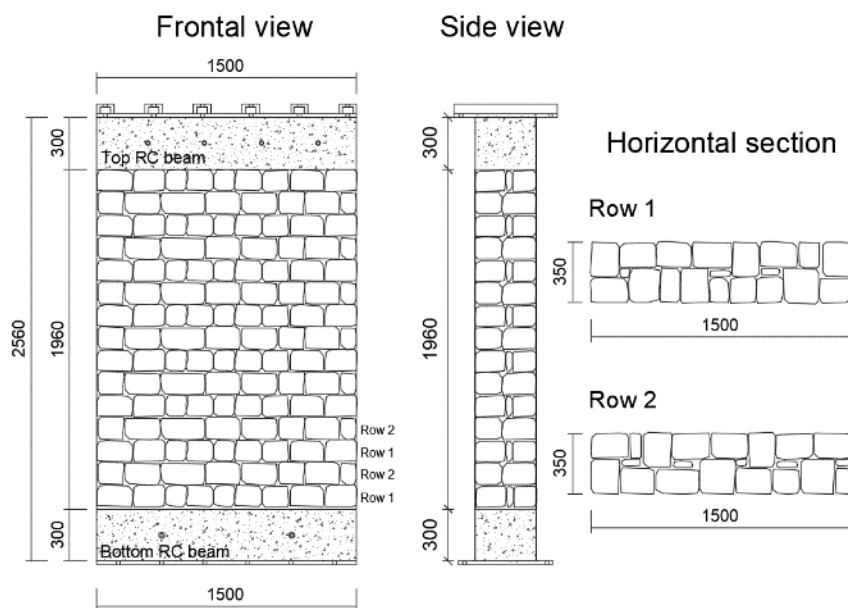
Fig. 32: Plan of the wall
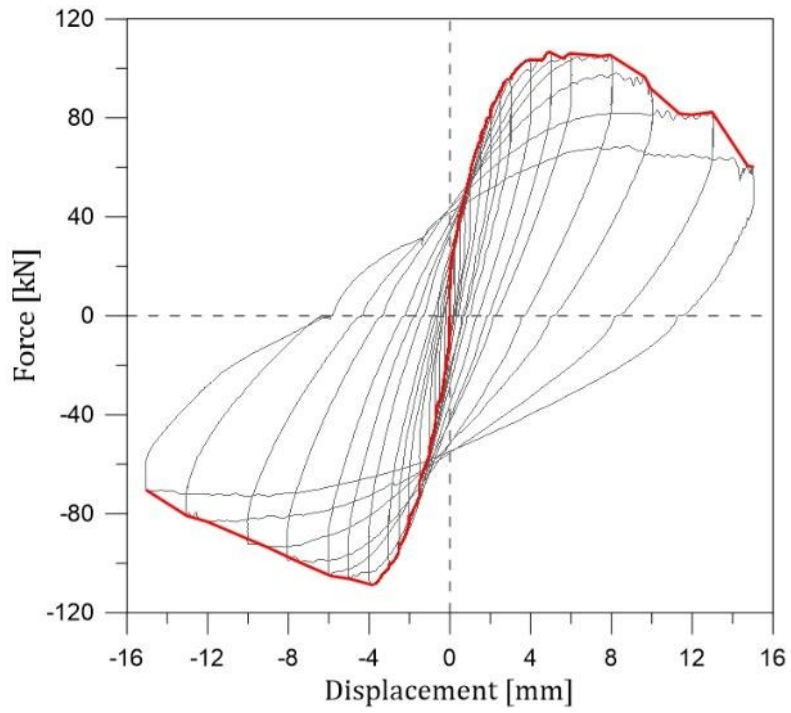
Fig. 33: Force-displacement curve and the envelope
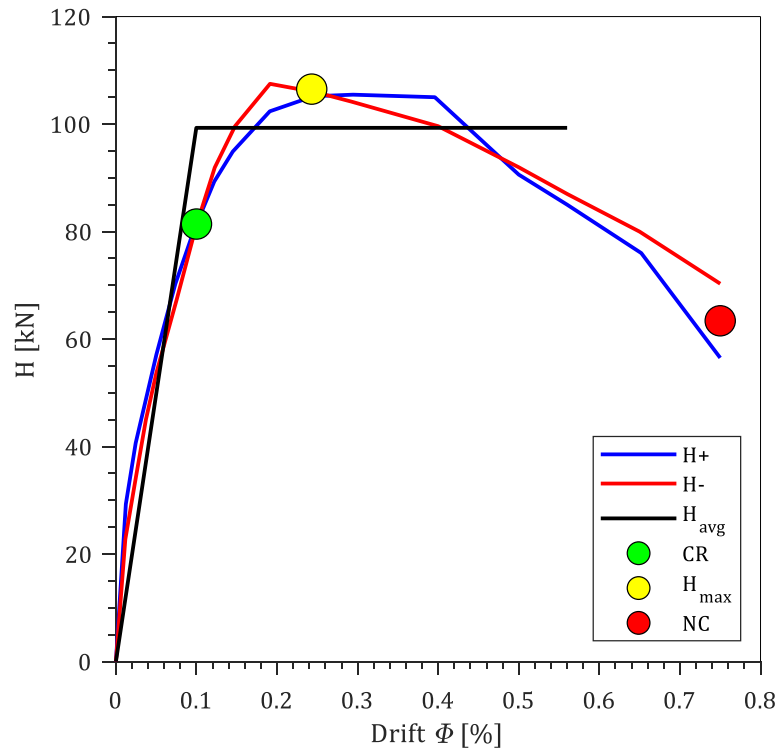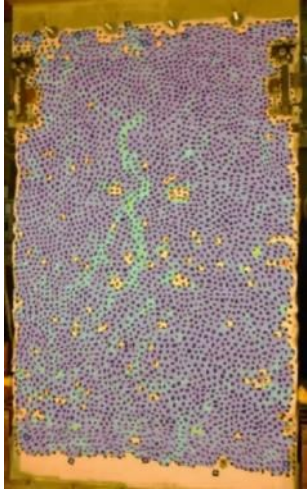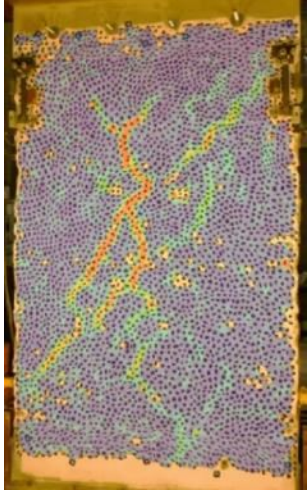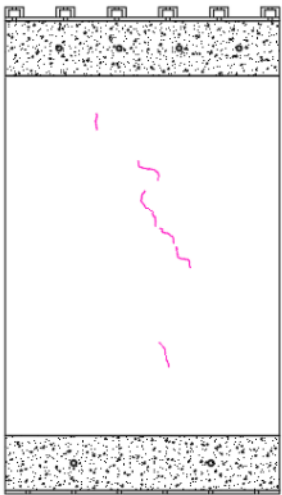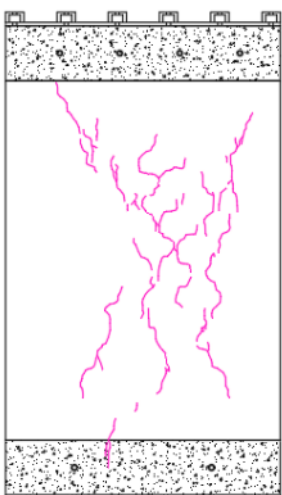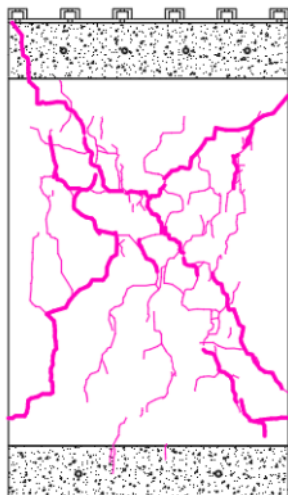
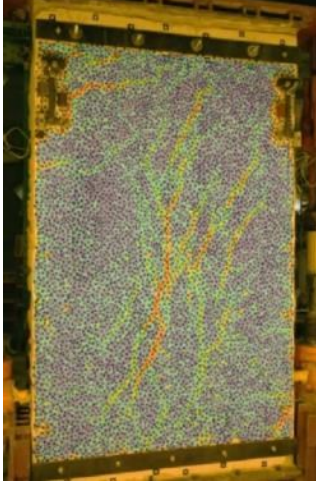*Fig. 34: Envelopes of the response, bilinear idealisation and limit states*

Table 15: Limit states of the wall

Damage LS 🟢		Max Resist LS 🟡		Near Col. LS 🔴	
H_{cr} [kN]	Φ_{cr} [%]	H_{max} [kN]	Φ_{Hmax} [%]	H_{ult} [kN]	Φ_{ult} [%]
81.4	0.10	107.8	0.24	63.4	0.75

Observations:

2 mm (0.1 %)	First vertical crack at the middle of the wall.
4 mm (0.2 %)	Diagonal cracking appears, which indicates shear response.
5 mm (0.24 %)	Peak resistance. Pure shear response.
15 mm (0.75 %)	Failure due to diagonal shear cracking. Damage is concentrated in two principal cracks.

6.5.2 P-R2R-1 (stone; coating on one side)

| P-R2R-1	Two leaf stone masonry;		
Strengthened: coating on one side; 3 cm thick mortar coating reinforced by GFRM mesh; twelve "L" anchors, six diatons			
Date of test:	2021/6/10 (age: 98 days)	Bilinear idealisation	
Dimensions (*l/h/t*):	1500/1960/350 mm	u_e	3.8 mm (0.19 %)
Vertical stress (σ_0):	0.5 MPa	u_u	28.9 mm (1.45 %)
		H_u	143.9 kN
Equivalent tensile strength	0.219 MPa		
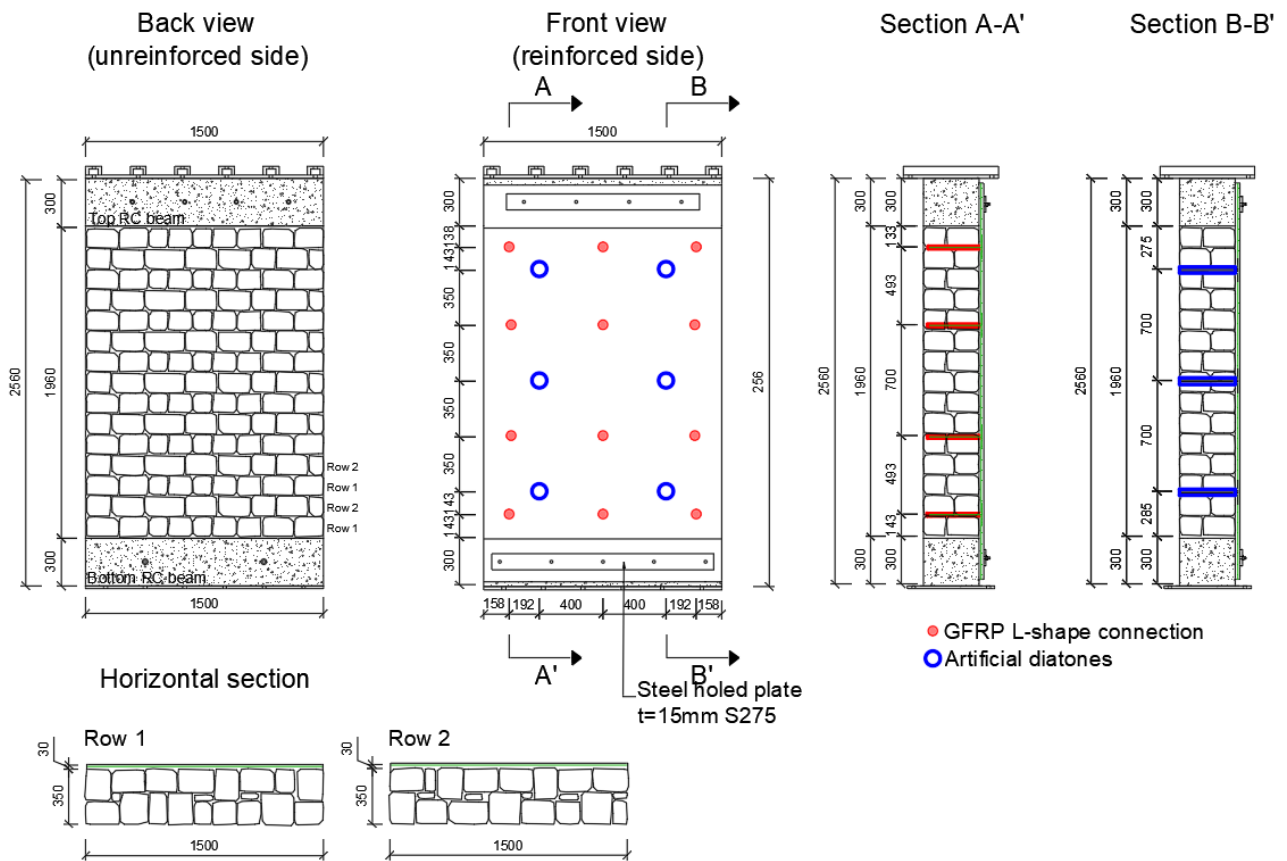
Fig. 35: Plan of the wall

37

P-R2R-1
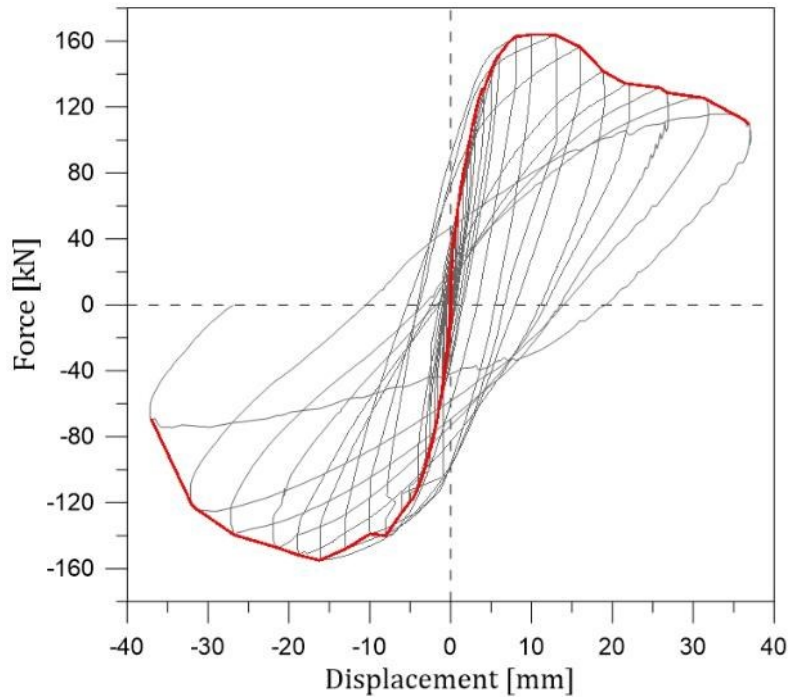
Fig. 36: Force-displacement curve and the envelope
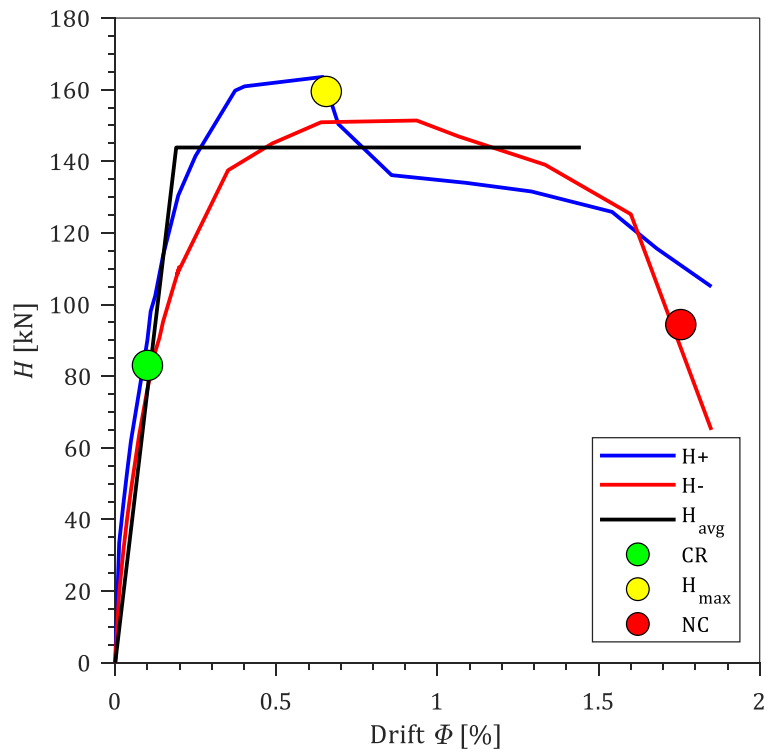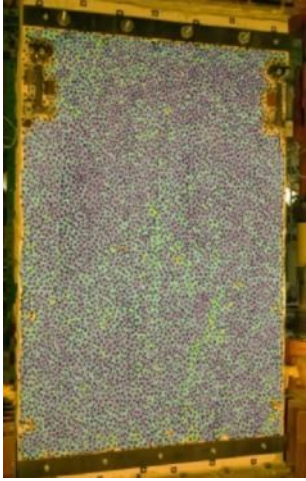
Fig. 37: Envelopes of the response, bilinear idealisation and limit states

P-R2R-1

Table 16: Limit states of the wall

Damage LS 🟢		Max Resist LS 🟡		Near Col. LS 🔴	
H_{cr} [kN]	Φ_{cr} [%]	H_{max} [kN]	Φ_{Hmax} [%]	H_{ult} [kN]	Φ_{ult} [%]
83	0.1	159,5	0.66	94,4	1.76

Front			
Back			

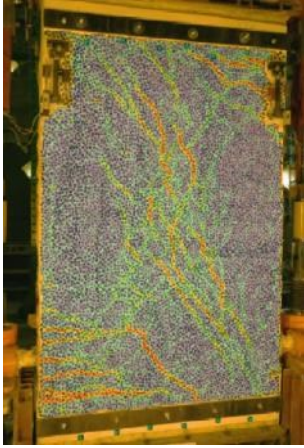| 2 mm (0.1 %)	A vertical crack appears in the middle of the wall on the coating and the unstrengthened side.
2 mm – 13 mm	Vertical cracks propagate and multiply on both sides of the wall.
13 -16 mm (0.65 – 0.8 %)	Peak resistance is reached. On the unstrengthened side, a big diagonal crack appears. In the coating, vertical cracks become inclined. Horizontal cracks appear at the base and top of the coating, indicating the presence of flexure. The shear response dominates in the coating.
16 mm – 37 mm	Large diagonal shear cracks on the unstrengthened side. Coating develops many parallel cracks and gradually loses contact with the masonry (Fig. 38, left). Eventually, mortar starts falling off, and GFRP mesh fractures near diatons (Fig. 38, right).
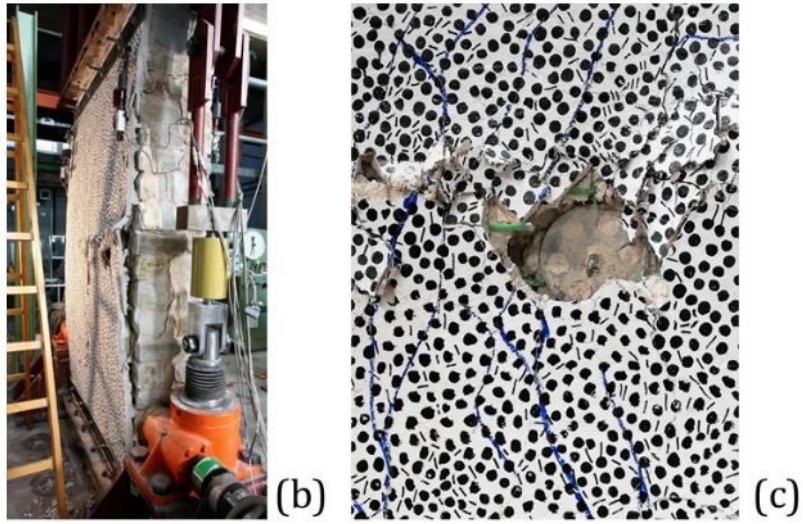
Fig. 38: (P-R2R-1) Detachment of the coating (left), fractured mesh near diatons (right).

6.5.3 P-R2R-2 (stone; coating on two sides)

P-R2R-2	Two leaf stone masonry;		
Strengthened: coating on both sides; 3 cm thick mortar coating reinforced by GFRM mesh; twenty passing through "L" anchors			
Date of test:	2021/6/29 (age: 48 days)	Bilinear idealisation	
Dimensions (l/h/t):	1500/1960/350 mm	u_e	4.5 mm (0.14 %)
Vertical stress (σ_0):	0.5 MPa	u_u	48.6 mm (2.67 %)
		H_u	208.8 kN
Equivalent tensile strength	0.373 MPa		
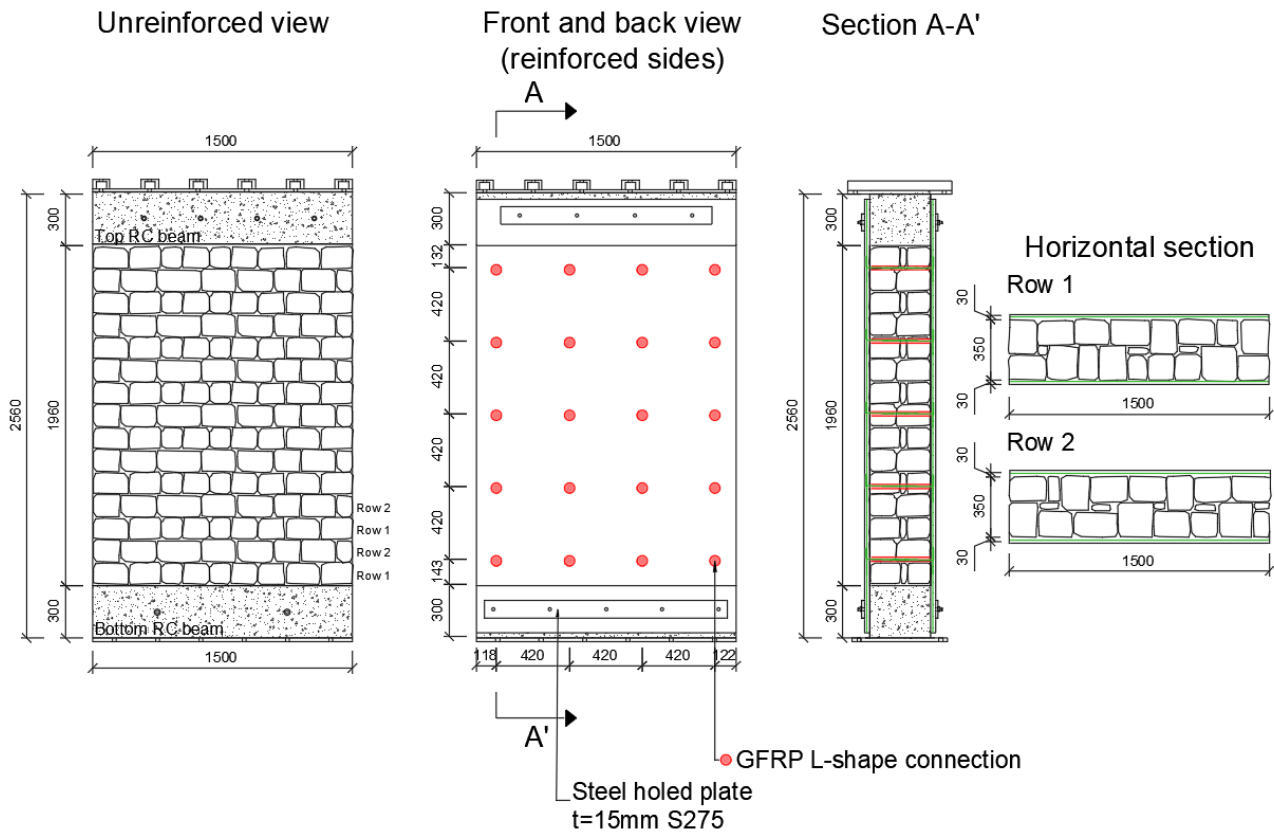
Fig. 39: Plan of the wall

P-R2R-2
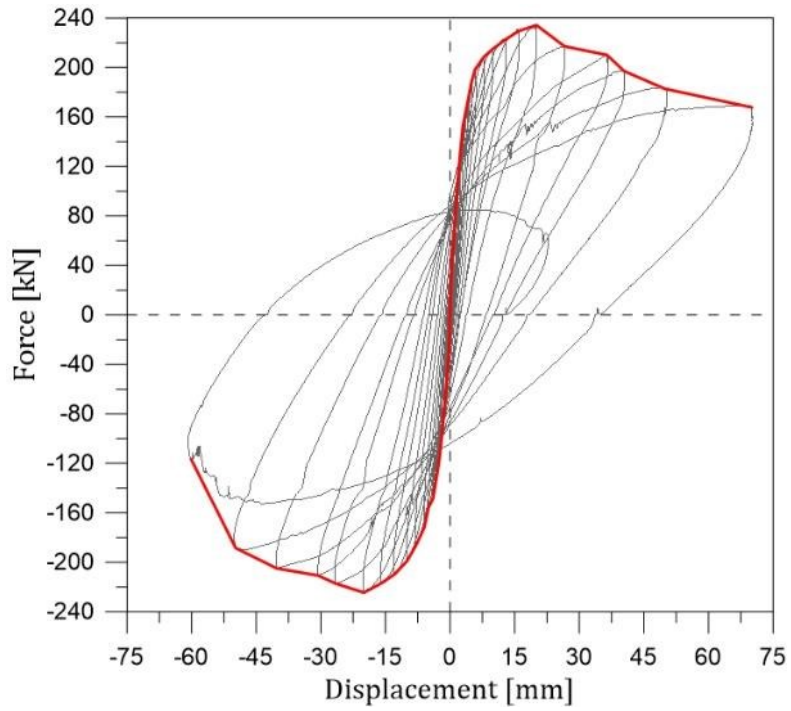
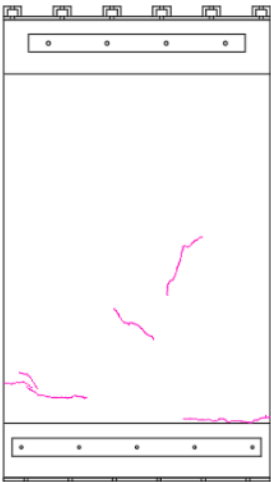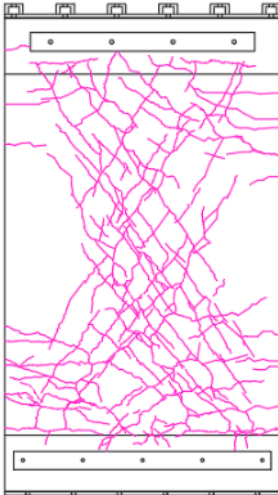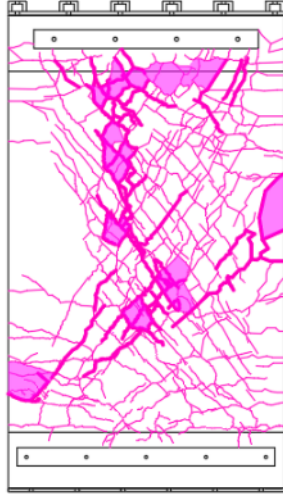*Fig. 40: Force-displacement curve and the envelope*
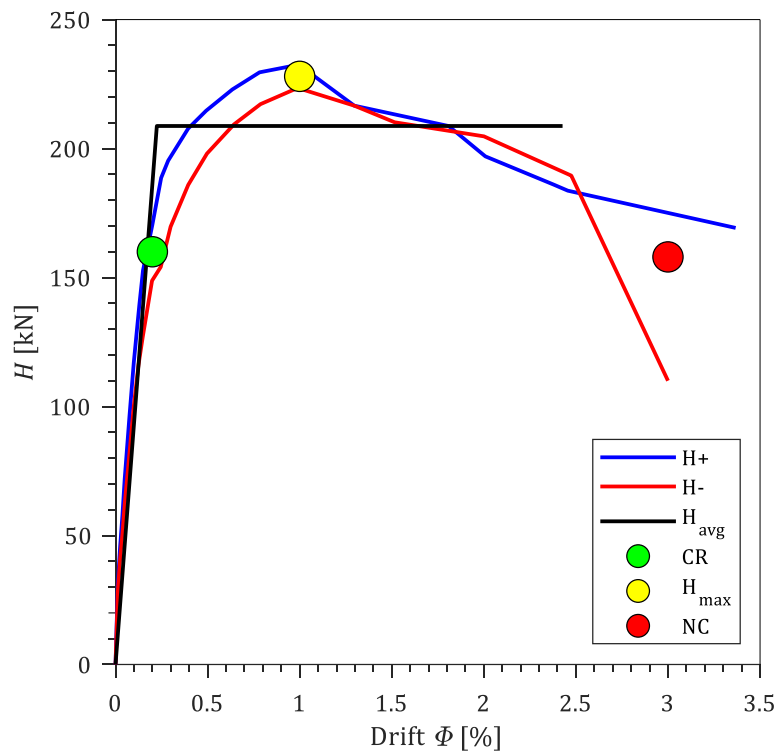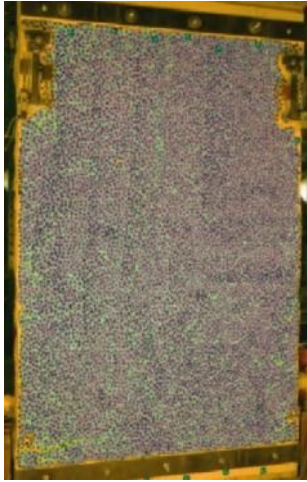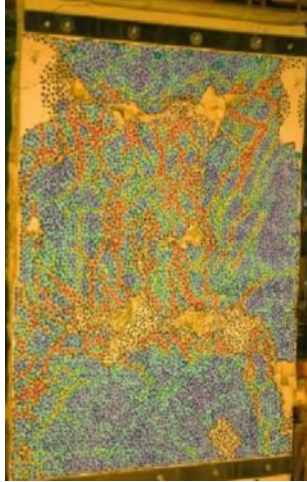
Fig. 41: Envelopes of the response, bilinear idealisation and limit states.

Table 17: Limit states of the wall

Damage LS ⬤		Max Resist LS ⬤		Near Col. LS ⬤	
H_{cr} [kN]	Φ_{cr} [%]	H_{max} [kN]	Φ_{Hmax} [%]	H_{ult} [kN]	Φ_{ult} [%]
159.5	0.20	228.0	0.99	157.6	3.01

|	
4 mm (0.2 %)	Horizontal cracks in the coating at the base of the wall were the first sign of damage.
4 mm – 5 mm	Inclined cracks appear in the middle of the wall (coating).
20 mm (1 %)	Peak resistance is reached. The damage in the coating consists of horizontal cracks at the base and top of the wall (flexure) and inclined cracks (shear). Several parallel cracks characterise damage due to flexural and shear mechanisms. Bending response dominates.
30 mm	Coating begins to crumble and detach from the wall Fig. 42a,b. There is a vertical crack between the leaves of the wall. Fig. 42c
70 mm	Wall collapses. Cracks at collapse are a mixture of shear and bending Fig. 42d.
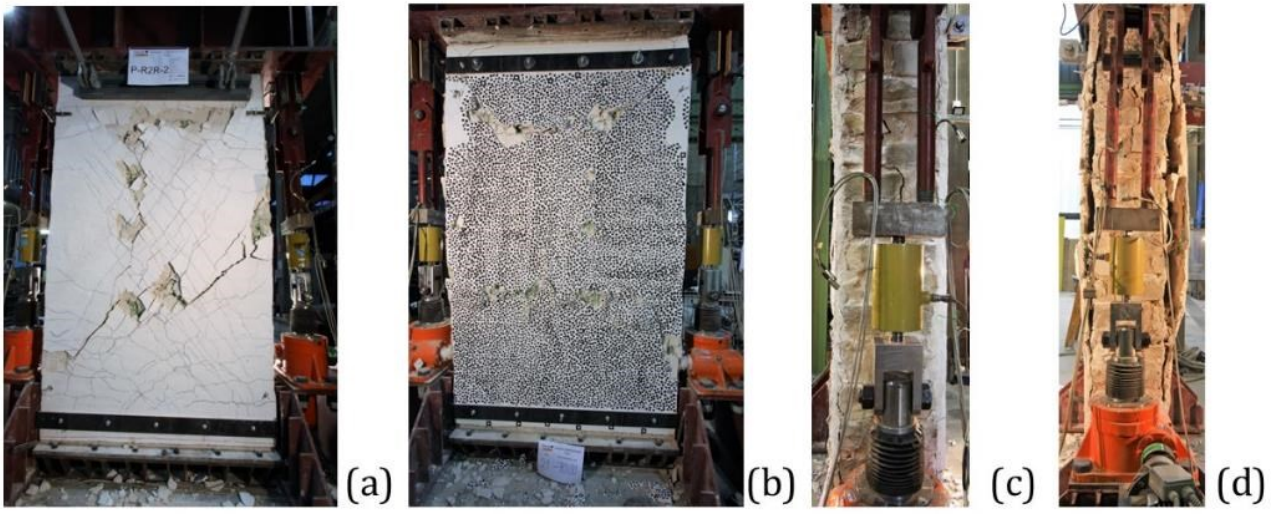
Fig. 42: (P-R2R-2) view of the wall at collapse (a and b), vertical cracks between the leaves of the wall (c), detachment of the coating at collapse (d)

6.5.4 P-B1U (brick; single leaf; unstrengthened)

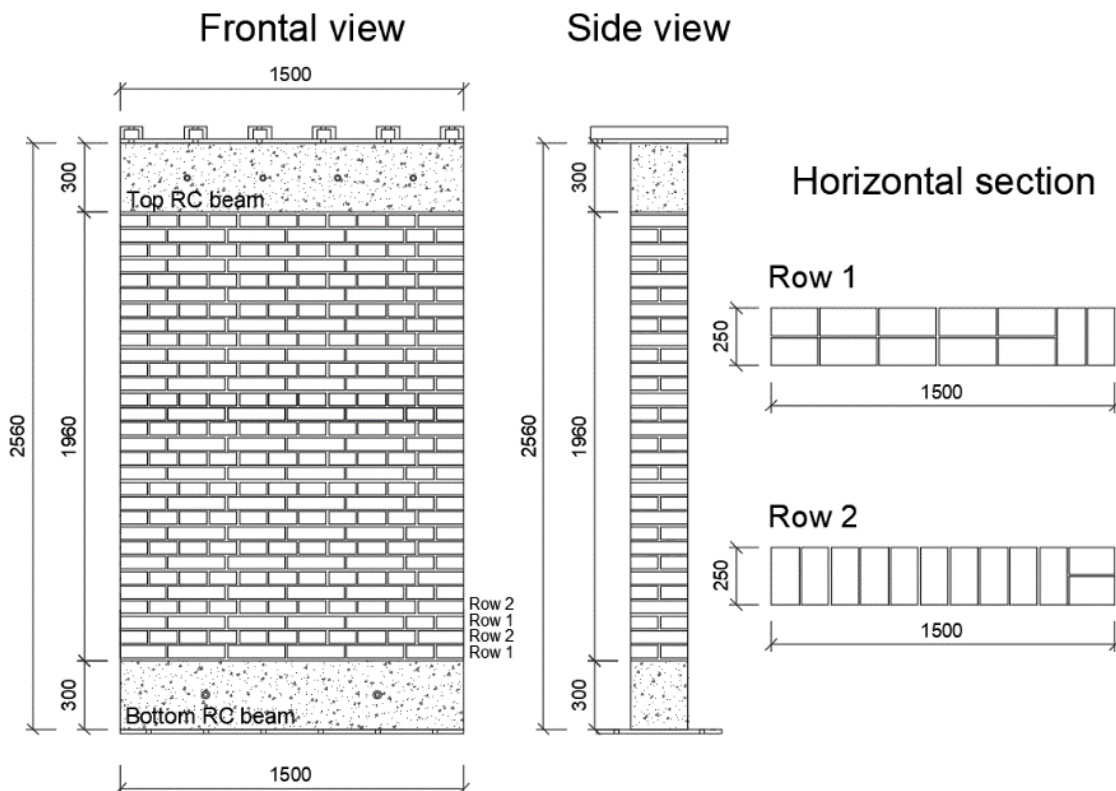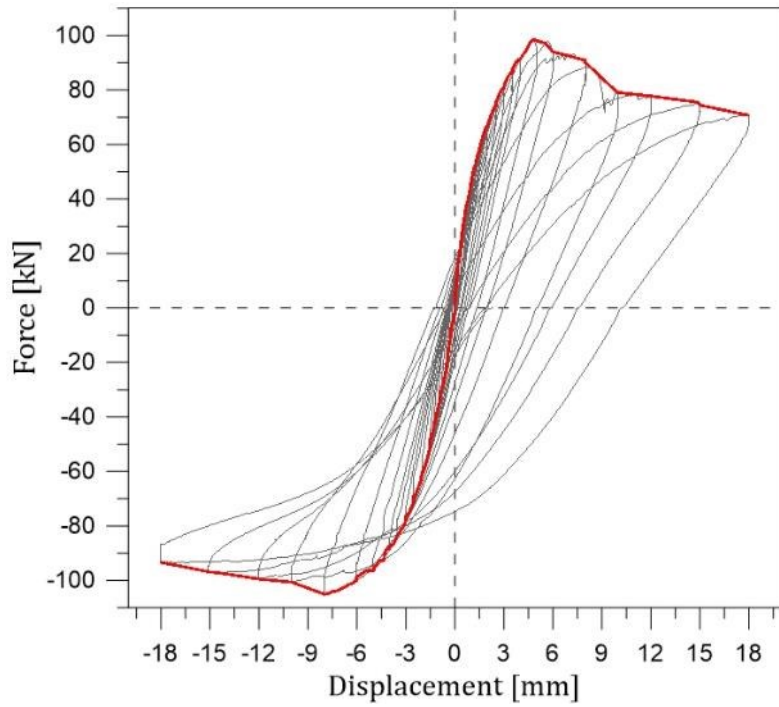| P-B1U	Single leaf brick masonry;
	unstrengthened
Date of test (age):	2021/8/9 (age: 63 days)
Dimensions (l/h/t):	1500/1960/250 mm
Vertical stress (σ_0):	0.5 MPa
Material characteristics	
f_c	6.7 MPa
E	2341 MPa
G	258 MPa
Tensile strength	
f_t (for design)	0.165 MPa
f_t (at H_{max})	0.190 MPa
Bilinear idealisation	
u_e	2.8 mm (0.14 %)
u_u	14.2 mm (0.71 %)
H_u	93.0 kN

Fig. 43: Plan of the wall

45

P-B1U

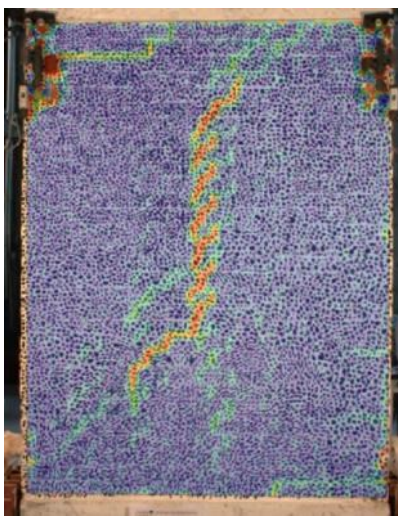*Fig. 44: Force-displacement curve and the envelope*
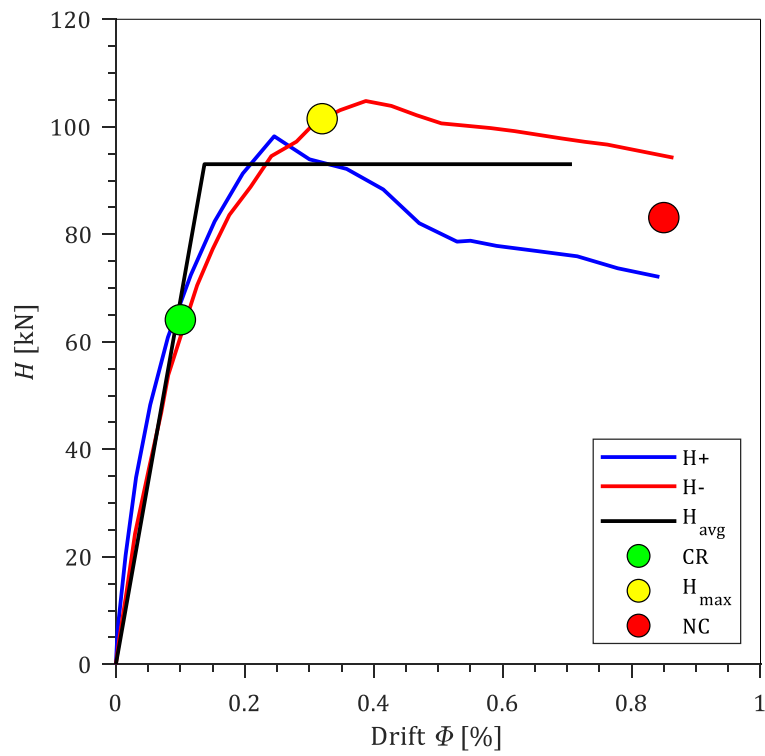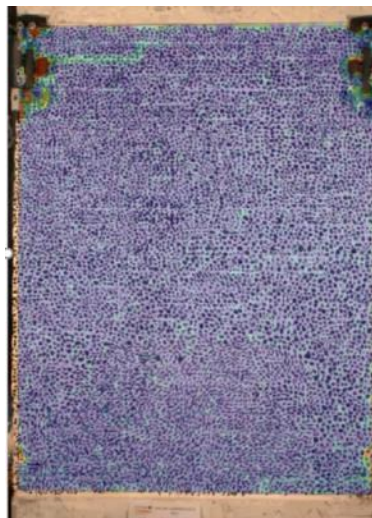
Fig. 45: Envelopes of the response, bilinear idealisation and limit states

P-B1U

Table 18: Limit states of the wall

Damage LS 🟢		Max Resist LS 🟡		Near Col. LS 🔴	
H_{cr} [kN]	Φ_{cr} [%]	H_{max} [kN]	Φ_{Hmax} [%]	H_{ult} [kN]	Φ_{ult} [%]
64.1	0.1	101.9	0.32	83.1	0.85

2 mm (0.1 %)	The damage is a horizontal crack at the top left corner.
4 mm – 5 mm	A vertical crack appears in the middle of the wall and runs from one-quarter to three-quarters of the height. Horizontal cracks are still active.
6 mm (0.3 %)	Peak resistance is reached. The vertical crack elongates diagonally towards the corners, which indicates a transition towards a more pure shear response.
6 - 18 mm (0.3 – 0.85 %)	The shear crack develops and dominates the response. All damage is concentrated in the single shear crack. Horizontal cracks in the wall are still visible but are not the primary response mechanism.

6.5.5 P-B1R (brick; single leaf; coating on one side)

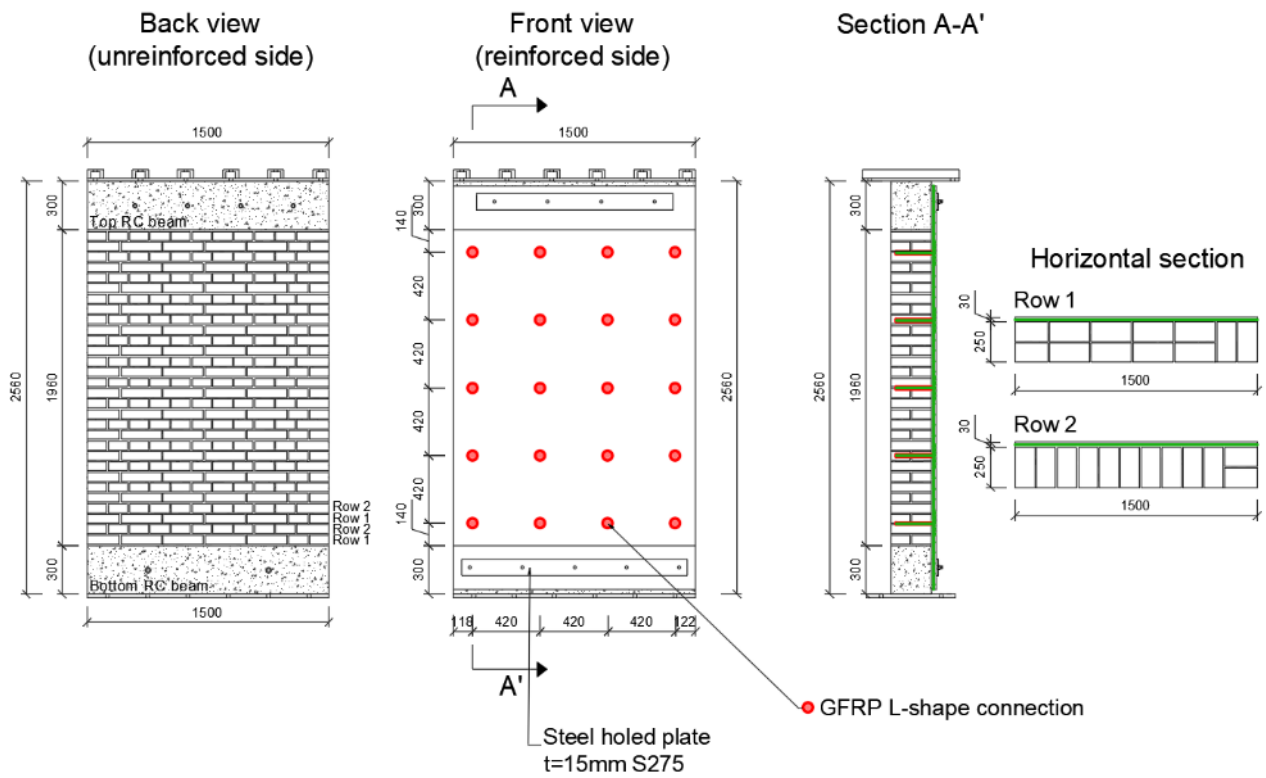| **P-B1R**		Single leaf brick masonry;	
Strengthened: coating on one side;			
3 cm thick mortar coating reinforced by GFRM mesh; twenty "L" anchors			
Date of test:	2021/9/10 (age: 95 days)	Bilinear idealisation	
Dimensions ($l/h/t$):	1500/1960/250 mm	u_e	4.95 mm (0.25 %)
Vertical stress (σ_0):	0.5 MPa	u_u	30.5 mm (1.53 %)
		H_u	154.6 kN
Equivalent tensile strength	0.380 MPa		

Fig. 46: Plan of the wall
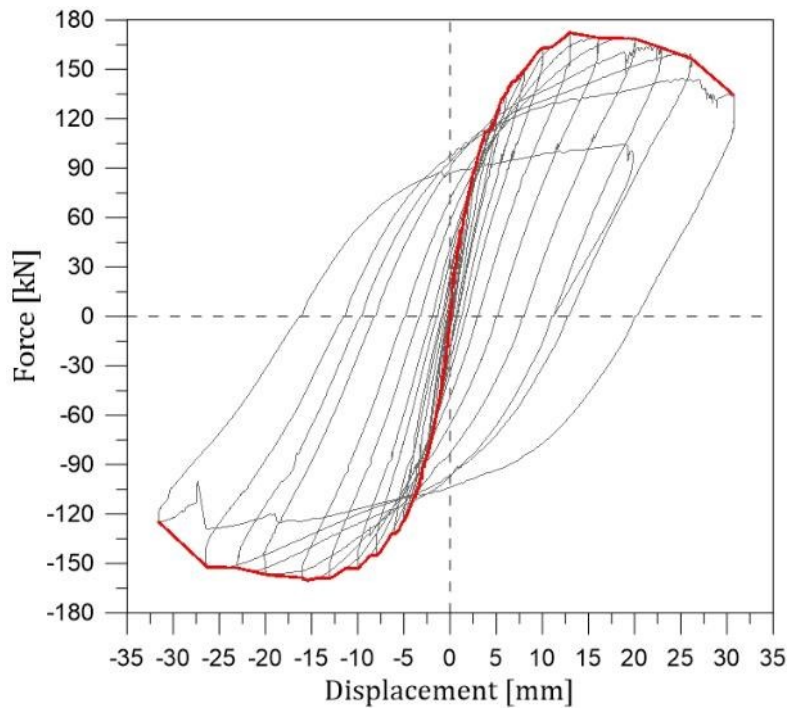
48

P-B1R

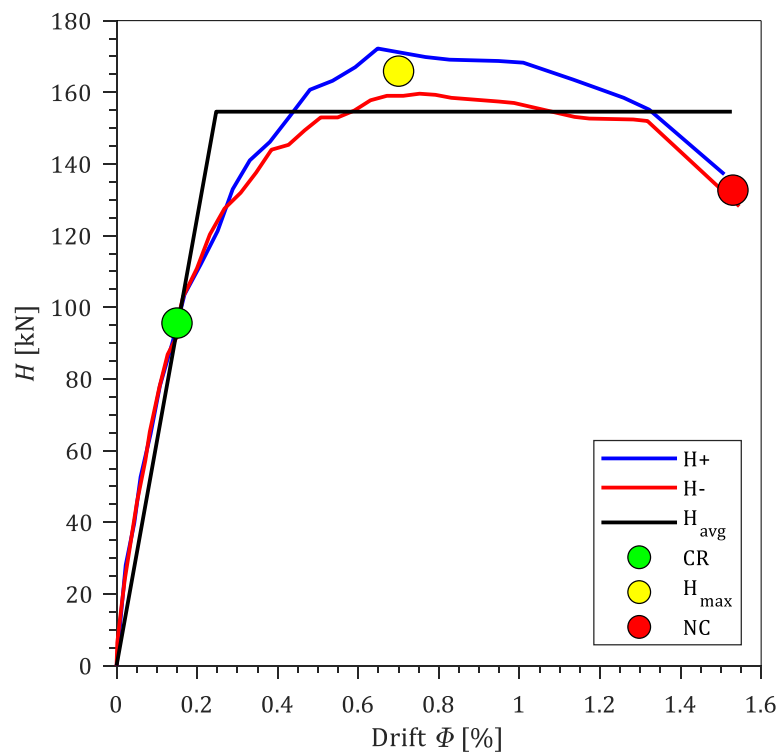*Fig. 47: Force-displacement curve and the envelope*

Fig. 48: Envelopes of the response, bilinear idealisation and limit states

P-B1R

Table 19: Limit states of the wall

Damage LS 🟢		Max Resist LS 🟡		Near Col. LS 🟣	
H_{cr} [kN]	Φ_{cr} [%]	H_{max} [kN]	Φ_{Hmax} [%]	H_{ult} [kN]	Φ_{ult} [%]
95.6	0.15	165.9	0.70	132.7	1.53

3 mm (0.15 %)	The first vertical crack appeared at the top of the wall on the side with the coating. On the unstrengthened side, the first crack was horizontal and appeared at the base of the wall.
3 mm – 14 mm (0.15 – 0.7 %)	Horizontal cracks at the top and bottom of the coating appear and propagate. The peak resistance is reached at 14 mm horizontal displacement, and the response is almost pure bending.
14 -33 mm (0.7 – 1.5 %)	Horizontal cracks are active and dominate the response. However, large shear cracks also appear in the coating and on the unreinforced side.

6.5.6 P-B2U (brick; double leaf; unstrengthened)

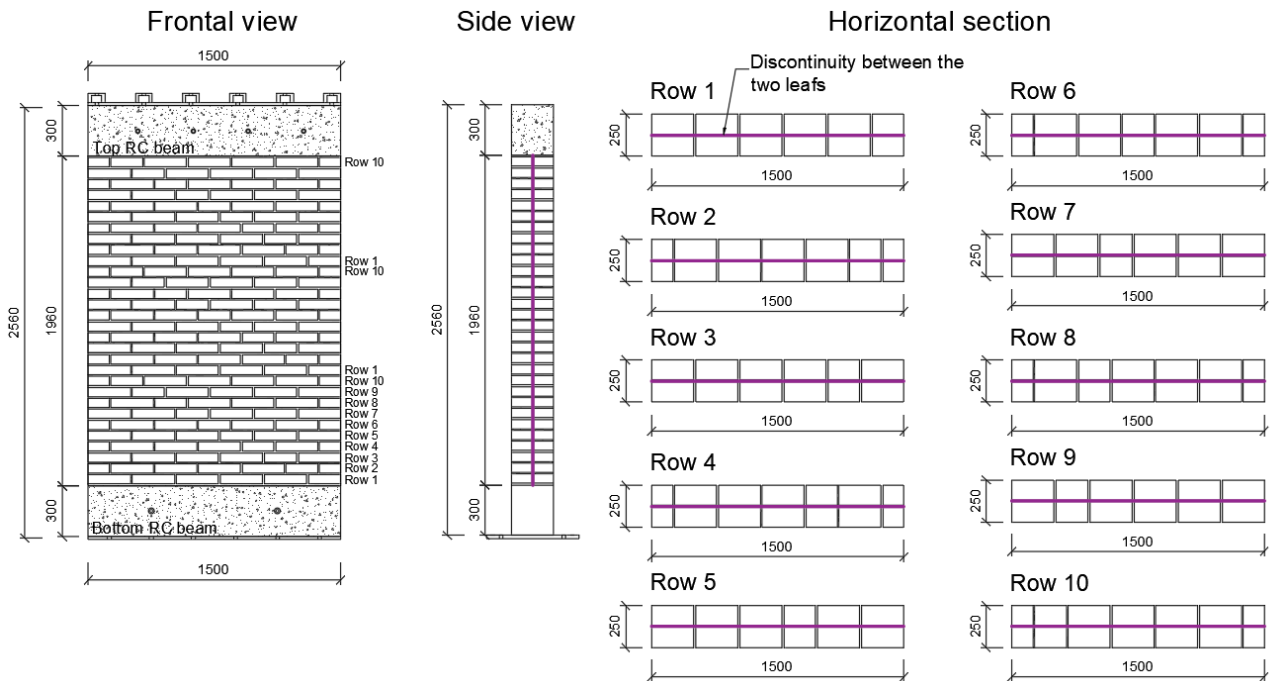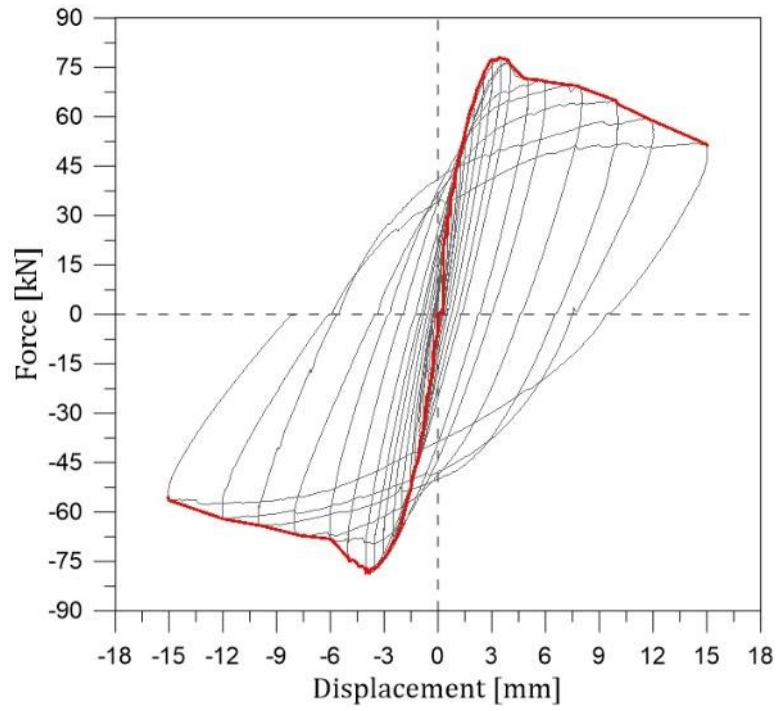| P-B2U	Two leaf stone masonry;
	unstrengthened
Date of test (age):	2021/11/12 (age: 36 days)
Dimensions (*l*/*h*/*t*):	1500/1960/250 mm
Vertical stress (σ_0):	0.5 MPa
Material characteristics	
f_c	6.43 MPa
E	2183 MPa
G	293 MPa
Tensile strength	
f_t (for design)	0.101 MPa
f_t (at H_{max})	0.124 MPa
Bilinear idealisation	
u_e	1.82 mm (0.09%)
u_u	11.1 mm (0.56 %)
H_u	69.43 kN

Fig. 49: Plan of the wall

P-B2U

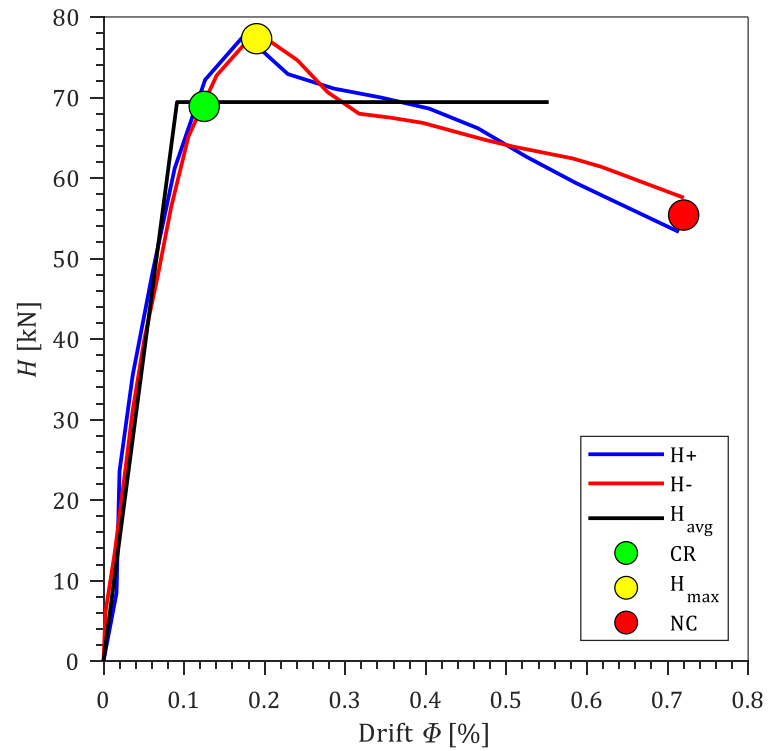*Fig. 50: Force-displacement curve and the envelope*
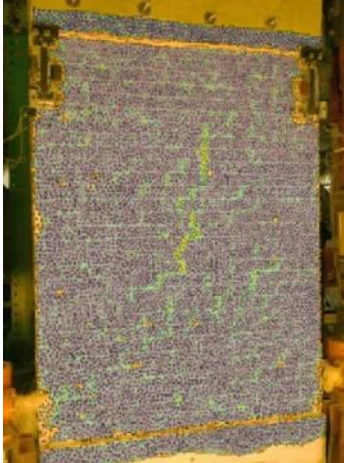
Fig. 51: Envelopes of the response, bilinear idealisation and limit states

P-B2U

Table 20: Limit states of the wall

Damage LS 🟢		Max Resist LS 🟡		Near Col. LS 🔴	
H_{cr} [kN]	Φ_{cr} [%]	H_{max} [kN]	Φ_{Hmax} [%]	H_{ult} [kN]	Φ_{ult} [%]
68.9	0.13	78.26	0.19	55.4	0.72

2-3 mm (0.13 %)	The first inclined crack appears in the middle of the wall.
4 mm (0.2 %)	At peak resistance, there is diagonal cracking, which indicates shear response.
8 mm (0.24 %)	Shear diagonal cracks grow in length and width. Cracks indicating separation of leaves are observed (Fig. 52).
15 mm (0.75 %)	Failure due to diagonal shear cracking occurs. Damage is concentrated in two principal cracks. Severe separation of wall leaves (Fig. 52).

Fig. 52: (P-B2U) Separation of wall leaves at 8 mm (left) and 15 mm (right)

6.5.7 P-B2R-1 (brick; double leaf; coating on one side)

P-B2R-1	Double leaf brick masonry;		
Strengthened: coating on one side; 3 cm thick mortar coating reinforced by GFRM mesh; twelve "L" anchors, six diatons			
Date of test:	2021/9/21 (age: 106 days)	Bilinear idealisation	
Dimensions (l/h/t):	1500/1960/250 mm	u_e	5.05 mm (0.25 %)
Vertical stress (σ_0):	0.5 MPa	u_u	34.9 mm (1.75 %)
		H_u	146.4 kN
Equivalent tensile strength	0.363 MPa		

Fig. 53: Plan of the wall
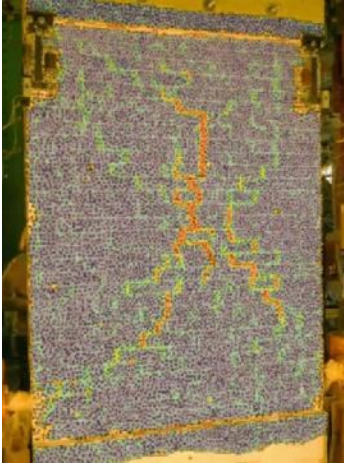
P-B2R-1

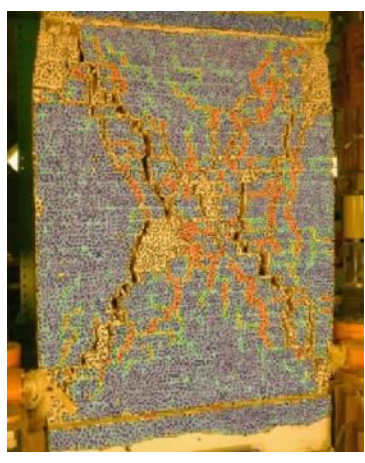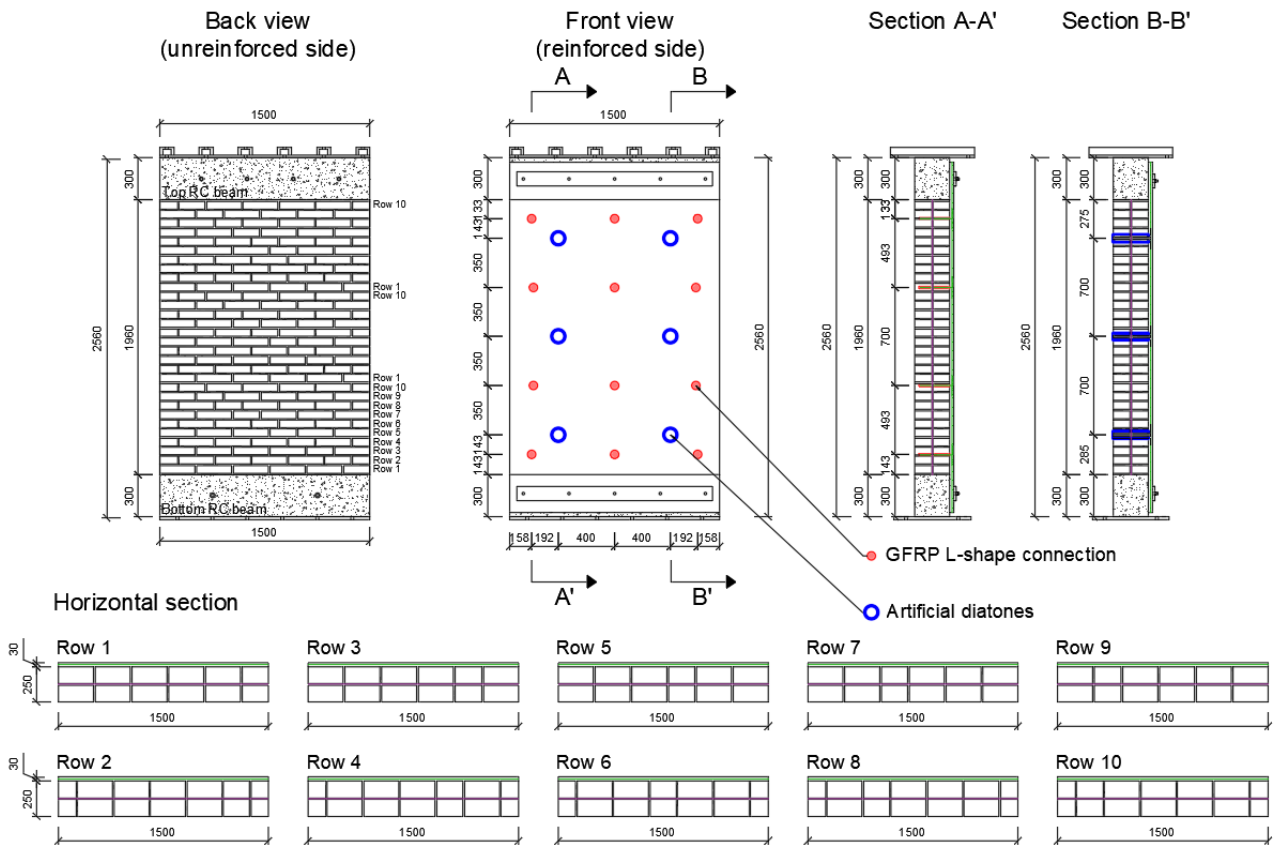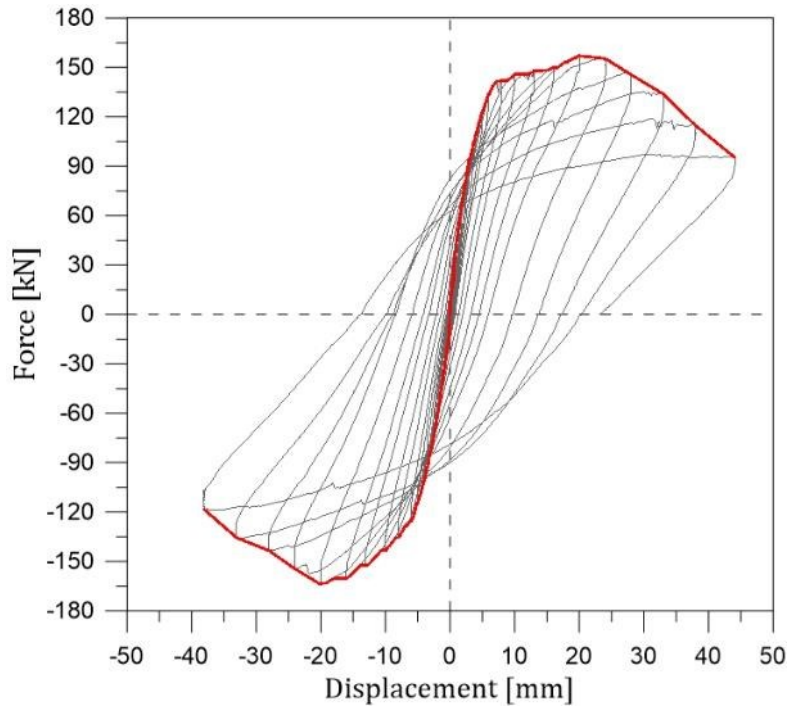*Fig. 54: Force-displacement curve and the envelope*
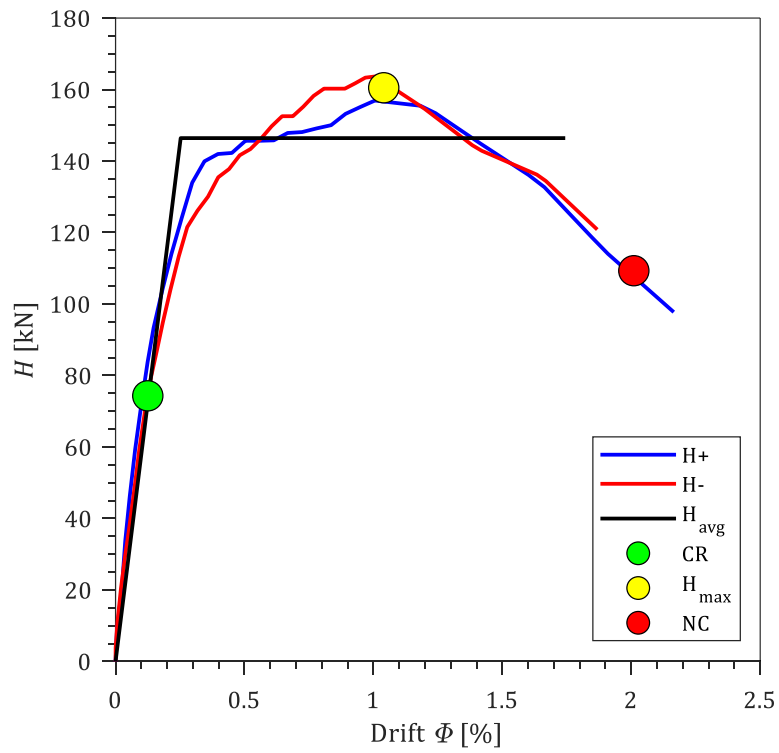
Fig. 55: Envelopes of the response, bilinear idealisation and limit states.

Table 21: Limit states of the wall

Damage LS 🟢		Max Resist LS 🟡		Near Col. LS 🟣	
H_{cr} [kN]	Φ_{cr} [%]	H_{max} [kN]	Φ_{Hmax} [%]	H_{ult} [kN]	Φ_{ult} [%]
74.3	0.13	160.5	1.04	109.3	2.01

3 mm (0.15 %)	Horizontal cracks in the coating at the top of the wall were the first sign of damage.
4 mm – 20 mm	Horizontal cracks also appear at the bottom of the wall, and cracks at both locations propagate. At about 10 mm, crack formation between wall leaves occurred (Fig. 56, left).
20 mm (1 %)	Peak resistance is reached. The damage in the coating concerns horizontal cracks at the base and top of the wall (flexure). Bending response dominates in the coating. However, a large diagonal crack appears on the unstrengthened side.
20 – 40 mm	In the coating, the flexural response continues to dominate. However, shear cracks also appear in the coating. On the unstrengthened side, shear damage progresses.
70 mm	Wall collapses. Cracks at collapse are a mixture of shear and bending. Wall leaves are entirely detached, and the leaf with the coating is leaning heavily out of the plane (Fig. 56, right)

Fig. 56: (P-B2R-1) Vertical crack between wall leaves at 10 mm (left) and separation of leaved at 70 mm (right).

6.5.8   P-B2R-2 (brick; double leaf; coating on two sides)

P-B2R-2		Double leaf brick masonry;	
Strengthened: coating on both sides; *3 cm thick mortar coating reinforced by GFRM mesh; twenty passing through "L" anchors*			
Date of test:	2021/12/15 (age: 69 days)	Bilinear idealisation	
Dimensions (*l*/*h*/*t*):	1500/1960/250 mm	u_e	7.62 mm (0.38 %)
Vertical stress (σ_0):	0.5 MPa	u_u	62.6 mm (3.13 %)
		H_u	181.4 kN
Equivalent tensile strength	0.494 MPa		
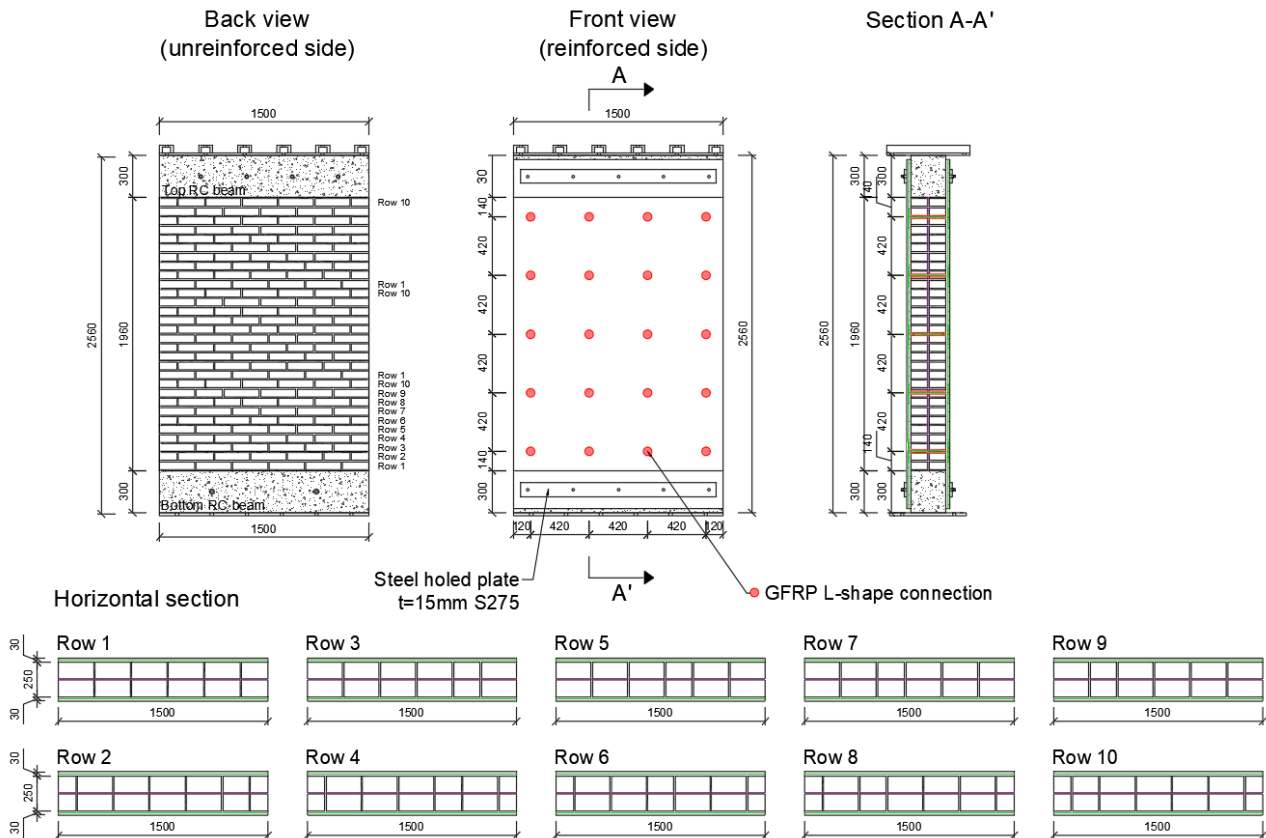
Fig. 57: Plan of the wall.

P-B2R-2

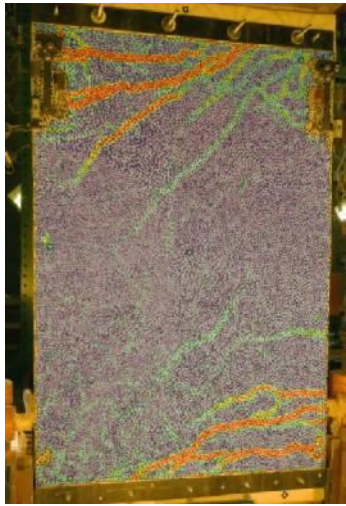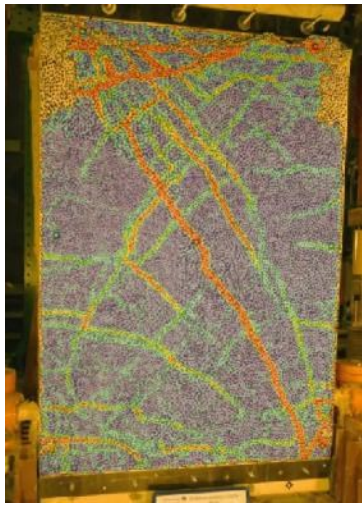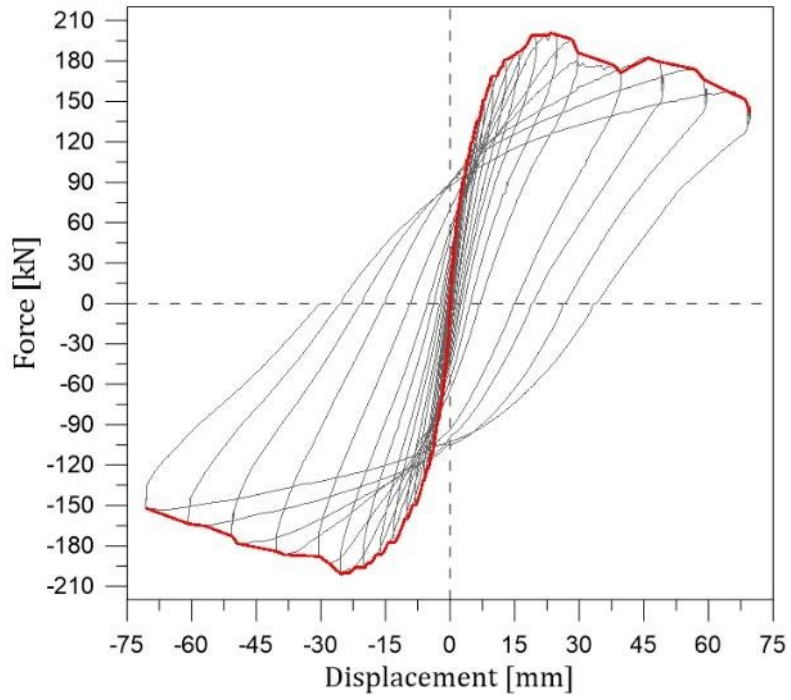*Fig. 58: Force-displacement curve and the envelope*
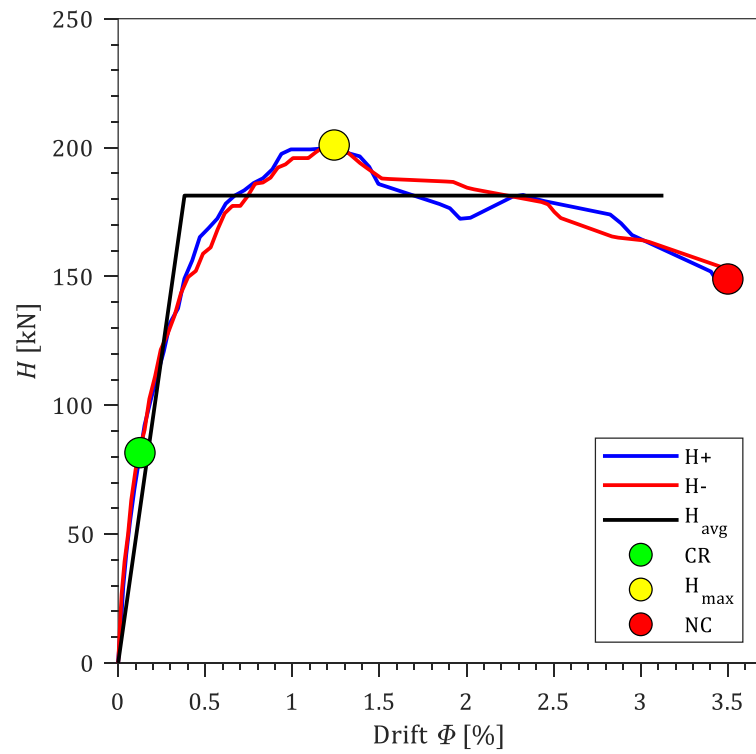
Fig. 59: Envelopes of the response, bilinear idealisation and limit states.

P-B2R-2

Table 22: Limit states of the wall

Damage LS 🟢		Max Resist LS 🟡		Near Col. LS 🔴	
H_{cr} [kN]	Φ_{cr} [%]	H_{max} [kN]	Φ_{Hmax} [%]	H_{ult} [kN]	Φ_{ult} [%]
81.6	0.13	201.1	1.24	149.0	3.48

Front

Back

2-3 mm (0.13 %)	Horizontal cracks in the coating at the base of the wall were the first sign of damage.
3 - 20 mm (1 %)	The damage in the coating concerns horizontal cracks at the base and top of the wall (flexure). The cracks open and close and propagate.
25 mm (1.25 %)	Peak resistance is reached. Small inclined cracks appear at 25 mm, but the bending response dominates.
25 – 70 mm (1.25 – 3.5 %)	The wall responds by bending with the horizontal cracks opening and closing. At the same time, shear cracks in the coating propagate
70 mm (3.5 %)	Wall collapses due to a fracture of the mesh in the horizontal crack at the top of the wall.

6.6   Summary and analysis

6.6.1   Stone masonry

Effect of strengthening from tests
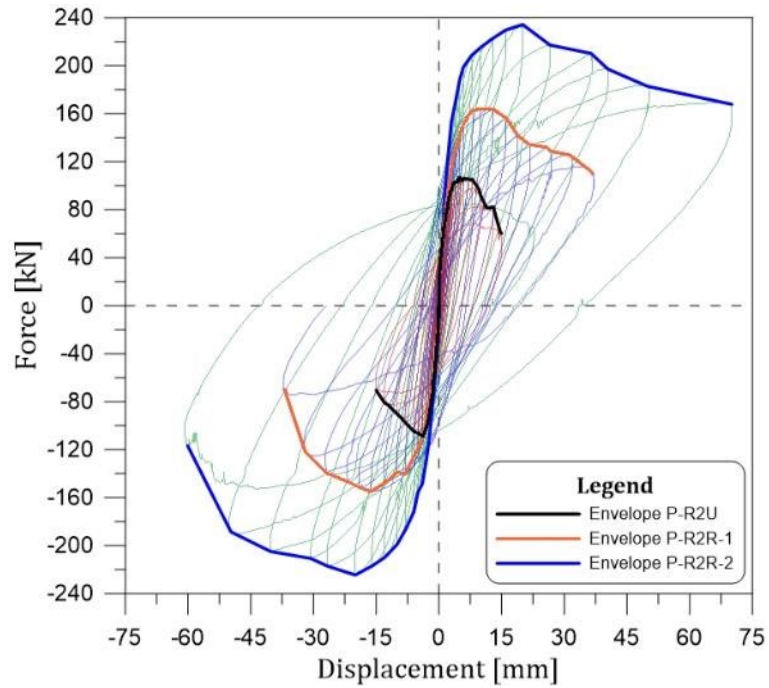
Fig. 60: Hysteretic curves and envelopes

Table 23: Results from the tests

Sample	H_{max} [kN]	$\Phi_{H_{max}}$ [%]	Φ_{ult} [%]
P-R2U	107.8	0.24	0.75
P-R2R-1	159.5	0.66	1.76
P-R2R-2	229.4	0.99	3.01

Table 24: Effect of strengthening (results relative to P-R2U)

Sample	Rel. change of H_{max} [ ]	Rel. change of $\Phi_{H_{max}}$ [ ]	Rel. change of Φ_{ult} [ ]
P-R2U	1	1	1
P-R2R-1	1.48	2.75	2.47
P-R2R-2	2.13	4.13	4.35

Effect of strengthening on idealised response
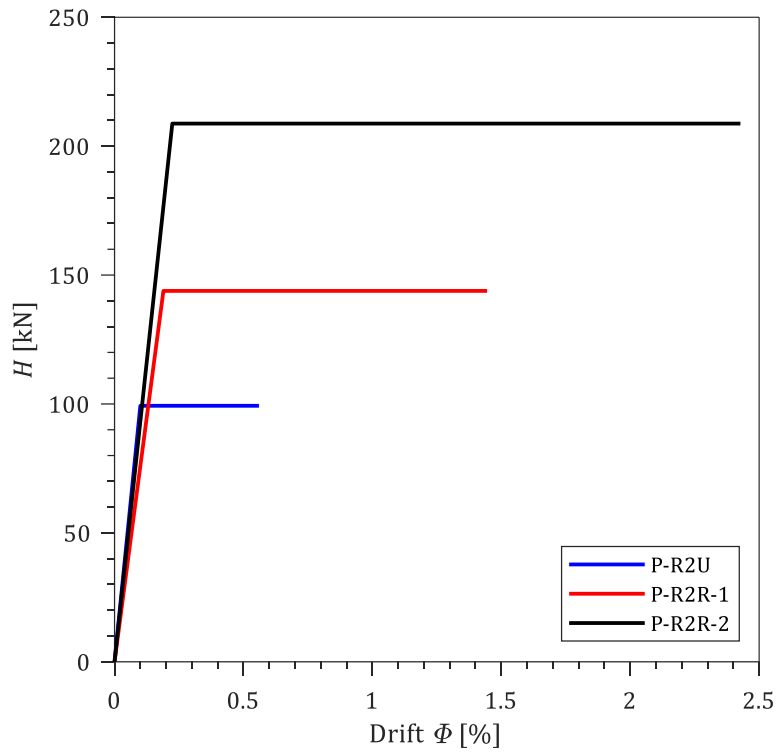
Fig. 61: Comparison of bilinear response curves

Table 25: Idealised response

	Φ_e [%]	H_u [kN]	Φ_u [%]	Φ_u/Φ_e [ ]
P-R2-U	0.10	99.3	0.56	5.6
P-R2R-1	0.19	143.9	1.45	7.6
P-R2R-2	0.22	208.8	2.43	10.8

Table 26: Effect of strengthening (results relative to P-R2U)

	Rel. change of Φ_e [ ]	Rel. change of H_u [ ]	Rel. change of Φ_u [ ]	Rel. change of Φ_u/Φ_e [ ]
P-R2-U	1	1	1	1
P-R2R-1	1.90	1.45	2.58	1.36
P-R2R-2	2.25	2.10	4.33	1.93

Energy dissipation
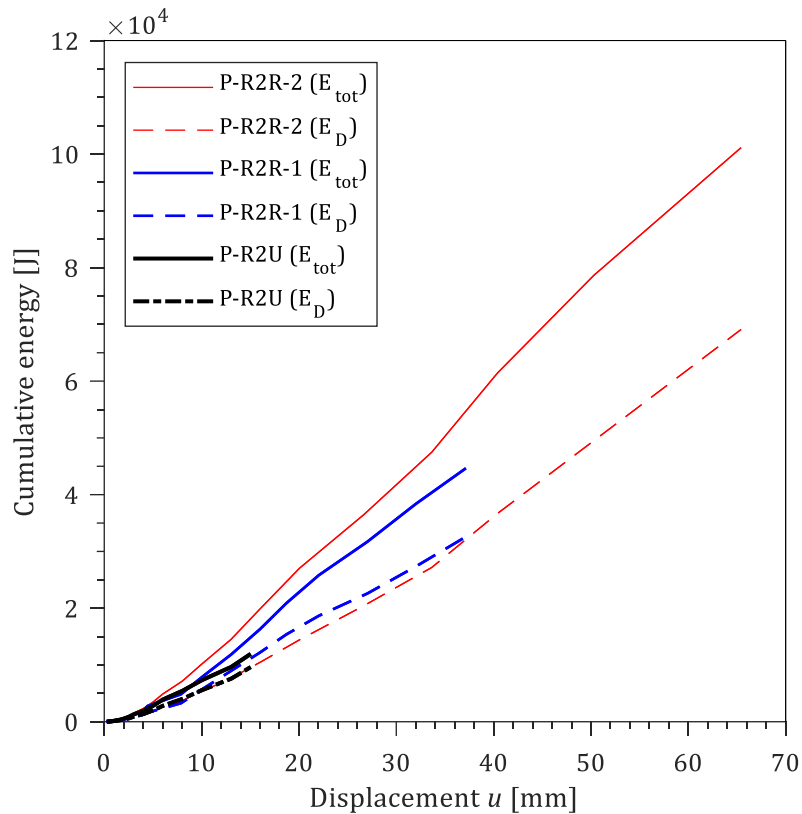
Fig. 62: Cumulative total and dissipated energy against displacement.

Summary

The one- and two-sided coating significantly improved seismic performance of stone masonry walls. In both cases, the coating and the wall acted as a composite element and performed adequately under seismic loads.

The mode of damage propagation was significantly different in the case of walls with coating compared to unstrengthened walls. Whereas the unstrengthened wall developed a few cracks in which all the damage was localised, the damage in strengthened walls was distributed over a larger area. The latter response is better as it increases energy dissipation capacity.

The unreinforced wall responded in shear. Applying coating on one side introduced some bending effects into the shear response. However, the dominant mode of response and failure was still shear. When the coating was applied to both sides of the wall, the response and failure transitioned from shear to bending.

One-sided and two-sided coating increased resistance to lateral load by about 50 % and 110 %, respectively. Furthermore, displacement capacity and ductility were also increased by large margins. Displacement capacity increased by 150 % and 330 % for one- and two-sided strengthening, respectively. Ductility also increased, and the improvement was by 35 % and 90 % for one- and two-sided strengthening, respectively.

6.6.2 Brick masonry (single leaf)

Effect of strengthening from tests
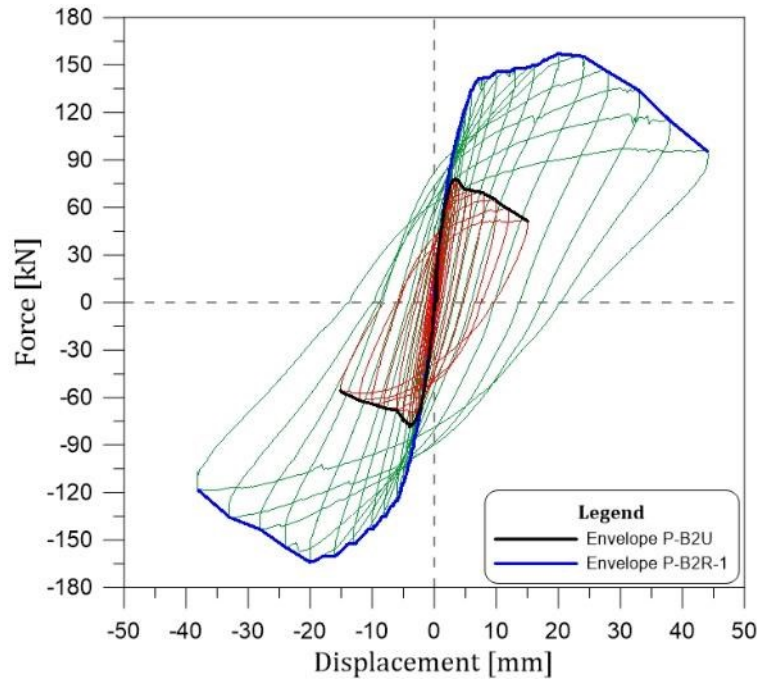
Fig. 63: Hysteretic curves and envelopes

Table 27: Results from the tests

	H_{max} [kN]	$\Phi_{H_{max}}$ [%]	Φ_{ult} [%]
P-B1U	101.9	0.32	0.91
P-B1R-1	166.4	0.7	1.558

Table 28: Effect of strengthening (results relative to P-B1U)

	Rel. change of H_{max} [ ]	Rel. change of $\Phi_{H_{max}}$ [ ]	Rel. change of Φ_{ult} [ ]
P-B1U	1	1	1
P-B1R-1	1.63	2.19	1.71

Effect of strengthening on idealised response
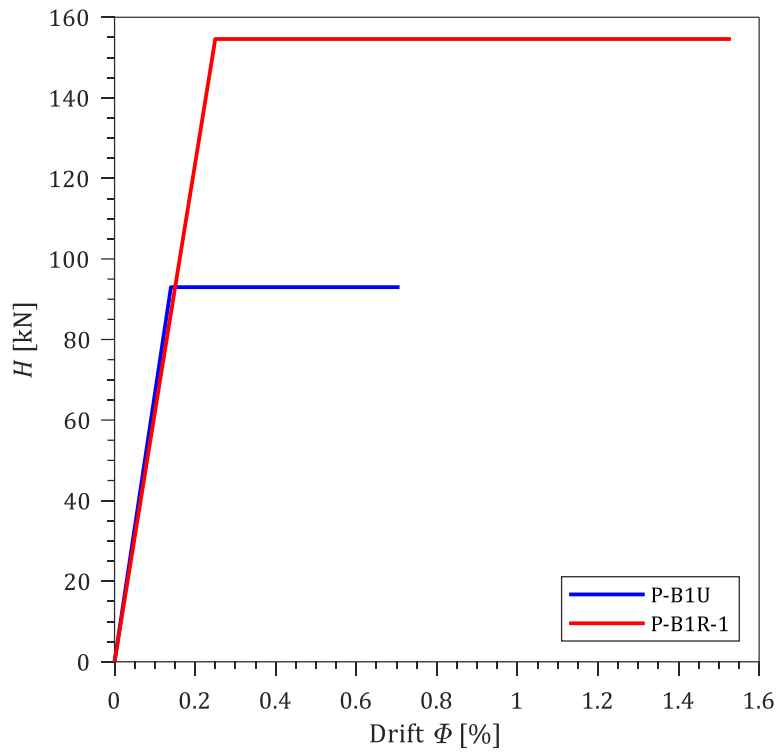
Fig. 64: Comparison of bilinear response curves

Table 29: Idealised response

	Φ_e [%]	H_u [kN]	Φ_u [%]	Φ_u/Φ_e [ ]
P-B1U	0.14	93.04	0.71	5.2
P-B1R-1	0.25	154.60	1.53	6.2

Table 30: Effect of strengthening (results relative to P-B1U)

|	Rel. change of Φ_e [ ]	Rel. change of H_u [ ]	Rel. change of Φ_u [ ]	Rel. change of Φ_u/Φ_e [ ]
P-B1U	1	1	1	1
P-B1R-1	1.80	1.66	2.16	1.20

Energy dissipation
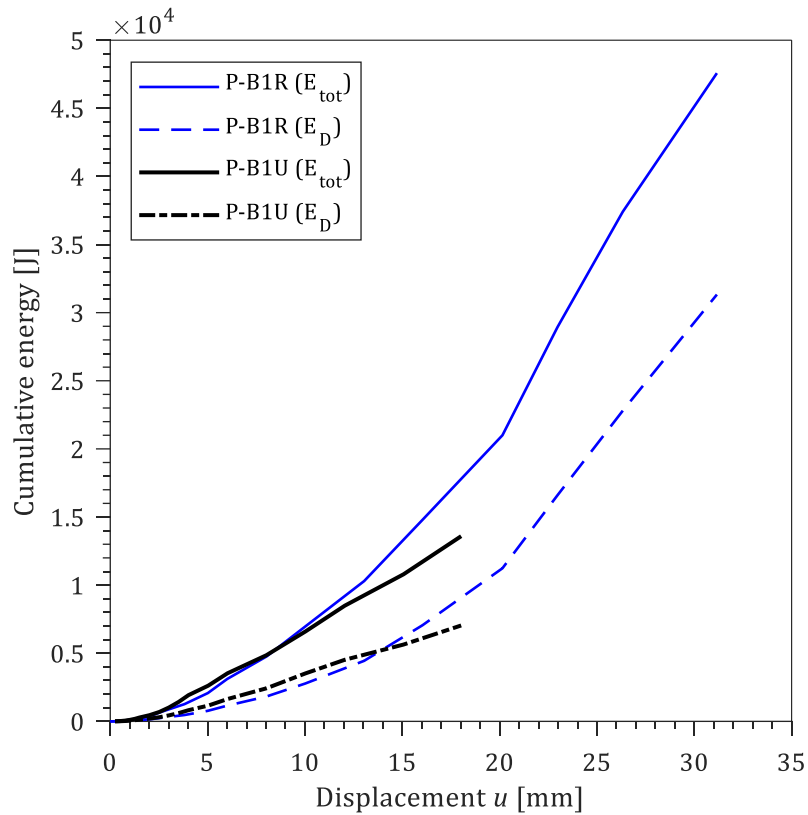
Fig. 65: Cumulative total and dissipated energy against displacement.

Summary

The one-sided coating significantly improved the seismic performance of the single-leaf brick walls. The coating and the wall acted as a composite element and performed adequately under seismic loads. This is evident by the observation that the composite effect of coating was not lost until the collapse despite different types of damage in the coating and the brick wall. The coating responded in bending, whereas the brick wall responded in shear. The composite effect was achieved because of sufficient anchoring.

The mode of damage propagation was significantly different in the coating and the walls. The damage in the unstrengthened wall was concentrated in two diagonal shear cracks. In the coating, on the other hand, cracks were at the top and bottom of the wall and oriented horizontally. Where there was cracking, it was spread over an area, and more cracks were activated. Such a response is better as it increases energy dissipation capacity.

The unreinforced wall responded in shear, whereas in the coating, there was bending.

The coating increased resistance to lateral load by about 60 %. Furthermore, displacement capacity and ductility were also increased by large margins. Displacement capacity increased by 70 %, and ductility increased by 20 %.

6.6.3 Brick masonry (double leaf)

Effect of strengthening from tests
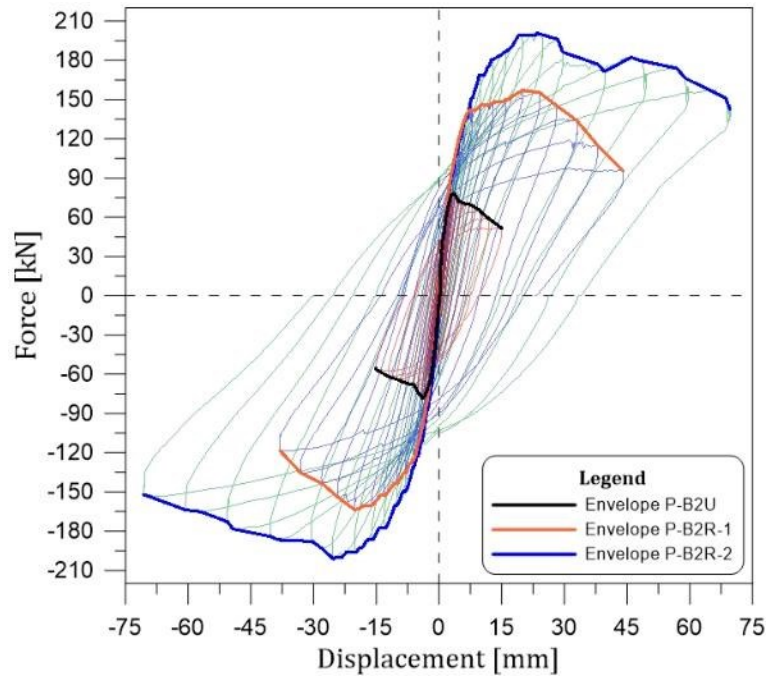
Fig. 66: Hysteretic curves and envelopes

Table 31: Results from the tests

	H_{max} [kN]	$\Phi_{H_{max}}$ [%]	Φ_{ult} [%]
P-B2U	78.3	0.19	15.03
P-B2R-1	160.5	1.04	41.12
P-B2R-2	201.1	1.24	70.21

Table 32: Effect of strengthening (results relative to P-R2U)

	Rel. change of H_{max} [ ]	Rel. change of $\Phi_{H_{max}}$ [ ]	Rel. change of Φ_{ult} [ ]
P-B2U	1	1	1
P-B2R-1	2.05	5.47	2.74
P-B2R-2	2.57	6.53	4.67

Effect of strengthening on idealised response
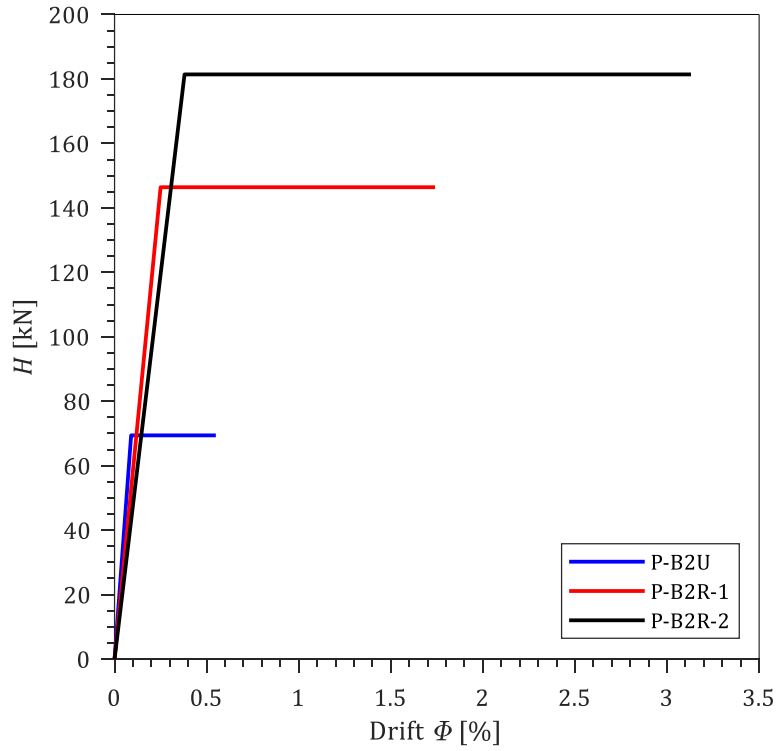
Fig. 67: Comparison of bilinear response curves

Table 33: Idealised response

	Φ_e [%]	H_u [kN]	Φ_u [%]	Φ_u/Φ_e []
P-B2U	0.09	69.4	0.55	6.1
P-B2R-1	0.25	146.4	1.74	6.9
P-B2R-2	0.38	181.4	3.13	8.2

Table 34: Effect of strengthening (results relative to P-R2U)

	Rel. change of Φ_e []	Rel. change of H_u []	Rel. change of Φ_u []	Rel. change of Φ_u/Φ_e []
P-B2U	1	1	1	1
P-B2R-1	2.77	2.11	3.16	1.14
P-B2R-2	4.17	2.61	5.67	1.36

Energy dissipation
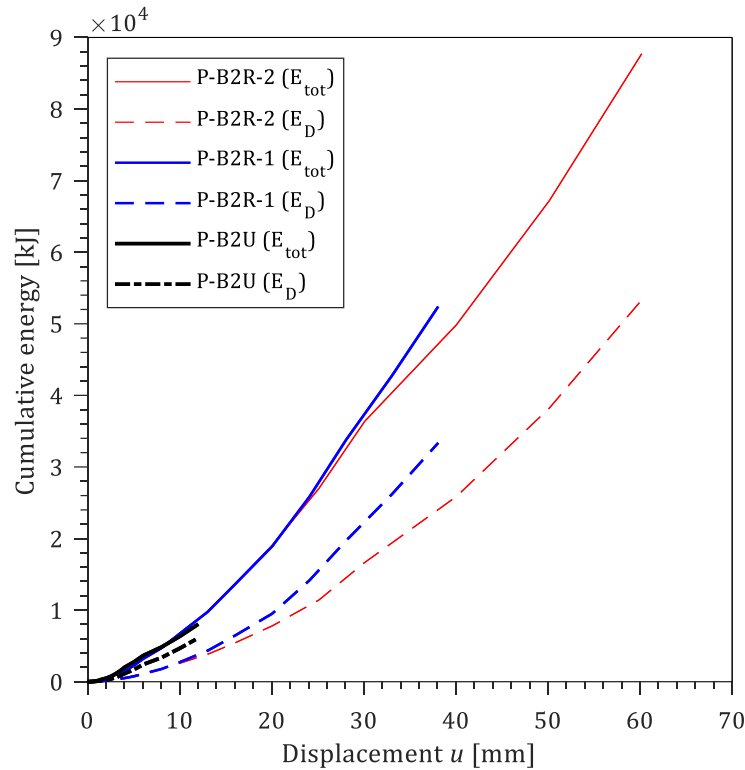
Fig. 68: Cumulative total and dissipated energy against displacement.

Summary

The seismic performance of two-leaf brick masonry walls was significantly improved by strengthening. The coating and the wall performed as a composite element until collapse. The weakest link was the connection between the wall leaves, where the damage occurred even when connected with artificial diatons. The two-sided coating performed best as it had the least problems with separating wall leaves.

The presence of coating causes the response of the system to change. In coating, the damage clearly indicates a bending response. At failure, there are also many inclined (shear) cracks. However, the primary response mechanism is bending in the coating. Shear cracks in the coating contribute to spreading the damage over larger areas and thus increase energy dissipation capacity.

Especially in the case of coating on both sides, shear damage in the coating indicates that the wall underneath probably failed in shear.

One-sided and two-sided coating increased resistance to lateral load by about 100 % and 150 %, respectively. Furthermore, displacement capacity and ductility were also increased by large margins. Displacement capacity

increased by 170 % and 360 % for one- and two-sided strengthening, respectively. Ductility also increased, and the improvement was by 14 % and 36 % for one- and two-sided strengthening, respectively.

7 Out-of-plane bending tests on piers

7.1 Test setup

The test setup for the out-of-plane response of piers is illustrated in Figs. 69 and 70. It consists of a steel truss reaction wall, restraining bars for the wall specimen, a trolley for the load distribution beams, and a hydraulic actuator. The test setup is a three-point bending test with the samples standing vertically and free to rotate at the top and bottom.
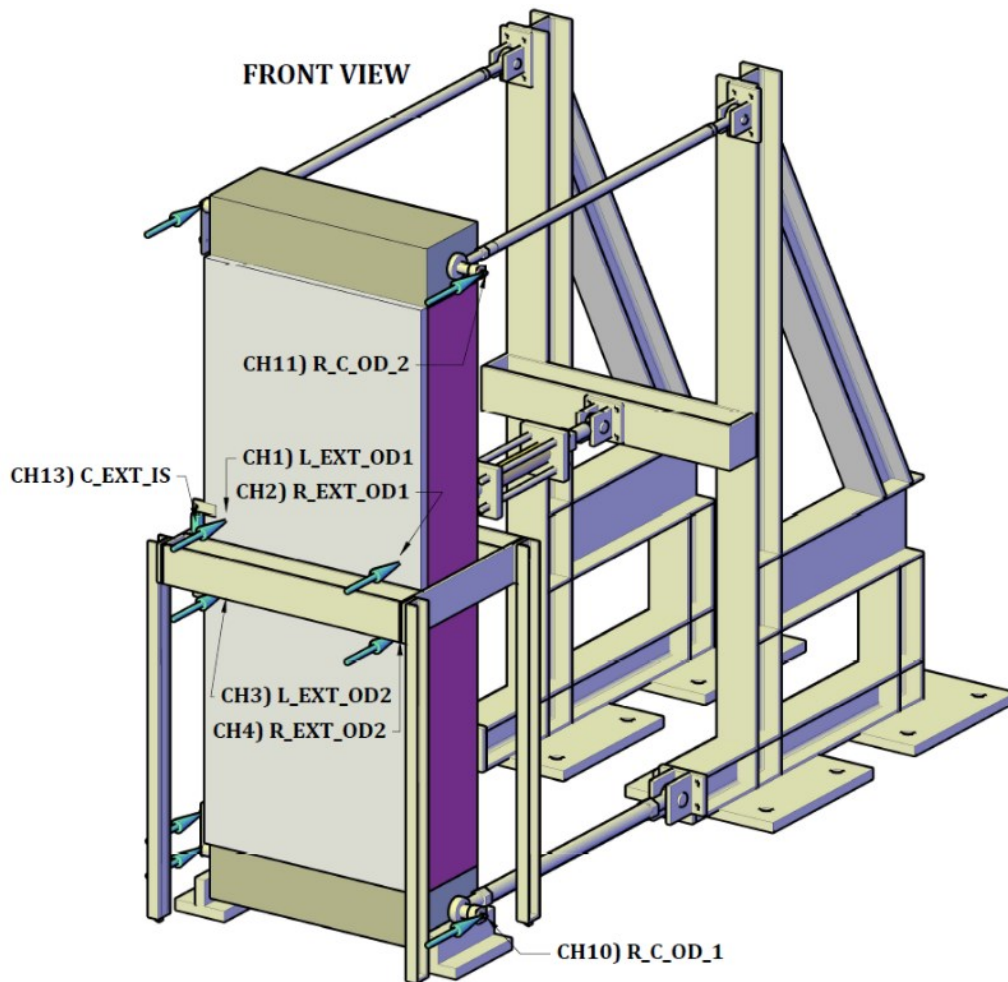
Fig. 69: Three-point out-of-plane bending test setup, front view.
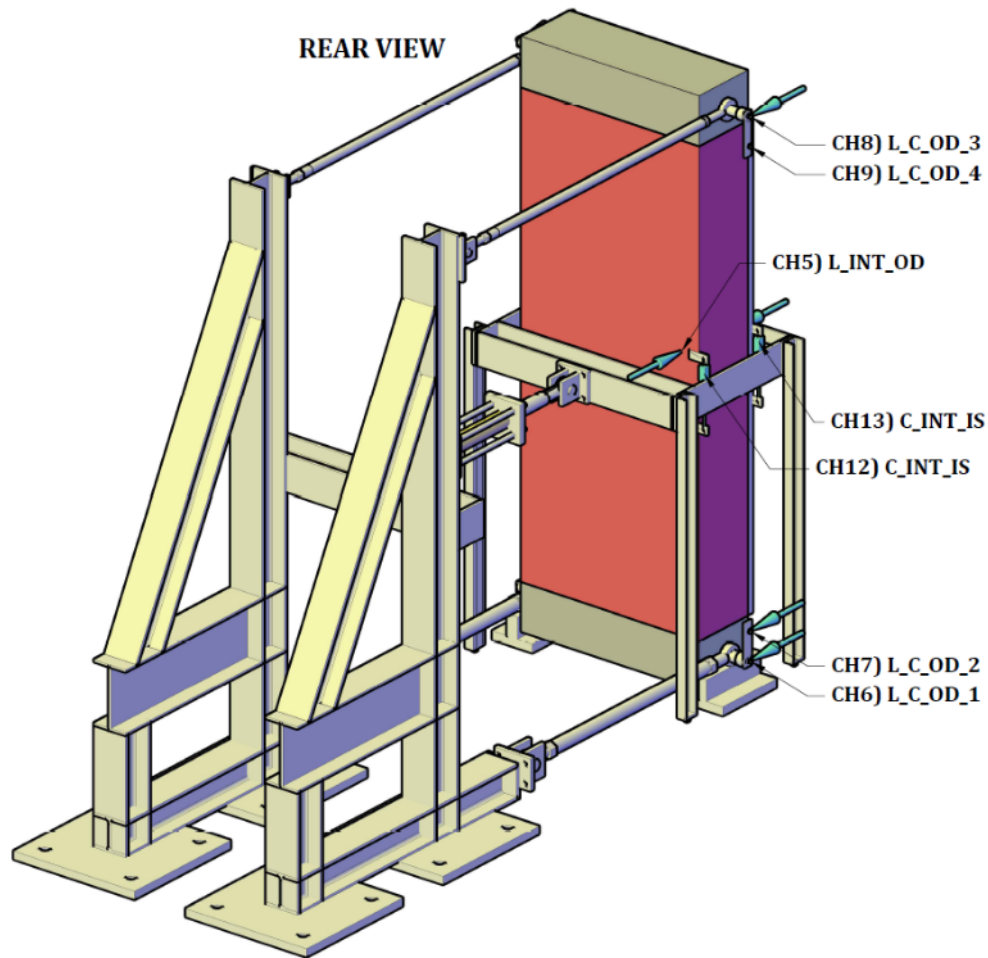
Fig. 70: Three-point bending test setup, back view

At the top and bottom of the masonry pier is a RC element, which has embedded horizontally in his axis a Ø40 mm steel bar. The element is connected to the reaction wall by horizontal steel pipes. At the bottom, the hinge joints rest on two steel profiles which bear all the weight.

To transfer the load, two HEA 160 steel beams, connected at the ends, are placed horizontally at both faces of the specimen at half height. They are kept in place by a trolley on ball bearings. Between the HEA 160 beams and the specimens are loading plates, which are free to rotate.

Part of the setup are some devices to prevent sliding between RC elements and the wall. The devices are shown in Figs. 71 and 72 for stone and brick masonry, respectively, and are used to increase friction by imposing compression. Each device is prestressed by manually screwing the bolts to about 10 kN force.
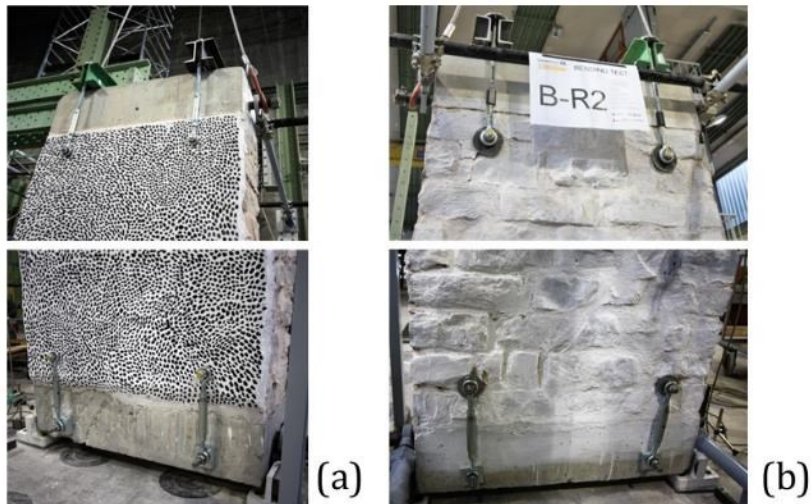
Fig. 71: Steel tie rods at the top and bottom of stone masonry pier. Strengthened side (a) and unreinforced side (b)
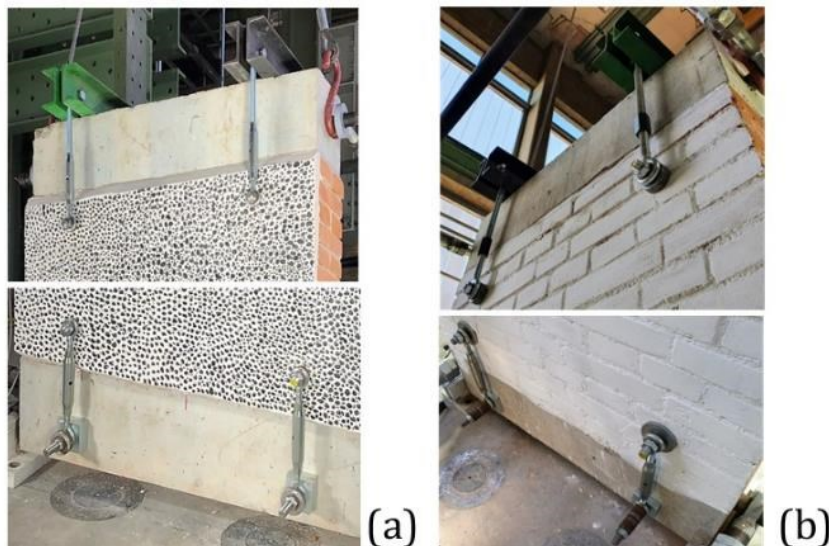
Fig. 72: Steel tie rods at the top and bottom of brick masonry pier. Strengthened side (a) and unreinforced side (b)

The samples dimensions and the steel carpentry are attached in the Appendix.

7.2 Instrumentation

Each specimen was equipped with 13 displacement transducers, as shown in Figs. 69 and 70 and two load cells. A digital image correlation system (DIC) was used to measure the displacement and strain fields on one surface of the wall. The side facing the cameras with the optical system was painted with a contrasting random speckle pattern, and the other was painted white to facilitate visual examination of cracks.

The forces in the actuator were measured by load cells. The transducers are explained in Table 35.

Table 35: Instrumentation for the OOP bending tests on piers

Transducer	Measurement
L_EXT_OD1, L_EXT_OD2, R_EXT_OD1, R_EXT OD2	Out-of-plane displacement of the middle section of the wall on the reinforced side
L_INT_OD	Out-of-plane displacement of the middle section of the wall on the unreinforced side, used to measure the separation of the masonry leaves
L_C_OD1, L_C_OD3, R_C_OD1, R_C_OD2	Out-of-plane displacements of RC elements
L_C_OD2, L_C_OD4	Rotation of the top and botom RC elements
C_INT_IS C_EXT_IS	(Vertical) relative displacement between two points at the middle of the wall
Load cells	Actuator load in the two loading directions

The middle height average displacement (C_OD_AVG) was calculated as:

$$C\_OD\_AVG = \frac{L\_EXT\_OD1 + L\_EXT\_OD2 + R\_EXT\_OD1 + R\_EXT\_OD2}{4}$$

The relative middle height average displacement (C_OD_AVG_REL) was calculated as:

$$C\_OD\_AVG\_REL = C\_OD\_AVG - \frac{L\_C\_OD\_1 + R\_C\_OD1 + L\_C\_OD3 + R\_C\_OD2}{4}$$

The top and base rotation of the RC beams were calculated as:

$$TOP\_ROT = \frac{L\_C\_OD2 - L\_C\_OD1}{150} \qquad BASE\_ROT = \frac{L\_C\_OD4 - L\_C\_OD3}{150}$$

In the equations above, 150 mm is the distance between the two instruments rotating with the steel bar.

The average out-of-plane displacements of the steel bars are calculated as:

$$BASE\_OD\_AVG = \frac{L\_C\_OD1 + R\_C\_OD1}{2} \qquad TOP\_OD\_AVG = \frac{L\_C\_OD3 + R\_C\_OD2}{2}$$

Wall leaves separation was calculated as:

$$LEAVES\_SEP = L\_EXT\_OD1 - L\_INT\_OD$$

7.3   Test protocols

In the test, the displacement at mid-height of the wall was controlled by manually pumping oil into the hydraulic jack. The load was applied cyclically in positive and negative directions according to the loading protocol. The first steps were performed by controlling the force until reaching the first crack on the reinforced side. After a certain degree of damage was reached, the load was applied monotonically towards the reinforced side until failure.

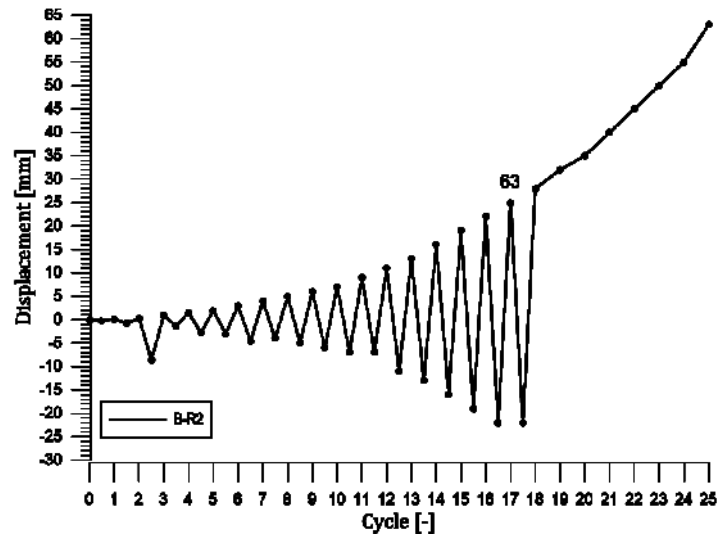A typical load protocol is shown in Fig. 73.

Fig. 73: Horizontal displacement sequence for specimen B-R2

Table 36: Loading used in the tests

Wall	B-R2		B-B1		B-B2	
Cycle	Positive amplitude [mm]	Negative amplitude [mm]	Positive amplitude [mm]	Negative amplitude [mm]	Positive amplitude [mm]	Negative amplitude [mm]
1.	0.18	-0.17	0.2	-0.2	0.2	-0.2
2.	0.33	-0.8	0.4	-0.4	0.4	-0.4
3.	1.0	-8.6	0.6	-0.6	0.6	-0.6
4.	1.5	-1.4	0.8	-0.8	0.8	-0.8
5.	2.0	-2.8	1.2	-1.2	1.2	-1.2
6.	3.0	-3.0	1.6	-1.85	1.6	-1.6
7.	4.0	-4.0	2.4	-2.4	2.4	-2.4
8.	5.0	-5.0	3.0	-3.0	3.0	-3.0
9.	6.0	-6.0	4.4	-4.0	4.0	-4.0
10.	7.0	-7.0	5.0	-5.0	5.0	-5.0
11.	9.0	-7.0	6.0	-6.0	6.0	-6.0
12.	11.0	-11.0	8.0	-8.0	8.0	-8.0
13.	13.0	-13.0	10.0	-15.0	10.0	-10.0
14.	16.0	-16.0	13.0	-13.0	13.0	-13.0
15.	19.0	-19.0	16.0	-16.0	16.0	-16.0
16.	22.0	-22.0	20.0	-20.0	20.0	-20.0
17.	25.0	-22.0	25.0	-25.0	25.0	-25.0
1.	28.0	-	30.0	-	30.0	-
19.	35.0	-	35.0	-	35.0	-
20.	40.0	-	40.0	-	40.0	-
21.	45.0	-	45.0	-	45.0	-
22.	50.0	-	50.0	-	50.0	-
23.	55.0	-	55.0	-	53.0	-
24.	63.0	-	59.0	-		

7.4 Evaluation of the response

7.4.1 Bending resistance (coating in compression)

The calculation is based on the assumption of the elastic response of the element and linear stress distribution in cross-section. The analysis makes it possible to evaluate the flexural strength of unstrengthened masonry f_{x1} (Fig. 74, left). The calculations are for the case when the coating is in compression and the unstrengthened side is in tension.

The bending moment in the element is shown in Fig. 74, right. The maximum bending moment in the beam is:

$$M = \frac{P}{2} \cdot \frac{h}{2}$$

It should be noted that h is the distance between the supports and not the height of the masonry.
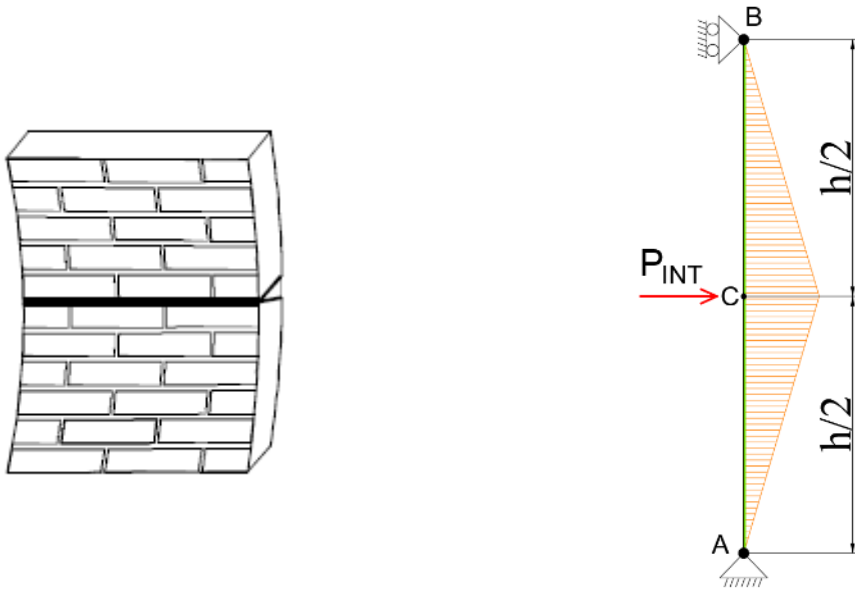

Fig. 74: Failure with exhausted f_{x1} (left), bending moment in the element (right)

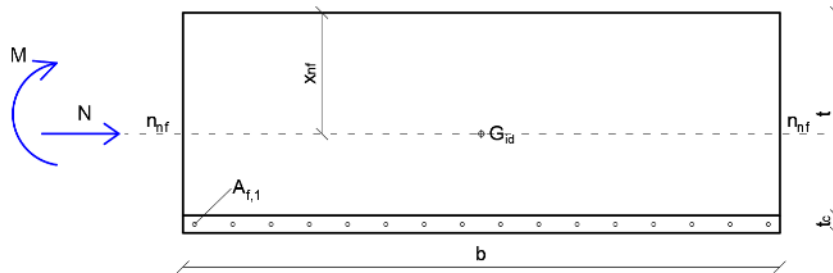The cross-section equilibrium is calculated on an idealised cross-section shown in Fig. 75.

Fig. 75: Scheme of the cross-section.

The variables used for calculating the idealised cross-section are summarized in Table 37.

Table 37: Variables for calculation of idealised cross-section.

Variable	Description	Variable	Description
b	Length of the wall	$A_{f,1}$	Area of yarn of fibres
t	Thickness of the wall	n_{nf}	Neutral axis of uncracked section
t_c	Thickness of the coating	x_{id}	Location of centre of gravity
$n_f = \dfrac{E_f}{E_m}$	Ratio of elastic moduli of fibres and masonry	G_{id}	Centre of gravity
$n_c = \dfrac{E_c}{E_m}$	Ratio of elastic moduli of coating and masonry	N, M	Axial force and bending moment

In the calculation, the location of centre of gravity of the idealised cross-section is calculated first:

$$x_{id} = \frac{S_{id}}{A_{id}}$$

Where A_{id} and S_{id} are the idealised cross-section and first moment of area, respectively. They are calculated as:

$$A_{id} = b \cdot t + n_f \, b \cdot t_c$$

$$S_{id} = \frac{b \cdot t^2}{2} + n_c \cdot b \cdot t_c \cdot \left(t + \frac{t_c}{2}\right) + n_f \cdot n_{yarns} \cdot A_{f,1} \cdot \left(t + \frac{t_c}{2}\right)$$

Known the centre of gravity, which is also the location of the neutral axis, the area moment of inertia (J_{id}) can be calculated:

$$J_{id} = \frac{b \cdot t^3}{12} + b \, t \left(x_{id} - \frac{t}{2}\right)^2 + \frac{n_c \cdot b \cdot t_c^3}{12} + n_c \, b \, t_c \left(t + \frac{t_c}{2} - x_{id}\right)^2 + n_f \, n_{yarns} \, A_{f,1} \cdot \left(t + \frac{t_c}{2} - x_{id}\right)^2$$

Finally, the flexural strength of masonry can be calculated:

$$f_{x1} = \frac{N}{A_{id}} + \frac{M_{cr}}{J_{id}} x_{id}$$

7.4.2   Bending resistance (coating in tension)

Bending resistance of a wall at ultimate resistance is based on the following assumptions: cracked cross-section and zero tensile resistance in masonry and coating, peak tensile resistance in the yarns of the mesh, perfect contact between the coating and the wall, and stress-block distribution in the compressed part. The stress state and internal and external loads in a cross-section are shown in Fig. 76.

The calculations are for the case when the coating is in tension, and the unstrengthened side is in compression. It makes it possible to estimate resistance to out-of-plane loads.
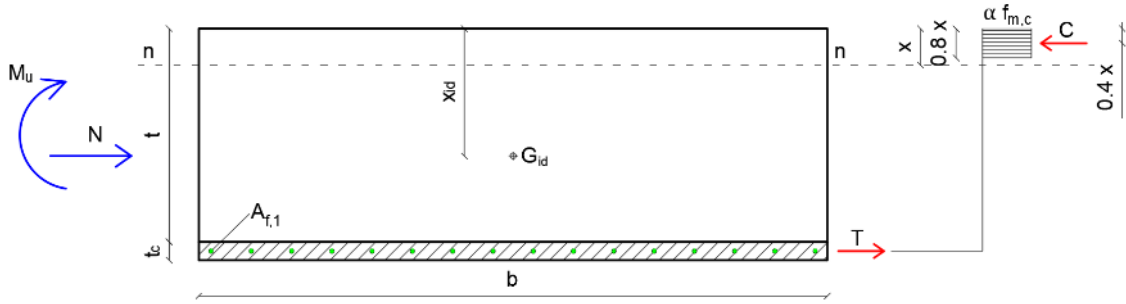
Fig. 76: Stress distribution at ultimate resistance

The first step in the calculation of bending resistance is determining the location of neutral axis (n):

$$x = \frac{N + n_{yarns} \cdot T_w}{0.8 \cdot b \cdot \alpha \cdot f_{m,c}}$$

Here T_w is the tensile strength of a single yarn, $f_{m,c}$ is the compressive strength of masonry, and $\alpha = 0.85$ is the parameter that accounts for long term effects on the compressive strength. Assuming h_{tot} is the total thickness $h_{tot} = t + t_c$ of the wall, and that a is the distance from the tensile edge to the centre of mesh yarns, flexural resistance is:

$$M_{u(R)} = 0.8x \cdot b \cdot \alpha \cdot f_{m,c} \cdot (x_{id} - 0.4x) + n_{yarns} \cdot T_w \cdot (h_{tot} - a - x_{id})$$

7.5 Tests

7.5.1 B-R2 (stone masonry)

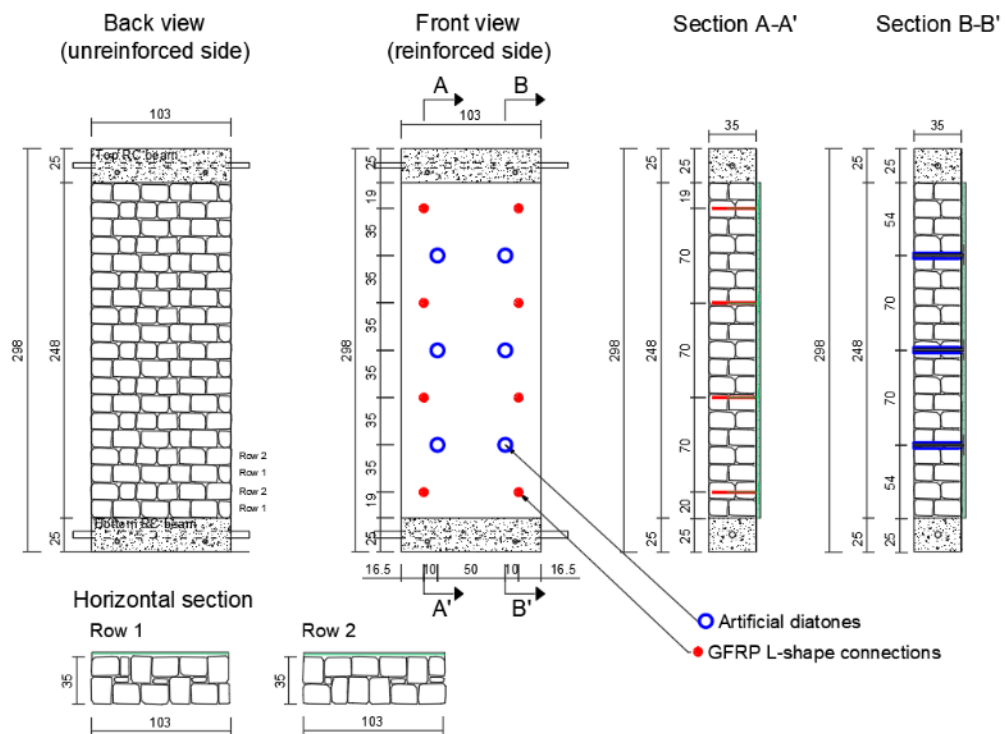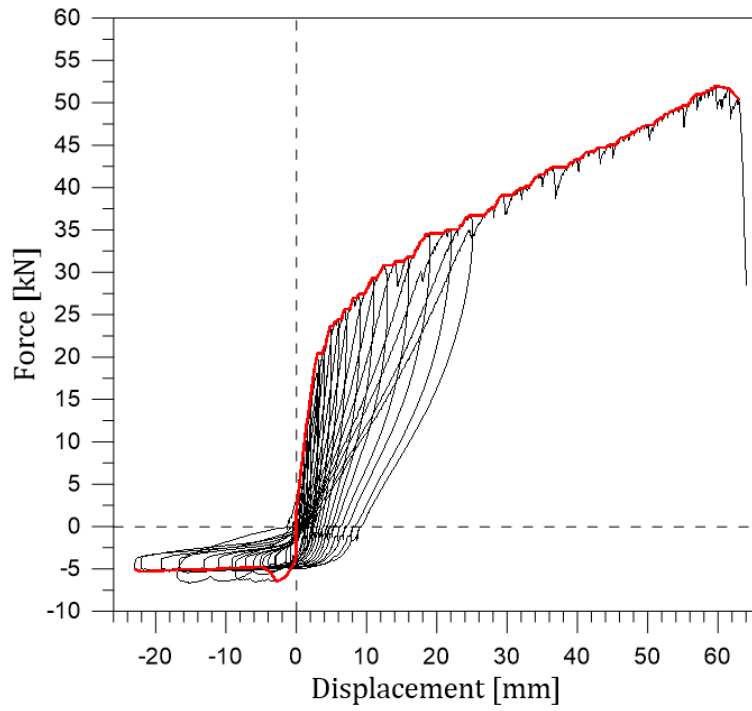| B-R2	Two leaf stone masonry;
	Strengthened on one side; GFRM mesh on one side, eight "L" connectors, six diatons
Date of test (age):	2021/12/23 (age: 294 days)
Dimensions (l/h/t):	2480/100/350 mm
Vertical stress (σ_0):	0.033 MPa (midsection)
Material characteristics	
f_c	2.48 MPa
E	1074 MPa
G	333 MPa

Fig. 77: Wall B-R2

B-R2

Fig. 78: Force – displacement curve for specimen B-R2; positive force = coating in tension;
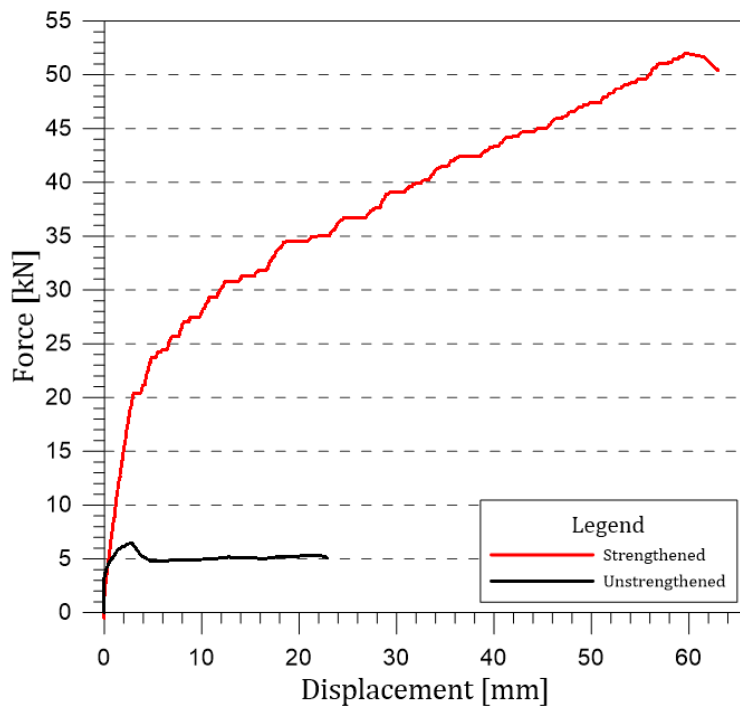

Fig. 79: Envelope curves for specimen B-R2

The first crack occurred on the unreinforced side, in the 13th and 14th mortar bed joints, at $u = -2.8$ mm, and a force of 6.5 kN. The test was conducted cyclically until $u = -22$ mm. Then a second horizontal crack formed in the 16th mortar bed joint (Fig. 80), and the test was changed to monotonically pushing towards the strengthened side (coating in tension).

Fig. 80: Cracks on the unstrengthened side at u = -22.0 mm

The first crack on the strengthened side was horizontal and located at the height of the loading apparatus, while at $u = 3$ mm, two horizontal cracks formed near the middle section, just outside the loading plate.

Starting at $u = 22$ mm, two diagonal cracks formed in the thickness of the wall due to punching shear. They originated from the loading plate and propaged in as shown in Fig. 81a and b.
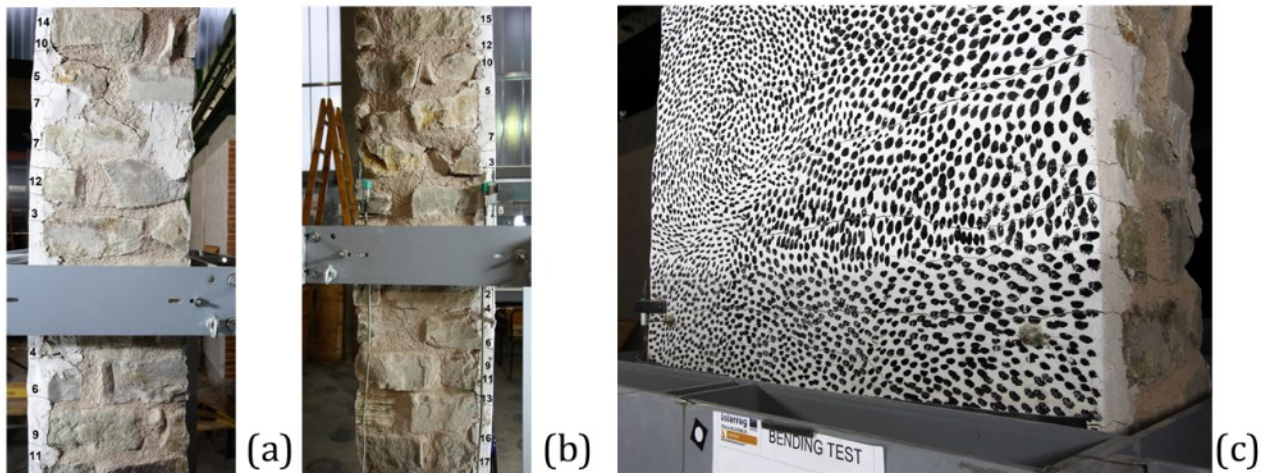

Fig. 81: Cracks due to punching shear at u = 35.0 mm, right view (a), left view (b) and front view (c)

Other horizontal cracks in the coating appeared with increasing load, as presented in Fig. 82.
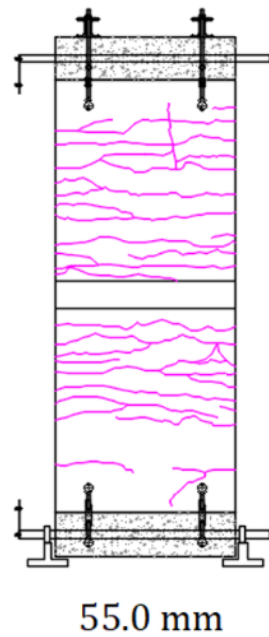

55.0 mm

Fig. 82: Cracks in the coating of specimen B-R2

At the end of the test ($u = 63.1$ mm), the coating had multiple, mostly horizontal cracks on the reinforced coating, and the main crack located at about ¾ of the masonry height. In Fig. 83 b, c and d, the final collapse of the specimen is shown.
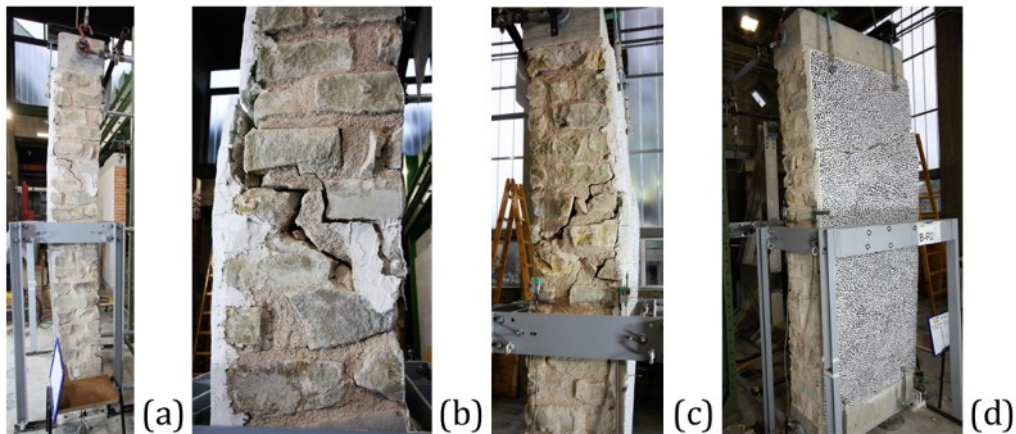

Fig. 83: Crack pattern at $u = 55.0$ mm (a) and at the end of the test, right view (b), left view (c), front view (d)

In the push direction, the specimen B-R2 reached a maximum load $H^+_{max} = 52.0$ kN and a maximum out-of-plane displacement $u_{max} = 62.98$ mm. In the pull direction, the maximum resistance before cracking was equal to $H^-_{max} = 6.49$ kN.

7.5.2 B-B1 (brick, single leaf)

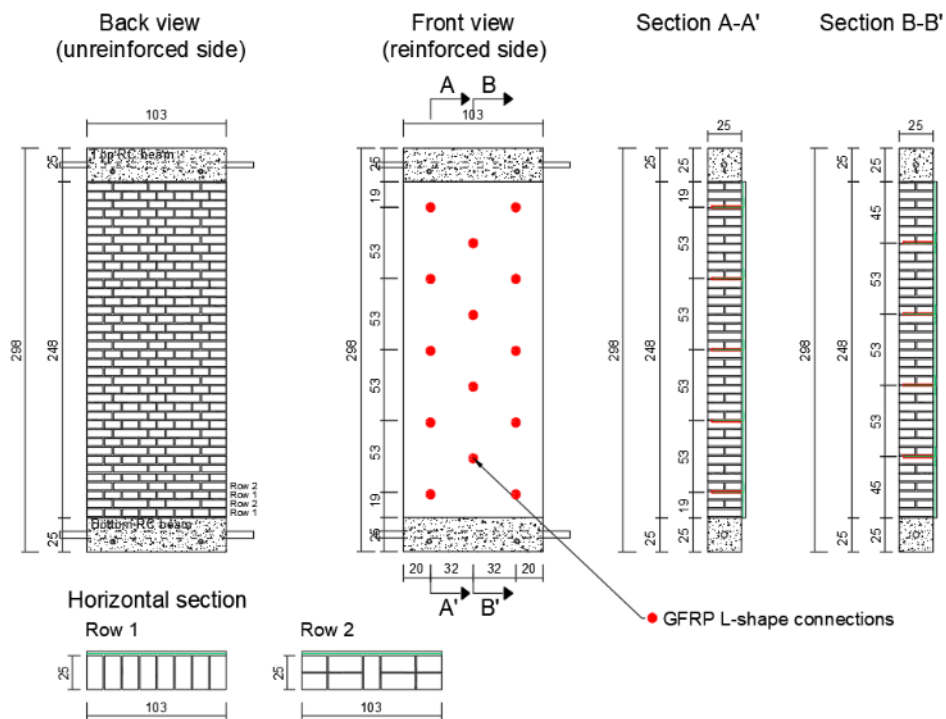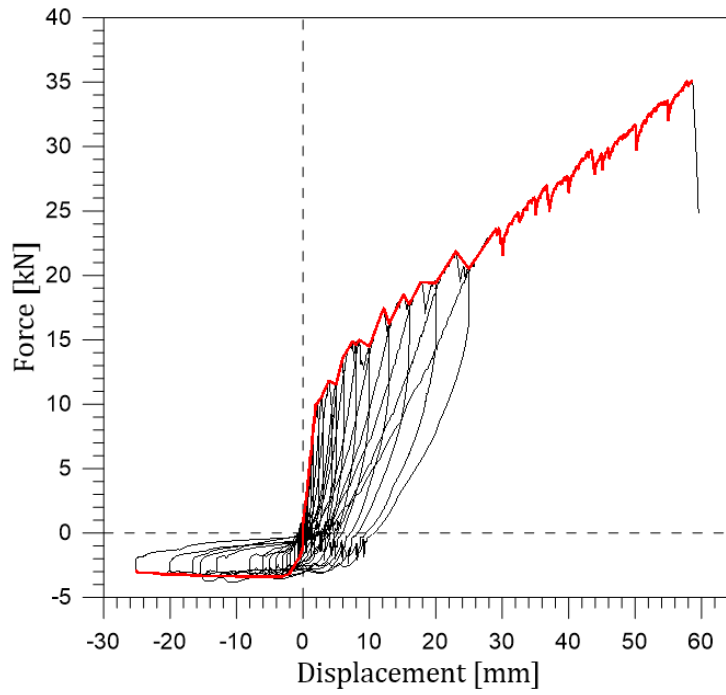| **B-B1**	Single leaf brick masonry;
	Strengthened on one side;
	CRM coating on one side, fourteen "L" connectors
Date of test (age):	2022/3/4 (age: 148 days)
Dimensions (*l*/*h*/*t*):	2500/100/250 mm
Vertical stress (σ_0):	0.029 MPa (midsection)
Material characteristics	
f_c	6.7 MPa
E	2341 MPa
G	258 MPa

Fig. 84: Specimen B-B1

84

B-B1

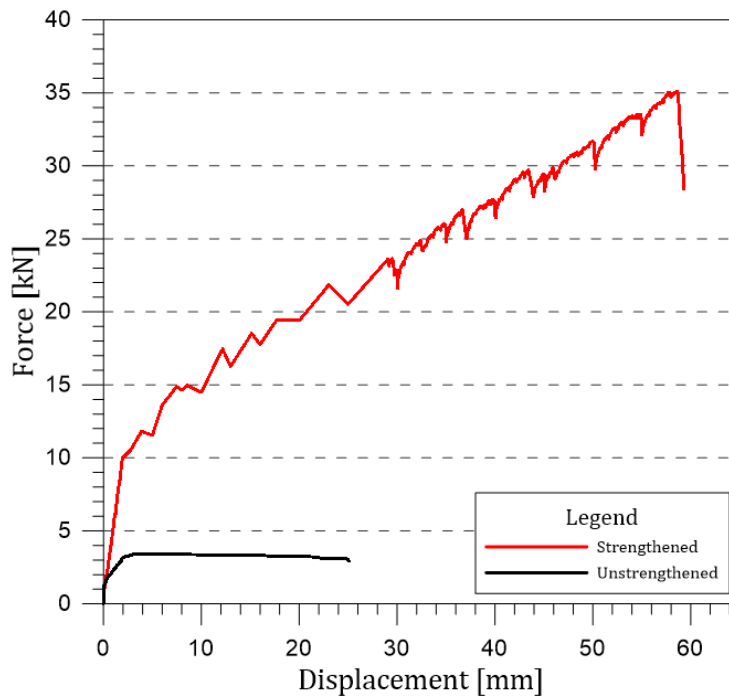*Fig. 85: Force – displacement curve for specimen B-B1; positive force = coating in tension;*

Fig. 86: Envelope curves for specimen B-B1

The first crack was horizontal in the bed joint of the unreinforced side. It appeared at midheight at $u = -4.3$ mm and a force of 3.4 kN. At $u = -11.0$ mm a second horizontal crack formed in the 26th bed joint (Fig. 87). The test was conducted cyclically until $u = -25$ mm when the crack pattern on the unstrengthened side stopped changing. From then, the load was applied monotonically by pushing towards the strengthened side (coating in tension).

Fig. 87: Cracks on the unstrengthened side at u=-22.0 mm

On the coated side, the first crack appeared next to the steel plates for imposing the load at midheight. As the load increased, new cracks appeared in the coating. All cracks in the coating were primarily horizontal, as shown in Fig. 88. The cracks originated from the midsection and gradually spread toward the top and bottom of the pier.

Fig. 88: Cracks pattern on the coating

At collapse, the GFRP mesh in the coating fractured (Fig. 89). The collapse occurred at a displacement of 58.6 mm and a force of 36 kN.

Fig. 89: Fracture of GFRP mesh at collapse.

7.5.3   B-B2 (brick, double leaf)

B-B2	Single leaf brick masonry;
	Strengthened on one side; CRM coating on one side, eight "L" connectors, six diatons
Date of test (age):	2022/3/22 (age:166 days)
Dimensions ($l/h/t$):	2500/100/250 mm
Vertical stress (σ_0):	0.029 MPa (midsection)
Material characteristics	
f_c	6.7 MPa
E	2341 MPa
G	258 MPa

SOLID BRICK MASONRY - DOUBLE LEAF (CRM on one side + diatons)
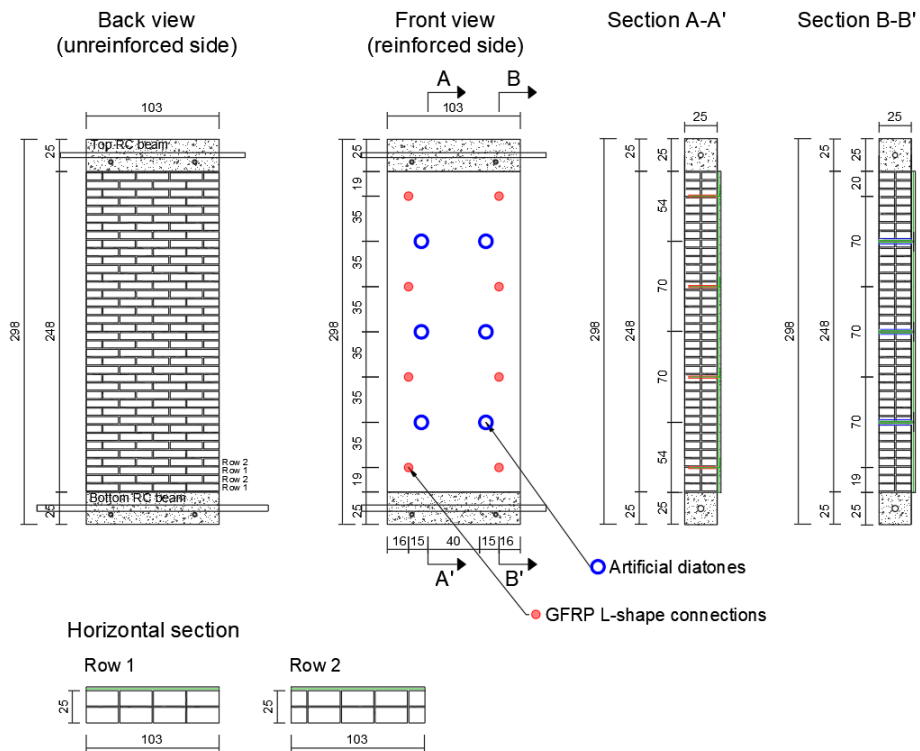
B-B2
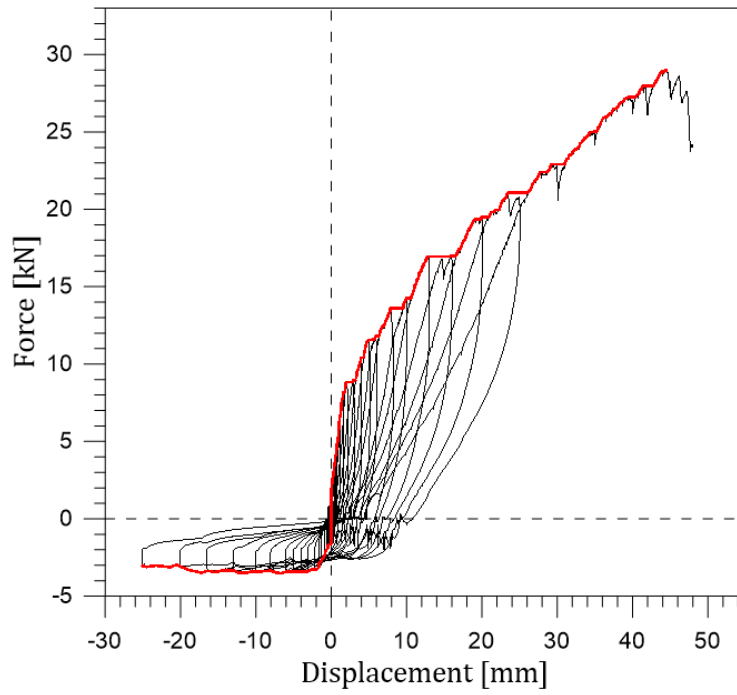
Fig. 90: Force – displacement curve for specimen B-B2; positive force = coating in tension;
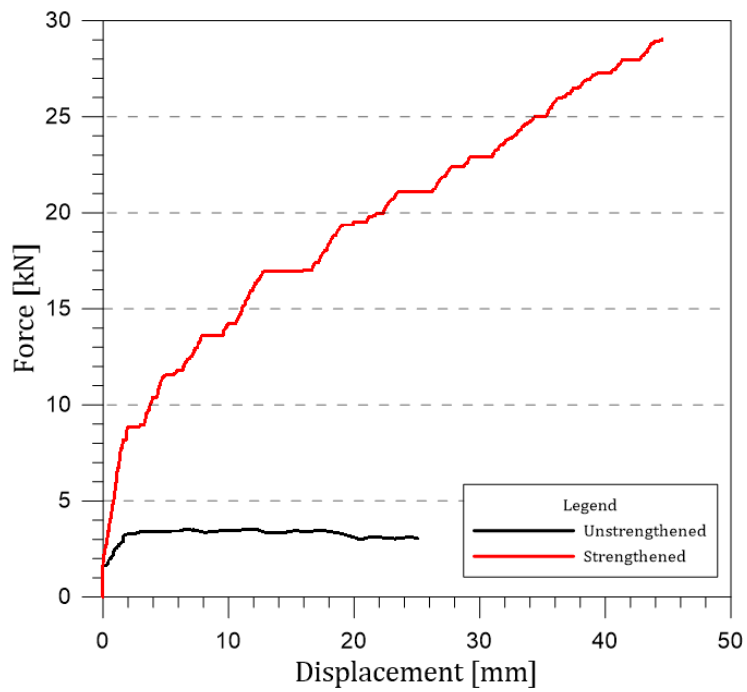
Fig. 91: Envelope curves for specimen B-B2

The first crack occurred on the unreinforced side, in the middle section (Fig. 92), at $u = -2.0$ mm and a force of 3.3 kN. The crack pattern (mechanism) on the unstrengthened side stabilized after $u = -5$ mm was reached. The test was conducted cyclically until $u = -25$ mm. After this, the test was conducted monotonically by pushing towards the strengthened side (coating in tension).

Fig. 92: Cracks on the unstrengthened side.

On the coated side, the first crack appeared next to the steel plates for imposing the load at midheight. As the load increased, new cracks appeared in the coating. All cracks in the coating were primarily horizontal, as shown in Fig. 93. The cracks originated from the midsection and gradually spread toward the top and bottom of the pier.
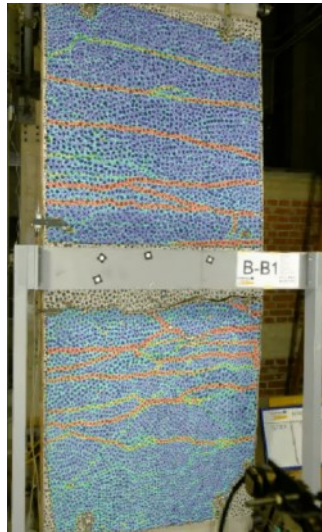

Fig. 93: Cracks pattern on the coating

At collapse, the GFRP mesh in the coating fractured (Fig. 89). The collapse occurred at a displacement of 44.5 mm and a force of 29 kN.
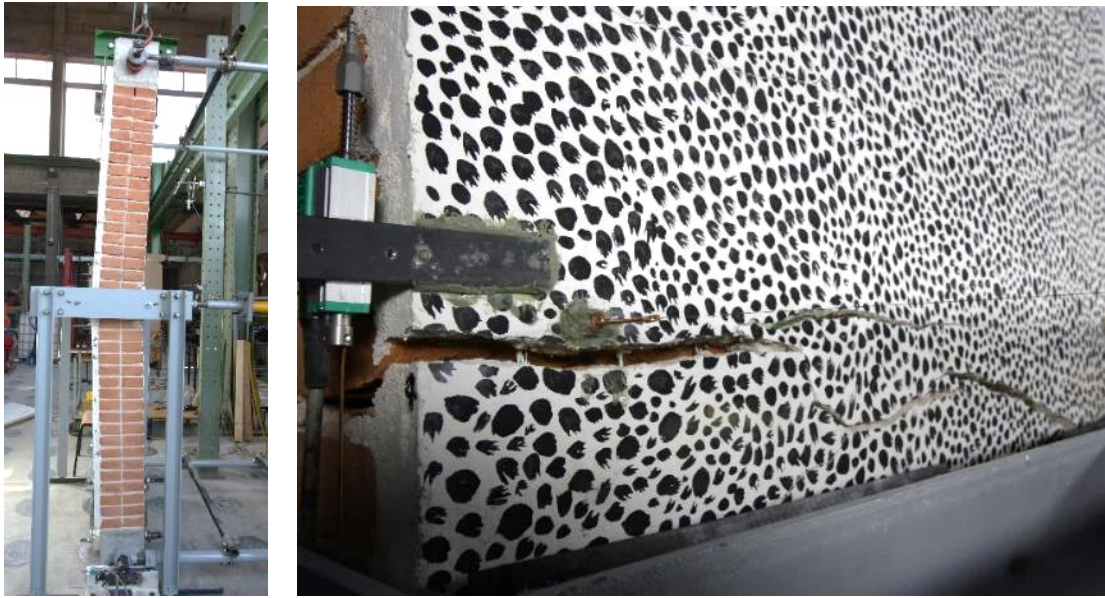
Fig. 94: Fracture of GFRP mesh at collapse.

7.6 Summary and analysis

The strengthening significantly improved the out-of-plane performance of the walls. The coating and the wall performed as a composite elemen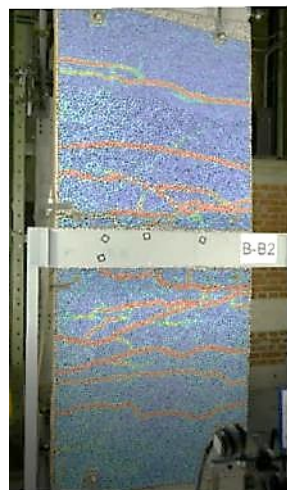t and efficiently resisted loads. The bond between the coating and the wall was not lost during the test. At collapse, the mesh fractured in tension, indicating all materials were used to their full potential.

There were many cracks in the coating, whereas, on the unstrengthened side, there was a concentration of damage in just a few cracks. Such a mechanism with more widespread damage increases the walls' displacement and energy dissipation capacities.

The improvement of the response due to strengthening is quantitatively assessed in Table 38. The strength increased 8 to 10 times, and the ratio between displacement at cracking and ultimate displacement was between 13.5 and 22.4.

The tests were also used to assess the flexural strength of masonry with plane failure parallel to bed joints (f_{k1}). The strength is 0.102 MPa for stone masonry and 0.111 MPa for brick masonry.

Finally, the very good predictions of the model shown in Table 39 validate the assumptions in the calculation, which (crucially) include the assumption about the perfect contact between the coating and the wall.

Table 38: Effect of strengthening on out-of-plane response

Specimen ID	P_{cr} [kN]	$P_{u(R)}$ [kN]	M_{cr} [kNm]	M_u [kNm]	M_u/M_{cr} [-]	d_{cr} [mm]	d_u [mm]	d_u/d_{cr} [-]	f_{x1} [MPa]
B-R2	6.5	52.0	4.4	35.5	8.01	2.81	63.0	22.41	0.102
B-B1	3.4	35.1	2.3	24.0	10.36	4.31	58.6	13.59	0.111
B-B2	3.4	29.0	2.3	19.8	8.50	3.13	44.5	14.23	0.111

Table 39: Precision of the model for bending resistance

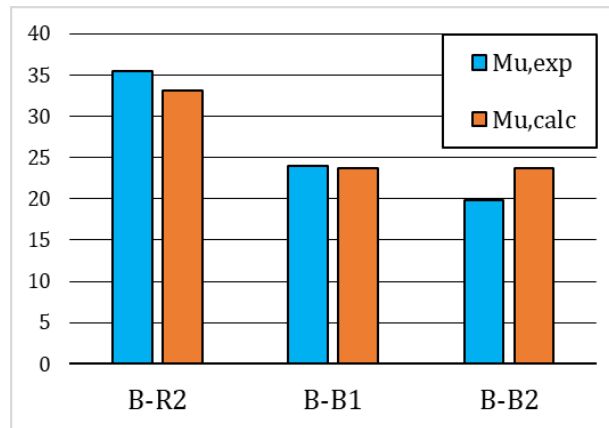| Specimen ID	$M_{u,exp}$ [kNm]	$M_{u,calc(inc)}$ [kNm]	$M_{u,exp}/M_{u,calc}$ [-]
B-R2	35.5	33.12	**1.07**
B-B1	24.0	23.66	**1.01**
B-B2	19.8	23.66	**0.84**

Fig. 95: Comparison between the experimental and the analytical prediction of the resisting moment
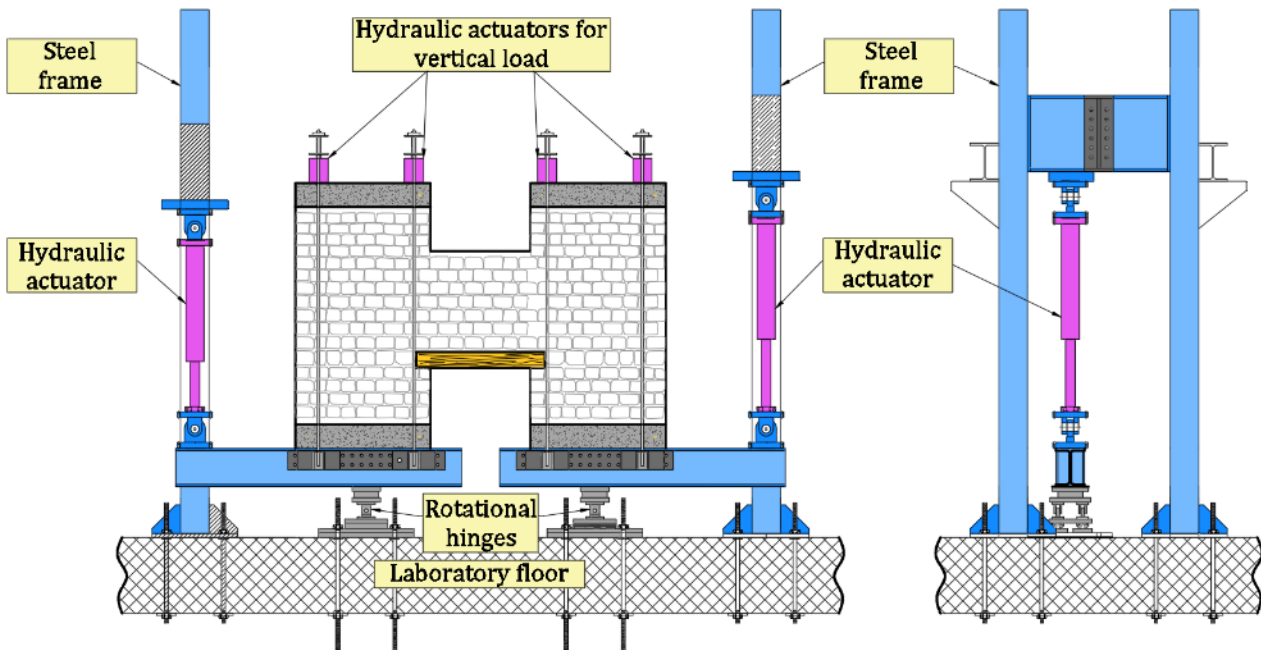
8 Tests on spandrels

8.1 Test setup

Fig. 96: Test setup for spandrels

The test apparatus consisted of two 3 meters long stiff steel beams HEB 400 ("lever beams") and a restraining steel frame, as shown in Fig. 96.

The right lever beam was supported by roller support that allowed rotation and sliding, while the left one allowed only rotations. Both supports were able to withstand tension and compression.

The beams were connected to servo-hydraulic actuators at their ends. The actuators had a loading capacity of 250 kN and a displacement capacity of 200 mm. During testing, the two actuators moved with the same velocity in opposite directions. As a result, both piers rotated in the same direction and caused shear forces in the spandrel.

The vertical load in the piers was applied using four hydraulic actuators. Two were placed at the top of each pier and connected to the lever beams via steel bars. The top reinforced concrete beams were used to distribute the vertical load to the masonry wall.

The samples dimensions are attached in the Appendix.

8.2 Instrumentation

Hard-wired contact transducers measured the forces and displacements at selected locations, and a 3D optical measurements system (digital image correlation) measured the displacement field on the front surface of the specimens (Fig. 97). The back of the spandrel was painted white to facilitate the observation of cracks. The transducers are explained in Table 40.
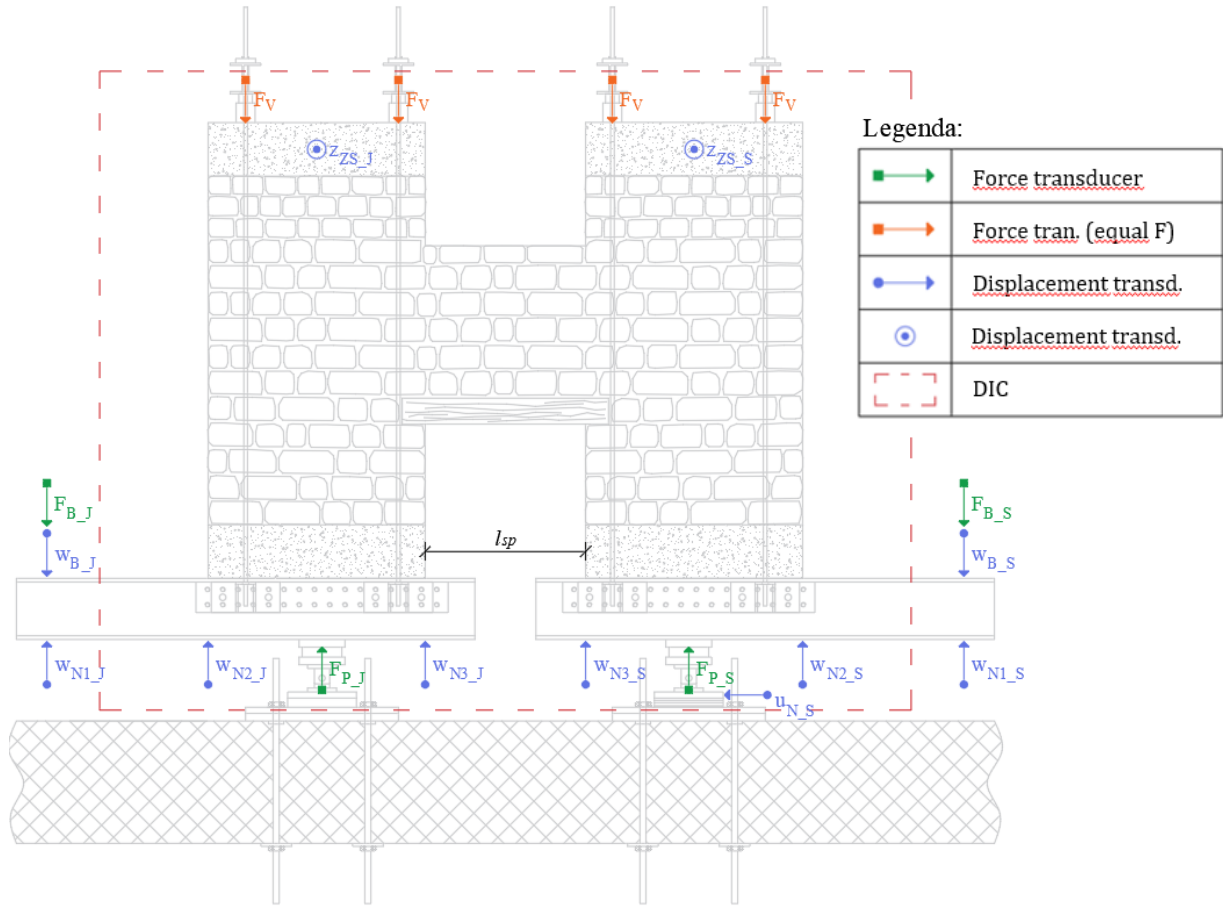
Fig. 97: Layout of the instruments.

Transducers w_{N3-J} and w_{N3-S} were placed directly under the spandrel to measure the spandrel's drift.

Table 40: Instrumentation of spandrel specimens

Transducer	Measurement
$w_{N1-J}, w_{N2-J}, w_{N3-J}$	Vertical displacements on the left beam
$w_{N1-S}, w_{N2-S}, w_{N3-S}$	Vertical displacements on the right beam
w_{B-J}, w_{B-S}	Vertical displacements of the left actuator and right actuator
F_{B-J}, F_{B-S}	Force in the left actuator and right actuator
F_{P-J}, F_{P-S}	Force in the left and right hinge support
z_{ZS-J}, z_{ZS-S}	Out-of-plane displacements of the piers
F_V	Vertical force in actuators for compressive stress in piers

8.3 Spandrel drift and shear force

Deformations of the spandrel were expressed with drift θ_{sp}. Drift was positive when the piers rotated clockwise and negative when they rotated counterclockwise (Fig. 98). It was computed from the measured displacement of the lever beams and the length of the spandrel (l_{sp}):

$$\theta_{sp} = \frac{w_{sp,L} - w_{sp,R}}{l_{sp}}$$

94
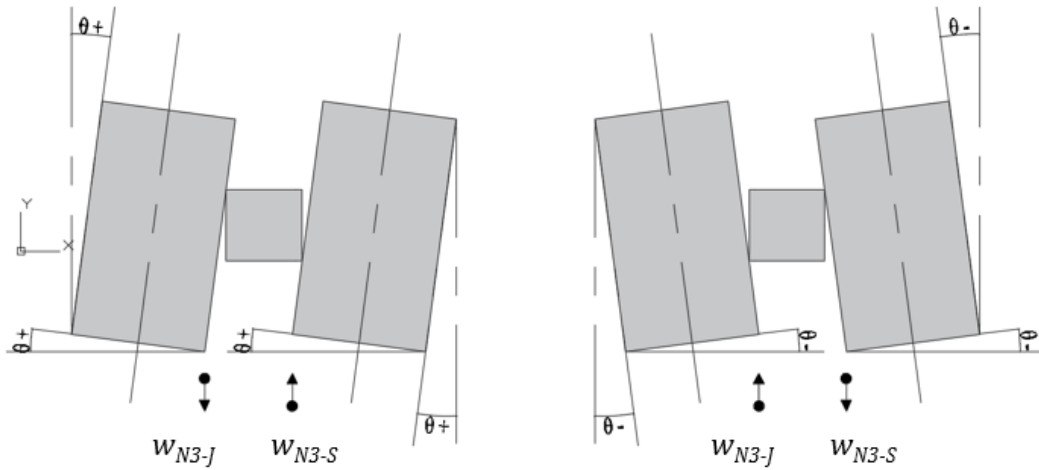
Fig. 98: Positive (left) and negative (right) directions of loading

Shear force in the spandrel (V_{sp}) was computed indirectly by considering the forces measured in the actuators (F_B) and the supports (F_P), which were set to zero at the beginning of the test, as shown in Fig. 99, thus self weight was not considered during the test. It should be noted that the load also causes bending moments in the spandrels.

Fig. 99: Shear force in the spandrel

By using this approach, we were able to calculate shear force from both ends (left and right) of the spandrel double check the measurements:

$$V_{sp-J} = F_{B-J} - F_{P-J}$$
$$V_{sp-S} = F_{B-S} - F_{P-S}$$

The shear force in the spandrel V_{sp} in the graphs is either V_{sp-J} or V_{sp-S}.

95

8.4   Test protocols

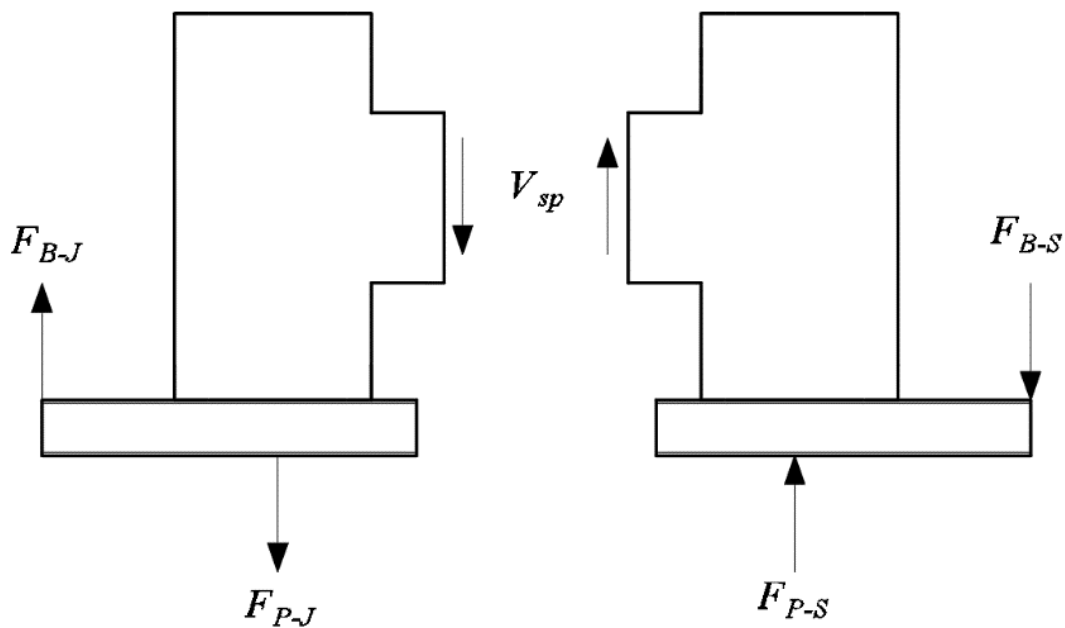Spandrel specimens were first tested in their unreinforced state up to significant damage. They were then repaired, strengthened and tested until near collapse. This allowed to compare the effectiveness of the strengthening.

The tests started by first applying the vertical load to the piers. After the desired stress state was attained (about 0.33 MPa), the shear forces were applied to the spandrel by moving the two actuators at the sides.

The shear load was imposed on the specimen by controlling the displacements in the actuators. The loads were applied in the positive and negative directions (cyclically), with three repetitions at each displacement amplitude. The load program is schematically shown in Fig. 100.
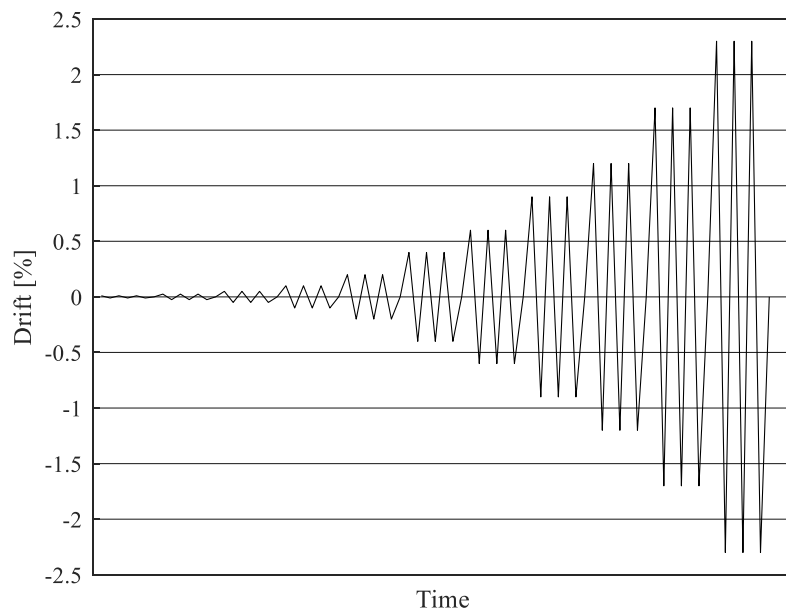

Fig. 100: Program of loading

Due to the different materials and types of strengthening, the load program varied from test to test. The exact data for each test are shown in Tables 41 and 42. Each test took several hours.

Table 41: Load protocols for stone masonry spandrels

| Load phase | S-R2-1, S-R2-2 | | S-R2-1R | | S-R2-1R | |
| | Unreinforced | | Single sided strengthening | | Double-sided strengthening | |
	Drift [%]	Displacement [mm]	Drift [%]	Displacement [mm]	Drift [%]	Displacement [mm]
1	0.025	0.26	0.01	0.11	0.035	0.37
2	0.05	0.53	0.025	0.26	0.06	0.63
3	0.10	1.05	0.05	0.53	0.10	1.05
4	0.15	1.58	0.10	1.05	0.20	2.10
5	0.20	2.10	0.20	2.10	0.40	4.20
6	0.30	3.15	0.40	4.20	0.60	6.30
7	0.40	4.20	0.60	6.30	0.90	9.45
8			0.90	7.35	1.20	12.60
9			1.20	12.60	1.70	17.85
10			1.70	17.85	2.30	24.15
11			2.30	24.15	3.00	31.50
12			3.00	31.50		

Table 42: Load protocols for stone masonry spandrels

| Load phase | S-B1, S-B2 | | S-B2 | | S-B1 | |
| | Unreinforced | | Single sided strengthening | | Single sided strengthening | |
	Drift [%]	Displacement [mm]	Drift [%]	Displacement [mm]	Drift [%]	Displacement [mm]
1	0.025	0.26	0.025	0.26	0.025	0.26
2	0.05	0.53	0.05	0.53	0.05	0.53
3	0.10	1.05	0.10	1.05	0.10	1.05
4	0.15	1.58	0.15	1.58	0.15	1.58
5			0.20	2.10	0.20	2.10
6			0.30	3.15	0.30	3.15
7			0.50	5.20	0.50	5.20
8			0.80	8.32	0.80	8.32
9			1.20	12.60	1.20	12.60
10			1.70	17.85	1.70	17.85
11					2.20	23.10

8.5   Tests

8.5.1   S-R2-1 (stone masonry, unstrengthened)

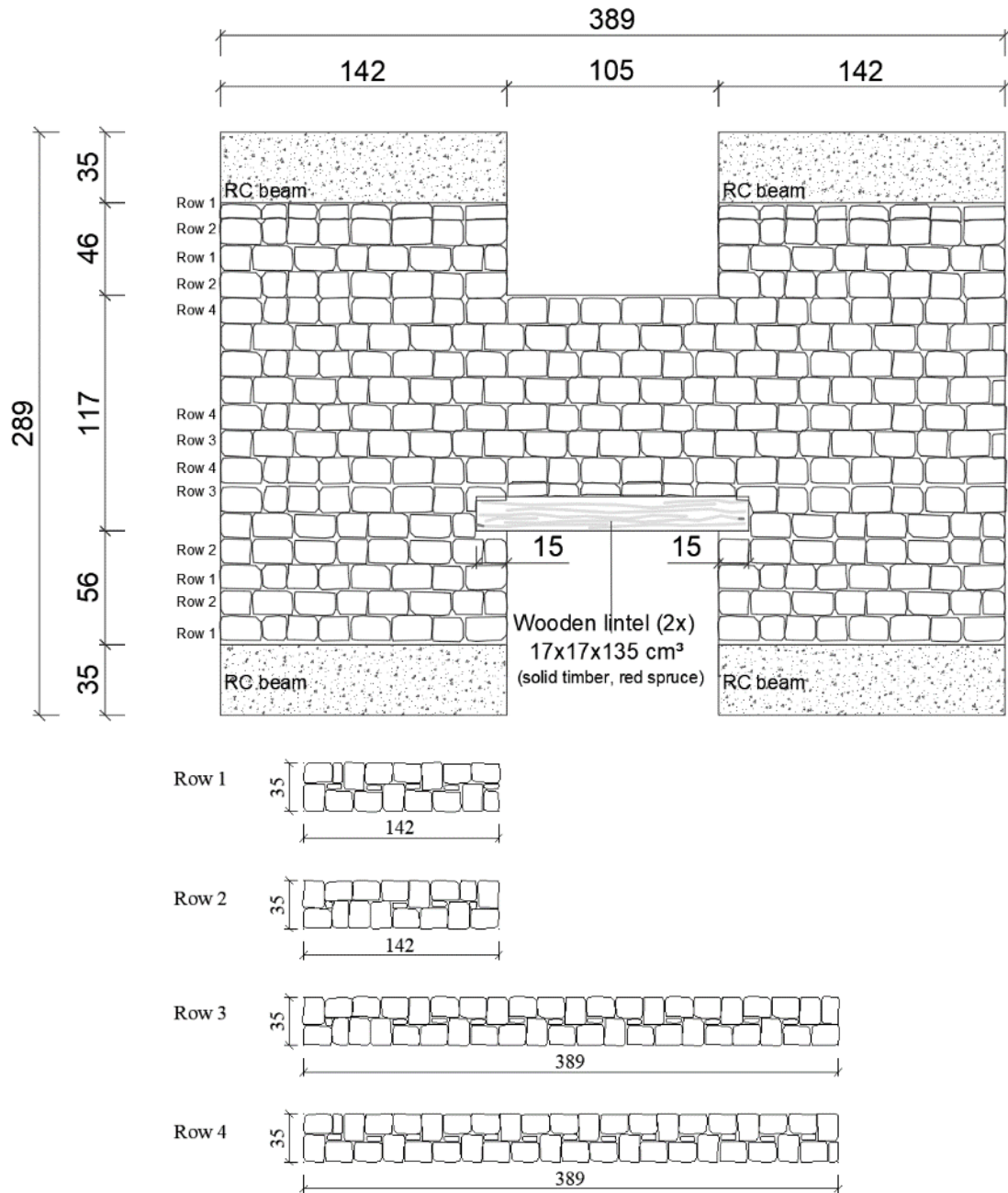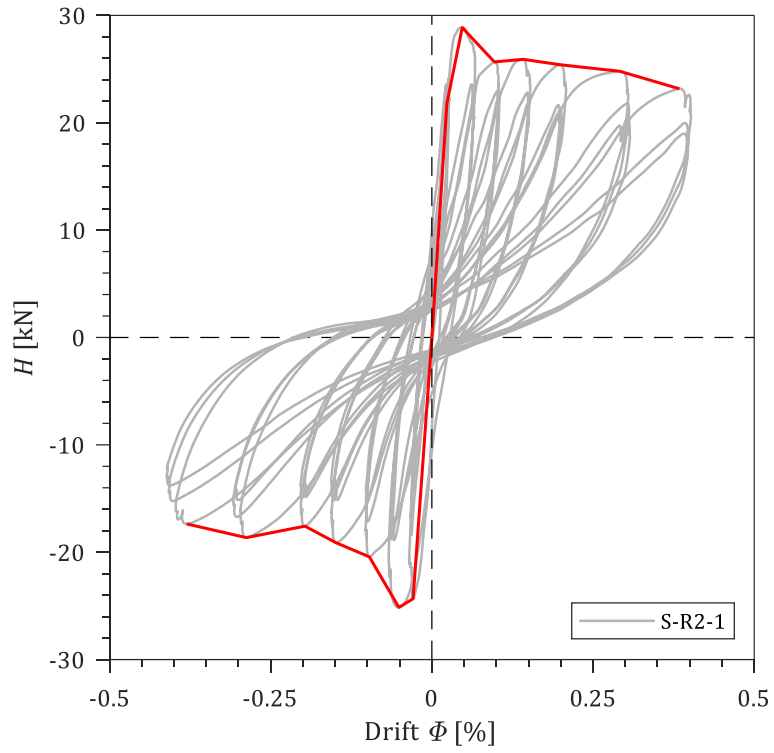| S-R2-1	Two leaf stone masonry;	Material characteristics	
	unstrengthened	f_c	2.48 MPa
Date of test (age):	2021/4/16 (age: 52 days)	E	1074 MPa
Spandrel length l_{sp}:	1065 mm	G	333 MPa
Vertical stress in piers (σ_0):	0.33 MPa	f_t	0.121 MPa

Fig. 101: Spandrel S-R2-1
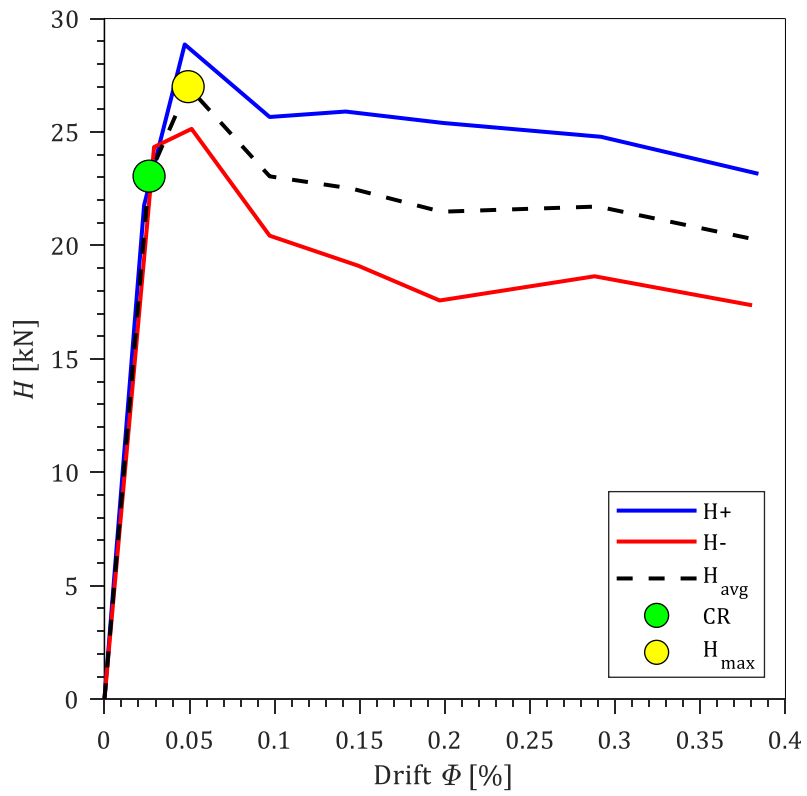
S-R2-1

Fig. 102: Force-displacement curve and the envelope.

Fig. 103: Envelopes of the response and limit states.
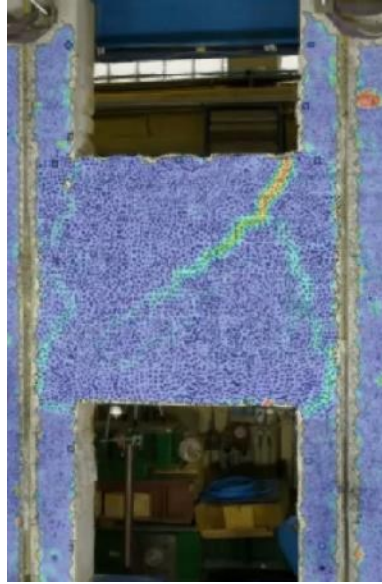
Table 43: Limit states of the wall

Damage LS 🟢		Max Resist LS 🟡		End of test 🔴	
H$_{cr}$ [kN]	Φ_{cr} [%]	H$_{max}$ [kN]	Φ_{max} [%]	H$_{ult}$ [kN]	Φ_{ult} [%]
23.1	0.027	27.0	0.042	20.3	0.4

Drift	Observation
0.025 %	The first crack was observed by the optical system. It was a vertical crack at the top left corner of the spandrel. Shear force at cracking was 23.1 kN
0.042 %	A vertical crack appeared at the bottom left corner. The shear force reached the maximum of 27 kN. A diagonal crack running from the top right corner appeared.
0.042 – 0.4 %	The cracks opened and closed and got gradually wider. The test was stopped at 0.4 % spandrel drift when the damage was still repairable.

8.5.2 S-R2R-1 (stone masonry; coating on one side)

Spandrel S-R2R-1 is repaired and strengthened spandrel S-R2-1.

S-R2R-1	Two leaf stone masonry; *Strengthened on one side* 19 »L« connectors, 8 diatons		
Date of test:	2021/6/1	Bilinear idealization	
Age of sample/coating:	96/40 days	Φ_e	0.13 %
Spandrel length l_{sp}:	1065 mm	Φ_u	2.21 %
Vertical stress in piers (σ_0):	0.33 Mpa	H_u	65.8 kN

Fig. 104: Schematic of strengthening for S-R2R-1. Red circles = L connectors, Blue circles = diatons.
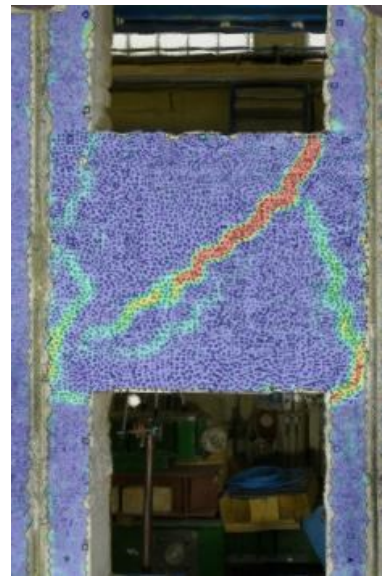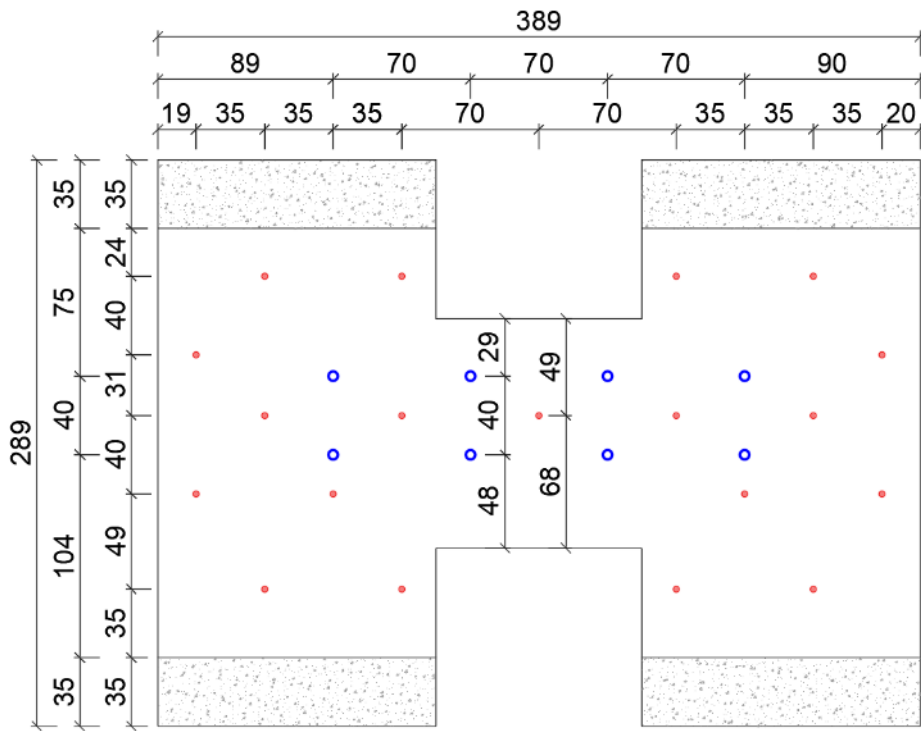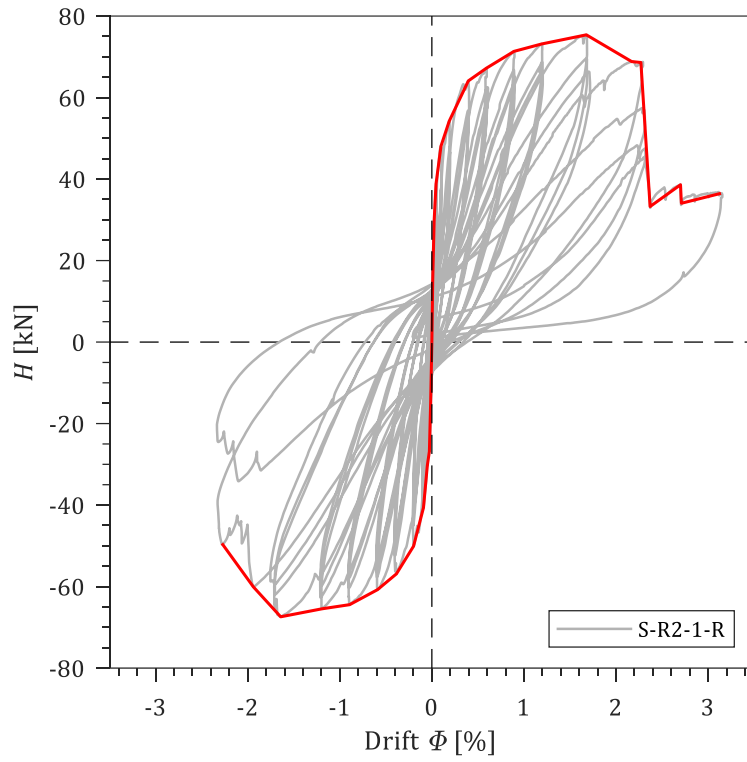
S-R2R-1

Fig. 105: Force-displacement curve and the envelope.
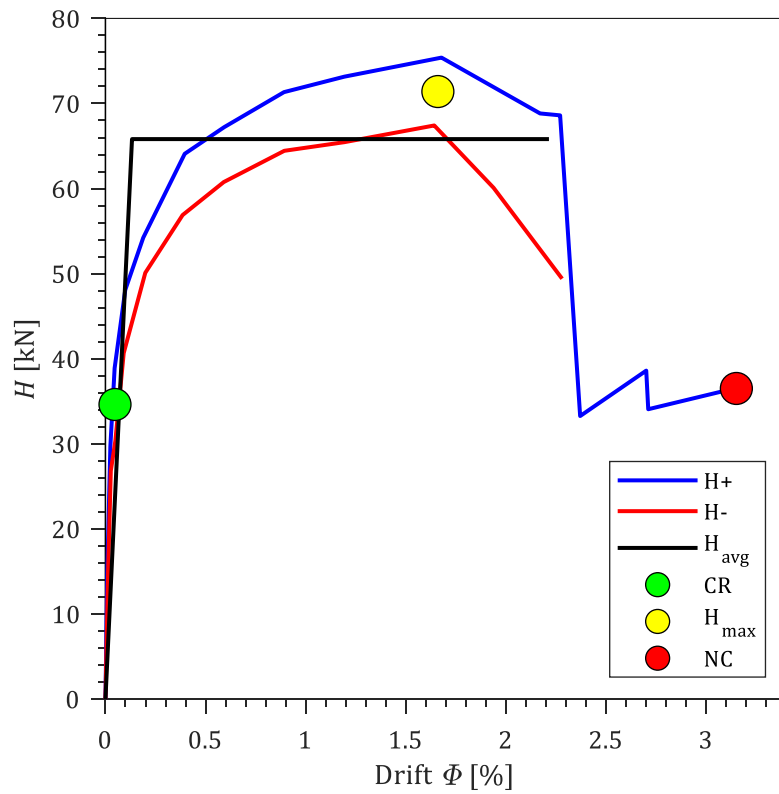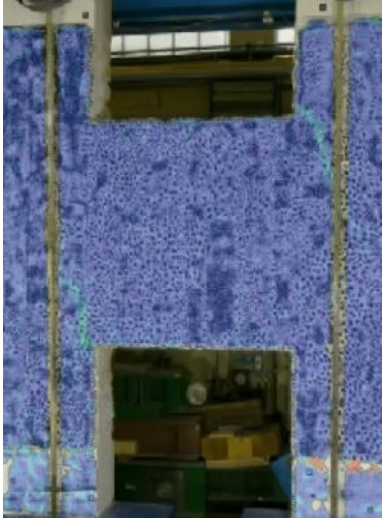
Fig. 106: Envelopes of the response, bilinear idealization and limit states.

Damage LS 🟢		Max Resist LS 🟡		Near Col. LS 🔴	
H_{cr} [kN]	Φ_{cr} [%]	H_{max} [kN]	Φ_{max} [%]	H_{ult} [kN]	Φ_{ult} [%]
34.6	0.025	75.4	1.66%	36.5	3.0

Front			
Back			

Drift	Observation
0.025 %	The first cracks were vertical at the top right and bottom left corner of the spandrel.
0.025 – 1.68 %	In addition to the vertical cracks, shear cracks also appeared in the coating. Other cracks gradually appeared and spread over the entire surface of the coating.
1.68 %	Peak resistance of 75.4 kN was reached at 1.66 % spandrel drift. On the unstrengthened side, there were inclined cracks, but fewer than in the coating (Fig. 107).
1.68 – 3.0 %	The cracks opened and closed and got gradually wider. New inclined cracks appeared in the coating. When nearing collapse, the ripping of the mesh could be heard. Toward the end of the test, the bond between the coating and the wall was lost over large parts of the spandrel area. Nevertheless, the coating remained effective because of the strong steel connectors (diatons).

Fig. 107: Damage on the unstrengthened side after the test.

8.5.3 S-R2-2 (stone masonry, unstrengthened)

S-R2-1	Two leaf stone masonry;	Material characteristics	
	unstrengthened	f_c	2.48 MPa
Date of test (age):	2021/7/19 (age: 32 days)	E	1074 MPa
Spandrel length l_{sp}:	1065 mm	G	333 MPa
Vertical stress in piers (σ_0):	0.33 MPa	f_t	0.121 MPa
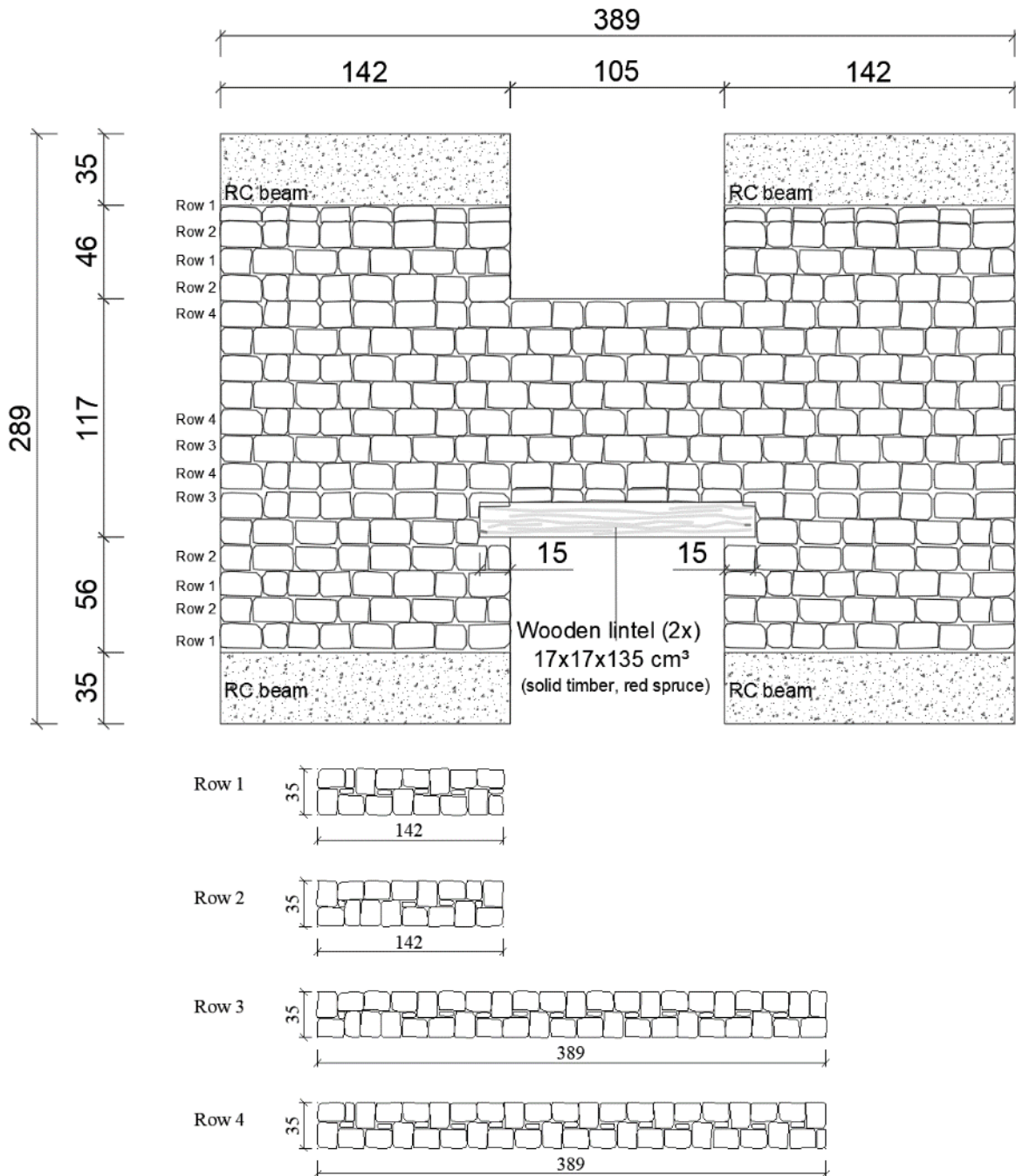
Fig. 108: Spandrel S-R2-2
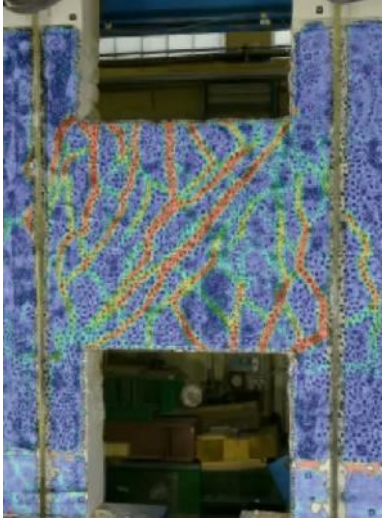
S-R2-2

Fig. 109: Force-displacement curve and the envelope.
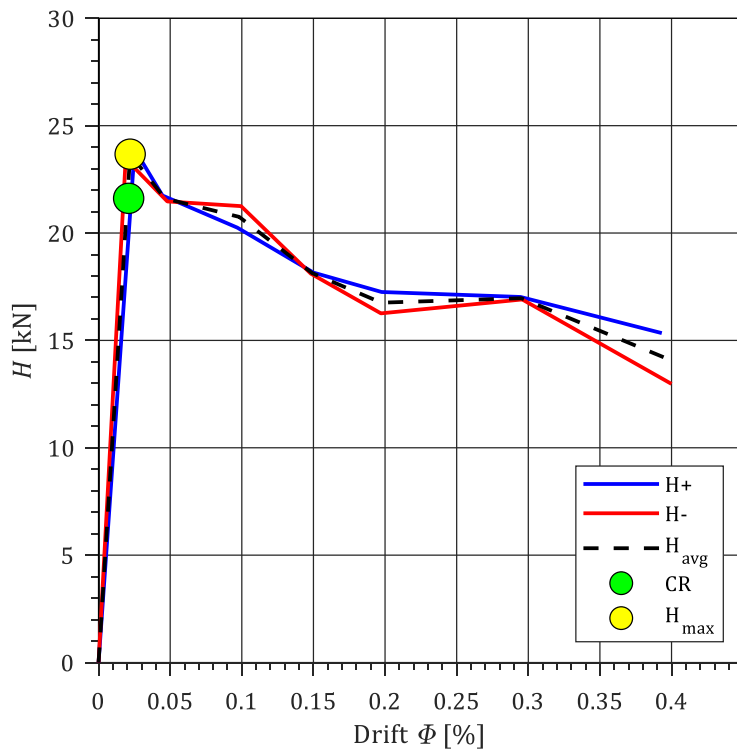
Fig. 110: Envelopes of the response and limit states.

Damage Limit State (DLS) 🟢		Maximum Resistance Limit State (MaxF LS) 🟡		End of test	
H_cr [kN]	Φ_{cr} [%]	H_max [kN]	Φ_{max} [%]	H_ult [kN]	Φ_{ult} [%]
21.6	0.021	23.6	0.022	14.2	0.40

Drift	Observation
0.021 %	The first cracks were vertical at the left and right sides of the spandrel. The damage indicated a bending response. Shear force at the first observed cracking was 21.6 kN
0.022 %	Peak resistance was reached very shortly after the first cracks appeared. The cracks were at the sides of the spandrel. The crack on the left was slightly inclined but could still be considered as characteristic of flexural behaviour.
0.022 – 0.4 %	The cracks opened and closed and got gradually wider. The test was stopped at 0.4 % spandrel drift when the damage was still repairable.

8.5.4   S-R2R-2 (stone masonry; coating on both sides)

Spandrel S-R2R-2 is repaired and strengthened spandrel S-R2-2.

S-R2R-2	Two leaf stone masonry; *Strengthened on one side* 44x2 »L« connectors		
Date of test:	2021/25/8	Bilinear idealization	
Age of sample/coating:	69/37 days	Φ_e	0.12 %
Spandrel length l_{sp}:	1065 mm	Φ_u	2.73 %
Vertical stress in piers (σ_0):	0.33 MPa	H_u	80.0 kN
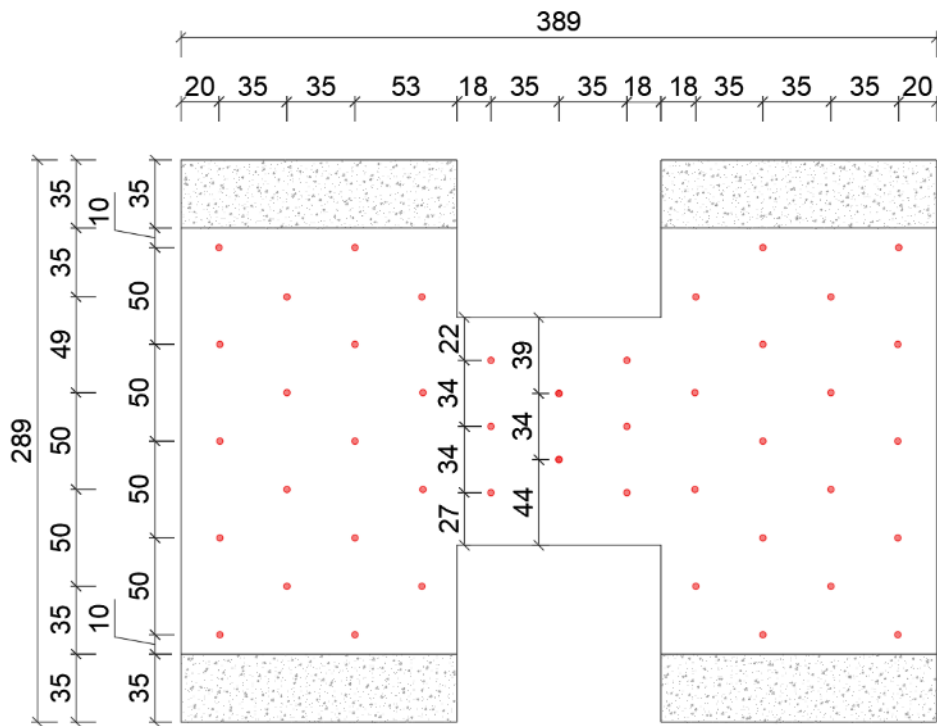
Fig. 111: Schematic of strengthening for S-R2R-2
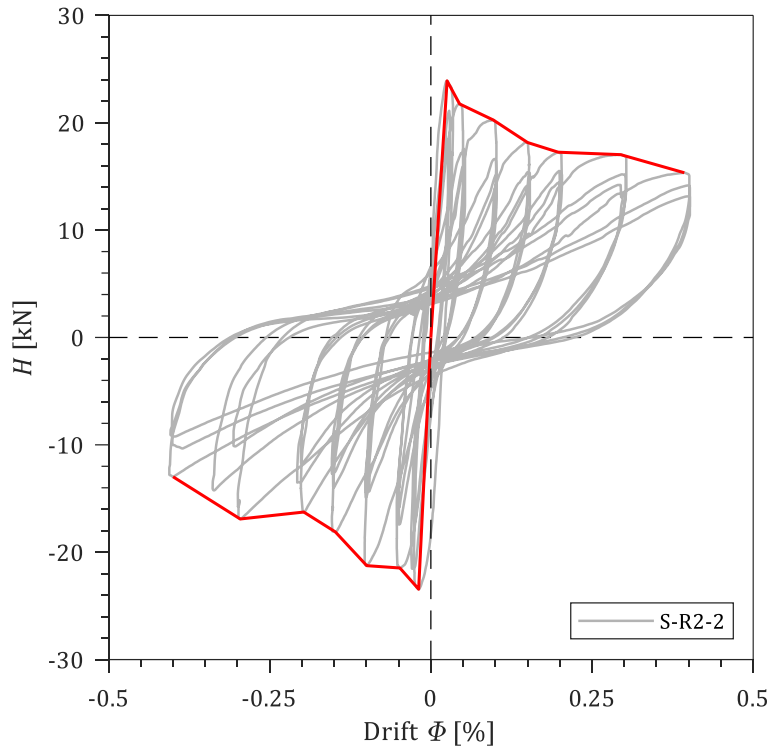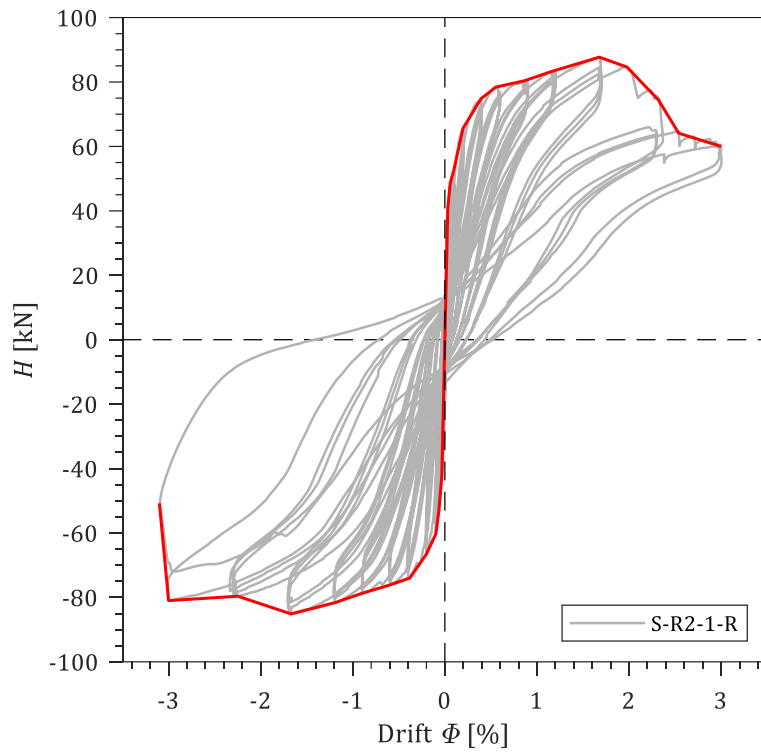
Fig. 112: Force-displacement curve and the envelope.
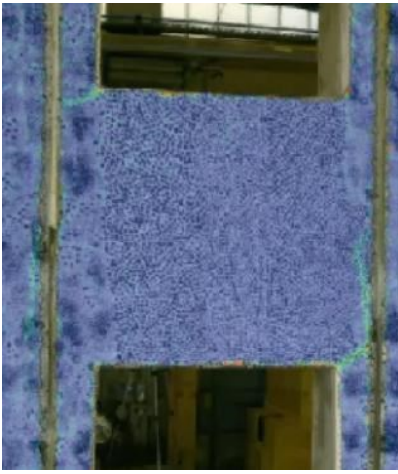
Fig. 113: Envelopes of the response, bilinear idealization and limit states.

Damage LS 🟢		Max Resist LS 🟡		Near Col. LS 🔴	
H_cr [kN]	Φ_{cr} [%]	H_max [kN]	Φ_{max} [%]	H_ult [kN]	Φ_{ult} [%]
56.4	0.025	86.4	1.67	70.5	3.05

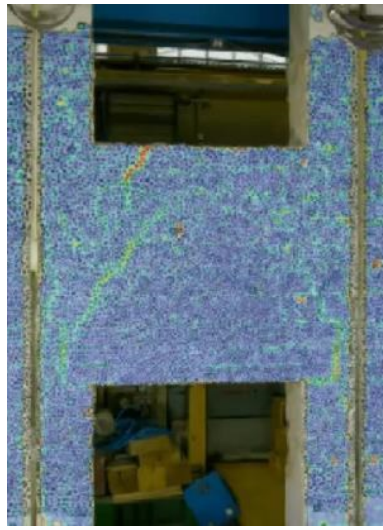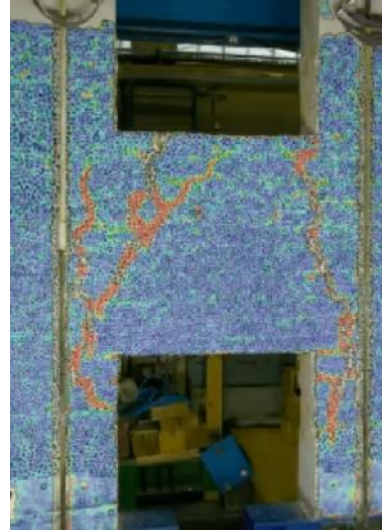| Drift	Observation
0.025 %	The first cracks were vertical at the top left and bottom right corner of the spandrel. The force at this stage was about 56.4 kN.
0.1 %	Vertical cracks extended and reached across the whole height of the spandrel.
0.1 – 1.69 %	Inclined cracks appeared in the coating. The number of cracks gradually increased and covered the whole surface of the coating.
1.69 %	Peak resistance was reached. The response at peak resistance was clearly flexural (Fig. 114) despite many inclined cracks.
1.68 – 3.0 %	The cracks opened and closed and got gradually wider. New inclined cracks appeared in the coating. Ultimately the vertical section at the edge of the spandrel failed (Fig. 115). Towards the end of the test, wall leaves separated in the piers below the lintel (Fig. 116).

Fig. 114: Crack pattern at maximum resistance

Fig. 115: Final failure

Fig. 116: Separation of wall leaves in piers

8.5.5 S-B2 (brick masonry; two leaves; unstrengthened)

S-B2	Two leaf brick masonry;	Material characteristics	
	unstrengthened	f_c	6.43 MPa
Date of test (age):	2021/12/14 (age: 42 days)	E	2183 MPa
Spandrel length l_{sp}:	1060 mm	G	293 MPa
Vertical stress in piers (σ_0):	0.33 MPa	f_t	0.124 MPa
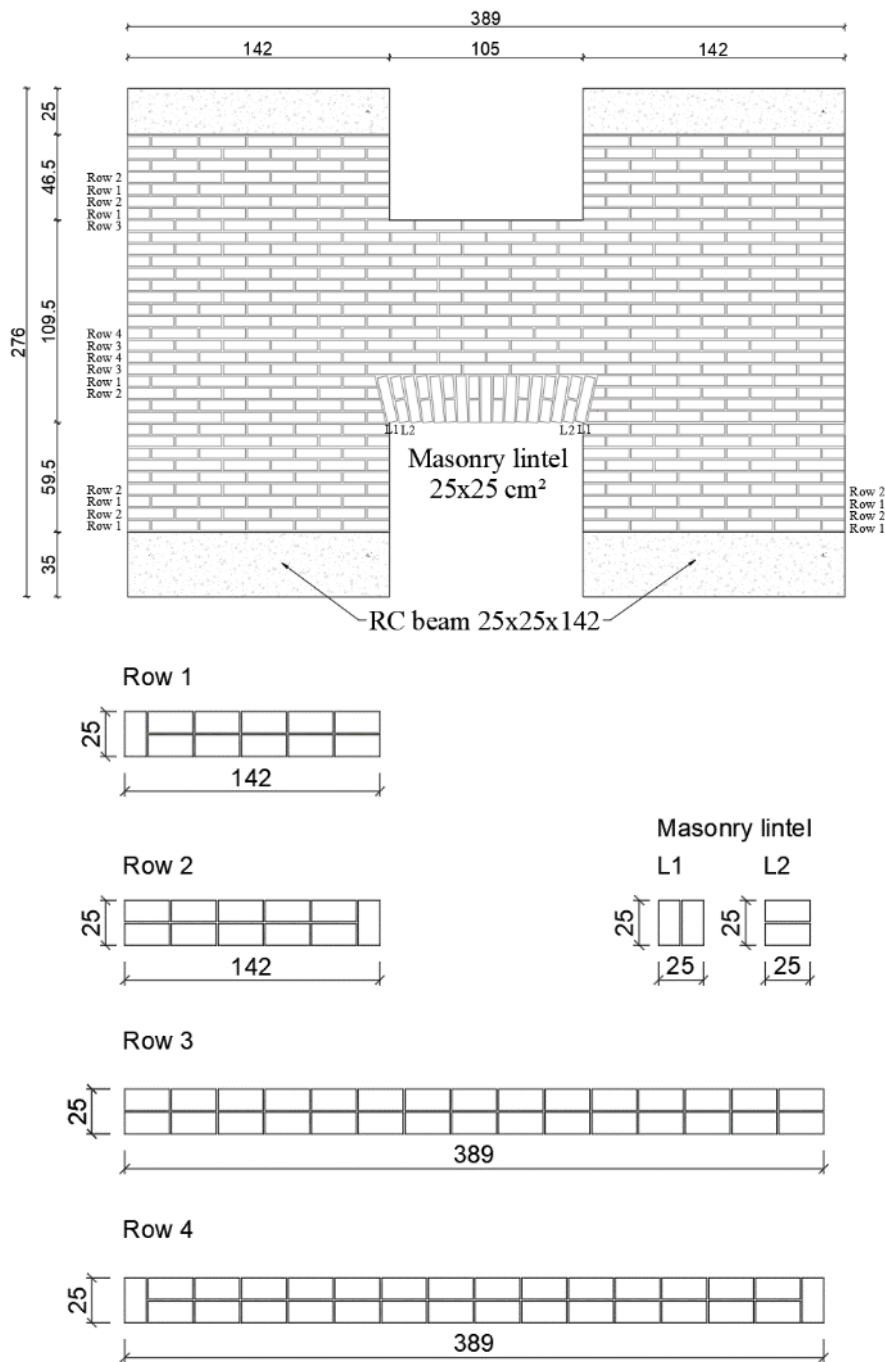
Fig. 117: Spandrel S-B2

S-B2

Fig. 118: Force-displacement curve and the envelope.
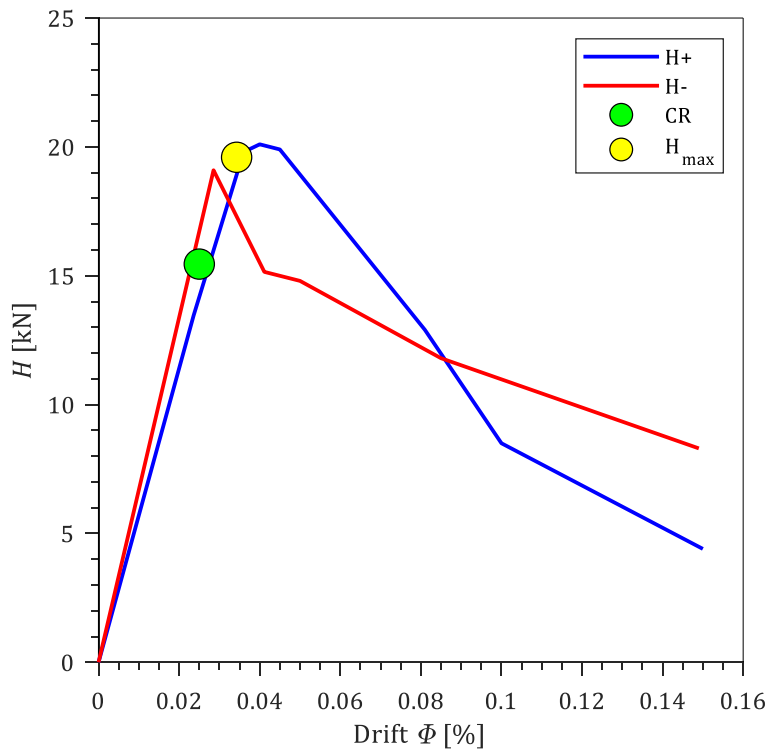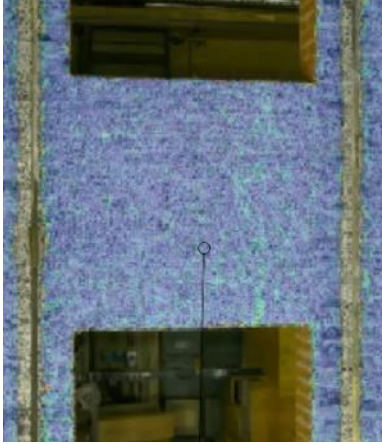
Fig. 119: Envelopes of the response, bilinear idealization and limit states.

Table 44: Limit states of the wall

Damage LS ⬤		Max Resist LS ⬤		End of test	
H$_{cr}$ [kN]	Φ_{cr} [%]	H$_{max}$ [kN]	Φ_{max} [%]	H$_{ult}$ [kN]	Φ_{ult} [%]
15.5	0.025	19.6	0.034	6.3	0.15

Drift	Observation
0.02 %	The first cracks appeared in the lintel at 0.025 % drift. Shear force at cracking was about 15.5 kN.
0.034 %	The damage pattern at maximum resistance was diagonal shear cracks running through the joints. Shear force was 19.6 kN.
0.15 %	The lintel was at risk of falling off. The test was stopped at 0.16 %.

8.5.6 S-B2R (brick masonry; coating on one side)

Spandrel S-B2R -1 is repaired and strengthened spandrel S-B2.

| S-R2R-1	Two leaf brick masonry; *Strengthened on one side* 25 »L« connectors, and 8 diatons		
Date of test:	2022/1/20	Bilinear idealization	
Age of sample/coating:	79/31 days	Φ_e	0.05 %
Spandrel length l_{sp}:	1060 mm	Φ_u	1.55 %
Vertical stress in piers (σ_0):	0.33 MPa	H_u	40.5 kN
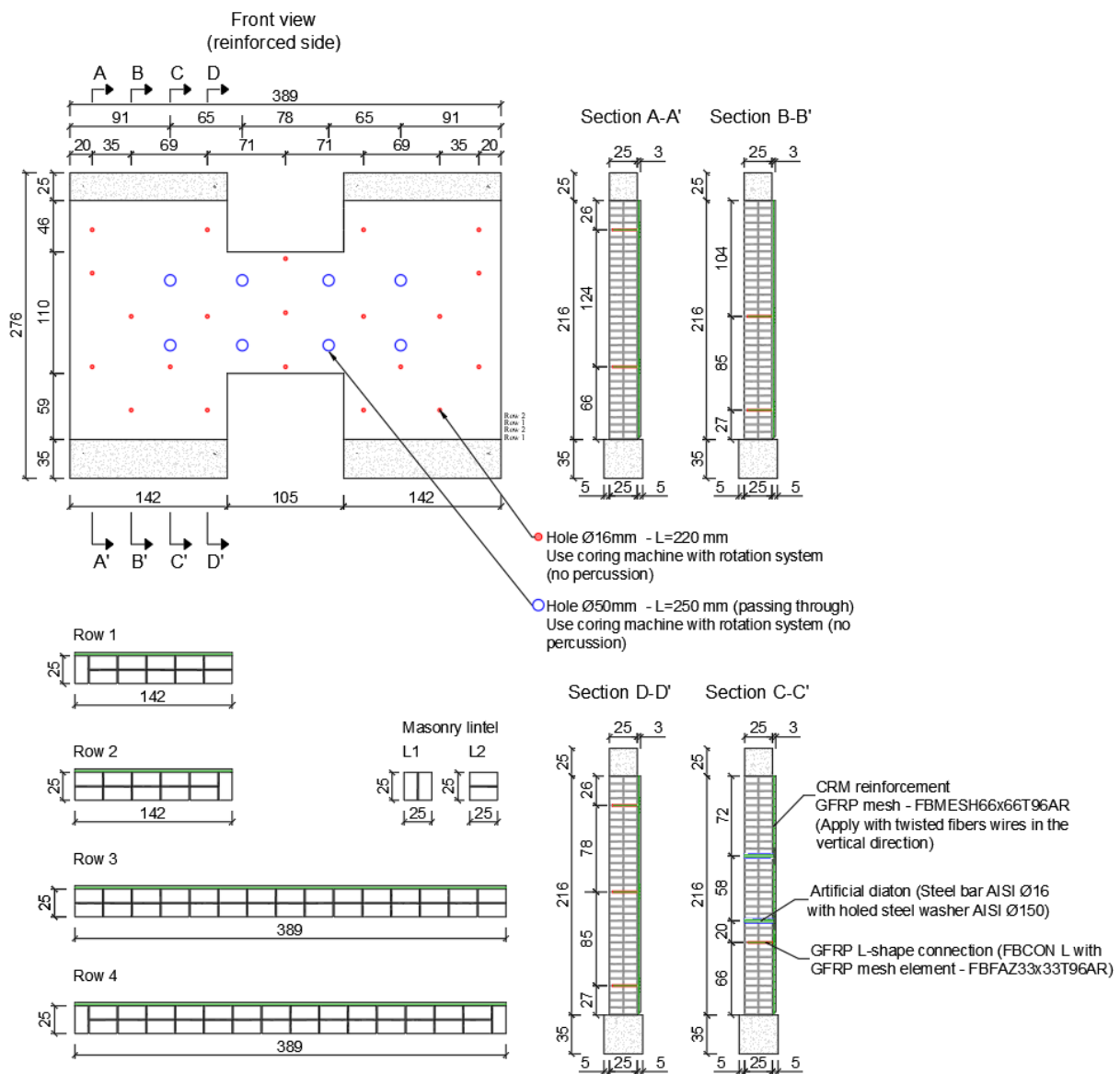
Fig. 120: Schematic of strengthening for S-B2R-1

115

S-B2R
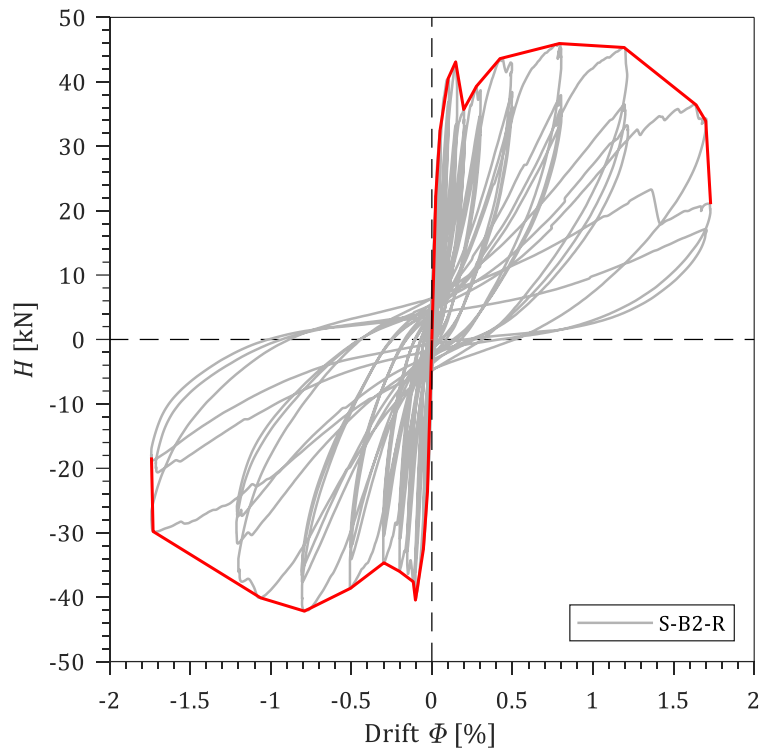
Fig. 121: Force-displacement curve and the envelope.
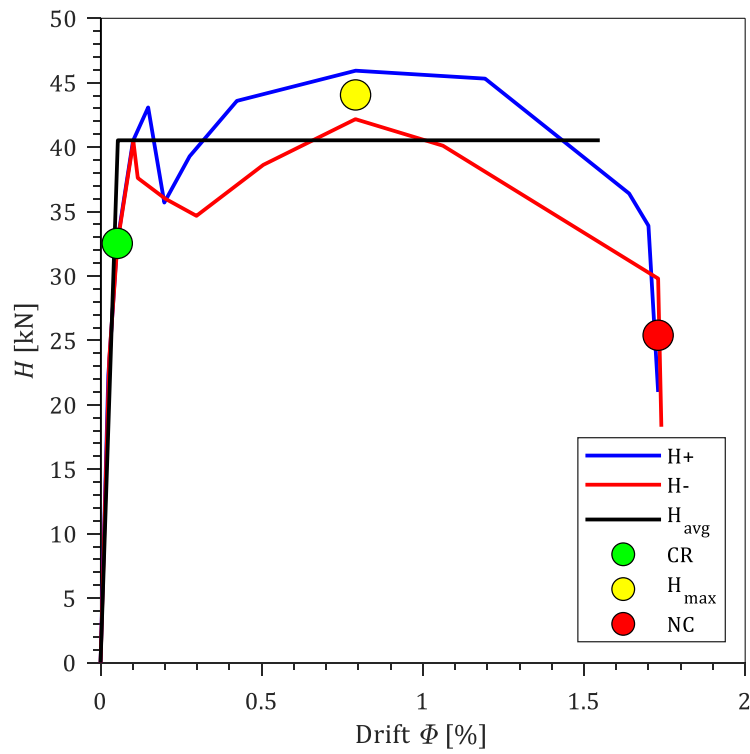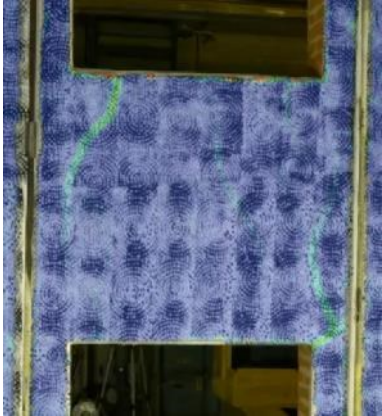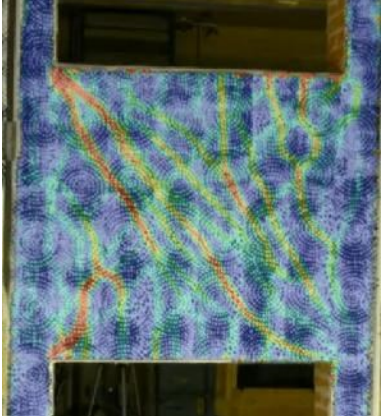
Fig. 122: Envelopes of the response, bilinear idealization and limit states.

Table 45: Limit states of the wall

Damage LS 🟢		Max Resist LS 🟡		Near Col. LS 🔴	
H_{cr} [kN]	Φ_{cr} [%]	H_{max} [kN]	Φ_{Hmax} [%]	H_{ult} [kN]	Φ_{ult} [%]
32.5	0.05	44.1	0.79	25.4	1.72

Drift	Observation
0.05 %	The first (vertical) cracks appeared in opposite corners of the spandrel. Shear force at cracking was about 32.5 kN.
0.05 – 1.0 %	Diagonal and inclined cracks develop in the spandrel. The cracks propagated over the entire surface of the spandrel. Vertical cracks in the corners remained active.
1.0 %	Maximum resistance of 44.1 kN was reached.
1.0 – 1.72 %	The cracks opened very wide and closed when the load was reversed. Both types were active: inclined shear cracks and vertical bending cracks.
1.72 %	The ultimate failure is due to the fracture of horizontal strands of the mesh (bending).

8.5.7 S-B1 (brick masonry; one leaf; unstrengthened)

S-B1	Single leaf brick masonry;	Material characteristics	
	unstrengthened	f_c	6.7 MPa
Date of test (age):	2022/2/25 (age: 31 days)	E	2341 MPa
Spandrel length l_{sp}:	1073 mm	G	258 MPa
Vertical stress in piers (σ_0):	0.33 MPa	f_t	0.190 MPa
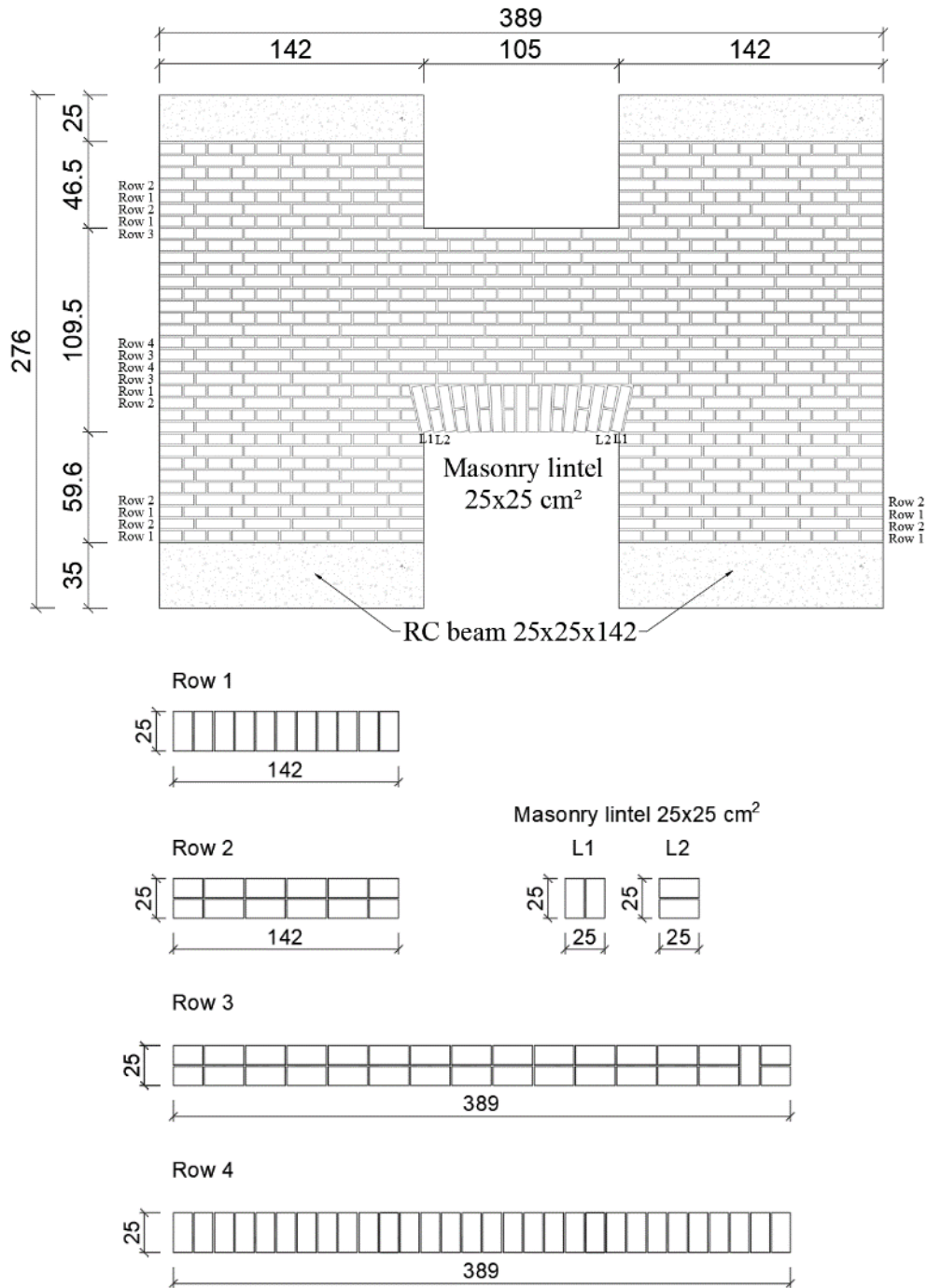
Fig. 123: Spandrel S-B1

S-B1
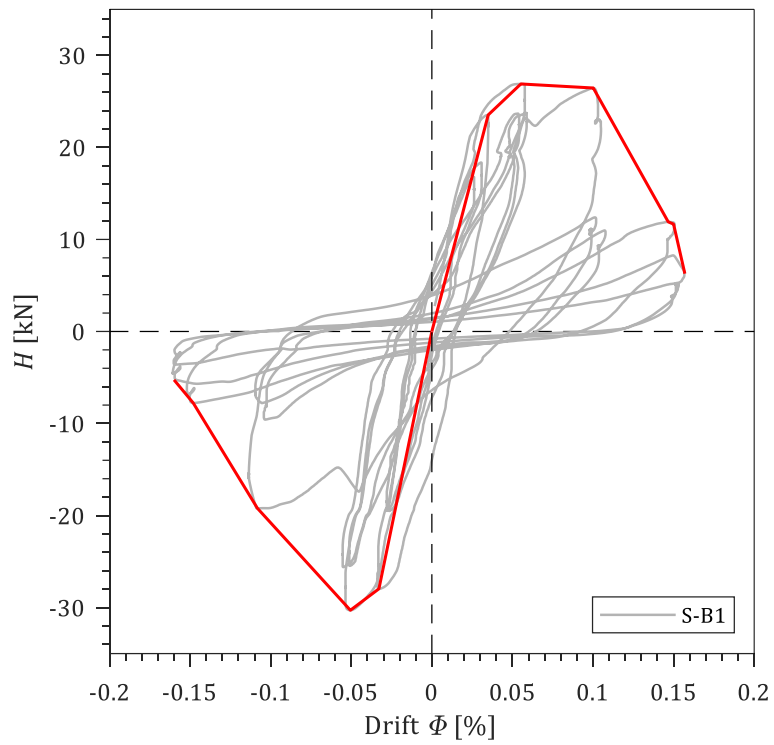
Fig. 124: Force-displacement curve and the envelope.

Fig. 125: Envelopes of the response, bilinear idealization and limit states.

Damage LS ●		Max Resist LS ○		End of test	
H$_{cr}$ [kN]	Φ_{cr} [%]	H$_{max}$ [kN]	Φ_{Hmax} [%]	H$_{ult}$ [kN]	Φ_{ult} [%]
19.1	0.025	28.6	0.054	5.7	0.16

Front			
Back			

Drift	Observation
0.025 %	The first cracks were vertical in the lintel at 0.025 % drift. Shear force at cracking was about 22 kN.
0.054 %	The maximum shear force of 28.6 kN was reached at about 0.54 % drift. There was very little damage to the wall.
0.10 %	Visible cracks ran the entire height of the spandrel. They mainly ran through the joints.
0.16 %	The test was stopped because of the risk of lintel falling. There were inclined cracks over most of the surface of the wall.

8.5.8   S-B1R (brick masonry; coating on one side)

Spandrel S-B1R -1 is repaired and strengthened spandrel S-B1.

S-B1R-1	Single leaf brick masonry; *Strengthened on one side* 52 »L« connectors		
Date of test:	2021/4/5	Bilinear idealization	
Age of sample/coating:	70/36 days	Φ_e	0.06 %
Spandrel length l_{sp}:	1073 mm	Φ_u	1.74 %
Vertical stress in piers (σ_0):	0.33 MPa	H_u	35.7 kN
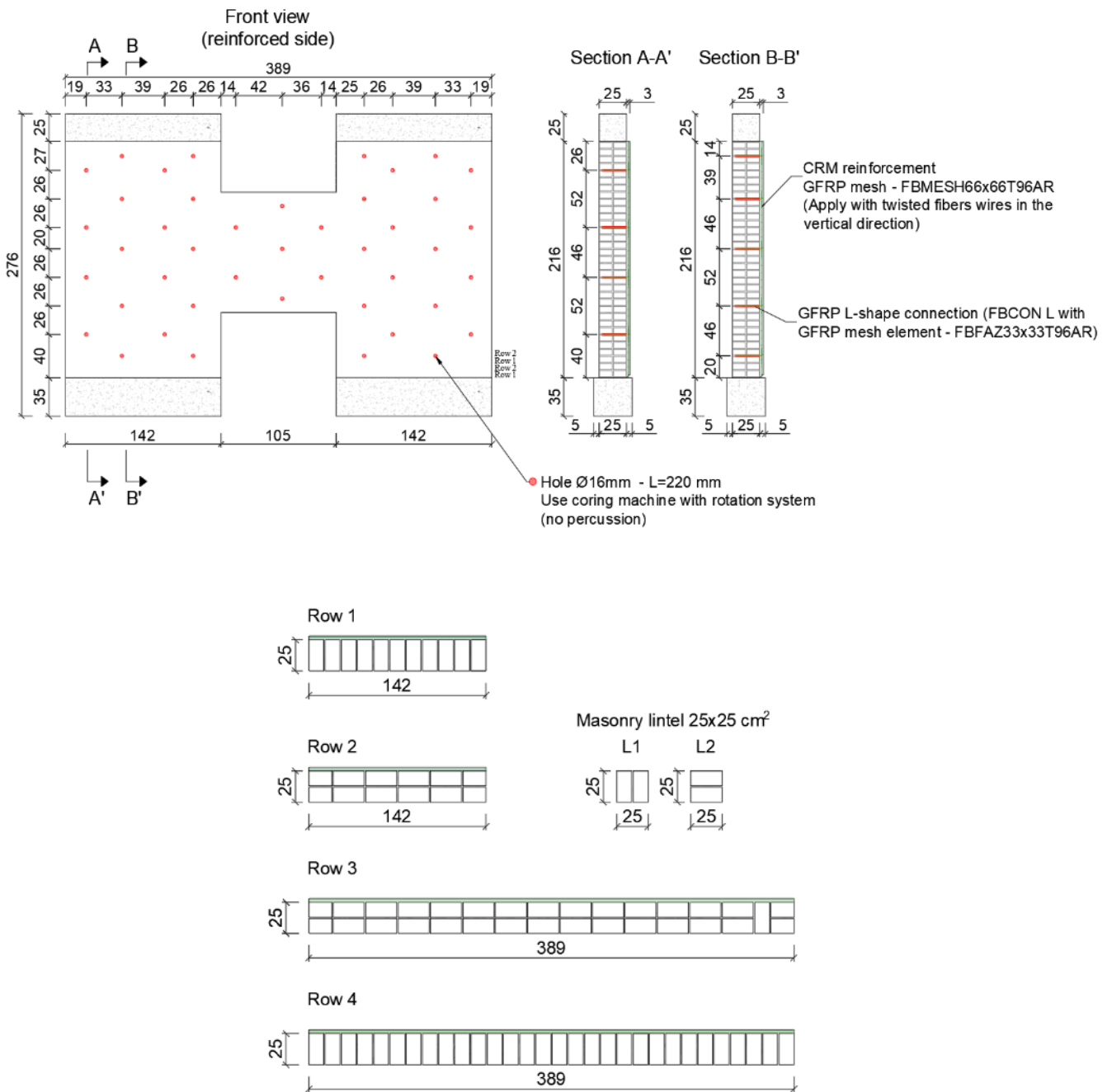
Fig. 126: Schematic of strengthening for S-B2R-1
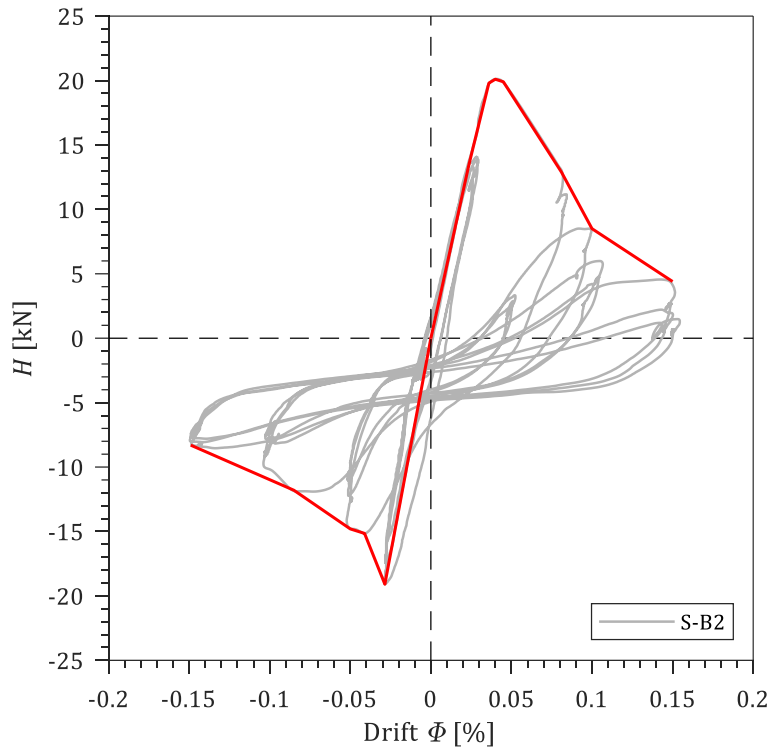
121

S-B1R
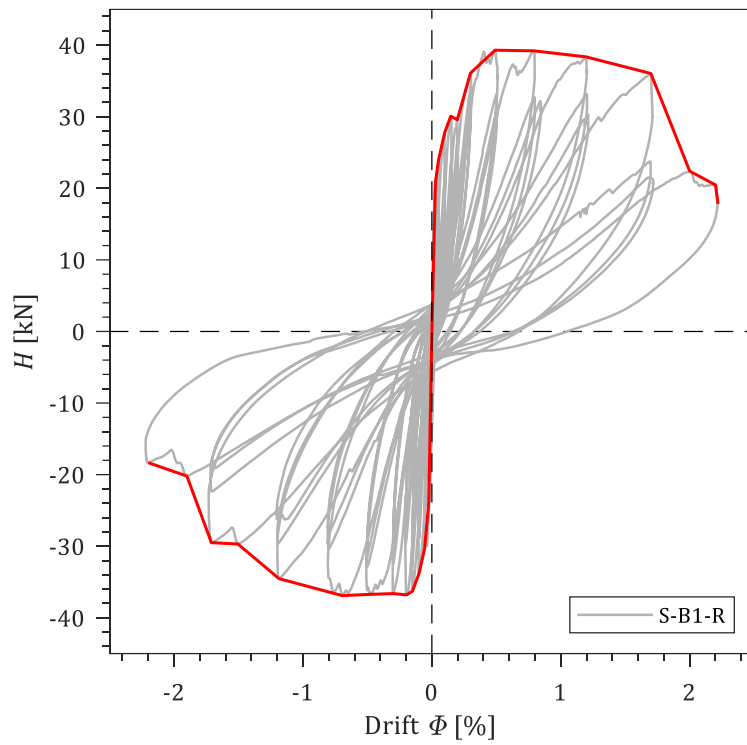
Fig. 127: Force-displacement curve and the envelope.
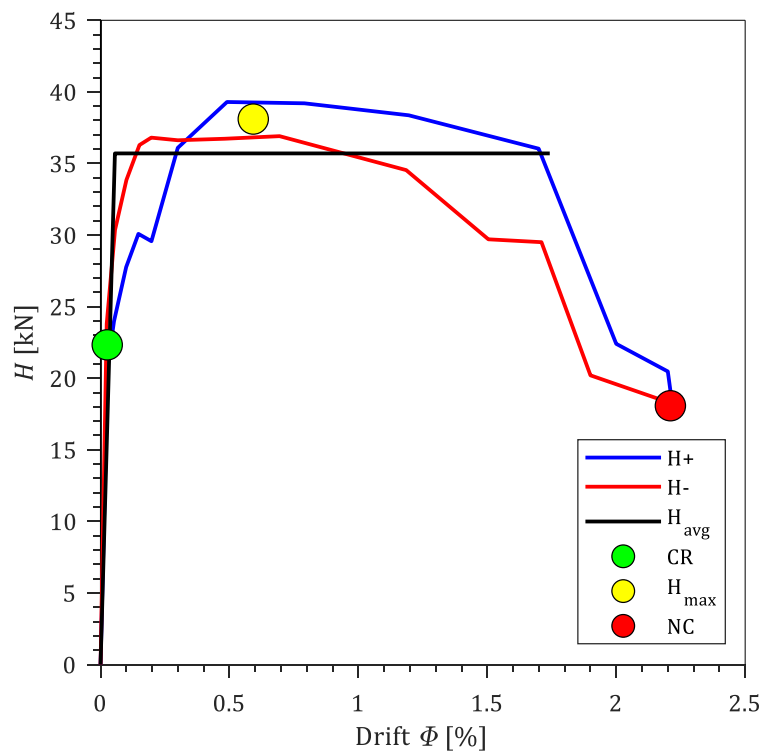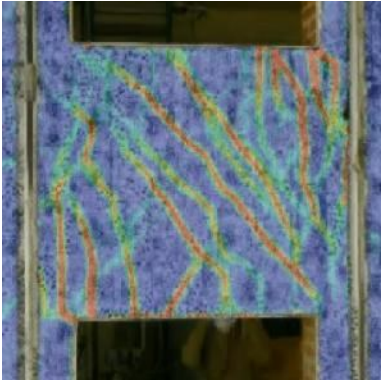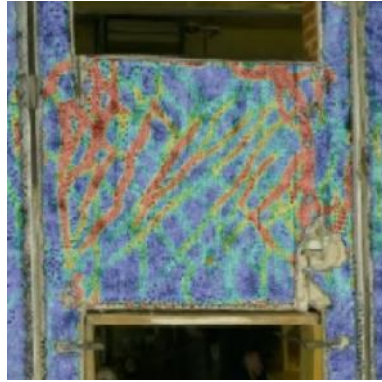
Fig. 128: Envelopes of the response, bilinear idealization and limit states.

Table 46: Limit states of the wall

Damage LS 🟢		Max Resist LS 🟡		End of test	
H$_{cr}$ [kN]	Φ_{cr} [%]	H$_{max}$ [kN]	Φ_{Hmax} [%]	Hu [kN]	Φ_u [%]
22.3	0.025	38.1	0.35	18.1	2.2

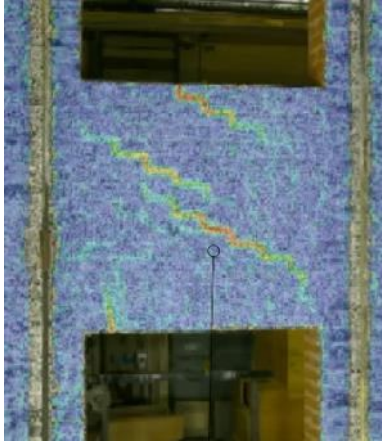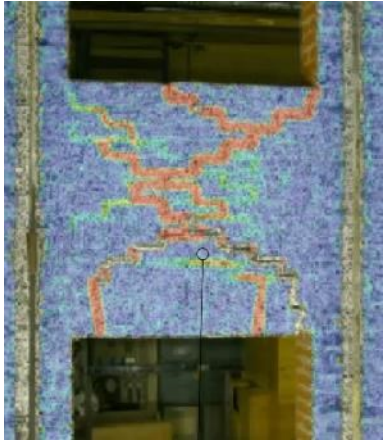| Drift	Observation
0.025 %	The first (vertical) cracks appeared in opposite corners of the spandrel. Shear force at cracking was about 22 kN.
0.05 – 0.2 %	Vertical cracks in the corners opened and closed with the cyclic loads.
0.2 – 0.35 %	Vertical cracks at the sides opened and closed along the entire height of the spandrel. First inclined cracks in the spandrel appeared.
0.35 %	Maximum resistance of 38.1 kN was reached. The response was predominantly in the vertical cracks, although several diagonal cracks run across the spandrel.
0.35 – 1.7 %	Vertical cracks opened and closed. Inclined cracks multiplied and covered the entire surface of the spandrel.
2.2 %	The ultimate failure was due to the fracture of horizontal strands of the mesh.

123

8.6   Summary and analysis

8.6.1   Stone masonry – strengthening on one side
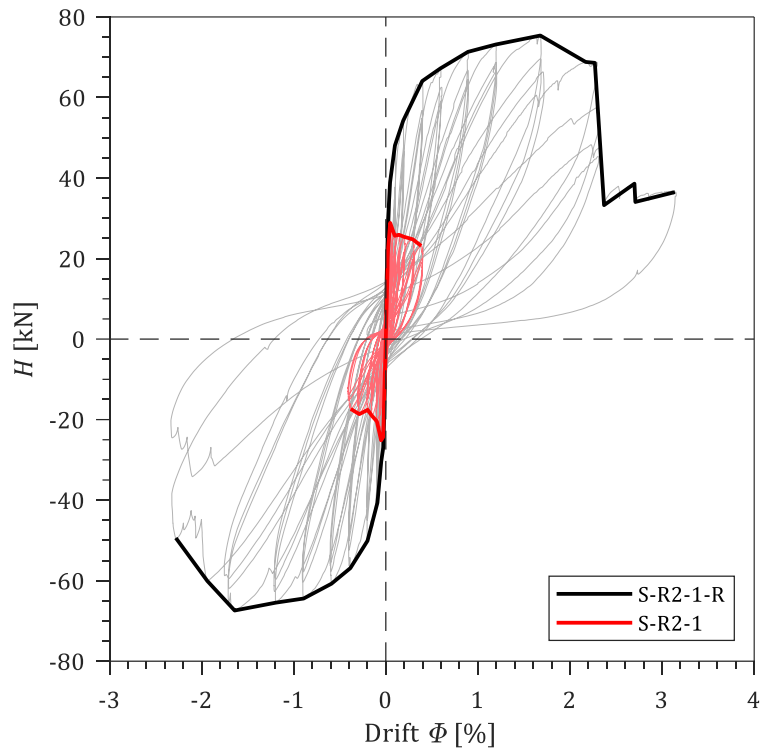
Fig. 129: Hysteretic curves and envelopes of unstrengthened and strengthened wall.
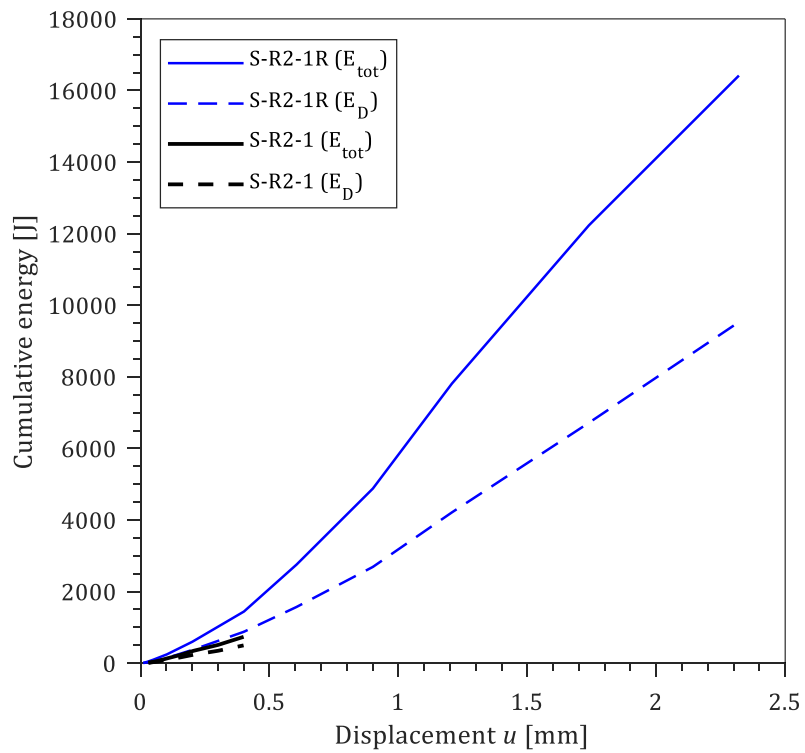
Fig. 130: Cumulative total and dissipated energy against displacement.

Table 47: Effect of strengthening stone masonry on one side

	Unstrengthened	Strengthened	Improvement (strengthened/unstrengthened)
Maximum resistance H_{max}	27.0 kN	75.4 kN	2.79
Ultimate displacement Φ_{ult}	0.4 %	2.7 %	6.75
Dissipated energy E_D	$6.0 \cdot 10^{-1}$ kJ	9.5 kJ	15.8

Summary

The coating on one side of stone masonry spandrels increased resistance by almost three times. The displacement capacity has also been drastically improved. Furthermore, the capacity for energy dissipation has improved by one order of magnitude.

The coating and the wall performed well together and functioned as a composite element. Although there was debonding under large areas of coating (especially under cracks), the combined action of the coating and the wall was maintained until the end due to sufficient anchoring. Ultimately, the mesh fractured, which indicated all materials were fully utilized.

8.6.2 Stone masonry – strengthening on both sides
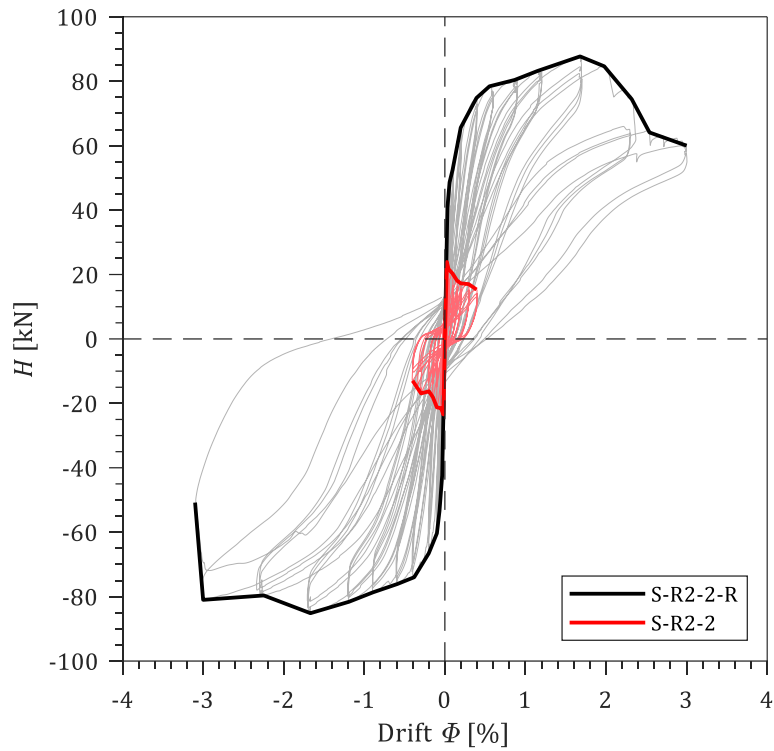
Fig. 131: Hysteretic curves and envelopes of unstrengthened and strengthened wall.
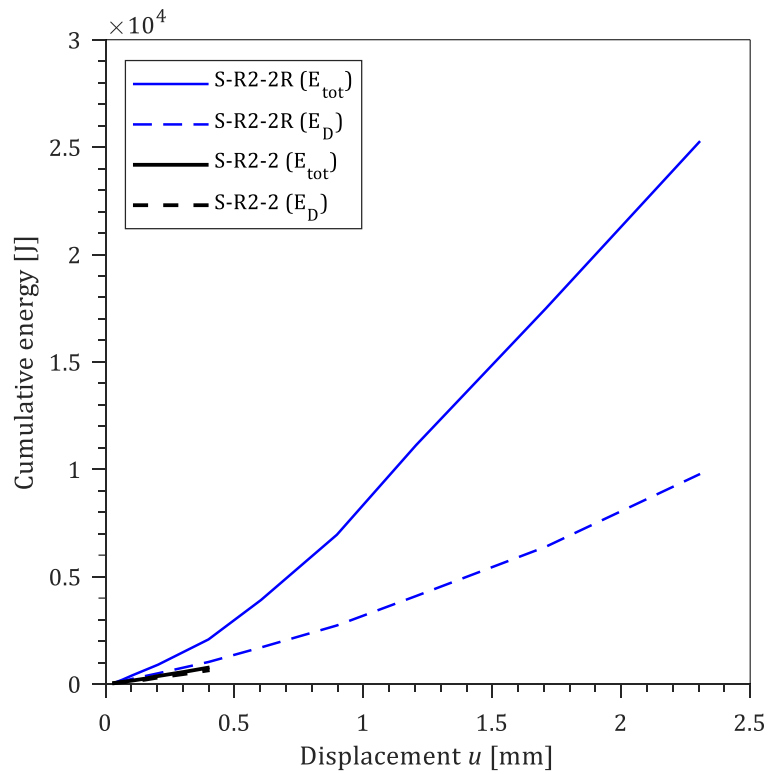
Fig. 132: Cumulative total and dissipated energy against displacement.

Table 48: Effect of strengthening stone masonry on one side

	Unstrengthened	Strengthened	Improvement (strengthened/unstrengthened)
Maximum resistance H_{max}	23.6 kN	86.4 kN	3.66
Ultimate displacement Φ_{ult}	0.4 %	3.1 %	7.54
Dissipated energy E_D	$6.0 \cdot 10^{-1}$ kJ	9.8 kJ	16.3

Summary

The coating on both sides of stone masonry spandrels increased resistance by more than three and a half times. The displacement capacity has also been drastically improved. Furthermore, the capacity for energy dissipation has improved by more than one order of magnitude.

The coating and the wall functioned as a composite element. Although there was debonding under large areas of coating (especially under cracks), the combined action of the coating and the wall was largely maintained due to sufficient anchoring. Compared to strengthening on one side, the improvement in strength should be larger. This indicates that the balance of strength between the coating and the wall was not perfect. Most likely, the coating was too strong for the masonry.

8.6.3 Two leaf brick masonry – strengthening on one side
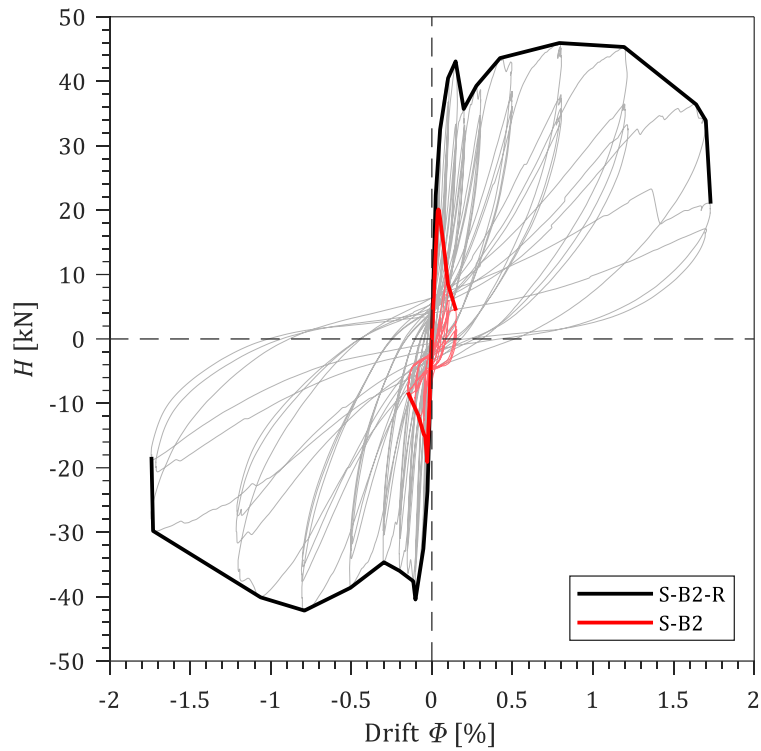
Fig. 133: Hysteretic curves and envelopes of unstrengthened and strengthened wall.
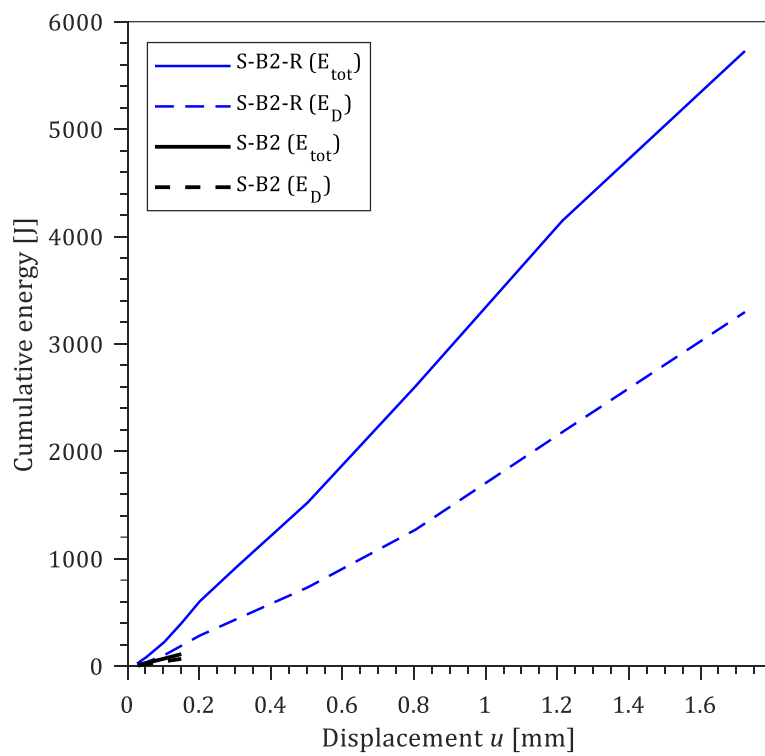
Fig. 134: Cumulative total and dissipated energy against displacement.

Table 49: Effect of strengthening two leaf brick masonry on one side

	Unstrengthened	Strengthened	Improvement (strengthened/unstrengthened)
Maximum resistance H_{max}	19.6 kN	44.1 kN	2.25
Ultimate displacement Φ_{ult}	0.2 %	1.7 %	11.4
Dissipated energy E_D	$1.3 \cdot 10^{-1}$ kJ	3.3 kJ	26.1

Summary

The coating on one side of brick masonry more than doubled the spandrel's resistance; because unstrengthened walls had very poor lintels, thus the increase of resistance was not so large as in stone spandrels. However, the displacement capacity was also drastically improved and the energy dissipation has improved by more than one order of magnitude.

8.6.4 One leaf brick masonry – strengthening on one side
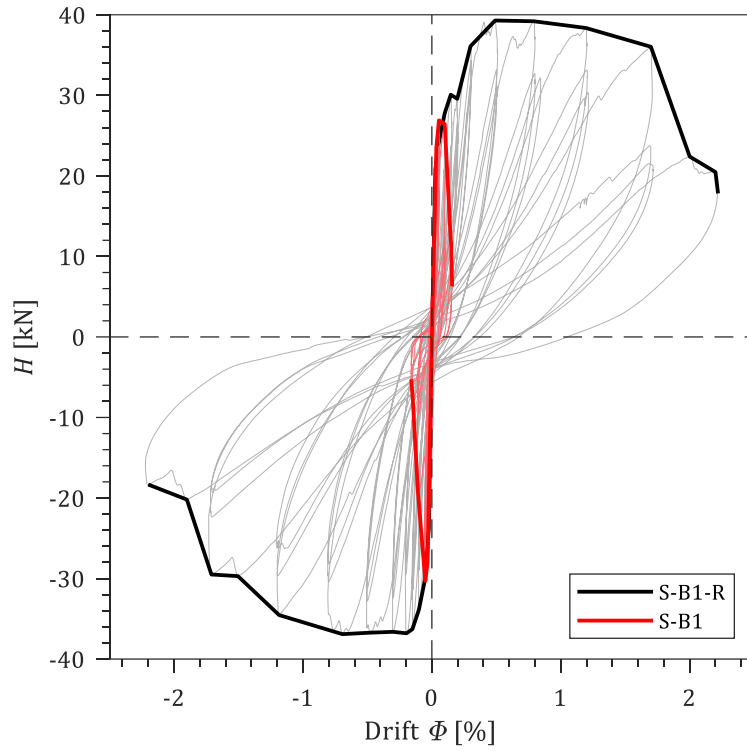
Fig. 135: Hysteretic curves and envelopes of unstrengthened and strengthened wall.
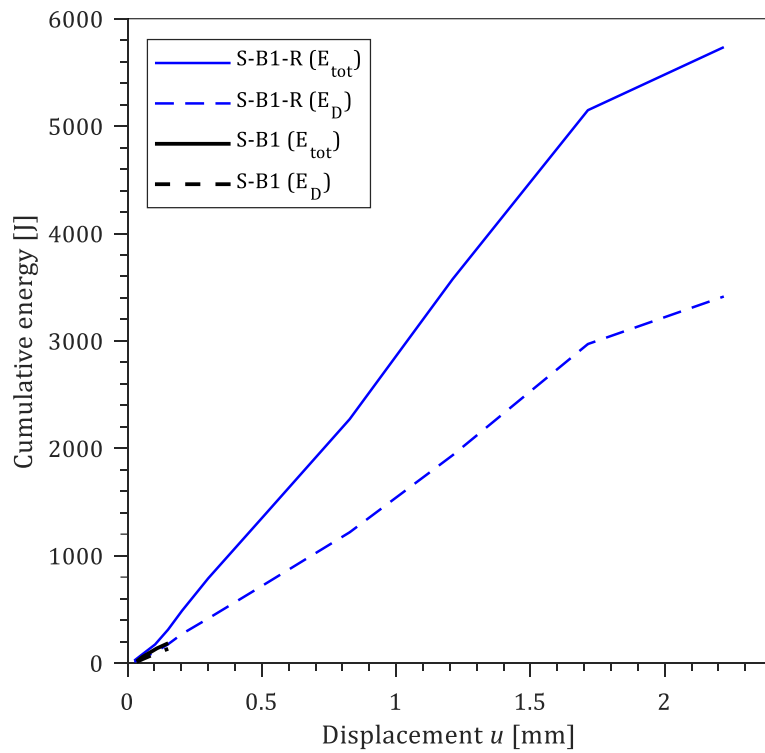
Fig. 136: Cumulative total and dissipated energy against displacement.

Table 50: Effect of strengthening one leaf brick masonry on one side

	Unstrengthened	Strengthened	Improvement (strengthened/unstrengthened)
Maximum resistance H_{max}	28.6 kN	38.1 kN	1.33
Ultimate displacement Φ_{ult}	0.2 %	2.2 %	13.99
Dissipated energy E_D	$1.5\cdot10^{-1}$ kJ	3.4 kJ	22.67

Summary

The coating on one side of brick masonry increased the spandrel's resistance by about 33 %, because the walls have very poor lintels. However, the displacement capacity has been drastically improved and the energy dissipation has improved by more than one order of magnitude.

Strengthening the two-leaf brick wall was more successful than the one-leaf brick wall. The difference is due mainly to the different type of damage occurred in the flat-arch constituting the lintel and the different crack formation at the ends of the spandrel. In fact, the flat-arch lost its effectiveness when the cracks in the spandrel started to open. Moreover, in the sample with two leaf masonry, vertical cracks did not form at the ends of the spandrel also in the strengthened sample, whereas, in the sample with a single leaf wall, rocking cracks (vertical cracks at th ends) occurred at the end of the test on the unstrengthened sample and appeared quite early also in the strengthened sample, that was , probably because of the different brick interlock in the two cases.

9 Tests on top tie-beam

9.1 Test setup

The test setup consists of wooden support with a sliding mechanism (Fig. 137), a restraining frame and a two-way hydraulic actuator (Fig. 138). The samples were built on wooden supports. Between the masonry and the support were two thick layers of plastic sheets with grease in between, to reduce friction.

The restraining frame provided support against movement at the sides of the sample. In the middle of the sample, there was an actuator for imposing the (out-of-plane) load.

There were thin elastic rubber strips at the contact between the wall and the support/load beam to reduce load concentrations at transfer points.

Fig. 137: Wooden support for the samples with sliding surface
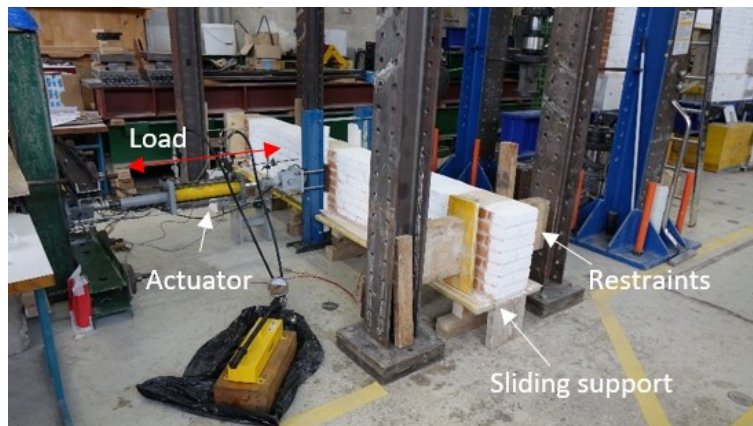
Fig. 138: Sample, restraining frame and the actuator.

The samples dimensions are attached in the Appendix.

9.2 Instrumentation

The instrumentation consists of two load cells on the actuator (one for pushing and one for pulling) and six displacement transducers. A pair of transducers were mounted on the left side (near support), at the centre (next to the actuator) and on the right side (near support). See also Fig. 139 and Table 51. The recordings of paired displacement instruments were averaged.

Fig. 139: Locations of displacement transducers.

Table 51: Description of instruments

Transducer	Measurement
1-LT	Displacement at left support, top
2-LB	Displacement at left support, bottom
3-CT	Displacement at the centre, top
4-CB	Displacement at the centre, bottom
5-RT	Displacement at right support, top
6-RB	Displacement at right support, bottom
7-Fpush	Force when pushing
8-Fpull	Force when pulling

9.3   Test protocols

The loading was applied by imposing prescribed displacement, and each displacement amplitude was applied once in the positive and negative directions. The amplitude was gradually increased until the collapse of the sample. The displacement was controlled manually acting on a hydraulic pump.

Table 52: Actual program of loading for tie-beam samples

Wall	T-R2	T-B1
Cycle	Amplitude [mm]	Amplitude [mm]
1.	1.4	1
2.	1.8	1.5
3.	2.8	2
4.	3.7	3
5.	4.5	4
6.	5.2	5
7.	5.9	5.9
8.	7.7	10.8
9.	9.2	12.8
10.	12.2	15.7
11.	14.4	19.2
12.	16.5	22.1
13.	18.4	25
14.	24.5	30.3
15.	29.7	35.5
16.	34.7	42.6
17.	42.6	52.6
18.	51.7	66
19.	64.8	89.2
20.	85.1	

9.4 Tests

9.4.1 T-R2 (two-leaf stone)

T-R2	Two leaf stone masonry;
Date of test (age):	2022/2/18 (age: 32 days)
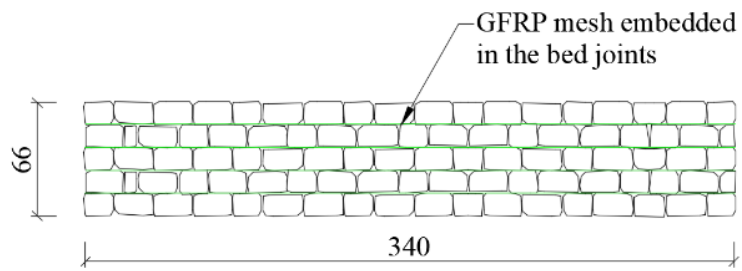
Fig. 140: Geometry of sample T-R2

Fig. 141: Mesh embedded in the bed joint.
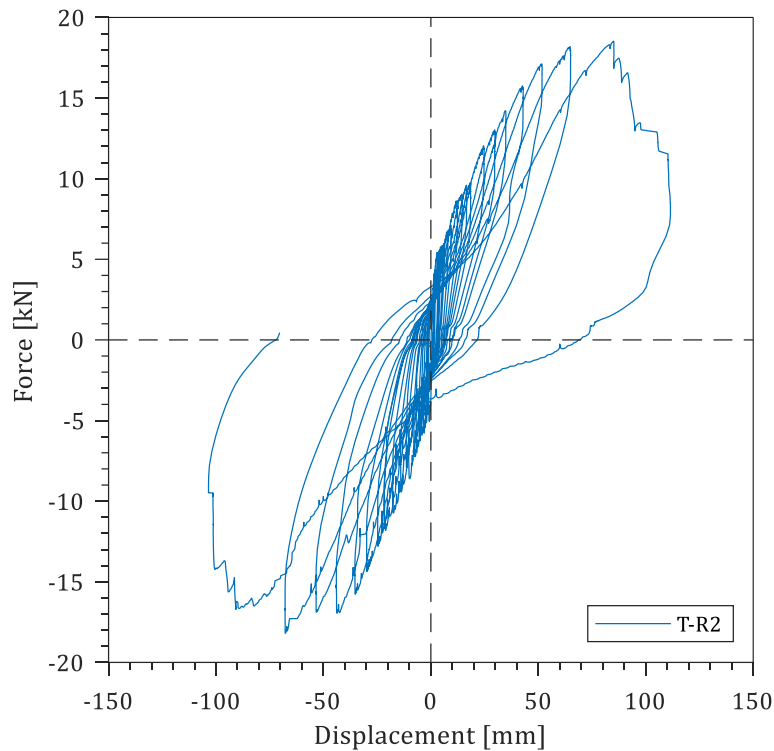
Fig. 142: Force-displacement hysteresis for T-R2.

Observations:

Displacement	Remark
1 mm	The first cracks appeared. The location of the cracks is at the top of the beam
2 mm	Cracks (at the middle of the sample) extended along the entire height.
4 – 7 mm	The crack pattern stabilized, and cracks opened and closed. Crack width increased with displacement amplitude. At 7 mm displacement, the cracks opened 1 mm wide.
13 mm	Cracks extended from top to bottom, and a mesh of cracks was spread over the entire length of the sample. The largest cracks were near the middle of the sample.
33 mm	Mortar started to fall out of the cracked joints. Cracks opened 3-4 mm wide.
42 mm	Mesh started fracturing (audible).
-65 mm	The external strand of mesh completely fractured in the negative direction. The peak force was about 18.2 kN.
+85 mm	The external strand of mesh completely fractured in positive direction. The peak force was about 18.4 kN. The beam at failure is shown in Figs. 143 - 145.

Table 53: Ultimate and cracking moment for T-R2

M_{cr} [kNm]	M_u [kNm]	M_u/M_{cr} [ ]
4.15	13.6	3.28

136

Fig. 143: Side view of T-R2 at collapse.
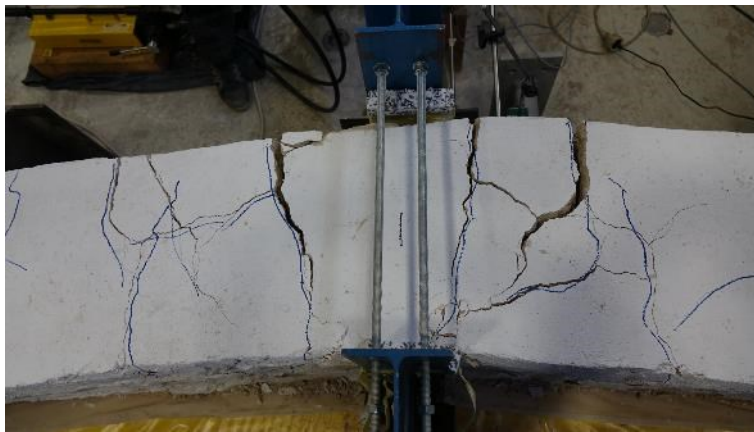
Fig. 144: Top view of T-R2 at collapse.

Fig. 145: Front view of T-R2 at collapse.

9.4.2   T-B1 (one leaf brick)

T-B1	One leaf brick masonry;
Date of test (age):	2022/2/17 (age: 30 days)
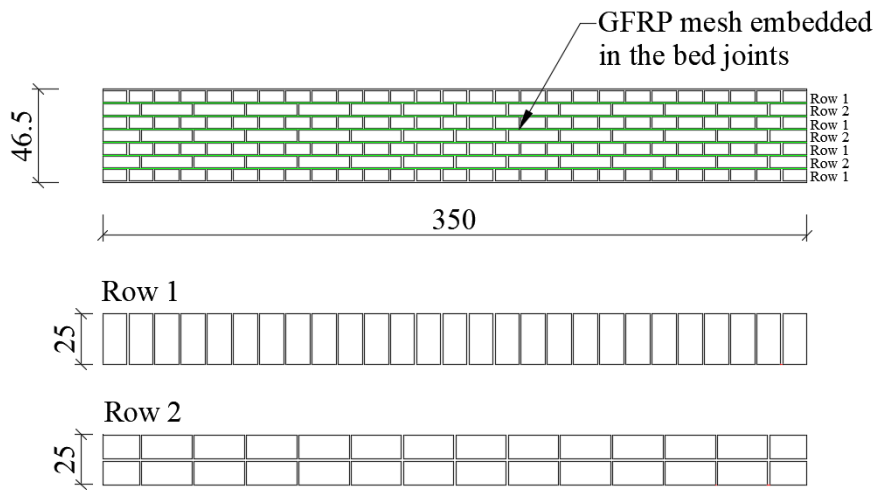
Fig. 146: Geometry of sample T-B1

Fig. 147: Mesh embedded in the bed joint.
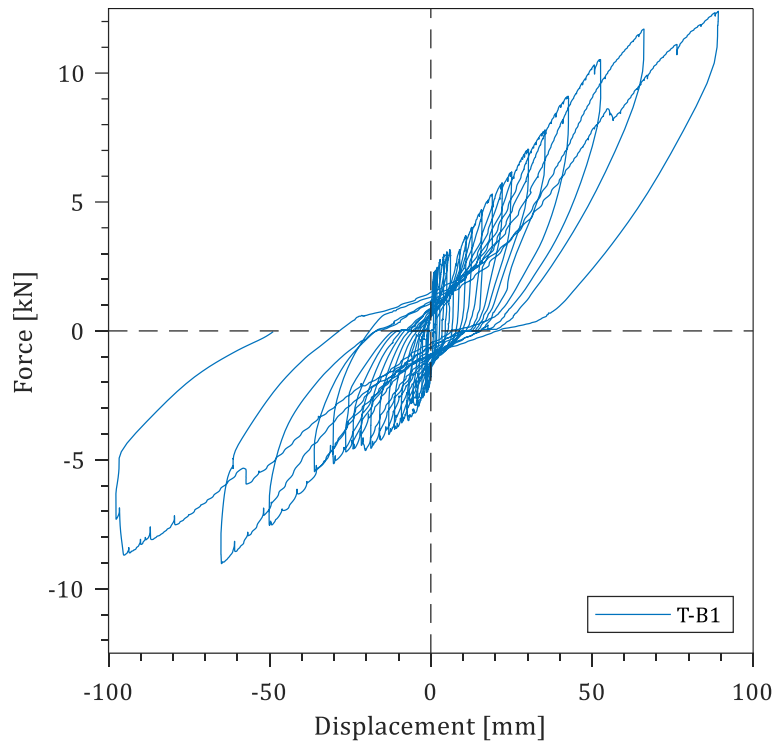
Fig. 148: Force-displacement hysteresis for T-B1.

Observations:

Displacement	Remark
3 mm	The first cracks appeared. The location of the cracks was at the top of the beam
5 mm	Cracks (at the middle of the sample) extended along the entire height.
11 mm	There were vertical cracks along the entire length of the beam.
25 mm	Cracks opened 3 mm wide.
33-90 mm	Cracks opened and closed with the load. Crack width increased with displacement amplitude.
90 mm	Mesh fractured, and the top row of bricks separated from the wall (Fig. 149). The peak force was about 12.4 kN. Beam at collapse is shown in Figs. 150-151.

Table 54: Ultimate and cracking moment for T-B1

M_{cr} [kNm]	M_u [kNm]	M_u/M_{cr} [ ]
2.12	8.1	3.82

Fig. 149: Top row separated from the wall at collapse.

Fig. 150: Side view of T-B1 at collapse.
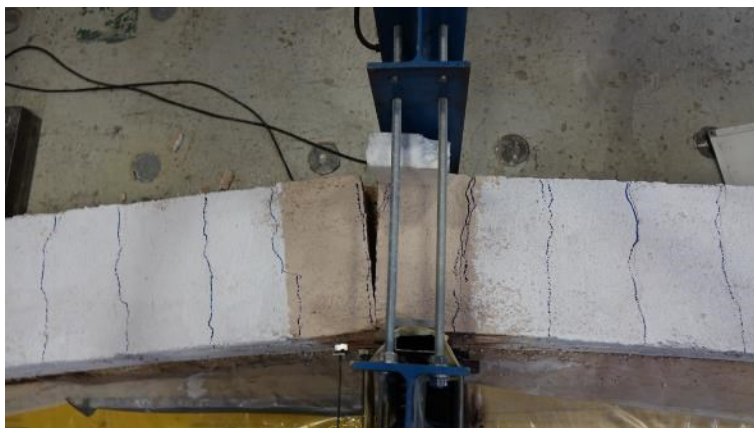
Fig. 151: Top view of T-B1 at collapse.

9.5   Summary and analysis

Equivalent flexural strength of masonry with GFRP mesh reinforced bed joints is calculated as:

$$f_{x2} = \frac{3\,F\,L}{2\,h\,t^2}$$

where h and t are the height and thickness of the cross-section. The results of the calculation are shown in Table 55. Comparing the results to average values of unreinforced masonry provided in standard Eurocode 6, the increase in strength is fourfold for stone masonry and sevenfold for brick masonry. The average values from Eurocode 6 were obtained by multiplying characteristic values by 1.2.

Table 55: Flexural strength of masonry

	f_{x2} (test) [MPa]	$f_{kx2} \cdot 1.2$ (Eurocode 6) [MPa]	Test/reference [ ]
T-R2	1.0	0.24	4.21
T-B1	1.7	0.24	6.97

The stone and brick masonry tie beams performed well. The cooperation between the masonry and the mesh was near optimal, and the final failure was due to mesh fracture. This observation is confirmed by cross-section calculation, which is presented next.

The cross-section calculation is based on the following assumptions:

- Planar cross-section, according to Bernoulli's hypothesis
- Linear stress distribution in compression in masonry
- Zero tensile strength in masonry
- Linear stress distribution in GFRP mesh
- Zero compressive strength of GFRP mesh
- On the tensile side, the deformation at ultimate resistance equals the maximum deformation of the GFRP mesh
- Deformation on the compressive side is calculated from the condition of equilibrium of forces

The calculation error is -14.3 % and +9.1 % for stone and brick masonry, respectively.

The calculation for stone and brick tie beams is shown in Tables 56 and 57.

Table 56: Calculation of stone masonry tie-beam T-R2

DATA		
T_m [kN]	4.9	traction resistance of the single fibre mesh bar
t [mm]	350	the thickness of the wall
l [mm]	2950	length of the beam
h [mm]	660	height of the beam
i	4	number of bed joints (rows)
s [mm]	66	mesh grid pitch
ε_{fu} [ ]	1.368%	ultimate tensile deformation of the single fibre mesh strand
E_m [MPa]	1074	Young's modulus of the masonry (hor. direction)
CALCULATION		
x [mm]	339.6	position of the neutral axis
$A_{m,c}$ [mm^2]	6859.1	masonry compressed section area
$M_{n,tot}$ [kNm]	11.31	resisting moment due to the traction of the net
$M_{m,tot}$ [kNm]	0.35	resisting moment due to the compression of masonry
M_u [kNm]	11.66	bending resistance
F_u [kN]	15.81	maximum force
$F_{u,exp}$ [kN]	18.44	maximum force in the experiment
$F_u/F_{u,exp}$ [ ]	**0.857**	calculation vs experiment

Table 57: Calculation of brick masonry tie-beam T-B1

DATA		
T_m [kN]	4.9	traction resistance of the single fibre mesh bar
t [mm]	250	the thickness of the wall
l [mm]	2950	length of the beam
h [mm]	465	height of the beam
i	6	number of bed joints (rows)
s [mm]	66	mesh grid pitch
ε_{fu} [ ]	1.329%	ultimate tensile deformation of the single fibre mesh strand
E_m [MPa]	2341	Young's modulus of the masonry (hor. direction)
CALCULATION		
x [mm]	242.6	position of the neutral axis
$A_{m,c}$ [mm^2]	3445.3	masonry compressed section area
$M_{n,tot}$ [kNm]	8.57	resisting moment due to the traction of the net
$M_{m,tot}$ [kNm]	0.26	resisting moment due to the compression of masonry
M_u [kNm]	8.83	bending resistance
F_u [kN]	11.98	maximum force
$F_{u,exp}$ [kN]	10.98	maximum force in the experiment
$F_u/F_{u,exp}$ [ ]	**1.091**	calculation vs experiment

10 Out-of-plane bending test of "C" walls

The purpose of the out-of-plane bending test of "C" walls is to investigate the possibility of using externally bonded CFRP strips instead of traditional steel ties. The continuity of the reinforcement was simulated at the horizontal supports to reproduce a CFRP strip applied around the outline of the building.

A displacement controlled test protocol was used to carry out each test. With this type of test protocol, the early rupture of the reinforcement while pushing towards the reinforced side is expected, due to its stiffer static scheme. In a structure excited by a seismic load, the force would distribute in the two opposite directions according to the stiffnesses of the actual loading schemes. As it will be seen in the test results, the resistances in the two loading directions are comparable and notably higher than the corresponding unreinforced values.

10.1 Test setup

The test setup of C experiments is illustrated in Figs. 152 – 154. It consists of a stiff steel truss reaction wall, two constraining horizontal steel beams acting as sliding supports, a trolley for vertical load distribution, and a hydraulic actuator. The test setup is an out-of-plane bending test of a C-shaped wall, reinforced with a 20 cm wide CFRP strip (FB-GV620U-HM) at middle height on one side of the wall and constrained at both ends. The mechanical characteristics of the reinforcement are summarized in Table 58.

When the load is pushing (reinforcement in tension), the ends of the wall are free to slide horizontally and to rotate. When the load is pulling (reinforcement in compression), the ends of the wall are free to slide horizontally but not to rotate.

Fig. 152: Out of plane bending of "C" walls tests setup, plan view.

Fig. 153: Out of plane bending of "C" walls tests setup, lateral view.

Fig. 154: Out of plane bending of "C" walls tests setup, section view.

At the bottom of the sample, six sliding supports made from tubular steel profiles with a plane dimension of 250x360 mm were positioned, as depicted in Fig. 155. The supports have ball bearings that move on 5 mm steel plates so to reduce the friction.

Two vertical HEA 160 steel beams were used to transfer the load from the actuator to the specimen. There were free-to-rotate loading plates between the HEA 160 and the specimen. The loading frame was placed on ball bearings to make slip friction negligible (Fig. 153).

Four "L" shaped steel rails were welded to the base steel plate. Two were used to keep the loading beams centred, and two were placed on the outer sides of the middle trolleys to allow for relative rotations. The support for the specimen was two concrete blocks of approximately 1x1x1 m^3, connected by injected threaded steel bars and bolted plates.

145

Base support for rubble stone wall

Plan view
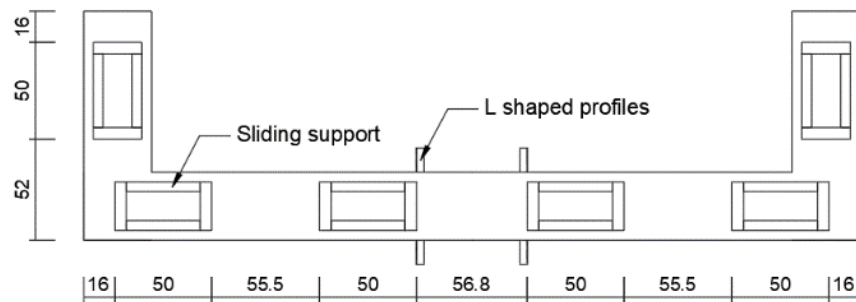
Base support for solid brick wall

Plan view
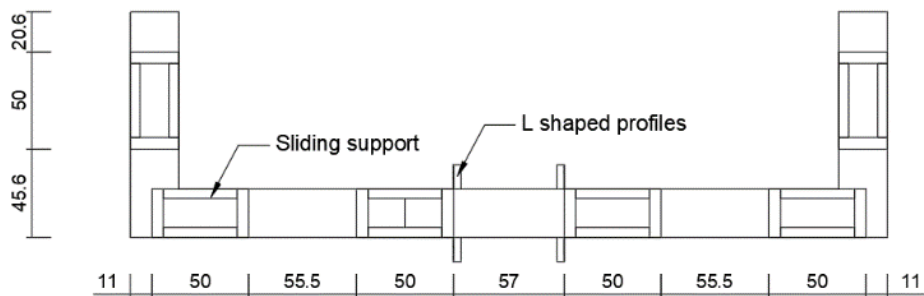
Fig. 155: Out of plane bending of "C" walls tests setup and positions of sliding supports, plan view.

The CFRP strip is restrained between bolted steel plates at both ends, welded to the vertical HEA 160 beams acting as supports for the samples. The sliding supports are made with two steel threaded sleeves pinned at both ends and connected on one side to the 2xHEB220 steel beam and on the other to the welded profile, which is then rigidly connected to the HEA 160 vertical beams.

Table 58: Mechanical characteristics of the CFRP strip.

Variable	Value	Variable	Value
Weight (g/m^2)	600	Fibre tensile resistance [MPa]	4700
Width (mm	200	Elastic modulus of the fibre [GPa]	390
Cross section area (mm^2)	66.6	Ultimate tensile deformation [%]	1.2
Equivalent fibre thickness (g/m^2)	600	Fibre density [g/cm^3]	1.80

The samples dimensions and the steel carpentry are attached in the Appendix.

10.2 Instrumentation

Each specimen was equipped with 28 displacement and two load transducers, as shown in Fig. 156 and 157. The forces in the actuator were measured by pressure transducers on the oil circuit of the actuator. The transducers are explained in Table 59.
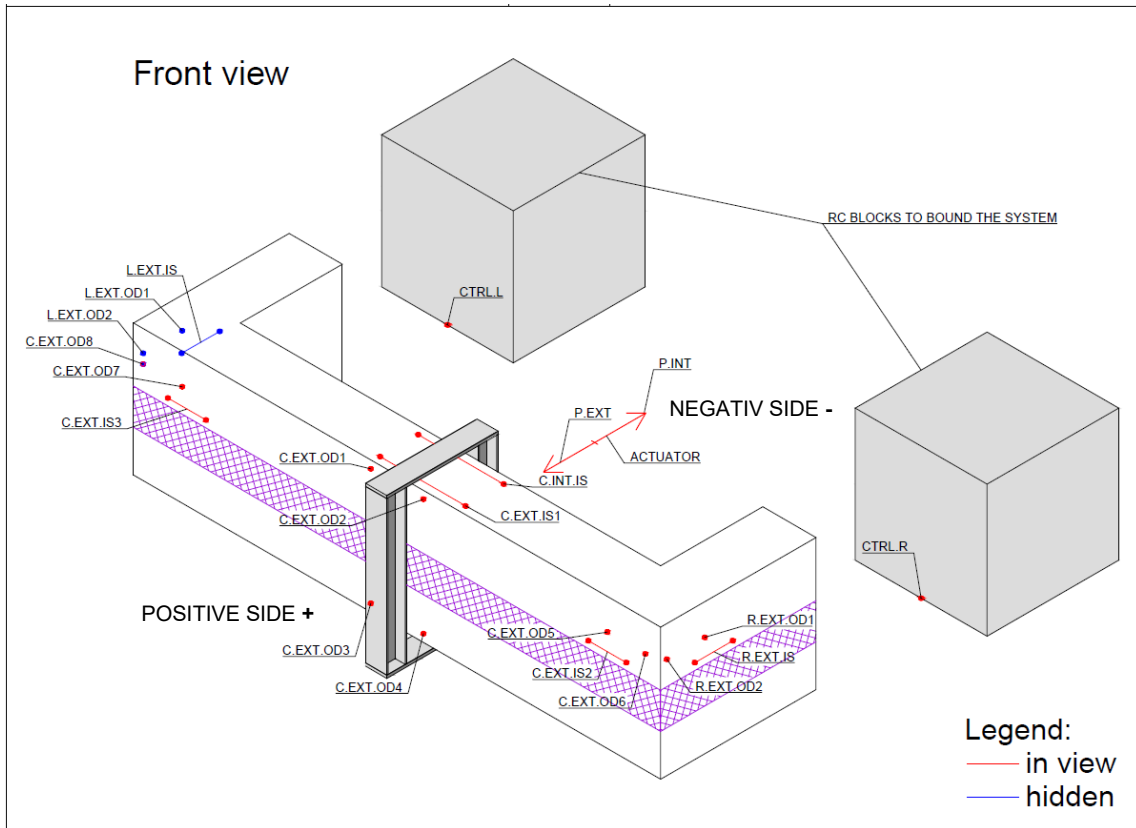
Fig. 156: Out of plane bending of "C" walls tests setup, measurement instruments, external view.
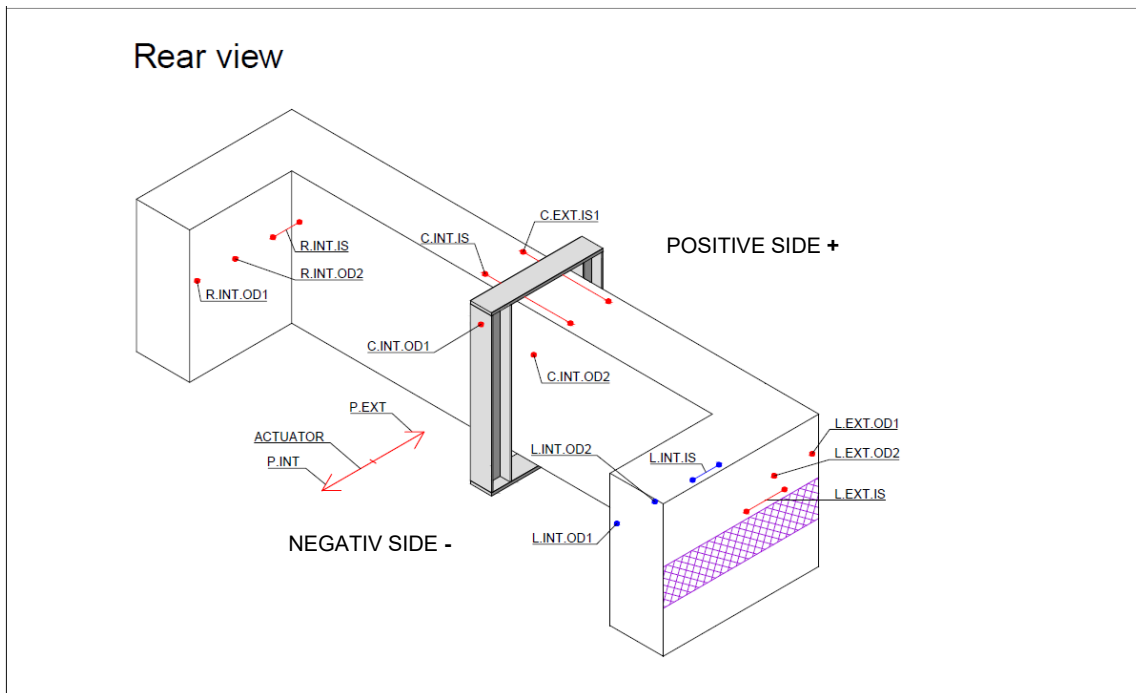
Fig. 157: Out of plane bending of "C" walls tests setup, measurement instruments, internal view.

147

Table 59: Instrumentation for the OOP tests on "C" walls

Transducer	Measurement
C_EXT_OD1, C_EXT_OD2, C_EXT_OD3, C_EXT OD4	Out-of-plane displacement of the middle section of the wall on the external side
C_INT_OD1, C_INT_OD2	Out-of-plane displacement of the middle section of the wall on the internal side
C_EXT_OD5, C_EXT_OD6	Out-of-plane displacement and rotation of the right corner of the wall
C_EXT_OD7, C_EXT_OD8	Out-of-plane displacement and rotation of the left corner of the wall
R_INT_OD1, R_INT_OD2	Out-of-plane displacement and rotation of the right end of the wall
L_INT_OD1, L_INT_OD2	Out-of-plane displacement and rotation of the left end of the wall
R_EXT_OD1, R_EXT_OD2	Out-of-plane lateral displacement and rotation of the right corner of the wall
L_EXT_OD1, L_EXT_OD2	Out-of-plane lateral displacement and rotation of the left corner of the wall
C_INT_IS C_EXT_IS1	(Horizontal) strain at the middle section of the wall (INT=internal side; EXT=external side)
C_EXT_IS2, C_EXT_IS3, R_EXT_IS, L_EXT_IS	(Horizontal) strain at the wall corners on the external side (C=central part of the wall; R=right part of the wall; L=left part of the wall)
R_INT_IS, L_INT_IS	(Horizontal) strain at the wall corners on the internal side
CRTL_R, CRTL_L	Out-of-plane displacement of the concrete blocks
P.INT, P.EXT	Pressure transducers to measure the load applied when the actuator is pushing (EXT) and when it's pulling (INT)

The relative middle height internal average out of plane displacement (C_INT_AVG_REL) was calculated as:

$$C\_INT\_AVG\_REL = \frac{C\_INT\_OD1 + C\_INT\_OD2}{2} - \frac{C\_EXT\_OD6 + C\_EXT\_OD8}{2}$$

10.3 Test protocols

In the test, the displacement C_INT_AVG_REL wall was controlled by manually pumping oil into the hydraulic actuator. The load was applied cyclically in positive and negative directions according to the loading protocol. After the reinforcement rupture was reached (while pushing) in the direction that presents a stiffer static scheme, an added dry strip of the same material was added in the middle section of the wall, using bolts and steel plates and impregnation with epoxy resin in the bounded ends. This was used to restore the reinforcement continuity. Then the load was applied monotonically towards the unreinforced side until failure.

A typical load protocol is shown in Fig. 158.
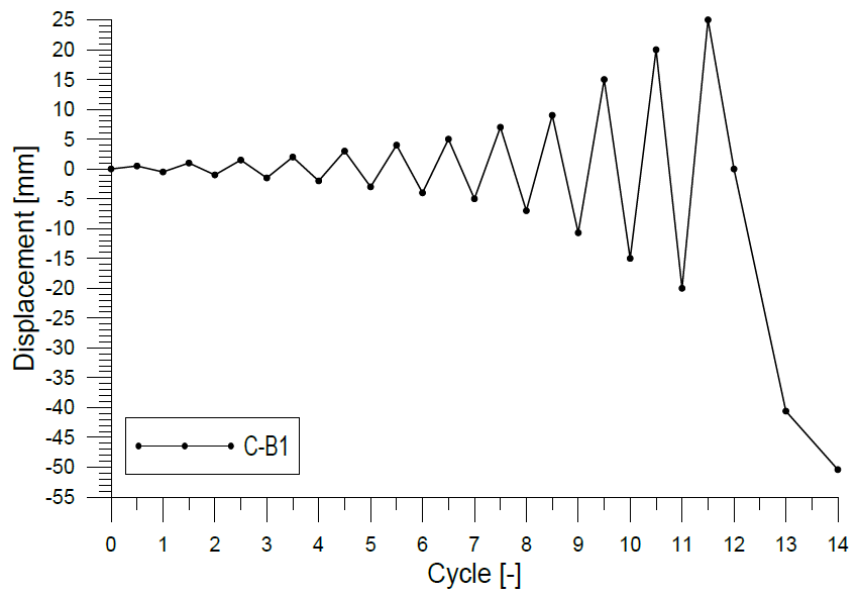
Fig. 158: Horizontal displacement sequence for specimen C-B1

The friction in the sliding supports was estimated between 0.5 kN and 1.5 kN, depending on the speed of oil pumping.

Table 60: Loading used in the tests

Wall	C-R2		C-B1	
Cycle	Positive amplitude [mm]	Negative amplitude [mm]	Positive amplitude [mm]	Negative amplitude [mm]
1.	0.5	-0.5	0.5	-0.5
2.	1.0	-1.0	1.0	-1.0
3.	1.5	-1.5	1.5	-1.5
4.	2.0	-2.0	2.0	-2.0
5.	3.0	-3.0	3.0	-3.0
6.	4.0	-4.0	4.0	-4.0
7.	5.0	-5.0	5.0	-7.0
8.	7.0	-7.0	7.0	-7.0
9.	9.0	-10.7	9.0	-10.7
10.	12.0	-12.0	15.0	-15.0
11.	15.0	-15.0	26.6	0
12.	20.0	0	-	-40.6
13.	-	-23.4	-	-50.4
14.	-	-44.9		

10.4 Evaluation of the response

10.4.1 Static analysis

The bending moment in the element is shown in Fig. 159. The maximum bending moment in the beam is:

$M_C = \frac{P \cdot l_2}{2} \left(\frac{l_2}{2 \cdot (l_1 + l_2)} - 1 \right)$; for the negative loading direction (pull);

$M_A = M_B = \frac{P \cdot l_2}{2}$; for the negative loading direction (pull) after the middle section cracked;

$M_C = \frac{P \cdot l_2}{2}$; for the positive loading direction (push).

It should be noted that lengths are considered from the centres of the masonry sections.
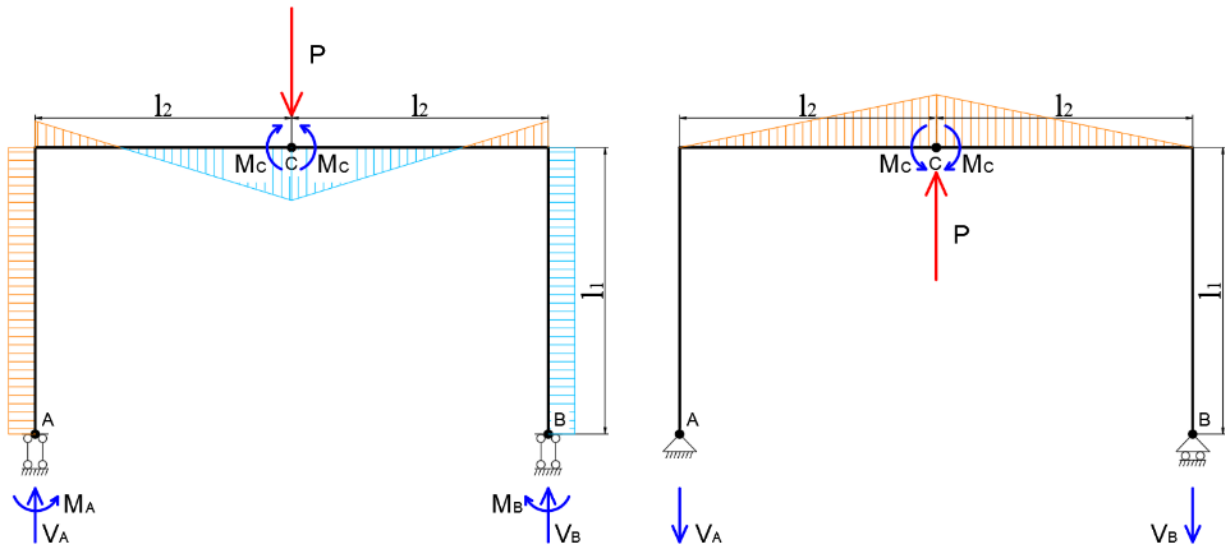
Fig. 159: Bending moment in the wall (uncracked elements) for negative (left) and positive direction (right)
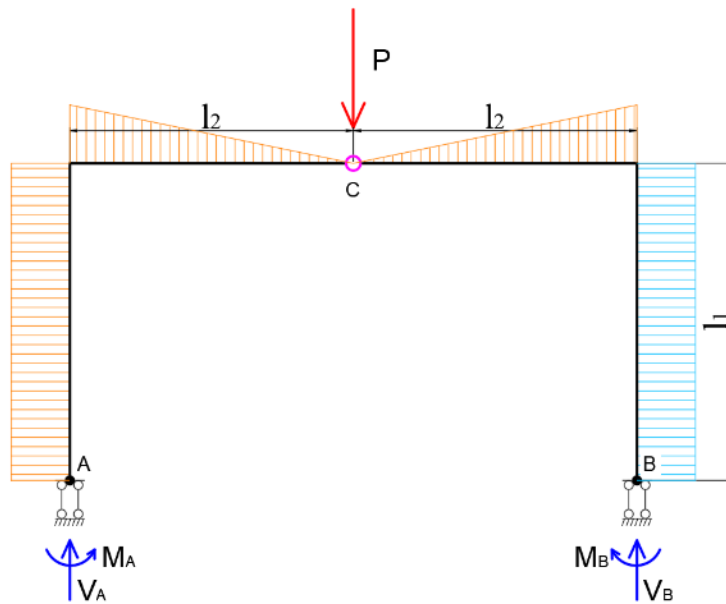
Fig. 160: Bending moment in the wall (cracked element) for negative direction

10.4.2 Bending resistance

Bending resistance of a wall at ultimate resistance is based on the following assumptions: cracked cross-section and zero tensile stresses in masonry, peak resistance of the bond between the CFRP strip and the masonry, perfect contact between the reinforcement and the wall, and linear stress distribution in the compressed cross-section part.

The calculations estimate out-of-plane loads for the case when FRP reinforcement is in tension, and the unstrengthened side is in compression.

The cross-section equilibrium is calculated on an idealised cross-section shown in Fig. 161.
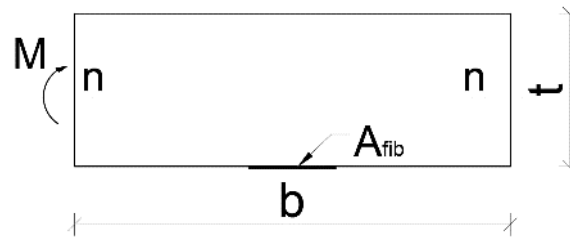
Fig. 161: Scheme of the cross-section.

Table 61: Variables for calculation of idealised cross-section.

Variable	Description	Variable	Description
b	Height of the wall	A_{fib}	Area of yarn of fibres
t	Thickness of the wall	n_{cr}	Neutral axis of the cracked section
$n_f = \dfrac{E_f}{E_m}$	Ratio of elastic moduli of fibres and masonry	$x_{id,cr}$	Location of centre of gravity of the idealised cracked section
$G_{id,cr}$	Centre of gravity of the cracked section	M	Bending moment
t_f	Thickness of the FRP strip	b_f	Width of the FRP strip

In the calculation, the location of the centre of gravity is calculated first:

$$x_{id,cr} = \frac{n_f \cdot A_{fib}}{b} \left(-1 + \sqrt{1 + \frac{2 \cdot t \cdot b}{n_f \cdot A_{fib}}} \right)$$

With the centre of gravity, which is also the location of the neutral axis, known, the moment of inertia ($J_{id,cr}$) of the cracked section can be calculated:

$$J_{n,id,cr} = \frac{b \cdot x_{id,cr}{}^3}{3} + n_f \cdot A_{fib} \cdot (t - x_{id,cr})^2$$

The analytical prediction of the resisting bending moment was calculated as per CNR-DT 200 R1/2013. The resistance to the intermediate debonding between the CFRP strip and the masonry can be calculated as:

$$f_{fdd,2} = \alpha \cdot f_{fdd}$$

Where $1.0 \leq \alpha \leq 2.0$ and f_{fdd} is the resistance to debonding between the CFRP strip and the masonry. It is calculated as:

$$f_{fdd} = \frac{1}{\gamma_{f.d}} \sqrt{\frac{2 \cdot E_f \cdot \Gamma_{Fd}}{t_f}}$$

Here $\gamma_{f.d}$ is a partial safety coefficient, which can vary between 1.2 and 1.5, based on the confidence of the debonding behaviour of the FRP strip. Γ_{Fd} is the design value of the specific fracture energy. It can be calculated as:

$$\Gamma_{Fd} = \frac{k_b \cdot k_G}{FC} \sqrt{f_{bm} \cdot f_{btm}}$$

Where:

- $k_b = \sqrt{\frac{3 - b_f/b}{1 + b_f/b}}$

- k_G can be assumed as (medium values) $\begin{cases} 0.093 \ mm \text{ for brick masonry} \\ 0.022 \ mm \text{ for sandstone masonry} \end{cases}$

- f_{bm} and f_{btm} are the medium values of the compression and tension resistances of the masonry blocks, respectively.

- FC is a confidence safety factor.

Finally, the resisting flexural moment of masonry can be calculated as:

$$M_u = \frac{f_{fdd,2} \cdot J_{id,cr}}{n_f \cdot (t - x_{id,cr})}$$

10.5 Tests

10.5.1 C-B1 (brick, single leaf)

C-B1	Single leaf brick masonry;
	Strengthened on one side; CFRP strip on one side at mid height,
Date of tests (age):	2021/07/06 (age: 236 days) and 2021/07/09 (age: 239 days)
Dimensions (span width/*h*/*t*):	3650/1000/250 mm
Material characteristics	
f_c	6.7 MPa
E	2341 MPa
G $(0.4 \cdot E)$	936 MPa
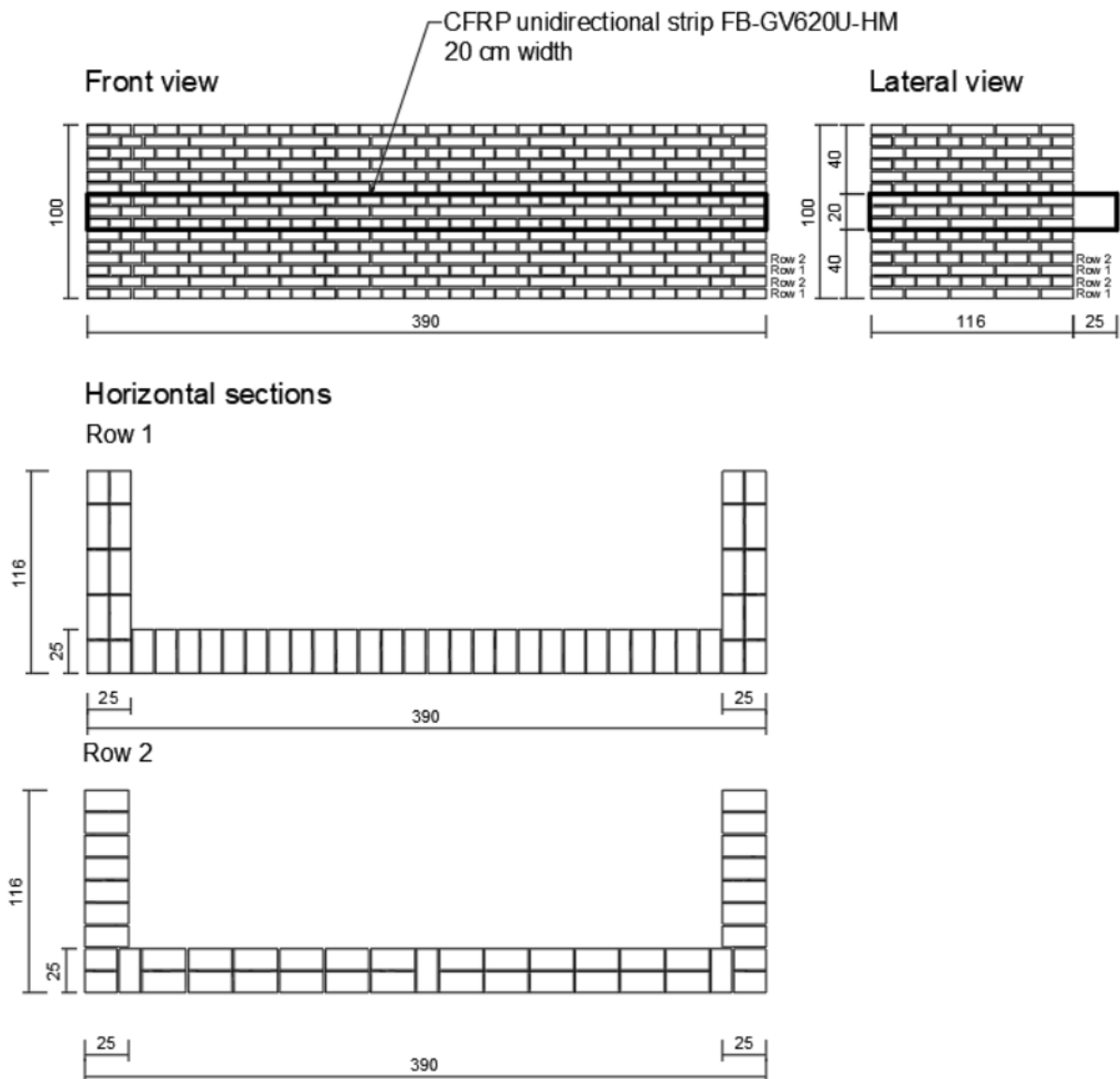
Fig. 162: Sample C-B1
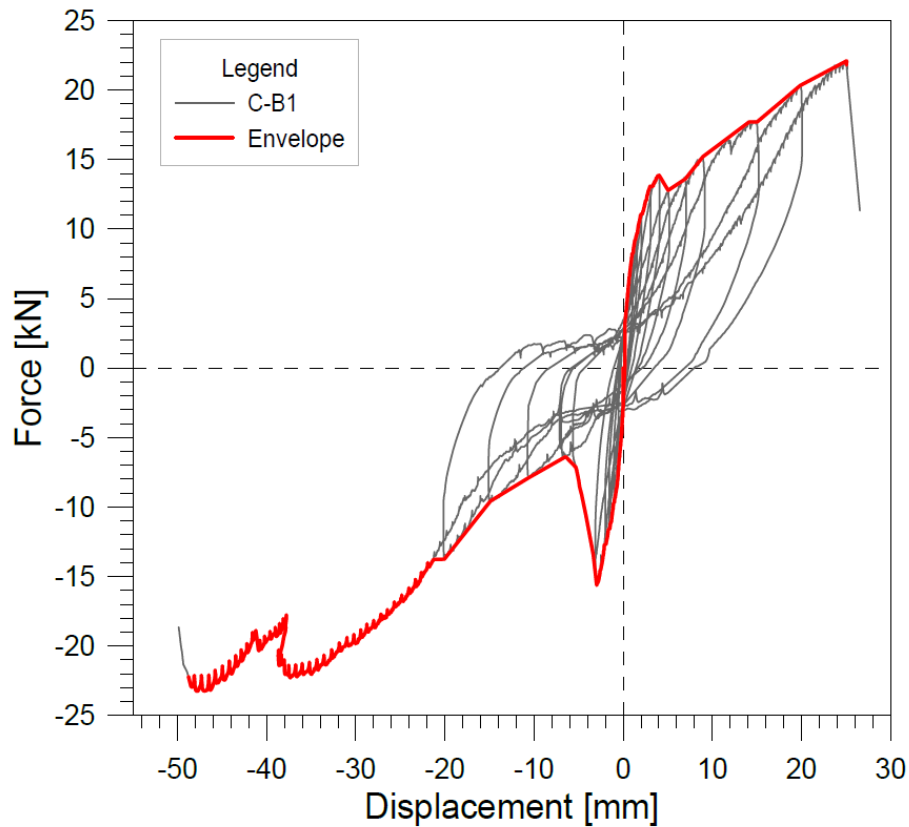
Fig. 163: Force vs out-of-plane displacement (C_INT_AVG_REL) curve and the envelope for sample C-B1

C_INT_AVG_REL	Observation
+1.50 mm (step 4)	The first crack was vertical in the middle section, on the unreinforced side in compression, detected by the instrument C_INT_IS. Shear force at cracking was about 9.6 kN.
+1.66 mm (step 5)	The second crack was located in the top part of the middle section, on the reinforced side, detected by the instrument C_EXT_IS1. Shear force at cracking was about 10.0 kN. The crack is shown in Fig. 164a.
-3.19mm (step 6)	Visible cracks ran the entire height of the wall in the middle section of the unreinforced side (Fig. 164b). They crossed both joints and bricks. Shear force at cracking was about 14.0 kN, and it decreased to about 6.4 kN after cracking (plastic hinge formation)
+15.0 mm (step 10)	Vertical cracks outside of the middle section (Fig. 164c). Debonding of the reinforcement (Fig. 165a).
+25.1 mm (step	The ultimate failure is due to the detachment of the CFRP strip from the masonry (Fig. 165b). Shear force at failure was about 21.8 kN.
CFRP strip repair (Fig. 165c)	
-40.6 mm (step 12)	Flexural horizontal and diagonal cracks along the mortar joints (Fig. 166)
-50.4 mm (step 13)	The ultimate failure is due to the rupture of the CFRP strip in the right corner (Fig. 167). Shear force at failure was about 23.3 kN.

Fig. 164: crack configuration during the test – (a) unreinforced side middle section at step 6 (-4.0 mm); (b) upper part of the middle section on the reinforced side at step 7 (+5.0 mm); (c) vertical cracks outside of the middle section, on the left part at step 10 (+15.0 mm)

Fig. 165: (a) debonding of the reinforcement from the surface regularization mortar layer on the right side; (b) CFRP strip failure at step 11 (+26.6 mm); (c) CFRP strip repairing
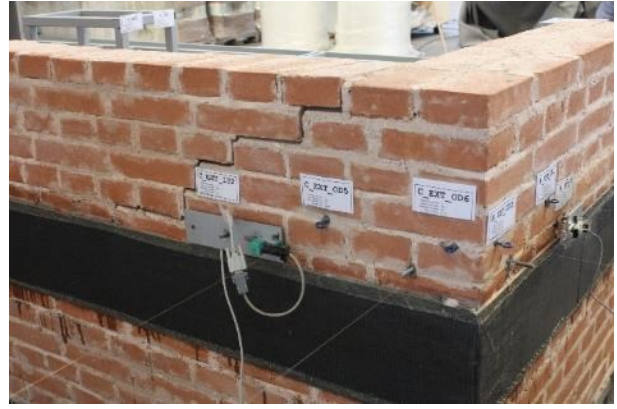
Fig. 166: crack configuration during the monothonic test – flexural craks at step 12 (-40.6 mm)

Fig. 167: failure of the CFRP strip in the right corner at -50.4 mm

10.5.2 C-R2 (Stone masonry)

C-R2	Two-leaf stone masonry
	Strengthened on one side; CFRP strip on one side at mid-height, 14 diatons
Date of tests (age):	2021/10/08 (age: 330 days) and 2021/10/11 (age: 333 days)
Dimensions (span width/*h*/*t*):	3650/1000/350 mm
Material characteristics	
f_c	2.48 MPa
E	1074 MPa
G (0.4 · E)	430 MPa
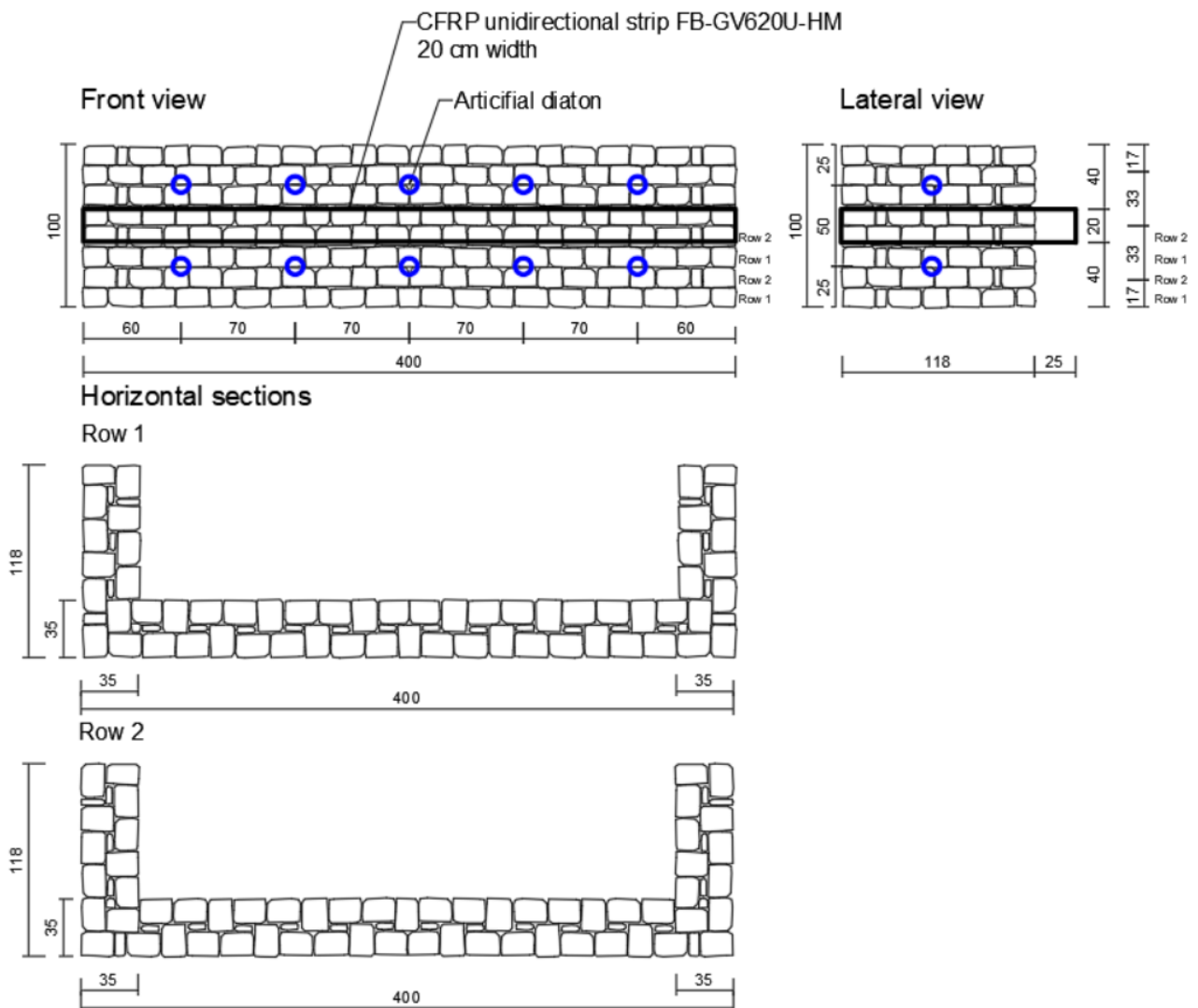
Fig. 168: Sample C-R2
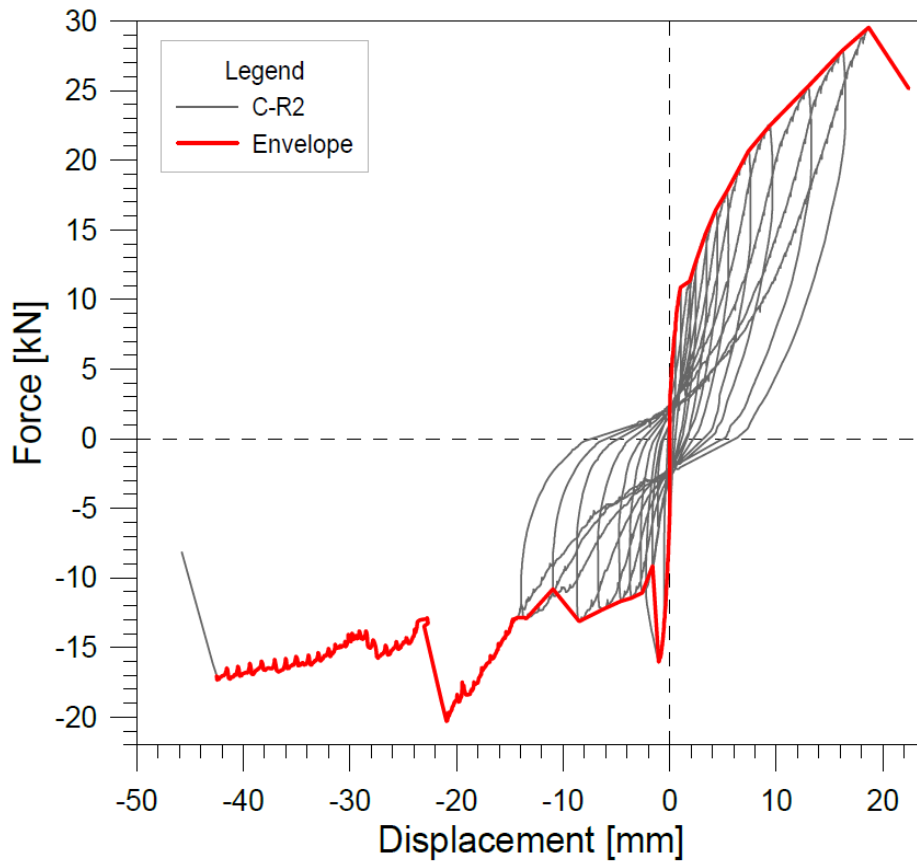
Fig. 169: Force vs out-of-plane displacement (C_INT_AVG_REL) curve and the envelope for sample C-R2

C_INT_AVG_REL	Observation
+0.76 mm (step 2)	The first crack was detected by the instrument C_EXT_IS1 before it was visible. Shear force at cracking was about 9.6 kN.
-0.58 mm (step 2)	The second crack was vertical and ran the entire wall height in the middle section on the unreinforced side in tension between the masonry joints (Fig. 170a). It was detected by the instrument C_INT_IS. Shear force at cracking was about 14.0 kN (plastic hinge formation).
+5.50 mm (step 7)	The crack in the middle section of the unreinforced side registered an opening of about 2.2 mm for a shear force of about 11.6 kN (Fig. 170b,c)
+18.66 mm (step 12)	The ultimate failure is due to the detachment of the CFRP strip from the masonry (Fig. 171a). Shear force at failure was about 29.5 kN.
CFRP strip repair (Fig. 171b)	
-23.88 mm (step 13)	Partial breakage of the FRP strip and detachment from the masonry at the left support (Fig. 172a). Shear force was about 20.2 kN, decreasing to about 13.0 kN after failure.
-45.91 mm (step 14)	The ultimate failure is due to the rupture of the CFRP strip in the right corner (Fig. 172bFig. 166). Shear force at failure was about 17.3 kN.

Fig. 170: crack configuration during the test – (a) unreinforced side middle section at step 2 (-0.58 mm); (b unreinforced side middle section at step 7; (c) reinforced side middle section at step 7

Fig. 171: (a) CFRP strip failure at step 12 (+18.66 mm); (b) CFRP strip repairing in the middle section

Fig. 172: (a) Detachment and partial breakage of the FRP strip from the masonry at the left support; (b) breakage of the CFRP strip in the right corner at -45.9 mm

10.6 Summary and analysis

To estimate the effect of strengthening, the push and pull directions are compared. In the pull direction, the specimen responds as if it was not strengthened (when FRP is in compression). In the push direction, the FRP is loaded in tension, and the strengthening effect can be observed

The tests have shown that the FRP strip and the wall performed as a composite element and effectively resisted loads. The bond between the reinforcement and the wall was not lost until collapse, when simultaneous debonding and fracturing of the CFRP strip occurred. The tensile fracture of carbon fibres shows that it was used to its full potential.

When pushing and the FRP was in tension, the cracks were oriented vertically and most dense near the middle of the wall. When pulling, the main crack, which acted as a hinge, was located in the middle section of the unstrengthened side. There were also vertical cracks near the corners of the wall, where debonding occurred. Such a mechanism with more widespread damage increases the walls' displacement and energy dissipation capacities.

The improvement of the response due to strengthening is quantitatively assessed in

Table 62. The ratio between the ultimate resistance and the resistance at cracking was between 1.85 and 2.29.

Finally, the analytical predictions of the resisting bending moment calculated according to CNR-DT 200 R1/2013 are presented in

Table 63. The error of the prediction is low, especially for the rubble stone sample. I the table, $M_{u+,exp}$ and $M_{u-,exp}$ are the experimental values of the bending moment at failure in the positive (push) and negative (pull) loading directions.

Table 62: Analytical prediction of the resisting bending moment

Sample	$M_{cr+,exp}$ [kNm]	$M_{cr-,exp}$ [kNm]	$M_{u+,exp}$ [kNm]	$M_{u-,exp}$ [kNm]	$M_{cr,exp,avg}$ [kNm]	$M_{u,exp,avg}$ [kNm]	$\frac{M_{u,exp,avg}}{M_{cr,exp,avg}}$ [-]
C-R2	9.91	9.96	26.95	18.52	9.94	22.74	2.29
C-B1	12.63	9.71	20.16	21.23	11.17	20.70	1.85

Table 63: Analytical prediction of the resisting bending moment

C-R2		
t_m	350	mm
b_m	1000	mm
b_f	200	mm
t_f	0.333	mm
A_f	66.6	mm^2
E_m	1200	N/mm^2
E_f	390000	N/mm^2
k_b	1.243	-
f_{bm}	160	N/mm^2
f_{btm}	0.6	N/mm^2
FC	1	-
k_G	0.022	mm
Γ_{Fd}	0.2680	N/mm
$\gamma_{f,d}$	1	-
f_{fdd}	792.26	N/mm^2
α	1.5	-
$f_{fdd,2}$	1188.39	N/mm^2
n_f	325	-
$x_{id,cr}$	103.3	mm
$J_{n,id,cr}$	1.68E+09	mm^4

M_u	25.0	kNm
$M_{u+,exp}$	26.95	kNm
$M_{u-,exp}$	18.52	kNm

C-B1		
t_m	250	mm
b_m	1000	mm
b_f	200	mm
t_f	0.333	mm
A_f	66.6	mm^2
E_m	1960	N/mm^2
E_f	390000	N/mm^2
k_b	1.106	-
f_{bm}	18	N/mm^2
f_{btm}	2.3	N/mm^2
FC	1	-
k_G	0.093	mm
Γ_{Fd}	0.6615	N/mm
$\gamma_{f,d}$	1	-
f_{fdd}	1244.81	N/mm^2
α	1.5	-
$f_{fdd,2}$	1867.22	N/mm^2
n_f	198.9796	-
$x_{id,cr}$	69.2	mm
$J_{n,id,cr}$	5.44E+08	mm^4

M_u	28.2	kNm
$M_{u+,exp}$	20.16	kNm
$M_{u-,exp}$	21.23	kNm

11 Tests on the pilot building

11.1 Pilot building

The two-story pilot building consisted of four unreinforced masonry (URM) walls (i.e., North, West, South, and East) with wooden floor and roof. A view of the whole building is shown in Fig. 173.

The structure has in-plane dimensions of 5,750 mm by 4,350 mm with a total height of 6733 mm (Fig. 174). The aspect ratio (height to width) of the piers ranged from 0.7 to 2.4 to promote both the shear and flexural collapse mechanisms. The loading was applied in the plane of West and East walls (North-South direction).

(a)   (b)

Fig. 173: View of the unreinforced test building: (a) East and North walls; (b) North and West walls

The 350 mm thick load-bearing walls are made of stones with approximate dimensions of 210 (length) x 150 (width)x 100 (height) mm, laid in a two-leaf masonry configuration. Both head and bed joints have an average thickness of 10 mm and are filled with lime-based mortar (see 3.1.3 for the the full description of mortar). The average compressive and flexural strength of mortar at 28 days was 1.5 MPa and 0.3 MPa, respectively. The average specific weight of masonry was about 21.0 kN/m^3. The first masonry row of the building was effectively connected to the foundation by 150x150x120 mm^3 reinforced concrete blocks, which were cast in situ and embedded within the wall thickness to prevent potential sliding at the masonry-concrete interface.
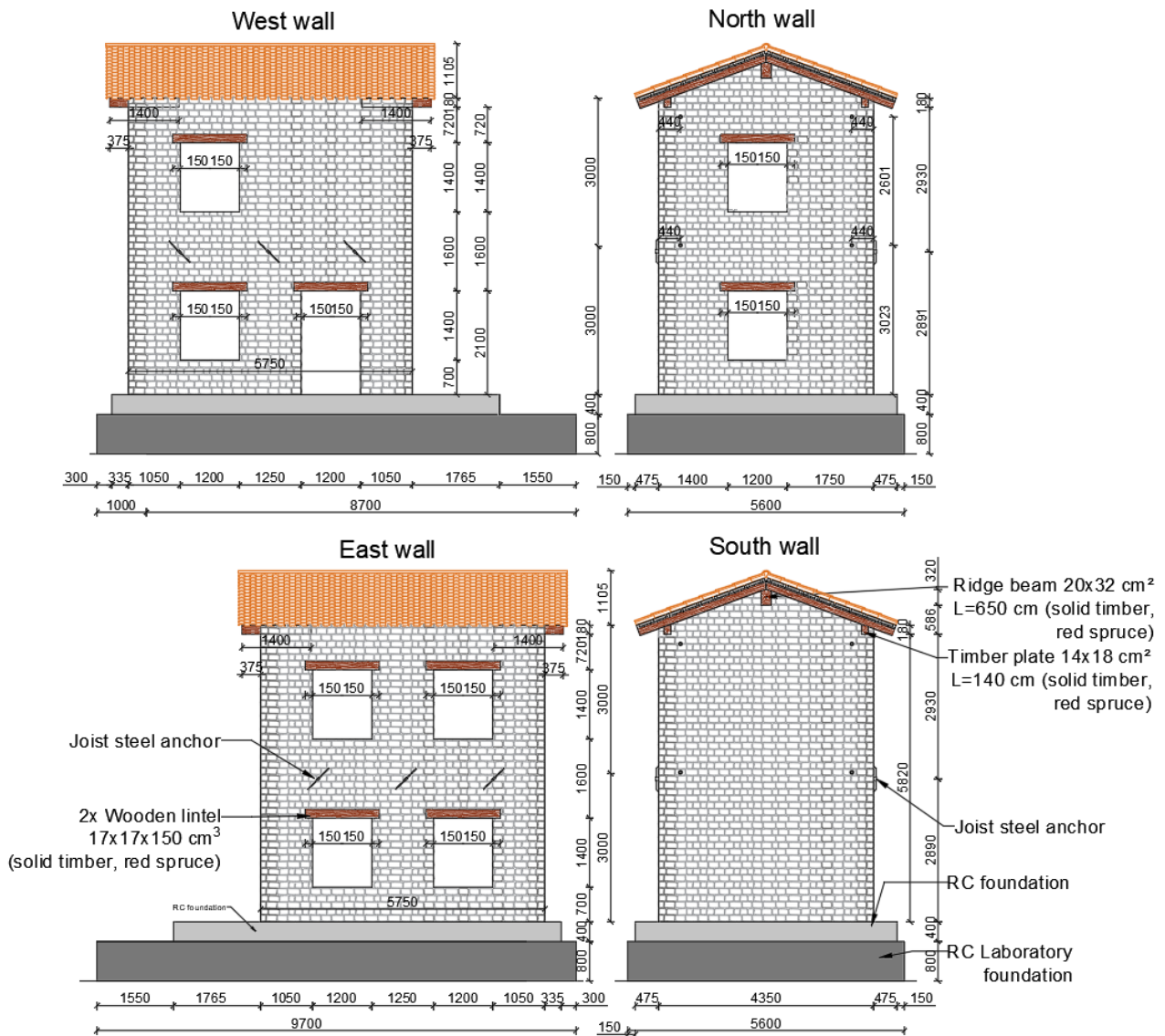
Fig. 174: Geometry of the pilot building (dimensions in cm).

The wooden floor consists of 9 solid timber long joists, which are located in masonry pockets providing a support length of 150 mm. Timber boards with a thickness of 25 mm are nailed to the top of the joists. Three joists composing the floor are connected to East and West walls by means of steel joist anchors, with a centre distance of 1800 mm, passing through the masonry wall and clamped by a steel wedge. It is worth noting that the wooden floor lacks stiffening elements and allows uneven distribution of seismic actions in bearing walls.

The wooden pitched roof is made of 26 solid timber joists laid on a solid timber ridge beam and on longitudinal walls. Timber boards with a thickness of 25 mm are nailed on top of the joists. The roof was covered by clay tiles.

All wooden elements are made of red spruce.

Fig. 175: Roof of the pilot building

Fig. 176: Concrete block weights for simulation of the load in the structure

The 1500 mm long lintels above the opening consist of two timber elements, with a cross section of 170 x 170 mm, next to each other. The lintels have an end support length of 150 mm on each side.

Concrete block (Fig. 176) and clay brick weights were placed respectively on the first and second floors to simulate the dead, permanent, and live load. The weight of the concrete blocks amounted to 3.7 kN/m^2 and the bricks one to 0.7 kN/m^2.

The construction of the building was completed in 65 days.

11.2 Strengthening

The URM building was tested up to significant damage but not too close to collapse. Afterwards, the cracks were superficially sealed with cement grout. Then, the building was strengthened by a 30-40 mm thick GFRP mesh reinforced coating, and the coating was anchored into the walls by L anchors and diaton connectors. The materials and strengthening procedures are described in Sections 0 and 0, respectively.

The arrangement of L-shaped connectors (4/m^2) and artificial diatons (2/m^2) is illustrated in Fig. 177.

Before applying the CRM coating, the mortar joints were removed to a depth of 10 mm. The masonry surface was washed with a high-pressure water cleaner to remove the white hydraulic lime paint and moisten the masonry surface to promote better adhesion of the CRM coating. The white paint was applied to the façade to make detecting cracks easier during the URM test.

Threaded stainless 8 mm diameter steel bars (characteristic yield strength 200 MPa) were anchored to the RC foundation by an epoxy resin and injected in predrilled holes with a depth of 250 mm. These bars were placed along the entire perimeter of the building, about 10-15 mm from the masonry wall surface, so to simulate the connection of the CRM coating with the foundation of the building. The density of the bars was three per meter to provide a good connection between the CRM coating and the concrete foundation. The threaded bars were installed beneath the GFRP mesh to avoid possible splitting failure mechanisms of the mortar coating. Along the four external corners of the building, GFRP angular meshes with a width of 330 mm were used to guarantee the continuity of the reinforcement.
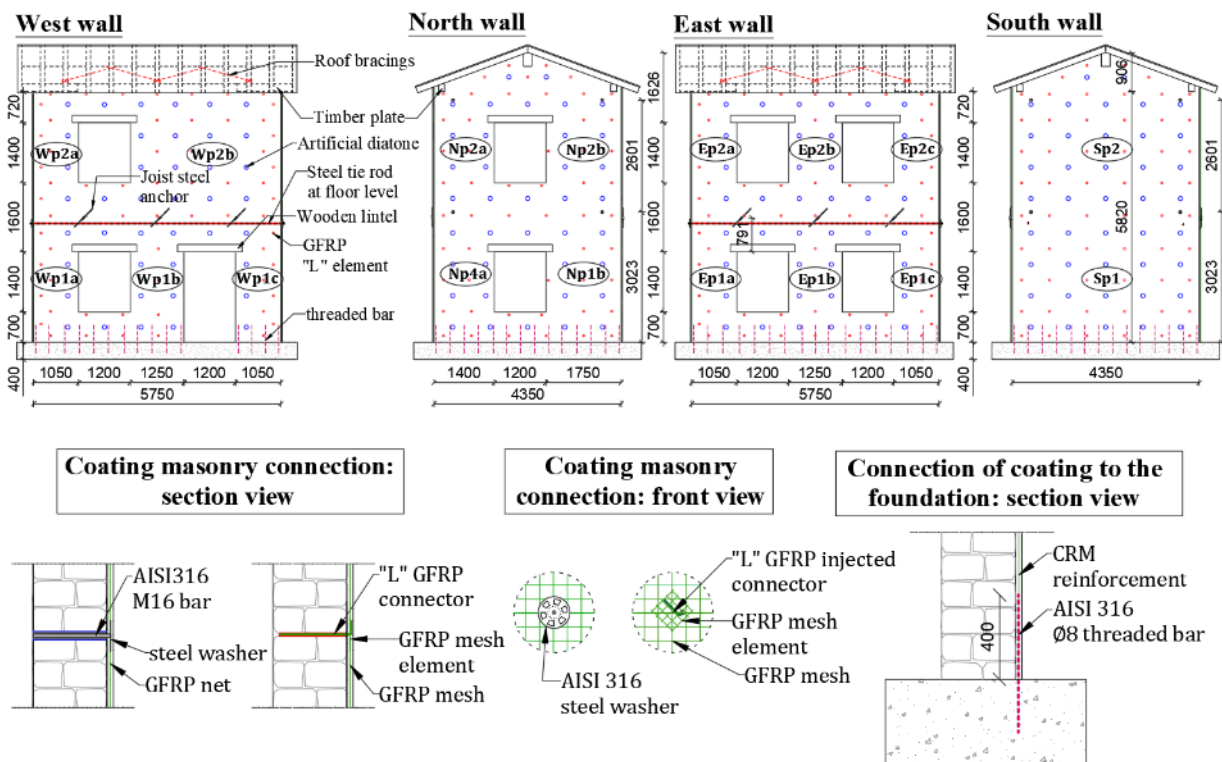
Fig. 177: Strengthening the structure by GFRP mesh reinforced coating and anchoring.

11.3 Test setup
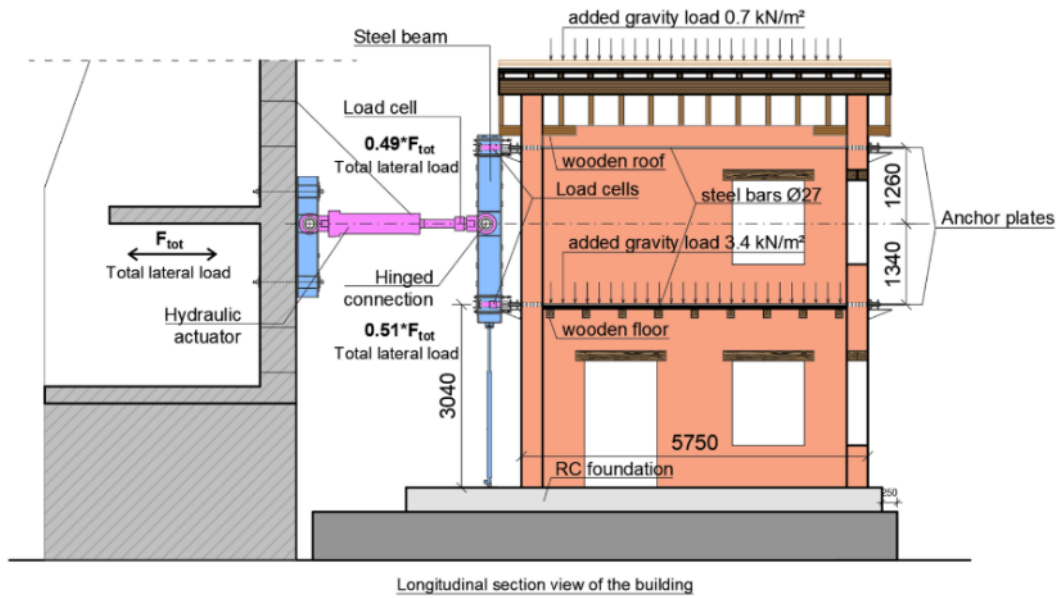
Fig. 178: Test setup (East wall)

The test setup consists of a stiff reaction wall (on the left-hand side in Fig. 178), a strong reinforced concrete platform, the pilot building (in orange in Fig. 178) and a system for applying the horizontal load. Concrete block weights simulated vertical load on the first floor and clay solid bricks on the roof.

Fig. 179: System for the application of horizontal load.

The horizontal load was applied to the structure by two hydraulic actuators (1500 kN capacity), one for the East wall and the other for the West wall. Each actuator was connected to a steel beam, which distributed horizontal load between the first floor and the top of the building. When pushing, the actuators pushed directly against the wall. When pulling, the load was transferred to the other side of the structure by steel bars. Steel bars (painted blue) can be seen in Fig. 179 at the side of the pilot building. Under each contact point, there were load cells to measure the forces. The horizontal load application system can be seen in Fig. 179.

The testing apparatus was dimensioned to resist the predicted maximum loads with limited elastic deformations and to allow for a lateral displacement of at least 150 mm in both loading directions. Hinged connections were designed between the actuator and the horizontal load transfer beams, and between the load transfer bar coupling system and the walls, to allow for the rotation of the system with the longitudinal walls. The load transfer bar coupling system was designed to accommodate the four load cells at each loading area. The sample dimensions and the testing apparatus drawings are attached in the Appendix.

11.4 Instrumentation

The instrumentation of the pilot building is shown in Fig. 180. It consists of 52 displacement transducers and four load cells. Additionally, two areas of the structure were measured by a DIC system: the entire east wall and the central pier on the ground floor of the West wall. Six accelerometers were used to measure the natural vibrations of the structure (Fig. 181).
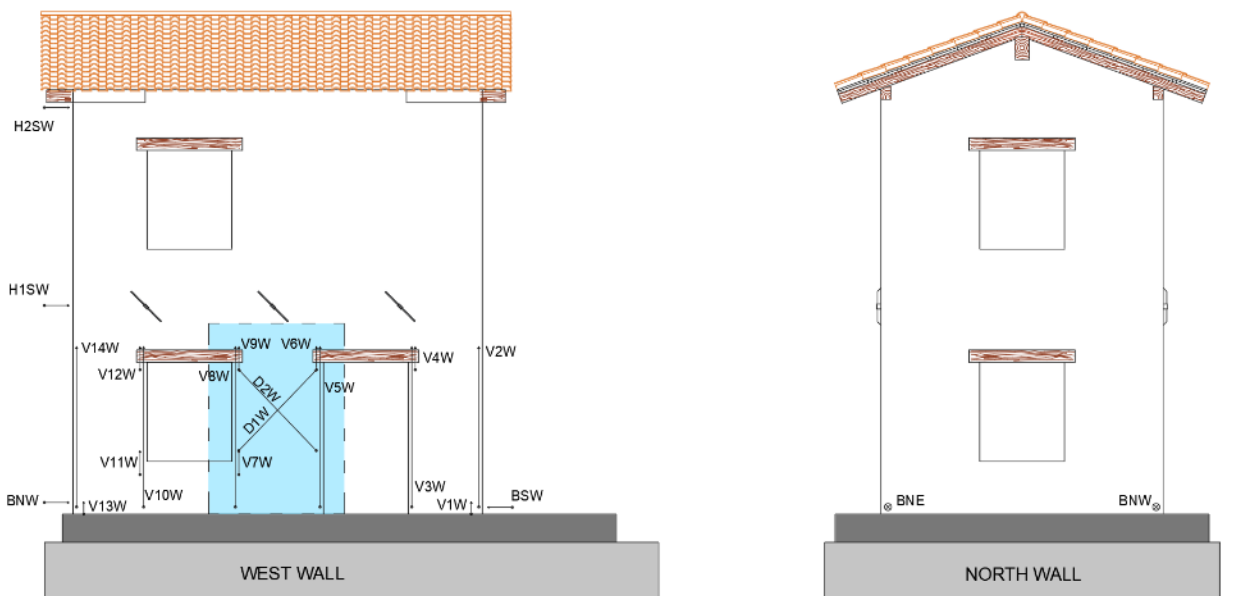
Fig. 180: Hard-wired displacement transducers and areas measured by the optical system (shaded blue)

Fig. 181: Positions of the accelerometers

Table 64: Description of instruments for pilot building test

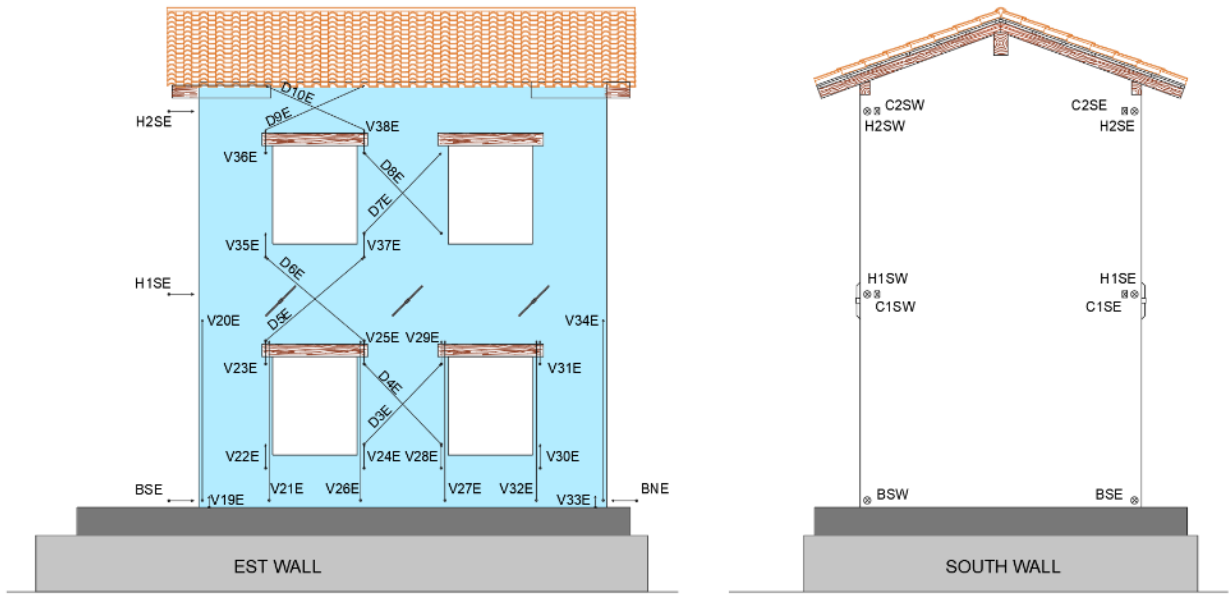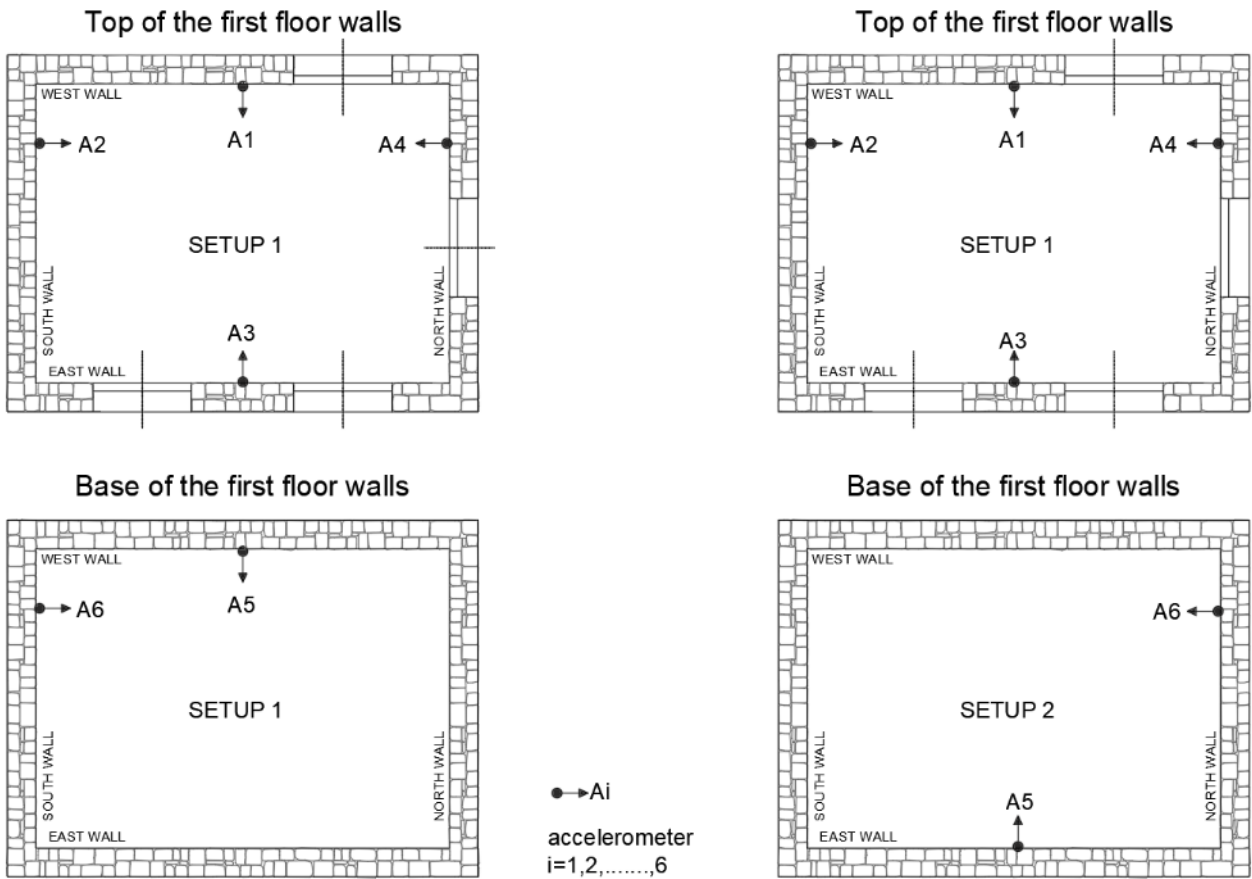| Transducer	Measurement
V24E /V28E	Vertical displacements – bottom of the central pier on ground floor – East wall
V25E/ V29E	Vertical displacements– top of the central pier on ground floor – East wall
V35E/ V36E	Uplift – on the left of the first floor left window (bottom and top) – East wall
V22E/ V23E	Uplift – on the left of the ground floor left window (bottom and top) – East wall
V30E/ V31E	Uplift – on the left of the ground floor right window (bottom and top) – East wall
V20E/V21E/ V26E/V27E/ V32E/V33E	Uplift of the first floor (left to right along the length of the structure) - East wall
V19E/V33E	Uplift of the structure on the left and right bottom corner (East wall)
D3E/D4E	Diagonal displacements – central pier on the ground floor – East wall
D7E/D8E	Diagonal displacements – central pier on the first floor – East wall
D5E/ D6E	Diagonal displacements of left spandrel between ground and first floor (East wall)
D9E/ D10E	Diagonal displacements of left spandrel between first floor and roof (East wall)
D1W/D2W	Diagonal displacements – central pier on the ground floor – West wall
V14W/V10W/ V8W/V5W/ V3W/V2W	Uplift of the first floor (left to right along the length of the structure) – West wall
V13W/V1W	Uplift of the structure on the left and right bottom corner (West wall)
V11W/ V12W	Uplift – on the left of the ground floor left window (bottom and top) – West wall
V7W/ V9W	Uplift – on the right of the ground floor left window (bottom and top) – West wall
V6W/V4W	Uplift – on the left and right of the door on the ground floor – West wall
BSE/BNE/ BSW/BNW	Slip of the structure at the first row of mortar (South East/North East/South West/North West)
H1SW/H1SE	Horizontal displacements on the first floor (South West/South East)
H2SW/H2SE	Horizontal displacements at the top (South West/South East)
C1SW, C2SW, C1SE, C2SE	Load cells at loading points
F1, F2	West (1) and East (2) actuator load cells
A1,…A6	Accelerometers

11.5 Test protocols

The load was imposed into the building in the form of prescribed displacements at the actuator shafts and by controlling the displacement at the top of the two longitudinal walls (H2SW, H2SE). Both actuators (East and West) moved in unison. Because of assembly tolerances, the displacement measured on the East and West sides was not identical.

Each displacement amplitude was repeated one, two or three times in the positive (push) and negative (pull) directions. Displacement amplitude was gradually increased until the end of the test.

In the case of the URM building, the test was stopped when the damage was significant but not too close to collapse. In the case of strengthened building, the test was performed up to near collapse.

The load protocols are shown in Table 65.

Table 65: Actual program of loading

Wall Cycle	URM pilot building			Strengthened pilot buliding		
	Number of cycles [-]	Positive amplitude [mm]	Negative amplitude [mm]	Number of cycles [-]	Positive amplitude [mm]	Negative amplitude [mm]
1.	1	0.4	-0.3	1	0.2	-0.2
2.	1	0.6	-0.6	1	0.4	-0.4
3.	1	0.9	-0.5	1	0.6	-0.6
4.	2	1.1	-0.8	1	0.8	-0.8
5.	3	1.4	-0.9	2	1.2	-1.2
6.	2	1.8	-1.3	2	1.8	-1.8
7.	2	2.3	-1.7	2	2.5	-2.5
8.	2	3.1	-2.4	2	3.5	-3.5
9.	2	3.9	-3.1	2	5.0	-5.0
10.	2	5.0	-4.2	2	7.0	-7.0
11.	2	5.9	-5.4	2	10.0	-10.0
12.	2	9.3	-7.9	2	14.0	-14.0
13.	2	12.7	-11.6	2	19.0	-19.0
14.	2	19.4	-17.0	2	25.0	-25.0
15.				2	33.0	-33.0
16.				1	42.0	-33.0
17.				2	55.0	-45.0
18.				1	79.0*	-

* The failure was reached when loading in the positive loading direction.

11.6 Parameters of seismic resistance

Base shear $V_b = F1 + F2$

Top of the structure displacement $\delta_2 = \dfrac{(H2SW - BSW) + (H2SE - BSE)}{2}$

Top of the structure drift $\gamma_2 = \dfrac{\delta_2 \ [mm]}{5640} \cdot 100$

First floor drift $\gamma_1 = \dfrac{\delta_1 \ [mm]}{3040} \cdot 100$

11.7 Test on the URM pilot building

The URM building was tested about six months after it was constructed. The damage after the test is shown in Figs. 182 and 183. The most significant cracks were in the piers of the first floor. In contrast, the damage observed at the ground story was smaller. The path of the cracks generally followed the mortar joints.

Fig. 182: Cracks on the East wall obtained by the DIC system. Red lines denote cracks. Damage when loaded in negative (left) and positive (right) directions.
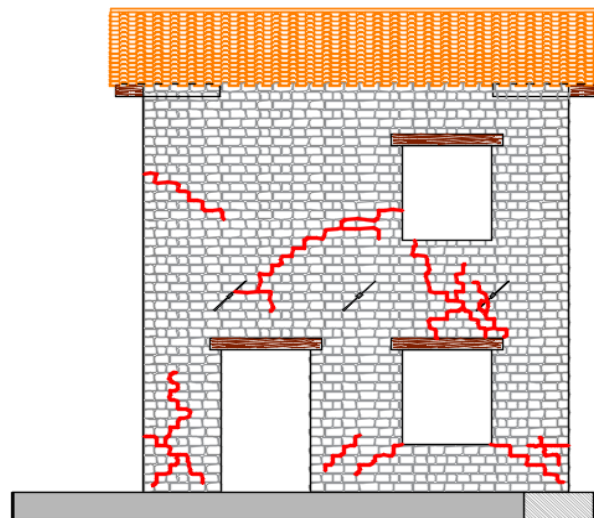
Fig. 183: Cracks on the West wall.

The experimental curve presented in Fig. 184 remained linear until the first flexural cracks occurred on the central pier on the second floor. These cracks occurred at a total base shear load V_b of about ± 70 kN ($\delta_2 = \pm 0.9$ mm). Once a displacement of around $\delta_2 = 1.2$ mm was attained ($V_b = \pm 77$ kN), the stiffness of the building started to reduce gradually, and new cracks developed at the corners of the openings. A further reduction of the lateral stiffness was caused by diagonal shear cracks in spandrels at $V_b = \pm 110$ kN and $\delta_2 = 2.1$ mm. Shear cracks of the spandrels extended to the corners of the first-floor windows. With increasing lateral displacements, shear cracks also formed on side piers on the first floor, at that point the building attained the maximum capacity, equal to $+267$ kN. After that, the resistance slightly decreased to $+251$ kN when additional

diagonal cracks formed in the piers. This damage pattern was indicative of a mechanism, and the structure could not offer more resistance. Based on the damage propagation discussed above, it may be concluded that the failure mechanism was a first story collapse mechanism.

It should be noted that damage evolution in positive and negative directions was substantially different, which caused an unsymmetric response shown in Fig. 184.

During the test, no up-lifting of the building was observed. There was no damage at the base of the walls.

Fig. 184: Hysteretic force-displacement response curves of URM pilot building

11.8 Test on the strengthened pilot building

About four months after the end of the test on the URM building, the strengthened building was tested. Inspection before the second test revealed some micro-cracking on the coating around the openings due to plastic shrinkage.

Damage at the end of the test is shown in Fig. 185. Most of the cracking is concentrated in the piers of the ground floor, and damage on the top floor is much less, which leads to the conclusion that the failure was due to the ground floor storey mechanism.

The experimental curve presented in Fig. 186 is almost linear until the first flexural cracks occurred in all ground floor piers (on East and West walls). This occurred at a total base shear load V_b of about ± 90 kN ($\delta_2 = \pm 0.3$ mm). Once a displacement reached almost $\delta_2 = 0.4$ mm ($V_b = \pm 110$ kN), the stiffness of the building gradually reduced as cracks developed on the coating. Cracking was mostly concentrated in areas close to the corners of the ground floor openings. With increasing lateral deflection, the same flexural cracks also appeared in piers on the second floor. In contrast, diagonal shear cracks appeared on the coating of spandrels at $V_b = \pm 235$ kN and $\delta_2 = \pm 1.2$ mm, which caused a further reduction of the stiffness.
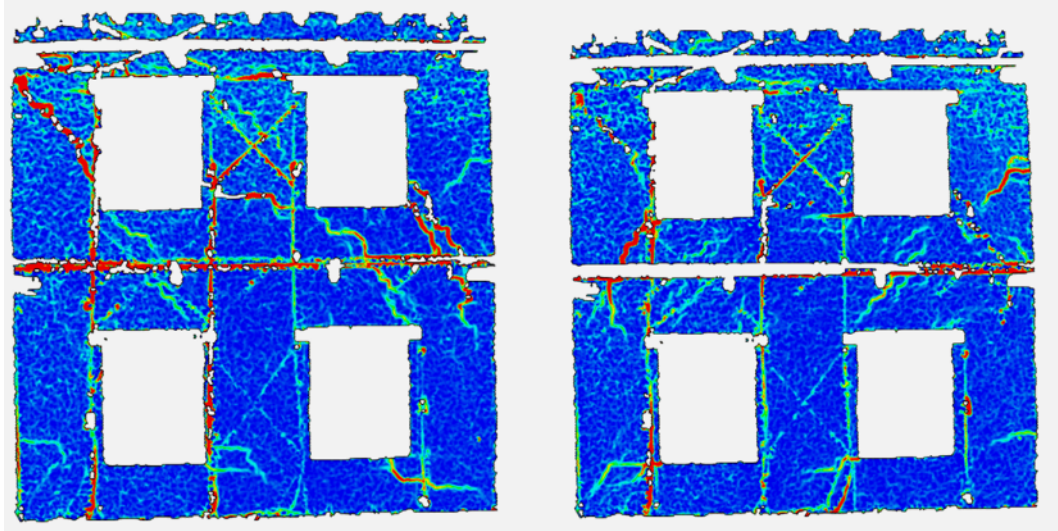
Fig. 185: Cracks on the East wall obtained by the DIC system. Red lines denote cracks. Damage when loaded in negative (left) and positive (right) directions.
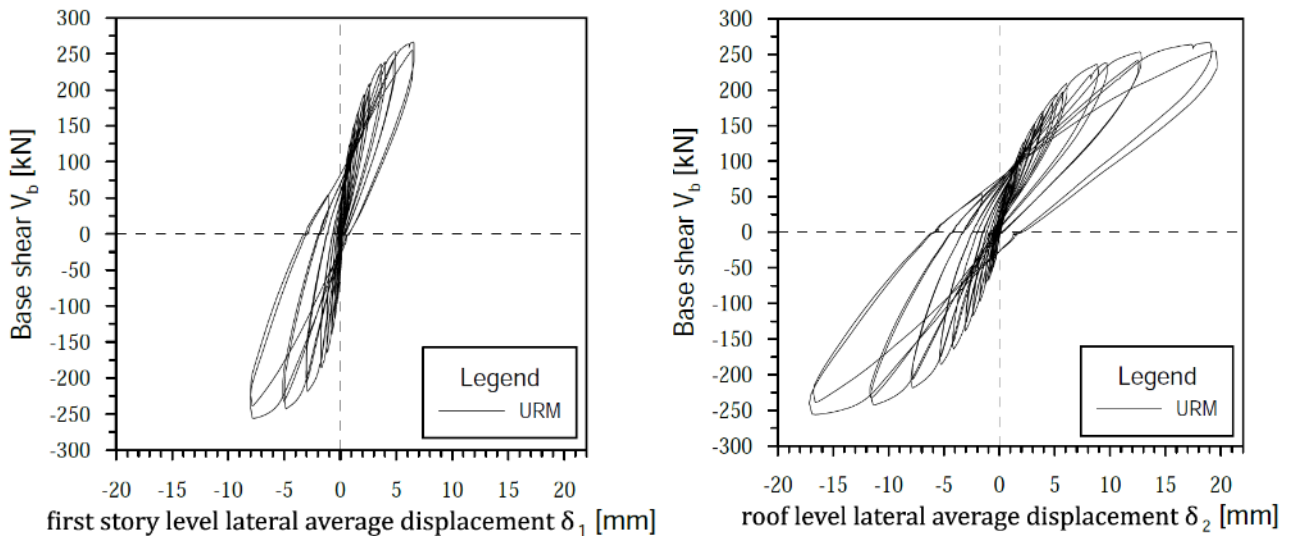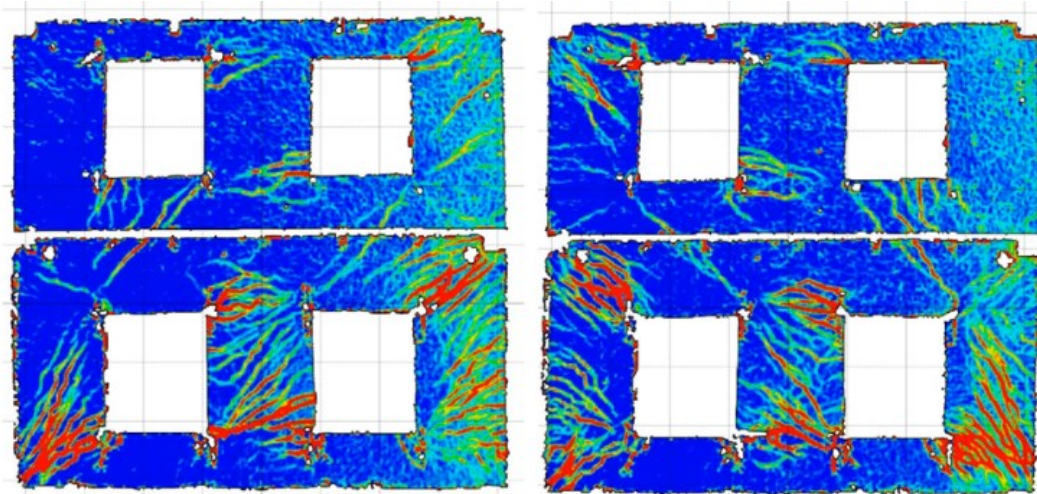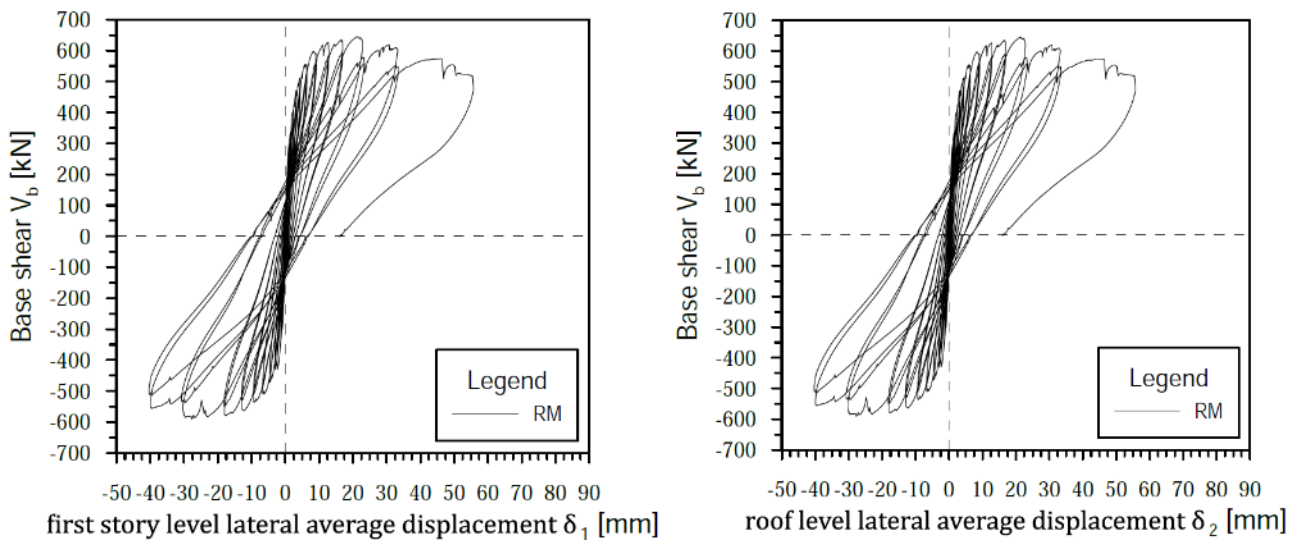

Fig. 186: Hysteretic force-displacement response curve of the strengthened pilot building

At a lateral deflection of about $\delta_2 = \pm 3.2$ mm ($V_b = \pm 390$ kN), the flexural cracks of the first story piers and the diagonal shear cracks of the spandrels began to spread. Additionally, shear cracks appeared in the ground floor piers. This caused a further reduction in stiffness with each new cycle.

After reaching a lateral deflection of about $\delta_2 = \pm 9.2$ mm ($V_b = \pm 525$ kN), cracks spread over most of the surface of the piers and spandrels of the ground floor.

When the maximum shear capacity was attained (+645 kN and -590 kN in the positive and negative loading directions), the response mechanism was fully developed, and the resistance started to decrease gradually. Once the displacement reached $\delta_2 = -33.0$ mm, the cracks in the ground-story piers opened significantly, which caused a sharp reduction of the global stiffness. Once resistance decreased by about 15% from the peak resistance (at $\delta_2 = \pm 45.0$ mm, $V_b = \pm 520$ kN), the test was changed. Instead of cyclic loads, the load was applied monotonically in the positive loading direction up to the near collapse. Near collapse was recorded at a lateral

displacement $\delta_2 = \pm 69.3$ mm and a total base shear load $V_b = +573$ kN. After that, it suddenly decreased to +509 kN as the GFRP mesh failed at the base of the piers of the ground floor.

The cross walls (South and North walls) developed out-of-plane bending damage (horizontal cracks), which was the most severe in the North-West corner.

In the elastic phase (up to $\delta_2 = \pm 3.2$ mm), an uplift of about 0.1–0.2 mm was detected by the potentiometers V1W, V13W, and V33E. This amount of uplift is negligible.

In the plastic phase, some vertical splitting cracks appeared ($\delta_2 = +33.0$ mm) along the threaded bars connecting the CRM coating of the South wall to the building foundation. The vertical uplift detected by the instrument V1W was about 16.6 mm at the highest measured top lateral displacement. Based on the damage propagation discussed above, it may be observed that a ground floor collapse mechanism dominated the structure's response.

The diagonal shear cracks intersected only two artificial diatons in the side piers. However, the connection between the leaves of the wall remained intact.

11.9 Natural frequencies and modes of vibration of the structure

The natural frequencies and modes of vibration of the pilot building were measured for four states:

- C1: URM building (undamaged)
- C2: URM building after the test (damaged)
- C3: Strengthened structure before the test (undamaged)
- C4: Strengthened structure after the test (damaged)

The results were obtained by measuring accelerations for forty minutes with a sampling rate of 300 Hz. Ambiental excitation (wind, traffic, etc.) caused vibrations of the structure.

The first and second vibration modes were always translational (see Fig. 187).

The list of all modes of vibrations, damping and eigenfrequencies is presented in Table 66.

The changes in frequencies are shown in Fig. 188. They indicate a significant decrease in frequency due to damage to the structure. Strengthening of the structure only slightly increases stiffness compared to the unstrengthened state.
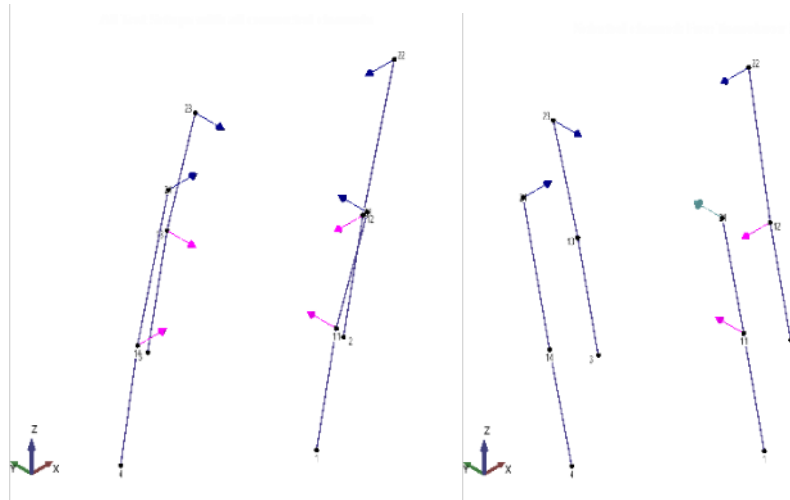
Fig. 187: The translational mode of vibration in X (left) and Y (right) directions.

Table 66: Vibration frequencies and damping.

mode	State C1		State C2		State C3		State C4	
	Freq. [Hz]	Damping [%]	Freq. [Hz]	Damping [%]	Freq. [Hz]	Damping [%]	Freq. [Hz]	Damping [%]
1	10.38	1.6	8.692	1.6	11.63	1.1	7.84	2.3
2	11.53	2.1	8.834	2.4	12.89	3.6	9.186	1.2
3	12.52	0.8	13.2	0.8	13.38	3.3	11.52	3.3
4	15.26	0.9	14.13	0.9	14.77	3	13.74	0.9
5	16.68	1.7	17.95	1.7	-	-	15.77	1
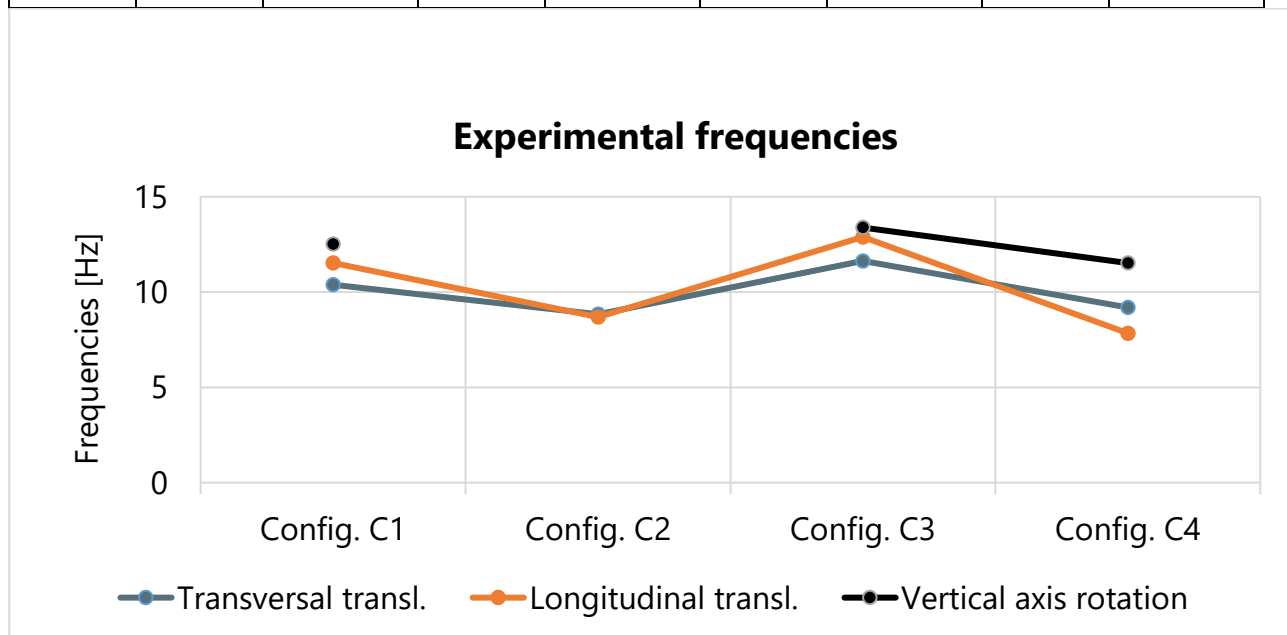
Fig. 188: Graph of changes in the frequencies.

177

11.10 Summary and analysis

Fig. 189: Effect of strengthening pilot building

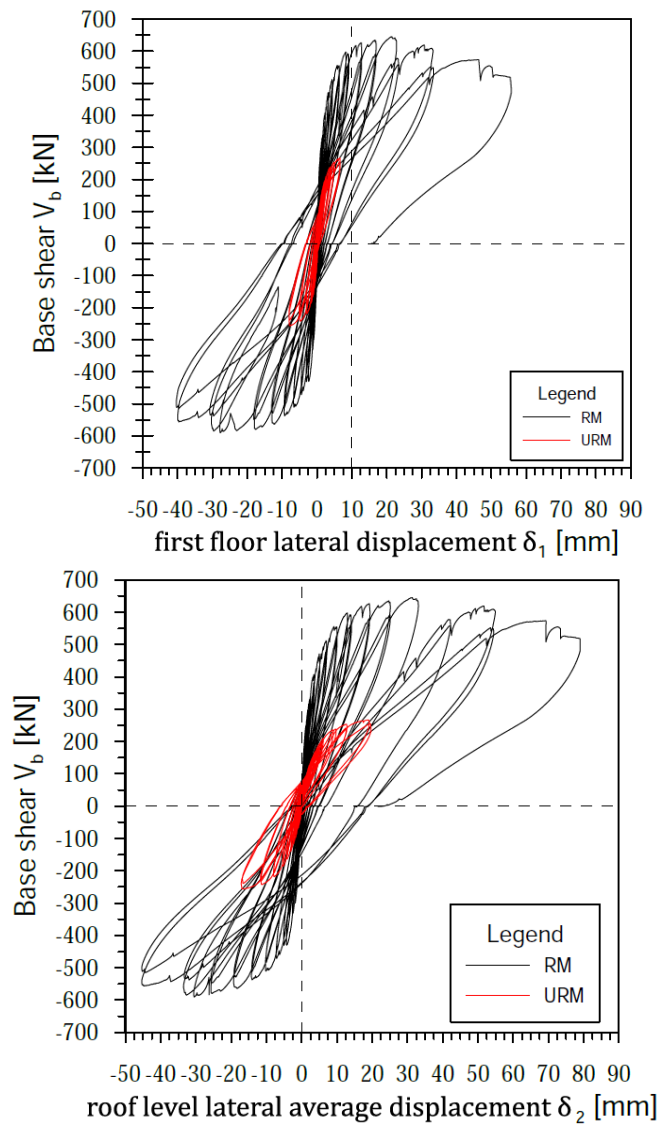The effect of the strengthening is best assessed by comparing the hysteretic response of the URM and strengthened buildings (Fig. 189). The maximum values of V_b (base shear), δ_2 (displacement at top) and γ_2 (drift of the structure) obtained in URM and RM building tests are summarized in Table 67.

Table 67: Comparison of the URM and strengthened pilot building

	Direction	$V_{b,max}$ [kN]	$\delta_{1,max}$ [mm]	$\gamma_{1,max}$ [%]	$\delta_{2,max}$ [mm]	$\gamma_{2,max}$ [%]
URM building	+	267	6.58	0.25%	19.68	0.35%
	-	256	8.02	0.31%	17.17	0.30%
Strengthened building	+	645	55.71	2.14%	78.95	1.55%
	-	590	40.35*	1.55%*	45.35*	0.89%*
Relative increase	+	2.42	8.47	8.47	4.01	4.01
	-	2.30	5.03*	5.03*	2.64*	2.64*

(*) the values of the displacement and drift do not correspond to the maximum ones because the test was stopped after loading in the positive direction.

Energy dissipation

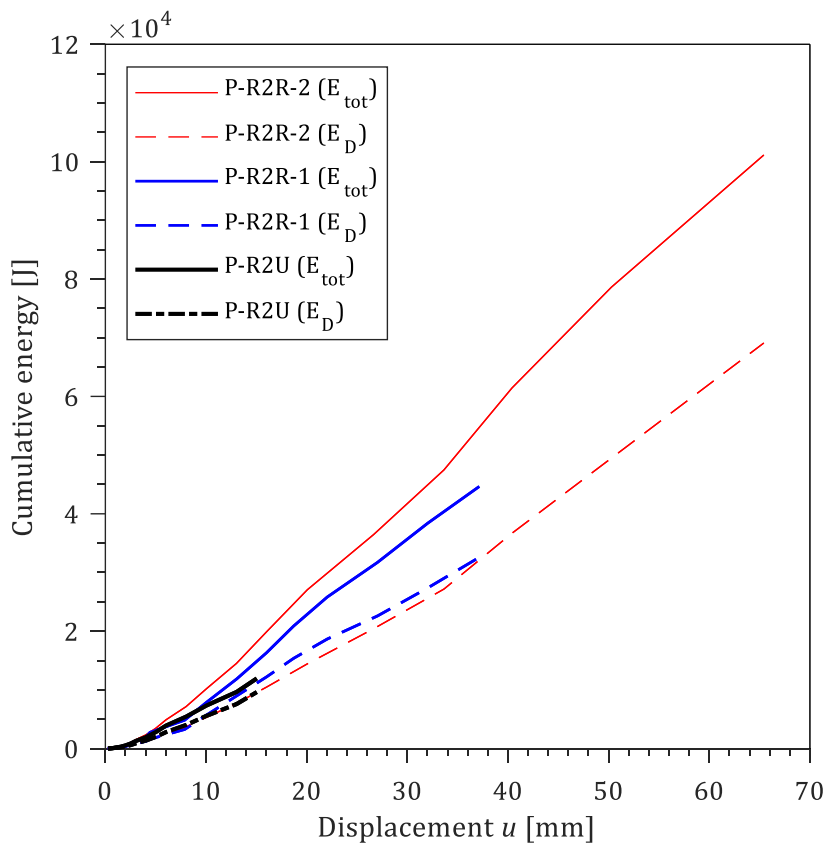*Fig. 190: Cumulative total and dissipated energy against displacement.*

Key observations

- The strengthening increased the lateral resistance of the pilot building by about 240 %, whereas the displacement capacity was four times larger.
- The energy dissipation was increased by strengthening by a factor of about 9. Note that this is lightly overestimated because the URM building was not tested up to collapse.

- In the URM masonry building, the damage (shear and bending cracks) occurred mainly in the second-floor walls, because of the low axial force in the piers. The top floor mechanism was primarily due to the flexural response of the piers.

- The reinforced coating, which has the capacity for tensile loads, has changed the response mechanism of the structure. The collapse mechanism of the strengthened structure was on the ground floor, where both bending and shear are significantly larger.

- The present test indicates that two artificial diatons per square meter are enough to prevent the separation of masonry leaves. The coating and the wall performed as a composite material until the mesh started to break.

- The reinforced building test evidenced the importance of the connection between the coating and the foundation. The connection detail should be further improved to prevent the vertical uplift phenomena of the building.

12 Summary and conclusions

This report presents the results of the CONSTRAIN project, which deals with developing and testing a new, more convenient and cost-effective system for seismic strengthening existing masonry structures. The newly developed method of strengthening is based on mortar coating, reinforced by a GFRP mesh and anchored into the masonry by two types of anchors. Crucially, the coating is applied on one side only.

Because the coating is applied only on the outside of the building, residents can stay in the building during strengthening works. Or, in the case of commercial buildings, the operation of a business does not have to be interrupted. These reasons make it much more likely for property owners to strengthen existing buildings. The alternative to strengthening is either to continue living in buildings seismically vulnerable or to demolish the building and replace it with a new one. In the former case, the situation presents a clear danger to the residents and their economic well-being. In the latter case, the cost of replacing the building is considerable in terms of money, resource use, and, by extension, emissions.

As mentioned in the introduction, designing a seismic intervention with coating on one side of the walls only is challenging. For the developed system to be successful, the existing masonry and coating should work together as a composite material. Achieving the composite action of both materials is not simple, as the materials are quite different in terms of stiffness and non-linear behavior. Proper composite action of both materials is achieved only if the coating and the masonry walls are balanced and adequately anchored together. Furthermore, it is virtually impossible to know if an intervention is efficient without extensive experimental testing. In the present project, a new seismic strengthening intervention was designed combining and merging the knowledge of all partners and subsequently extensively tested to verify its efficiency.

The cyclic shear compression tests on masonry piers (presented in Section 6) were carried out on stone and brick masonry in reference and strengthened states. One and two-sided wall strengthening were tested for comparison. The tests showed that all types of considered strengthening significantly changed the response of the piers. The response mode was changed, and if the unstrengthened walls developed extensive damage in a few concentrated cracks, the strengthened walls developed dispersed damage over a large area. This change allowed the piers to dissipate more energy by orders of magnitude and thus improving their seismic response. The resistance and displacement capacities were also substantially increased. The bond between the coating and the wall was lost under cracks. Still, the anchoring provided a sufficient connection to ensure the composite action of the wall-coating system until collapse. The two-sided strengthening offered higher strength and displacement capacity increase than the one-sided strengthening, but the effect of one-sided strengthening was already substantial.

The out-of-plane bending tests on piers (presented in Section 7) were performed to obtain information for design against local failures. The tests showed that the out-of-plane resistance of strengthened walls is about ten times larger than the resistance of unstrengthened walls and thus conclusively demonstrated that the developed intervention all but prevents out-of-plane failure.

Masonry spandrels specimens were so large that they had to be constructed on the newly developed and assembled test apparatus. The results (shown in Section 8) were very interesting and showed the positive effect of a strong lintel, as was the case of stone masonry. In contrast, the poor performance of the unstrengthened brick masonry spandrel with flat brick arch clearly evidenced low resistance and brittle failure. The peculiarity of spandrels compared to piers is that they have negligible axial force. This crucial difference makes the effect of coating more pronounced. As in the case of piers, damage to strengthened walls was distributed over the entire surface of spandrels, whereas in the unreinforced walls, it was concentrated in a few cracks. This has again contributed to much higher energy dissipation and displacement capacity. In the case of stone masonry, also the strength increased substantially. In the case of brick masonry, however, the increase in strength was more modest. The overall assessment from the tests was that coating and wall performed well together and functioned as a composite element until collapse.

As part of the systematic intervention solution, a new method was proposed to strengthen the top tie-beam of walls and is presented in Section 9. It consists of demolishing the top few rows of masonry and rebuilding it with GFRP mesh in bed joints. The tests were carried out as a cyclical three-point bending test in the horizontal direction to analyze the out-of-plane performance of such an intervention. The results for stone and brick masonry indicated a significant increase in strength. The final collapse was always by fracture of the strands of the composite mesh.

An alternative to classical steel bar tie beams at mid-floor levels was tested on C-shaped samples with carbon strips applied on only one side (Section 10). The tests showed that the strips could be very effective in increasing the walls' displacement and energy dissipation capacities, which was confirmed also by numerical simulations.

In Section 11, the tests on the pilot building are presented. The two-storey pilot building was tested next to a reaction wall to a (pseudo-static) simulated seismic load. The test's purpose was to demonstrate the performance of the systemic intervention with actual boundary conditions. This is in contrast to the boundary conditions in tests on structural elements, which are always idealised, and presents the most realistic assessment of seismic performance.

The building was first tested up to considerable but still repairable damage in order to assess the performance of the unreinforced structure. The damage was partly repaired by sealing the cracks, and then, the pilot building was strengthened using the newly developed one-sided strengthening technique. The strengthened building was tested the same way as the unreinforced one until near collapse.

The difference in response between unreinforced and strengthened structures was substantial. In the unreinforced building, the top floor was only lightly loaded in compression (weight of the timber roof), and due to the negligible tensile strength of masonry, the failure occurred on the top floor. The damage was concentrated in a few large cracks, and the energy dissipation and displacement capacity were low. On the other hand, the strengthened building had a coating with substantial tensile strength. This altered the response mechanism and the strengthened structure failed on the ground floor. The damage in the form of many smaller

cracks was distributed over a large area of the structure. The strengthened structure's strength (capacity) was increased by 140 % compared to the unreinforced state. Displacement capacity and energy dissipation increased by substantial margins. The final failure was due to mesh fracture, which indicated that the materials were fully utilized, and that the intervention worked as intended.

Acknowledgements

References

M. Dolce, «Schematizzazione e modellazione per azioni nel piano delle pareti, Corso sul consolidamento degli edifici in muratura in zona sismica, Ordine degli Ingegneri, Potenza». 1989.

Federal Emergency Management Agency, *ATC FEMA 306: Evaluation of earthquake damaged concrete and masonry wall buildings – Basic Procedures Manual*, n. ATC FEMA 306. 1999.

midas Gen. MIDASoft, Inc., 2021.

V. Turnsek e F. Čačovič, «Some experimental results on the strength of brick masonry walls», *Proceedings of the 2nd international brick masonry conference, Stoke-on-trent*, pagg. 149–56, 1970.

I. Boem e N. Gattesco, «Rehabilitation of Masonry Buildings with Fibre Reinforced Mortar: Practical Design Considerations Concerning Seismic Resistance», *Key Eng. Mater.*, vol. 898, pagg. 1–7, ago. 2021, doi: 10.4028/www.scientific.net/KEM.898.1.

European Union, *EN 1996-1-1: Eurocode 6: Design of masonry structures - Part 1-1: General rules for reinforced and unreinforced masonry structures*. 2005.

European Union, *EN 1998-1: Eurocode 8: Design of structures for earthquake resistance – Part 1: General rules, seismic actions and rules for buildings*. 2004.

S. Cattari e S. Lagomarsino, «A Strength Criterion For The Flexural Behaviour Of Spandrels In Unreinforced Masonry Walls», 2008.

N. Gattesco, L. Macorini, e A. Dudine, «Experimental Response of Brick-Masonry Spandrels under In-Plane Cyclic Loading», *J. Struct. Eng.*, vol. 142, n. 2, Art. n. 2, feb. 2016, doi: 10.1061/(ASCE)ST.1943-541X.0001418.

Ministero delle Infrastrutture e dei Trasporti, *NTC 2018: Aggiornamento delle «Norme tecniche per le costruzioni».*

Ministero delle Infrastrutture e dei Trasporti, *CIRCOLARE 21 gennaio 2019, n. 7 C.S.LL.PP.: Istruzioni per l'applicazione dell'«Aggiornamento delle "Norme tecniche per le costruzioni"» di cui al decreto ministeriale 17 gennaio 2018.*

CNR DT 200 R1/2013 (2013) 'Instructions for the Design, Execution and Control of Static Consolidation Interventions through the use of Fiber-reinforced Composites'. National research Council, Rome, Italy.

CNR-DT 203/2006 (2007) 'Guide for the Design and Construction of Concrete Structures Reinforced with Fiber-Reinforced Polymer Bars'. National research Council, Rome, Italy.

N. Gattesco e I. Boem, «Experimental and analytical study to evaluate the effectiveness of an in-plane reinforcement for masonry walls using GFRP meshes», *Constr. Build. Mater.*, vol. 88, pagg. 94–104, lug. 2015, doi: 10.1016/j.conbuildmat.2015.04.014.

N. Gattesco e I. Boem, «Out-of-plane behavior of reinforced masonry walls: Experimental and numerical study», *Compos. Part B Eng.*, vol. 128, pagg. 39–52, nov. 2017, doi: 10.1016/j.compositesb.2017.07.006.

N. Gattesco e I. Boem, «Characterization tests of GFRM coating as a strengthening technique for masonry buildings», *Compos. Struct.*, vol. 165, pagg. 209–222, apr. 2017, doi: 10.1016/j.compstruct.2017.01.043.

Abaqus/CAE v.6.12 Documentation Collection, Dassault Systèmes, 2012.

N. Gattesco, C. Amadio, e C. Bedon, «Experimental and numerical study on the shear behavior of stone masonry walls strengthened with GFRP reinforced mortar coating and steel-cord reinforced repointing», *Eng. Struct.*, vol. 90, pagg. 143–157, mag. 2015, doi: 10.1016/j.engstruct.2015.02.024.

J. Lubliner, J. Oliver, S. Oller, e E. Oñate, «A plastic-damage model for concrete», *Int. J. Solids Struct.*, vol. 25, n. 3, pagg. 299–326, 1989, doi: 10.1016/0020-7683(89)90050-4.

J. Lee e G. L. Fenves, «Plastic-Damage Model for Cyclic Loading of Concrete Structures», *J. Eng. Mech.*, vol. 124, n. 8, pagg. 892–900, ago. 1998, doi: 10.1061/(ASCE)0733-9399(1998)124:8(892).

A. K. Pandey e R. S. Bisht, «Numerical Modelling of Infilled Clay Brick Masonry under Blast Loading», Adv. Struct. Eng., vol. 17, n. 4, pagg. 591–606, apr. 2014, doi: 10.1260/1369-4332.17.4.591

X. Y. Xiong, R. J. Xue, S. Zhang, e L. J. Wang, «The Finite Element Analysis on Seismic Performance of Ring Beam and Constructional Column with Different Storey in Masonry Building», *Adv. Mater. Res.*, vol. 919–921, pagg. 1016–1019, apr. 2014, doi: 10.4028/www.scientific.net/AMR.919-921.1016.

N. Gattesco, I. Boem. «Characterization tests of GFRM coating as a strengthening technique for masonry buildings», Composite Structures, 2017, doi: 10.1016/j.compstruct.2017.01.043